

HIERARCHICAL DECENTRALIZED OPTIMAL CONTROL AND  
RECONFIGURATION OF NETWORKED MICROGRIDS IN THE POWER  
DISTRIBUTION SYSTEM

by

Aravind Ingalalli

A dissertation submitted to the faculty of  
The University of North Carolina at Charlotte  
in partial fulfillment of the requirements  
for the degree of Doctor of Philosophy in  
Electrical Engineering

Charlotte

2023

Approved by:

---

Dr. Sukumar Kamalasan

---

Dr. Valentina Cecchi

---

Dr. Abasifreke Ebong

---

Dr. Russell Keanini

©2023  
Aravind Ingalalli  
ALL RIGHTS RESERVED

## ABSTRACT

ARAVIND INGALALLI. Hierarchical decentralized optimal control and reconfiguration of networked microgrids in the power distribution system. (Under the direction of DR. SUKUMAR KAMALASADAN)

Advancements in information and communication technology, decentralized digital economic structures, and data-driven learning-based technology have transformed distribution networks as a system of systems in recent decades. With the rapid integration of sustainable energy resources, the ecosystem surrounding the electricity consumer is getting socially, economically, and politically complex. The key operational challenge is the coexistence of large-scale distributed energy resources (DER) to achieve stable load power sharing while regulating the voltage and frequency in the network to the nominal values.

The vision of the dissertation work is to formulate a hierarchical decentralized control structure to accommodate three-level research objectives. First, at the DER level, considering the low  $X/R$  and unbalanced nature of the distribution network, appropriate cascaded primary control loops are designed. A unified control architecture is proposed for stable multiple DER power sharing, achieving ride-through capability, and maintaining the network voltage and frequency close to nominal values. The unified control architecture is devised through a systematic definition of steady-state operating modes and the interaction among hierarchical entities in the grid. Second, a decentralized predictive optimal constrained secondary control framework is formulated at the microgrid level to maintain the nominal voltage and frequency. The proposed strategy is built on a first-order model of the primary controller and local/global measurements-based state estimation, facilitating the deployability to grid edge devices. The framework is further extended to incorporate a data-driven approach when model parameters are unavailable. Finally, at the network level, detailed network dynamics are modeled in a real-time environment by incorporating primary, and secondary control and protection functions. The reinforcement learning agent is designed using an extended Q-routing methodology, which interacts with the environment through event-driven communication and performs optimal network reconfiguration during events in the environment. Another goal of this dissertation work is to bring value to engaged stakeholders in the process of achieving a 100% sustainable power grid. There exists an execution gap between the aforementioned hierarchical technology solutions and business delivery models. This gap is addressed in the dissertation by fostering an implementation strategy for resiliency services through the energy-as-a-service model. The regulatory framework and ownership agreements are yet to evolve to support the delivery model acceptable to the involved stakeholders.

DEDICATION

To Anjana & Arya

## ACKNOWLEDGEMENTS

Professor Sukumar Kamalasan, I would like to express my sincere gratitude to you as my advisor, for offering the opportunity to be a part of your research projects. It is my pleasure to have you as my academic teacher, research advisor, mentor for lab projects, and behavioral guide. Thank you for giving me the option to choose a research area of my interest at the beginning of the Ph.D. program, for the freedom you have given me to explore research problems, and for the guidance, patience, and care with which you have helped me grow as a researcher. I would like to sincerely thank Professor Abasifreke Ebong, Professor Valentina Cecchi, and Professor Russell Keanini, for being part of my dissertation committee. You all have given valuable inputs to improve my research work and helped me gain the knowledge required for completing my Ph.D. program. I am thankful to Professor Tim Hansen and Professor Reinaldo Tonkoski for their support and guidance during my early academic research days at South Dakota State University.

Special thanks to Phani Harsha Gadde from Clemson University for fruitful discussion and knowledge sharing during the DOE project execution. A big thanks to my collaborators Guna Bharati and Zerui Dong from Opal-RT, who helped me to demonstrate a part of my research ideas on the real-time simulator. To all my peers in the UNCC PEISL lab - Ali Aygun, Tarik Chowdhury, Roopa Ramachandran, Anuprabha Nair, Krishna Murari, Arun Suresh, Biswajit Dipan Biswas, Bilkis Banu, Sheikh Jakir Hossain, Robin Bisht, Aniket Joshi, and many others, thank you for the interesting discussions, collaboration, and assistance. I would also like to thank the Department of Energy, National Science Foundation, Duke Energy, UNC Charlotte EPIC, ECE department, and graduate school for providing me with financial assistance to accomplish my research work.

Professor R. I. Ingalalli, as your son, I am fortunate to get affectionate guidance and feedback on my research progress throughout my Ph.D. journey. My mother Basavanti, you have been offering continuous comfort, emotional support, and encouragement to accomplish my research goals. I would like to express my sincere gratitude to both of you. I would like to thank my in-laws, for the visit and support here in Charlotte that helped me to focus on my research work. Brother Vijay, I am blessed to share this ride with you and thank you for the inputs and suggestions from your Ph.D. experience. My wife Anjana, you have been there with me all the way through, with unconditional love and support and always a listening ear. I am enormously grateful to you for managing our family along with your work during the challenging times of my Ph.D. Arya, you have been my motivation and one of the reasons to take up the Ph.D. program and when you grow up, I am sure I have got a lot of stories to tell you.

## TABLE OF CONTENTS

LIST OF TABLES	xi
LIST OF FIGURES	xii
CHAPTER 1: Introduction	1
1.1. Clean Energy for Humanity	1
1.2. Decentralization: Key to a Democratic Power System	2
1.3. Timescale of Control Applications	3
1.4. Outline of the Dissertation	4
1.5. Main Contribution of the Dissertation	6
CHAPTER 2: DER Integrated Power Distribution Network	9
2.1. Modern Power Distribution Network	9
2.1.1. Network Characteristics and Challenges	10
2.1.2. IBR Power Sharing Strategies	11
2.1.3. Theory Behind Droop Law	12
2.1.4. Need for the Decentralized Secondary Control	14
2.2. Review of Control Frameworks	16
2.2.1. Centralized Frameworks	16
2.2.2. Distributed Frameworks	16
2.2.3. Decentralized Frameworks	17
2.2.4. Network Control Frameworks	17
2.3. Review of Discrete-time Control Methods	18
2.3.1. PI Control	18
2.3.2. PR Control	19
2.3.3. LTI MPC	19
2.3.4. Q-learning-based Control	21
2.3.5. Comparison of the Control Methods	21
2.4. Scope of the Dissertation	22
2.5. Summary	23

CHAPTER 3: A Sequence-based Unified Control Architecture for Multiple IBR Modes of Operation	24
3.1. Introduction	24
3.2. Research Contributions	26
3.3. Control Architecture for IBRs in an Unbalanced System	27
3.3.1. System Description in terms of PNS Components	27
3.3.2. Design Approach for the PNS Controller	29
3.3.3. Description of <i>LCL</i> Plant Representation	29
3.3.4. PS Voltage-based PLL	30
3.3.5. Design of PNS Current Control Loop	31
3.3.6. Design of PNS Voltage Control Loop	32
3.3.7. Strategy for PNS Current Limiting in <i>dq</i> -frame	33
3.4. Unified Architecture for Multiple IBR Operation with Seamless Transition	34
3.4.1. PS Power Control Methodology	35
3.4.2. NS Power Control Methodology	37
3.4.3. Mode Transitioning and Synchronization Mechanism	38
3.4.4. Stability Analysis	39
3.5. Real-time Multi-rate MIL Set-Up and Results	40
3.5.1. Unbalanced Fault in Type 0 PS Mode	42
3.5.2. Unbalanced Fault in Type 1 PS Mode	43
3.5.3. Type 1 PS Mode Power Sharing Analysis	44
3.5.4. Impact of Communication Network Latency	46
3.5.5. Dynamic Change in the IBR Roles	47
3.5.6. CL Estimation with % Grid Unbalance	48
3.5.7. Transition from Type 1 to Type 0 PS Mode	48
3.6. Summary	49
CHAPTER 4: Decentralized State Estimation-based Optimal Integral Model Predictive Control of Voltage and Frequency	50
4.1. Introduction	50
4.2. Research Contributions	53

4.3. Overview of Hierarchical PC and SC	54
4.3.1. Description of Control Architecture	54
4.3.2. Review of the Problem Description	55
4.3.3. DER - MG Interaction Model	56
4.3.4. Synthesis of Decentralized Secondary Controller	58
4.4. Decentralized IMPC Framework	58
4.4.1. Formulation of Decentralized Optimal Control	58
4.4.2. AIM Incorporating the Output Integral Action	60
4.4.3. Dynamic Synchronization of the AIM states	61
4.4.4. Prediction Model	63
4.4.5. Formulation of Optimal Control with the Constraints	63
4.4.6. Communication Network Performance	65
4.5. RT multi-core multi-rate MIL set up and Results	66
4.5.1. Discrete-time AIM-based Stability Analysis	67
4.5.2. Analysis of Primary Controller and State Estimation	68
4.5.3. Voltage and Frequency Restoration Post Islanding	69
4.5.4. Regulation during Load Change	70
4.5.5. Controller Performance during Fault Scenario	70
4.5.6. Impact of Latency on Voltage Restoration	72
4.5.7. Plug-and-Play Capability Performance Analysis	72
4.5.8. Controller Performance with Noisy Measurements	73
4.6. Summary	73
CHAPTER 5: Data-driven Decentralized Online System Identification-based Integral Model Predictive Control of Voltage and Frequency	75
5.1. Introduction	75
5.2. Research Contributions	77
5.3. System Overview	78
5.3.1. Distribution Network Characteristics	78
5.3.2. Description of Primary Controller	79
5.3.3. Description of Secondary Controller	79

5.4. Mathematical Preliminaries and Problem Formulation	80
5.4.1. Large Signal Dynamic Model of an Islanded MG	80
5.4.2. Synchronization of Local and Global States	81
5.4.3. Formulation of Data-driven Decentralized System Dynamics	82
5.5. Decentralized IIMPC Framework	82
5.5.1. Online Identification of the Subsystem Dynamics	83
5.5.2. Augmented Model Incorporating the Integral Action	84
5.5.3. Formulation of Optimal Control with the Constraints	85
5.5.4. Controller Feasibility and Stability Analysis	88
5.5.5. Impact of Communication Latency	89
5.6. Real-Time (RT) multi-rate Model-in-the-Loop (MIL) Test-Bed and Results	89
5.6.1. Verification of Primary Controller Response	90
5.6.2. Analysis of Voltage and Frequency Regulation	91
5.6.3. Plug-and-Play Capability Performance Analysis	92
5.6.4. Controller Performance during Fault Scenario	94
5.6.5. Influence of Communication Delay	95
5.6.6. Voltage Signal Quality at POI	95
5.7. Summary	95
CHAPTER 6: An Extended Q-routing-based Event-driven Dynamic Re-configuration of Networked MGs	97
6.1. Introduction	97
6.2. Research Contributions	99
6.3. Components of MG Control and Protection	100
6.3.1. Overview of the IBR control	101
6.3.2. Primary Controller	101
6.3.3. Secondary Controller	103
6.3.4. Protection Functions	103
6.4. Event Driven Dynamic Optimal Reconfiguration Framework	104
6.4.1. Graph Theory-based Dynamic Networked MG Model	104

6.4.2.	Formulation of RL-based Optimal Reconfiguration	105
6.4.3.	Proposed Q-routing based Optimal Path Identification	108
6.5.	RT Set-up and Discussion of Results	108
6.5.1.	Implementation of Event-driven Communication	110
6.5.2.	Comparison Between the Q-routing and BFS Methods	111
6.5.3.	Sequence of Events	112
6.5.4.	Behavior of the Environment and RL Agent Actions	112
6.5.5.	Timing Analysis during an Event	115
6.5.6.	IBR Powers during Reconfiguration	115
6.5.7.	MG Voltage and Frequency during Reconfiguration	116
6.6.	Summary	116
CHAPTER 7:	Participation of Networked Microgrids in Energy-as-a-Service Model for Enhancing Grid Resiliency	117
7.1.	Introduction	117
7.2.	Technology Potential of Networked MGs	119
7.2.1.	Networked MGs in Distribution System	119
7.2.2.	Market Needs and Underlying Opportunities	120
7.3.	EaaS Delivery Model for the Networked MG	121
7.3.1.	EaaS Delivery Model Architecture	121
7.3.2.	Resiliency-as-a-Service Framework	123
7.3.3.	Demonstration of Load Support Use Case	125
7.4.	Need for Sustainable Business Model Innovation	126
7.5.	Summary	128
CHAPTER 8:	Conclusions	129
8.1.	Future Research Directions	131
CHAPTER 9:	List of Publications	134
REFERENCES		135

## LIST OF TABLES

TABLE 2.1: Comparison between different control methods.	22
TABLE 3.1: Variable and parameter configuration.	35
TABLE 3.2: Summary of system and controller parameters	41
TABLE 3.3: Comparison between proposed droop and robust angle droop.	46
TABLE 4.1: Electrical parameters and phase-wise loading.	66
TABLE 4.2: System and controller parameters	68
TABLE 4.3: Comparison of IMPC and optimal PI controller performance.	71
TABLE 4.4: Performance under communication latency	72
TABLE 5.1: IIMPC system and controller parameters.	91
TABLE 5.2: IIMPC performance evaluation.	94
TABLE 5.3: Voltage THD during steady-state and events	94
TABLE 6.1: Load shedding nodes in the islanded mode.	109
TABLE 6.2: Generation capacity and loading	109
TABLE 6.3: IBR electrical parameters.	110
TABLE 6.4: System and controller parameters	110
TABLE 6.5: Optimal paths from BFS and Q-routing methods.	111
TABLE 7.1: Critical load clustering in the section of IEEE 123 bus system.	126

## LIST OF FIGURES

FIGURE 1.1: Decentralized decision systems	3
FIGURE 1.2: Summary of literature survey for control applications.	4
FIGURE 1.3: Dissertation outline	6
FIGURE 2.1: Comparison between droop and VOC control	12
FIGURE 2.2: Parallel IBR operation.	13
FIGURE 2.3: IBR-grid Interaction dynamics.	14
FIGURE 2.4: Control framework categories	17
FIGURE 2.5: Distribution network control architecture.	18
FIGURE 3.1: IBR PNS primary controller overview.	27
FIGURE 3.2: PNS voltage in dq-axis	28
FIGURE 3.3: LTI system theory-based design	29
FIGURE 3.4: Linearized small signal model of PLL	30
FIGURE 3.5: Linearized PS voltage-based PLL Bode plot	31
FIGURE 3.6: CC Bode plot	32
FIGURE 3.7: VC Bode plot	33
FIGURE 3.8: Proposed current limiter.	34
FIGURE 3.9: Proposed unified architecture for multiple IBR operation	36
FIGURE 3.10: PS PLL-based synchronized grid connection for IBRs.	39
FIGURE 3.11: Eigenvalue-based stability analysis	39
FIGURE 3.12: Opal-RT-based real-time verification set-up	41
FIGURE 3.13: Fault response in Type 0 PS mode	42
FIGURE 3.14: Power spectrum for Type 0 and Type 1 mode	43
FIGURE 3.15: Fault response in Type 1 mode	44
FIGURE 3.16: Verification of Type 1 mode operation	45
FIGURE 3.17: Response to nonlinear load in Type 1 mode	46
FIGURE 3.18: Transition to Type 1 PS mode considering latency.	47
FIGURE 3.19: Dynamic role changing of IBRs	47
FIGURE 3.20: Grid Thevenin impedance vs IBR peak current	48
FIGURE 3.21: Transition to Type 0 PS mode considering latency.	49

FIGURE 4.1: Overview of the decentralized secondary control.	54
FIGURE 4.2: Nature of robust droop behavior.	56
FIGURE 4.3: IMPC-DEKF framework	59
FIGURE 4.4: RT set-up to validate model-based IMPC framework.	67
FIGURE 4.5: Stability analysis of decentralized IMPC control	69
FIGURE 4.6: Voltage and frequency without the secondary controller.	70
FIGURE 4.7: Secondary control action for islanding and load changes.	71
FIGURE 4.8: Validation of plug-and-play feature.	73
FIGURE 4.9: Performance under noisy measurements.	73
FIGURE 5.1: Decentralized IIMPC framework.	83
FIGURE 5.2: Verification of system identification and state correction.	92
FIGURE 5.3: Real-time simulator results for IIMPC test cases.	93
FIGURE 5.4: POI voltage signal quality.	94
FIGURE 6.1: Hierarchical IBR control	100
FIGURE 6.2: IBR integrated IEEE 123 node network.	105
FIGURE 6.3: Proposed dynamic framework.	106
FIGURE 6.4: Event-based RT communication set-up.	109
FIGURE 6.5: Fault detection and clearing.	112
FIGURE 6.6: RL agent actions.	113
FIGURE 6.7: Timing analysis.	113
FIGURE 6.8: Case studies with the graphical flow.	114
FIGURE 6.9: MG status during reconfiguration.	114
FIGURE 6.10: IBR powers during reconfiguration.	114
FIGURE 6.11: Voltage and frequency at SSs.	115
FIGURE 7.1: Simplistic representation of networked MG	119
FIGURE 7.2: EaaS delivery model and its primary properties.	122
FIGURE 7.3: RaaS framework for networked MGs.	124
FIGURE 7.4: Load support use case.	125
FIGURE 7.5: Load support use case demonstration.	126

## CHAPTER 1: Introduction

*The measure of greatness in a scientific idea is the extent to which it stimulates thought and opens up new lines of research.*

---

Paul Dirac

At the outset, the dissertation discusses the broader aspects such as the necessity of clean energy for the benefit of humanity in Section 1.1, and decentralization as a key entity to achieve the democratization of the power system in Section 1.2. Section 1.3 provides the background of the timescale of control applications in the power distribution network. With this background, Section 1.4 illustrates the core problem for the dissertation including the organization of the upcoming chapters. The major contribution of the dissertation is discussed in Section 1.5.

### 1.1 Clean Energy for Humanity

The impact of climate change has increased the frequency and severity of weather-related events globally. The year 2019 is the sixth consecutive year in which ten or more billion-dollar weather and climate disaster events have affected the United States [1]. The prevailing electric power infrastructure is prone to disastrous events leading to larger power outages in a distribution system. Consequently, the decarbonization targets due to the concerns of climate change and the loss of traditional economies of scale have led to the rapid integration of distributed energy resources (DER) in the power distribution systems [2]. The affordable clean energy DER technology such as photo-voltaic and battery energy storage is predominantly integrated into the power distribution grid. Sophisticated control and management of DERs have led to the emergence of microgrids (MG). According to the Department of Energy, the MG is defined as, "*a group of interconnected loads and DERs within clearly defined electrical boundaries that act as a single controllable entity with respect to the grid and that connects and disconnects from such grid to enable it to operate in both grid-connected or islanded mode.*" For the concerned stakeholders, the objectives of deploying an MG, such as economic benefits, sustainable generation, reliability, energy security, and resiliency during extreme weather events are implicit in the business case. [3].

The conventional power management and delivery model is highly centralized and vertically integrated. To enable grid resiliency under the circumstances, traditional reliability

requirements such as contingency criterion (N-1, or N-2) are not sufficient to ensure the availability of power. Such measures are rather feasible for low-impact/highly-probable events than high-impact events [4]. The DERs that are part of MGs are interfaced with the power distribution system through the inverter-based resources (IBR) with a hierarchical control and communication system [5]. IBRs play an important role in coupling the DC side of the DERs to the AC power grid, enabling distributed generation, and improving the utilization of local renewable energy-based resources at the network level. Thus the power distribution system is evolving towards a highly sustainable and resilient cyber-physical energy platform, where multiple MGs can be seamlessly interconnected. An aggregatory layer can be built to coordinate and distribute the energy and information in real-time, enabling market opportunity for emerging business models such as energy-as-a-service. The technology deployment of networked MGs is feasible as more end users are willing to install in-house generation and storage either by owning or leasing the assets to reduce electricity costs and secure critical loads. Technology maturity together with appropriate business models facilitate higher penetration levels of renewable generation aiding the transition towards clean-energy infrastructure [6]. This dissertation aims to work towards developing comprehensive methodologies to integrate hierarchical decentralized control technologies to achieve 100% sustainable energy resource-based power grid operation. The solution approach definitely would enhance the stability and resiliency of the power distribution network, meanwhile generating value for the involved stakeholders.

## 1.2 Decentralization: Key to a Democratic Power System

The scope of the dissertation is to study structure and design of the hierarchical optimal control problem in large-scale networks such as power distribution networks. In such networks, designating control and decision-making ability to a centralized entity has multi-fold demerits. The central entity requires an expensive computation and communication infrastructure that is prone to single point of failure and design complications [7–9]. This is the motivation to decentralize control and decision-making ability through the systematic design of the localized control strategies [10–13]. Local entities would require limited communication and computational resource, and offer the capability of plug-and-play, and self-healing, thereby achieving greater autonomy in the network behavior [14–16]. Decentralization of control and decision-making is observed in widespread applications in various domains such as biology, a market economy, computer science, political science, and power system [17–26] (see Fig. 1.1). In these applications, central control and decision-making authority are systematically localized, and the local entities independently or with limited interaction achieve the network-level goals.

The objective of this dissertation is to systematically classify the controller goals at the

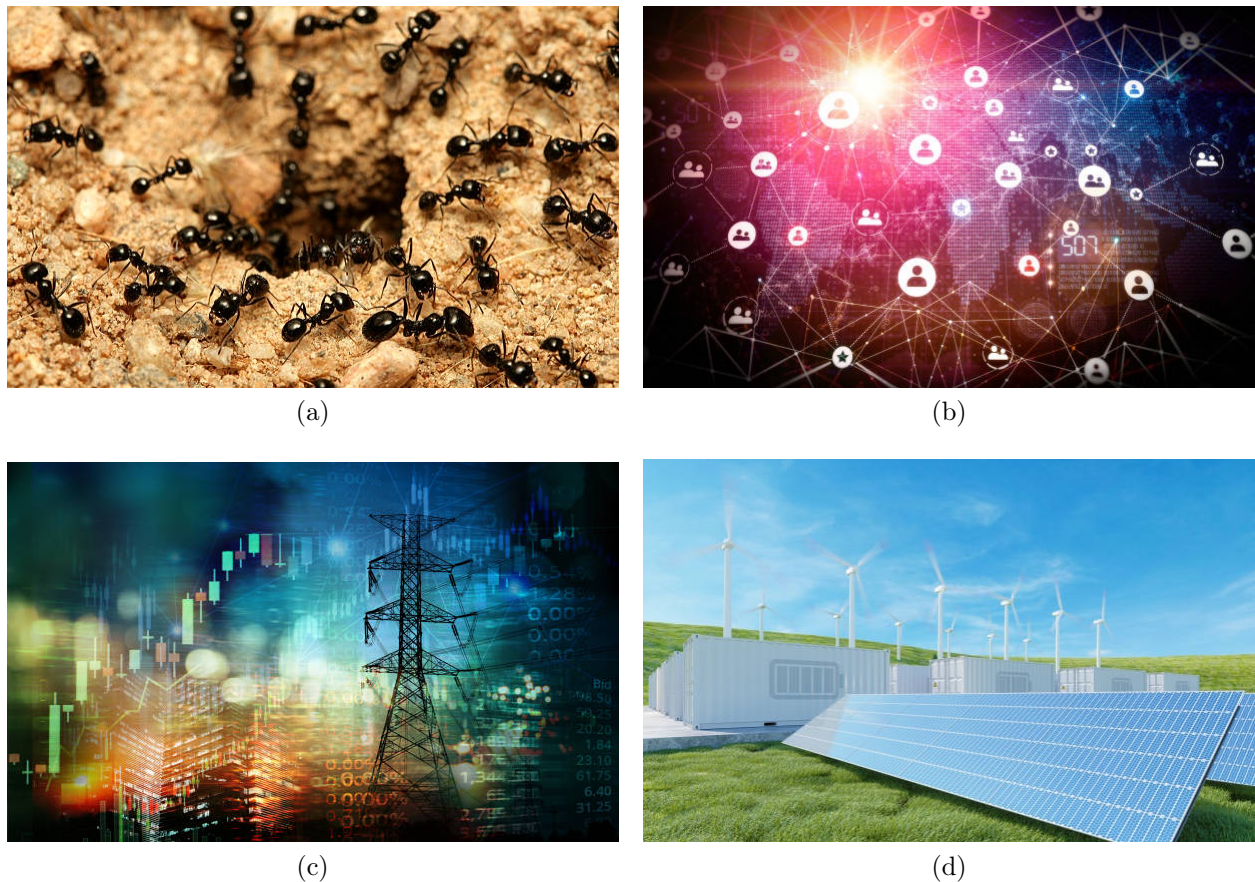


Figure 1.1: (Image courtesy: [www.istockphoto.com](http://www.istockphoto.com)) Decentralized decision systems (a) without a leader, ants work together using simple olfactory interactions, and collective behavior solves the ecological problems such as building a new colony [17, 18] (b) a decentralized autonomous organization is an emerging legal structure that takes decision based on bottoms-up management approach without having any central governing body [19–21] (c) peer-to-peer energy markets can perform a decentralized decision making for optimal price clearance [22,23] (d) sustainable generators in the power grid share the load power using a communication-less droop technique without the need of a central controller [24–27].

device level, system level, network level and develop a hierarchical decentralized methodology to optimally achieve the identified goals. The design aspects incorporate (a) no information exchange among the subsystems leading to design scalability, (b) high fidelity low order models enabling deployability to the grid edge devices, (c) the learning behavior to achieve a network topology agnostic solution. By shifting the control and decision power to the grid edge, and enabling necessary hierarchical interactions among various entities in the grid, the power generation, consumption, and storage altogether are decentralized. This shall provide an opportunity for every consumer to produce and store the power (termed as a prosumer) and coordinate the exchange of power with their peers for the greater benefit of society. The large-scale emergence of the prosumer may lead to the democratization of the power grid requiring sophisticated decentralized technology solutions as the key enablers. There is a huge necessity to transition towards a net-zero power grid and democratizing the power grid would be a major step toward attaining a healthy sustainable environment.

### 1.3 Timescale of Control Applications

The power grid is a complicated network requiring the coexistence of various applications for a stable operation. The higher penetration of DERs in such networks requires systematic

hierarchical execution of applications at different timescales. Fig. 1.2 summarises the time scale separation of hierarchical control applications and associated communication protocols. Typically, primary control is applicable at the device (DER) level, secondary control is applicable at the system level (MG), and tertiary control is applicable at the network level (power distribution network). Applications in the primary control level are highly decentralized while the applications in the tertiary control layer are highly dependent on communication infrastructure. The trend for applications in the secondary control level is shifting from distributed architecture to decentralized architecture. This shift in the trend is to reduce the dependency on communication networks and increase real-time performance. At the primary control level, the main objective is to track the power set-points during grid-tied operation and share stable power in the islanded mode of operation [28–33]. Furthermore, as per the IEEE 1547-2018 standard, fault ride-through and other grid support functions are the key requirements at the DER level primary control [34–37]. Voltage and frequency regulation to nominal values and achieving seamless transfer are the key requirements at the MG level secondary control [38–42]. Topology reconfiguration, economic dispatch, optimal power flow control, and unit commitment are some of the key control requirements at the network level [9, 43–46].

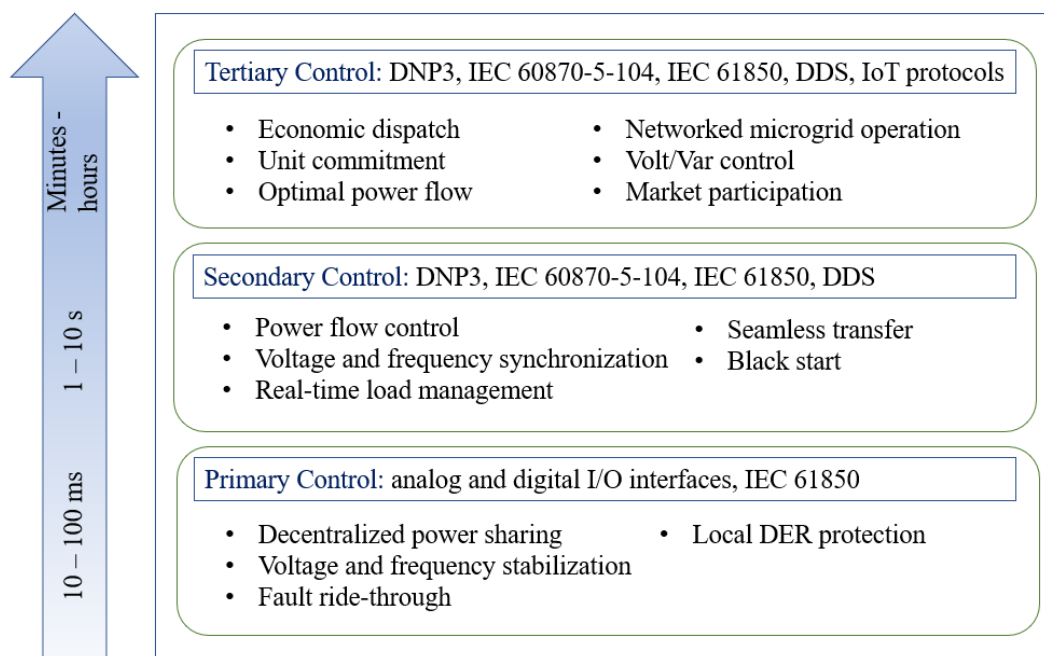


Figure 1.2: Summary of control applications in the power distribution system along with the timescale of operation and associated communication protocols.

#### 1.4 Outline of the Dissertation

Considering the rapid integration of DERs in the power distribution network, the core research problem of this dissertation is as follows.

*Problem statement: How to ensure stability and enhance the resiliency in a DER-dominated power distribution network that requires the coexistence of various applications at multiple spatiotemporal scales?*

The implicit challenge of the aforementioned problem also involves addressing the controller design scalability concerns. The author attempts to solve the problem by categorizing the research objectives in a hierarchical approach. Through the thorough investigation of the state-of-the-art research, core objectives at each of the layers in the hierarchy are defined as depicted in Fig. 1.3. In the subsequent chapters, a systematic methodology to achieve those objectives is proposed. The author believes this approach will be successful in managing the high penetration of the DERs, including 100% DER-based power grid operation.

In Chapter 2, characteristics and challenges in DER integrated modern distribution network are discussed. This chapter also highlights the key challenges in multiple IBR operations in a distribution network and the need for decentralized secondary controller frameworks. A brief discussion about different control architectures and methods that are in the scope of this dissertation is provided. Lastly, the scope of the dissertation is defined and discussed.

Chapter 3 addresses the challenge of systematic classification of control goals for grid-forming and grid-following inverters in an unbalanced, low  $X/R$  distribution grid. In this chapter, a sequence-based unified control architecture and the underlying building blocks for the multiple IBR operation are proposed. Basic linear control theory concepts, unbalanced network theory concepts, controller design approach, stability analysis, and real-time validation results of the unified architecture are as well provided.

In Chapter 4, the challenge of utilizing a first-order high-fidelity IBR primary controller model and state-estimation techniques to create a platform for a decentralized control mechanism is addressed. Furthermore, the integral model predictive control (IMPC) framework is proposed for regulating the MG voltage and frequency to the nominal values even in presence of the measurement noise. The framework is validated in real-time simulation set-up for various grid events and communication latency. The proposed solution is computationally less expensive and it can be deployed on grid-edge devices.

Chapter 5 addresses the challenge of how data-driven learning methods and state estimation techniques can aid the design of decentralized optimal control. This serves the use case of voltage and frequency regulation when model parameters are unavailable in an interoperable DER-integrated system. A decentralized adaptive identification-based integral model predictive control (IIMPC) framework is formulated based on the definition and synchronization of local and global states. The framework is validated in a real-time MIL setup for various grid events.

In Chapter 6, the challenges involved in optimally operating a systematic sectionalized feeder with connected multi-MGs are addressed. In this chapter, the building blocks of connected MGs are described spanning from the primary controller of IBRs to primary protection functions for the network. An extended Q-routing-based algorithm is proposed for

optimal reconfiguration of networked MG during extreme events. The algorithm is validated in an event-driven real-time experimental set-up and the actions of the reconfiguration agent are analyzed.

Chapter 7 illustrates a three-layer delivery model for networked MG operation. The resiliency-as-a-service utility is proposed and the underlying possible use cases are described. A load restoration use case is demonstrated to validate the effectiveness of the delivery model. Chapter nevertheless provides the roles and responsibilities of utilities, aggregators, technology providers, and prosumers in attaining 100% sustainable generation-based power grid. Chapter 8 concludes the dissertation with direction and research questions for future work.

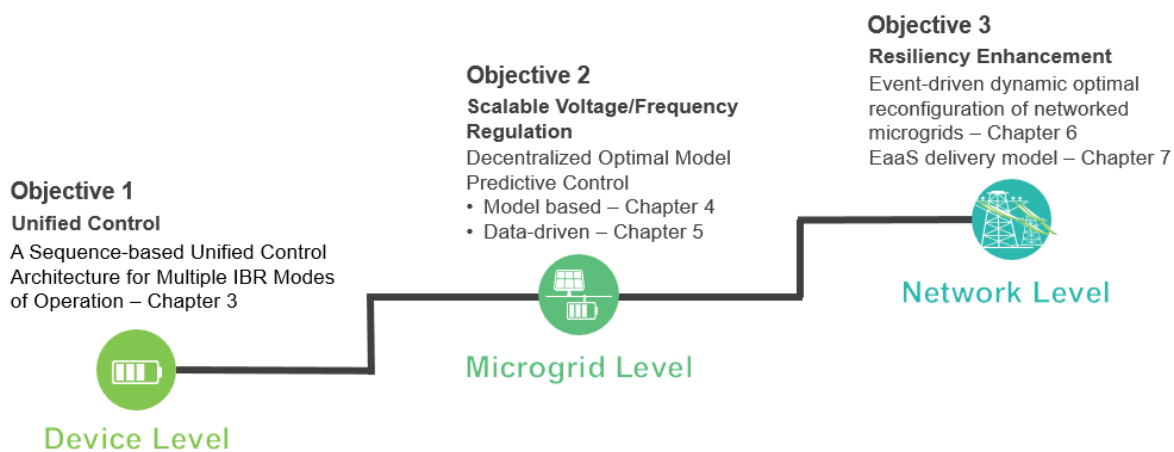


Figure 1.3: Outline of the dissertation including the research objectives and the associated chapters.

## 1.5 Main Contribution of the Dissertation

The stable operation of multiple IBRs with communication-free power sharing, scalable optimal control solutions to maintain the MG system parameters close to the nominal values, and optimal reconfiguration of networked MGs are the key research challenges that need to be addressed to enhance the stability and resiliency of the grid operation. The major contributions of the research work at each of the levels in the hierarchy are described below.

- **Device Level:** at the IBR level, a unified architecture for grid forming and grid following IBRs is proposed and validated for various grid events. Modified positive sequence droop law (with an integral element) for improving the IBR power sharing is orchestrated resulting in maintaining the system voltage and frequency close to nominal values. A negative sequence IBR power control mechanism is demonstrated for mitigating the power ripples occurring during unbalanced faults, thereby assuring the ride-through capability of the IBR. A straightforward, generic PNS current limiting method is proposed to empower the IBRs with ride-through capability during different modes of operation. Real-time model-based verification is performed for various grid events such as linear and nonlinear load changes, ride-through during unbalanced

faults, seamless transitioning between the proposed modes of operation, and dynamic role change of IBRs.

- **Microgrid Level:** at this level, a decentralized model-based (IMPC framework), and data-driven (IIMPC framework) quadratic optimal control problem is solved to achieve the voltage and frequency regulation. The predictive integral action mechanism accelerates the restoration of voltage and frequency, especially advantageous when communication latency is considered. The approach utilizes a computationally inexpensive first-order model (known or identified) and extended Kalman filter-based state estimation technique-based, hence deployable to grid edge devices. The state estimation facilitates the dynamic synchronization of system states locally, thereby offering a balance between the communication requirement and the computational complexity. The estimator does not require communication among the subsystems and from the controller perspective, the subsystems are completely decoupled, hence offering design scalability. The IMPC/IIMPC controller is formulated to incorporate constraints such that the control input signal is accounted for explicit amplitude and rate constraints. Thus during short-term grid faults, the secondary controller assists the primary controller in performing ride-through activity by providing the constrained references. IIMPC framework is an extension to IMPC when model parameters are unavailable, further enhancing the controller robustness in case of model mismatch or system uncertainties. Frameworks are foolproof against various grid events such as islanding, load change, generation loss, and grid faults, and robust against communication latency and measurement noise as validated by the real-time model-in-the-loop simulation.
- **Network Level:** To capture the detailed network level dynamics, a detailed dynamic model of the network is developed including IBR primary control, secondary control, protection, synchronization, and load-shedding schemes. The design is optimized for real-time operation using distributed modeling and is capable of communicating its states to the agent at a millisecond timescale post-event. Proposed dynamic reconfiguration is formulated as a Markov decision process, and the extended Q-routing-based reconfiguration method efficiently discovers the optimal path between the source and destination nodes. The extended Q-routing algorithm utilizes the edge weights to compute the optimal path and the approach is capable of finding multiple optimum paths, unlike the breadth-first search method. Real-time agent-in-the-loop validation of the proposed method showcases the optimal network reconfiguration, including stable power sharing, and nominal voltage in respective MGs. Furthermore, the networked MGs with dynamic boundaries, technology aggregation, and resiliency service offering

through a layered architecture of the EaaS delivery model are presented. Such models can successfully match the distributed generation with highly dynamic local or neighboring loads with or without the availability of the grid. Lastly, a framework to offer resiliency-as-a-service to the end-users through resiliency metrics is presented and the need for sustainable business model innovation by technology players, startups, and utilities to position themselves in the market is emphasized.

## CHAPTER 2: DER Integrated Power Distribution Network

*There can be no compromise on basic principles. There can be no compromise on moral issues. There can be no compromise on matters of knowledge, of truth, of rational conviction.*

---

Ayn Rand

In this chapter, basic details of distributed energy resource (DER) integrated power distribution networks are provided. Section 2.1 describes the modern distribution network characteristics and the requirements of DER control strategies. Section 2.2 provides the details of controller frameworks followed by various control methods in Section 2.3 to introduce the context of control use cases in the power distribution networks. Section 2.4 discusses the scope of the dissertation and the identified research problems in the context of DER integrated power distribution network. Lastly, Section 2.5 provides the summary.

### 2.1 Modern Power Distribution Network

Conventional power distribution networks are designed for unidirectional power flow from the substation to the end user. Such networks require limited sensing and minimal control actions by the components such as transformer tap changers, and capacitor banks. Networks are usually oversized considering the long-term peak load conditions and hence they offer robustness and reliability. However, in recent times, due to the clean energy policies, and DER cost reduction, large-scale integration of DERs is foreseen. DERs are the smaller power generation units often installed on the consumer side, unlike centralized power generation plants. Photovoltaic (PV), battery energy storage, and wind generators are a few examples of DERs not necessarily installed behind the meters. On the policy front, North Carolina Clean Energy Plan has a goal to reduce electric power sector greenhouse gas emissions by 70% below 2005 levels by 2030 and reach carbon neutrality by 2050 [47]. On the cost front, the Solar Energy Technologies Office report [48] has the cost targets for solar electricity by 2030 are \$0.05/kWh, \$0.04/kWh, and \$0.03/kWh for residential, commercial, and utility-scale PV applications, respectively. These costs support greater affordability of DERs by lowering the solar energy costs by around 50% and battery energy storage costs in the range of 40-70% between 2020 and 2030 [49].

### 2.1.1 Network Characteristics and Challenges

The modern distribution network is witnessing a large-scale integration of the DERs. The DERs are asynchronously coupled to the AC power grid through power electronic converters, termed inverter-based resources (IBR). Usually, an IBR output AC voltage is less than the network line voltage. Hence, a  $\Delta - Y_g$  transformer is used to interface an IBR to the network line. Smart switches (SS) are controllable breakers that can be tripped or closed to isolate or reconnect a part of the network. The distribution network follows the radial topology with one substation node powering the entire network at any given point in time. To design the controllers of IBRs, network characteristics play a critical role [28]. Two major characteristics of the distribution network are as below [50].

- **Low  $X/R$  compared to the bulk power grid:** The distribution network lines operate at a much lower voltage than the transmission lines of the bulk power system. Therefore the distance between the wires is much shorter than the transmission line which leads to much lower magnetic energy storage and consequently its inductance per unit length will be smaller. Furthermore, due to the high current carrying capacity requirement, the larger cross-sectional area of the distribution lines leads to higher resistance per unit length compared to the transmission lines.
- **Unbalanced network:** Due to many single-phase and two-phase laterals, the network is unbalanced. To balance the network voltage, the substation node supplies negative sequence currents into the network. Thus depending on the phase-wise loading (including line impedance) in the network, an equivalent phase-wise current is supplied by the substation node.

Based on the aforementioned characteristics of the network, appropriate IBR control strategies need to be developed. The strategy must enable efficient IBR operation in the presence and absence of the substation node, basically forming an MG. Especially, when the target is to achieve 100% IBR-based network operations, significant challenges include achieving stability and performing optimal network reconfiguration. At the ground level, it opens up a new research paradigm, as IBR behavior and dynamics are different compared to the synchronous-generator dynamics. IBR-based network (MG) is also termed as a weak grid that tends to have lower inertia, lower short circuit ratio, lower  $X/R$ , and higher grid impedance compared to the bulk power grids [51]. Furthermore, at the network level, there is a need for systematic sectionalization (through the appropriate operation of SSs) leading to multiple connected MGs, hence increasing the overall resiliency of the network.

### 2.1.2 IBR Power Sharing Strategies

The co-existence of multiple IBRs along with the grid source and during the absence of a grid source requires a sophisticated and dedicated control strategy. Decentralized primary control techniques are typically utilized to achieve stable and efficient autonomous operation of IBRs in a network without the need for communication [52, 53]. Droop and voltage oscillator control (VOC) strategies as a part of primary control can enable power-sharing among multiple IBRs in a distribution system. Control design aspects of both strategies are investigated before applying them to an unbalanced system. Since the distribution system has low  $X/R$ , correlation of the form  $P \sim V$  and  $Q \sim \omega$  is proposed as a universal droop law for an IBR with any type of output impedance [28]. A robust droop controller for IBRs with low  $X/R$  output impedance is presented to reduce the voltage drop due to the load and droop effect [29]. In [30] an adaptive droop control architecture is illustrated to improve the transient performances. The proposed approaches are valid for multiple IBR operations; however, the authors did not consider operations in unbalanced conditions and grid-feeding modes of operation. On the other hand, various incarnations of VOC-based strategy exist in literature offering different dynamic performances. Andronov-Hopf oscillator [31], dead-zone oscillator [54], Lienard-type circuits [32], Poincare-Bendixson Oscillator [55], space-vector oscillator [56] are some examples of adoption of oscillator dynamics to facilitate multiple IBR operation.

The fundamental control objective of droop and VOC methods is to maintain the power balance between the load and generation. In a cascaded control, the voltage and current reference tracking loops are the lower loops with relatively faster responses compared to the droop loop. The droop method enables decentralized power balance by allowing deviation from the nominal voltage and frequency, which would be corrected by the secondary controller. For a stable operation, the droop-based control strategy requires systematic time-scale separation (decrease in bandwidth for outer loops) among the cascaded control loops as depicted in Fig. 2.1. Furthermore, dedicated voltage and current controllers can be designed to meet the requirement of positive and negative sequence (PNS) component supply from the IBR. In grid-tied mode, DERMS provides the power set-points and the same droop loop can be used to perform accurate power set-point tracking. Appropriate design solution of the secondary controller along with the primary controller, the IBR can meet the desired performance in both grid-tied and islanded modes including seamless mode transitions.

VOC strategy offers faster synchronization and power-sharing by combining the voltage tracking control (secondary control) with primary control in islanded mode [57]. Fig. 2.1 shows the typical bandwidths for hierarchical controls in a VOC-based network. Unlike droop, VOC does not require active and reactive power computation at the terminal. More-

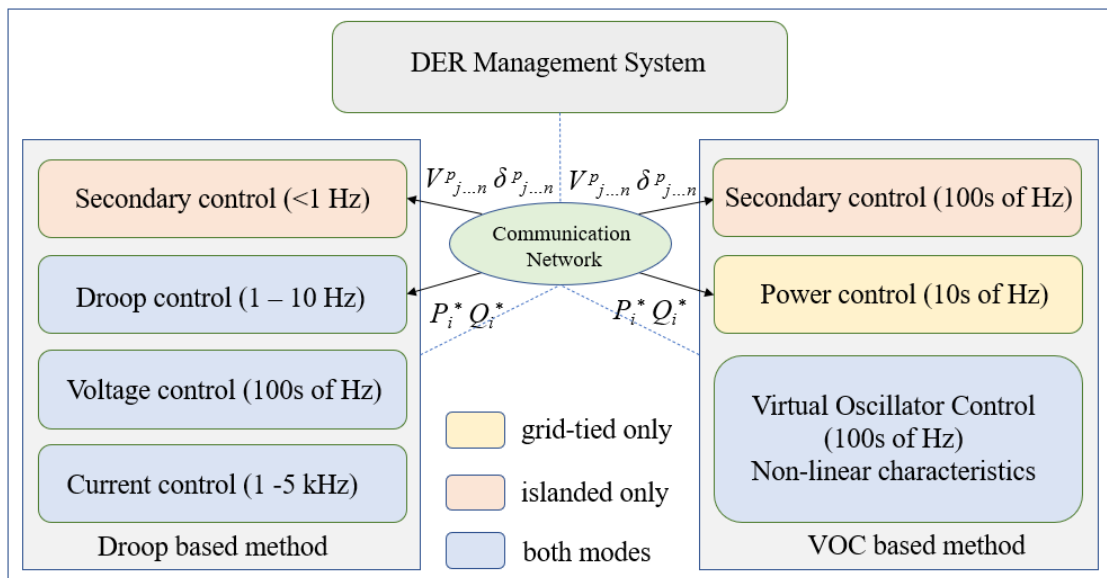


Figure 2.1: Comparison between droop-based and VOC-based power sharing strategies and the typical bandwidth for designed control loops.

over, VOC does not require dedicated voltage and current loops. However, to achieve power set-point tracking in grid-tied mode, an isolated power control loop is needed which requires power computation based on terminal voltage and currents [54] [56]. This loop provides voltage reference to the primary VOC loop and requires the explicit calculation of real and reactive power at the converter terminal. Since it is not clear from the literature about the capability of VCO-based IBRs to supply negative sequence components, droop based method is investigated in this dissertation to achieve primary controller goals. Such primary controller of an IBR consists of an inner PNS current loop, and an outer PNS voltage loop followed by a power loop that deploys appropriate droop laws [58].

### 2.1.3 Theory Behind Droop Law

The equivalent circuit of multiple parallel IBRs that are operating in islanded mode is depicted in Fig. 2.2. The circuit represents the SS state as open, and multiple IBRs ( $n$ ) operating in parallel cater to the load in the system ( $Z_L$ ).  $V_i$ ,  $\angle\delta_i$  are the voltage magnitude and angles of  $i^{th}$  IBR respectively. All the IBRs are assumed to have different output impedance magnitude and phase ( $Z_i$ ,  $\angle\delta_i$ ), representing aggregated output impedance of the IBR system and the line impedance of the distribution system. Since different IBR sizes would have different  $LCL$  filter parameters and controller parameters, output impedance may vary. Furthermore, when IBRs are spatially distributed in the grid, the line impedance seen at the PCCs of respective IBRs could be different from one another.

From the basic power flow, the apparent power supplied by the IBRs operating as a voltage source in islanded mode is represented as (2.1).

$$S_i = \frac{V_i V_p e^{-j(\theta_i - \delta_i)} - V_p^2 e^{j\theta_i}}{Z_i} \quad (2.1)$$

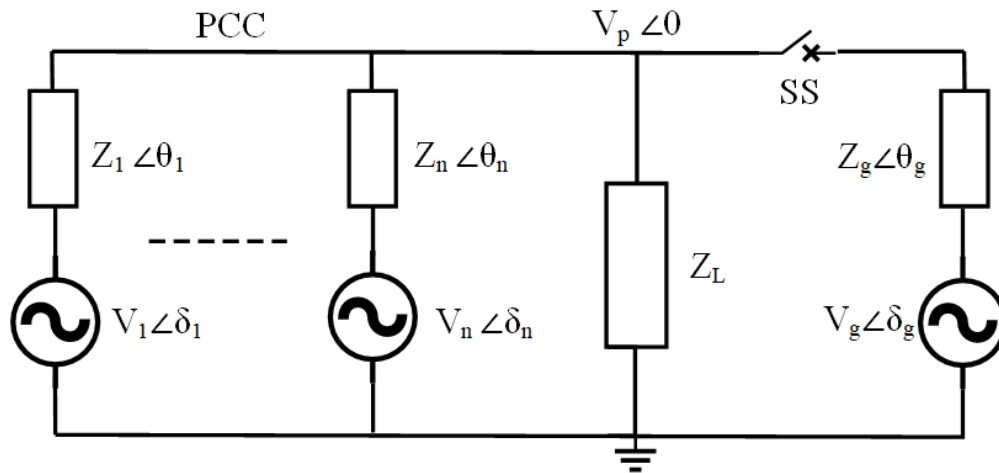


Figure 2.2: Parallel IBR operation based on power-flow to identify droop laws in a low  $X/R$  system

Active and the reactive power components of (2.1) are described by (2.2) and (2.3).

$$P_i = \left( \frac{V_i V_p \cos \delta_i - V_p^2}{Z_i} \right) \cos \theta_i + \left( \frac{V_i V_p}{Z_i} \right) \sin \theta_i \sin \delta_i \quad (2.2)$$

$$Q_i = \left( \frac{V_i V_p \cos \delta_i - V_p^2}{Z_i} \right) \sin \theta_i - \left( \frac{V_i V_p}{Z_i} \right) \cos \theta_i \sin \delta_i \quad (2.3)$$

where  $i = 1, 2$  represents the number of IBRs,  $E_i$  and  $V$  are the amplitudes of the IBR output voltage and the point of common coupling (PCC) voltage,  $Z_i$  and  $\theta_i$  are the magnitude and the phase of the output impedance respectively. By considering the transformation matrix that rotates the power vector  $(P_i + jQ_i)$  by  $-\theta$  power vector can be aligned along the IBRs with the resistive output impedance.

$$T(\theta) = \begin{bmatrix} \cos(\theta) & \sin(\theta) \\ -\sin(\theta) & \cos(\theta) \end{bmatrix} \quad (2.4)$$

$$\begin{bmatrix} P_i^T \\ Q_i^T \end{bmatrix} = T \begin{bmatrix} P_i \\ Q_i \end{bmatrix} = \begin{bmatrix} \frac{E_i V}{Z_i} \cos(\delta_i) - \frac{E^2}{Z_i} \\ -\frac{E_i V}{Z_i} \sin(\delta_i) \end{bmatrix} \quad (2.5)$$

From (2.5),  $P_i$  and  $Q_i$  have positive correlation with  $V$  and  $-\delta_i$  respectively for IBRs with different output impedance [28]. For low  $X/R$  network such as distribution grid, we can assume  $Z_i \approx R_i$ , hence  $\theta_i = 0$  (same correlation in (2.5)).

With the aforementioned theory, the objective of a droop law is to generate appropriate voltage magnitude  $V_i$  and angle  $\delta_i$  for each of the IBR operating in parallel such that they share the active and reactive powers proportionally as given by (2.6) and (2.7).

$$V_r^i = V_i^* + k_p^V \Delta V_i - k_p^P \Delta P_i \quad (2.6)$$

$$\omega_r^i = \omega_i^* + k_p^Q \Delta Q_i \quad (2.7)$$

where  $\Delta P_i = (P_i - P_i^*)$  is the deviation of measured active power from the set-point value,  $\Delta Q_i = (Q_i - Q_i^*)$  is the deviation of measured reactive power from the set-point value,  $\Delta V_i = (V_i^* - V_p^{rms})$  is the deviation of measured PCC voltage from the nominal value,  $V_i^*$  and  $\omega_i^*$  are the voltage magnitude and frequency set-point values.

### 2.1.4 Need for the Decentralized Secondary Control

Section 2.1.3 described the droop correlations that are valid for a low  $X/R$  distribution system. As per the droop laws, the rated power delivery from the IBR would lead to maintaining the rated voltage and frequency at PCC. When there is a change in the system operating condition, the power delivered changes from rated value to  $P_i$  and  $Q_i$  in respective relations. As a result, voltage and angle deviate from their respective nominal values. So there is a need for secondary control that can perform a corrective action to restore the voltage and angle to rated values as described by (2.8) and (2.9).

$$V_{(r,i)}^+ = V_i^* + k_p^V \Delta V_i - k_p^P \Delta P_i + dV \quad (2.8)$$

$$\omega_{(r,i)}^+ = \omega_i^* + k_p^Q \Delta Q_i + d\omega \quad (2.9)$$

The role of secondary control is to eliminate these deviations while at the same time maintaining the stability of power-sharing in the MG. Closed loop dynamics of IBR integration into the grid are represented by Fig. 2.3.

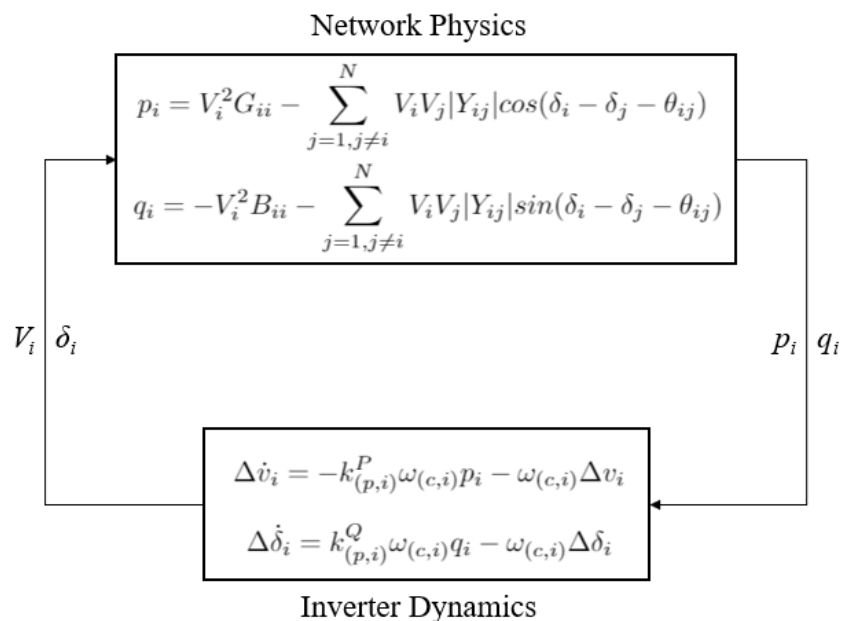


Figure 2.3: Closed loop dynamics representation of IBR integrated into distribution grid

$$P_i = \frac{1}{k_{(p,i)}^P} (V_{(r,i)} - V_i^*) + P_i^* \quad (2.10)$$

$$Q_i = \frac{1}{k_{(p,i)}^Q} (\omega_{(r,i)} - \omega_i^*) - Q_i^* \quad (2.11)$$

The time-domain representation of power signals from the power control loop and the low pass filter (LPF) of the IBR is given by

$$\dot{P}_i = \omega_i^c (p_i - P_i) \quad (2.12)$$

$$\dot{Q}_i = \omega_i^c (q_i - Q_i) \quad (2.13)$$

where  $\omega_i^c$  is the cut-off frequency of the low pass filter which is usually in the range of 2 Hz to 10 Hz.

The generic power flow equation is given by:

$$p_i = V_i^2 G_{ii} - \sum_{j=1, j \neq i}^N V_i V_j |Y_{ij}| \cos(\delta_i - \delta_j - \theta_{ij}) \quad (2.14)$$

$$q_i = -V_i^2 B_{ii} - \sum_{j=1, j \neq i}^N V_i V_j |Y_{ij}| \sin(\delta_i - \delta_j - \theta_{ij}) \quad (2.15)$$

where  $|Y_{ij}| = \sqrt{G_{ij}^2 + B_{ij}^2}$  and admittance angle  $\theta_{ij} = \arctan(\frac{B_{ij}}{G_{ij}})$

substituting (2.12) through (2.15) in (2.8) and (2.9) that are applicable in islanded mode with zero integral gain coefficients, and ignoring reference values, small signal model representation is given by:

$$\dot{V}_i = (-k_{(p,i)}^P \omega_{(c,i)} V_i G_{ii} - \omega_{(c,i)}) V_i + k_{(p,i)}^P \omega_{(c,i)} \sum_{j=1, j \neq i}^N V_i V_j |Y_{ij}| \cos(\delta_i - \delta_j - \theta_{ij}) \quad (2.16)$$

$$\dot{\delta}_i = -k_{(p,i)}^Q \omega_{(c,i)} V_i^2 B_{ii} - \omega_{(c,i)} \delta_i - k_{(p,i)}^Q \omega_{(c,i)} \sum_{j=1, j \neq i}^N V_i V_j |Y_{ij}| \sin(\delta_i - \delta_j - \theta_{ij}) \quad (2.17)$$

Some assumptions and approximations to linearize (2.16) and (2.17):

1. Small signal modeling: term outside summation  $V_i^2 = V_i v_i + v_i V_i = 2V_i v_i$ , similarly term inside summation  $V_i V_j = v_i V_j + V_i v_j$
2. For a set of IBRs in the network operating in an island, grid forming IBR would set the angle and rest of the IBRs would follow the angle. So  $(\delta_i - \delta_j) = 0$ . Similarly, in grid-connected mode (if applicable for other studies), grid would provide the angle and all the IBRs in the network would follow that.

With the above assumptions, the closed-loop small signal model is given by:

$$\begin{aligned} \Delta \dot{v}_i = & \left( -2k_{(p,i)}^P \omega_{(c,i)} G_{ii} V_i + \sum_{j=1, j \neq i}^N k_{(p,i)}^P \omega_{(c,i)} V_j |Y_{ij}| \cos(\theta_{ij}) - \omega_{(c,i)} \right) \Delta v_i \\ & + \sum_{j=1, j \neq i}^N \left( k_{(p,i)}^P \omega_{(c,i)} V_i |Y_{ij}| \cos(\theta_{ij}) \right) \Delta v_j \end{aligned} \quad (2.18)$$

$$\begin{aligned} \Delta \dot{\delta}_i = & \left( -2k_{(p,i)}^Q \omega_{(c,i)} B_{ii} V_i + \sum_{j=1, j \neq i}^N k_{(p,i)}^Q \omega_{(c,i)} V_j |Y_{ij}| \sin(\theta_{ij}) \right) \Delta v_i - \omega_{(c,i)} \Delta \delta_i \\ & + \sum_{j=1, j \neq i}^N \left( k_{(p,i)}^Q \omega_{(c,i)} V_i |Y_{ij}| \sin(\theta_{ij}) \right) \Delta v_j \end{aligned} \quad (2.19)$$

The small signal model representation depicts the entire MG dynamic behavior that can be used to devise a higher hierarchical controller. Large scale model of the same is clearly non-linear and the representation hints that a dense communication network is required for the development of a higher-level controller. This necessitates the design of a decentralized controller to meet the system-level objectives with the limited communication requirement.

## 2.2 Review of Control Frameworks

To enhance the reliability and performance of the DER integrated distribution network, a hierarchical control structure is necessary. The such structure ensures the accurate power sharing/tracking of the IBRs, MG voltage and frequency synchronization, and optimal and economic management of the network. In this section, types of control frameworks are critiqued and the highlights of the proposed framework of this dissertation are provided.

### 2.2.1 Centralized Frameworks

*Centralized frameworks* have the complete perspective of the system in terms of model and measurements. Central controllers interact with the devices in the network to fetch the measurement and status information and provide them back appropriate set points to keep the voltage and frequency of the system within the required limits [9, 33]. Usually, this framework utilizes client-server communication infrastructure for exchanging messages [59] as shown in Fig. 2.4a. Optimal power flow [60–62], economic dispatch of the resources [13, 63, 64], grid synchronization [65, 66], and demand response [60] are some of the typical applications developed using a central controller. The framework serves the use case of controlling the distribution network with fewer DERs without adding to the cost and complexity of the prevailing network [9]. Distribution networks are expanding tremendously with the integration of DERs. The integration of DERs is highly distributed in nature. This brings limitations to a centralized architecture as they are less scalable, offer low reliability, and are prone to single point of failure [7, 8].

### 2.2.2 Distributed Frameworks

*Distributed frameworks* have complete access to the system states based on which they can conduct local control decisions. System-level voltage and frequency synchronization, and power quality improvement strategy are some of the applications that utilize distributed frameworks. Local controllers interact with the other controllers in the network to fetch the state information and provide them back the local state information [67] as shown in Fig. 2.4b. Usually, this framework utilizes publish-subscribe communication infrastructure for exchanging messages [68]. The framework serves the use case of controlling the DERs within the MG leading to an autonomous operation [69]. The framework is typically developed as a multi-agent synchronization system realized by various techniques discussed in the literature such as feedback linearization [70], adaptive cooperative control [71], finite-time control [68, 72], consensus-based control [73], distributed-averaging-control [74, 75], mixed voltage angle and freq droop [76], and event-triggered strategy [77]. Though distributed frameworks utilize sparse communication, the large-scale integration of DERs is often challenging [14].

### 2.2.3 Decentralized Frameworks

Distributed nature of DERs facilitates the adoption of *decentralized framework* that can enable autonomous operation. The control decisions are taken by the local controllers usually considering the local measurements [78] without requiring communication as shown in Fig. 2.4c. The design of the local controllers is dependent on the distribution network parameters including resistive, inductive, and or capacitive output impedance of the IBRs [28, 79]. Typical local controllers can incorporate multiple control loops with decreasing bandwidth from inner to outer loops [80]. The local controllers can be developed in three different reference frames: natural ( $abc$ ), rotating ( $\alpha\beta$ ), synchronous ( $dq$ ) using proportional-integral (PI) or proportional resonant (PR) controllers [58]. The underlying closed loop system is linearized around an operating point to conduct the stability analysis according to the linear time-invariant (LTI) system theory [81].

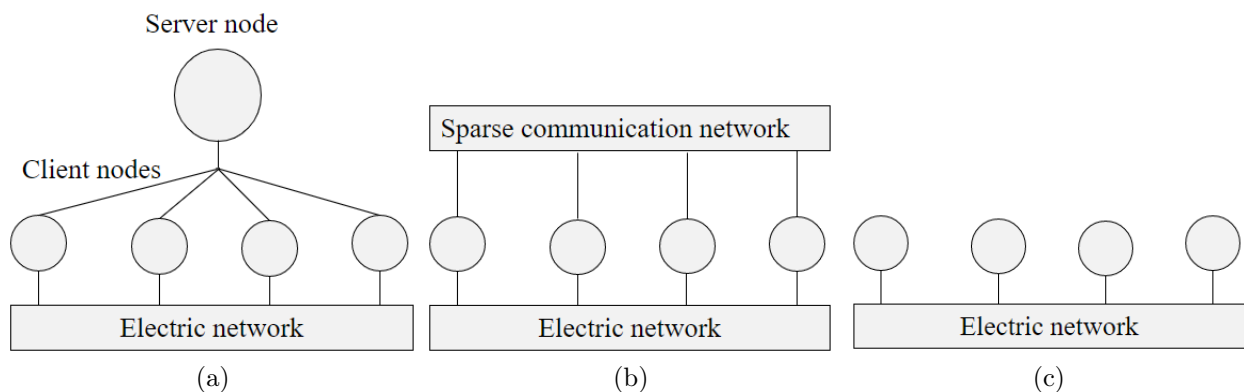


Figure 2.4: Control architecture categories (a) centralized (b) distributed (c) decentralized

### 2.2.4 Network Control Frameworks

Network control synthesis is primarily achieved through the hierarchical multi-layer control structure as shown in Fig. 2.5a. The primary controller (PC) layer has the goal of IBR power tracking/sharing without using communication infrastructure. Droop laws are widely used as a part of this layer, and this layer fits into a decentralized control framework. The secondary controller (SC) layer ensures the voltage and frequency in the system are close to the nominal values, including synchronization of MG with the utility grid. With the growing penetration of DERs, these functions are often designed in distributed frameworks requiring sparse communication. Lastly, the central controller manages the optimal power flow and power generation between the MG and the utility grid through applications such as economic dispatch of the DERs. The operation of the central controller for these applications can span from a few seconds to a few minutes, hence requiring low bandwidth for communication.

A major challenge in the architecture of Fig. 2.5a is at the SC and PC layers. At PC layer, the unification of power-sharing/tracking control of the IBRs and the maintaining of the voltage and frequency of the MG system are attempted in this dissertation. This

unification empowers IBR manufacturers to market their products as major cost savers since SC layer control is accomplished at the PC layer. At the SC layer, this dissertation attempts to offer a decentralized voltage and frequency regulation as shown in Fig. 2.5b. This enables the IBR manufacturer or a third-party controller vendor to incorporate SC (relatively slower timescale) as a part of PC or place SC alongside PC respectively. This facilitates a great deal of design scalability in large-scale DER-integrated power networks. From the central controller perspective, an optimal network reconfiguration scheme is proposed in this dissertation and is verified in an event-driven communication-based dynamic model that includes SC and PC as per the architecture shown in Fig. 2.5b.

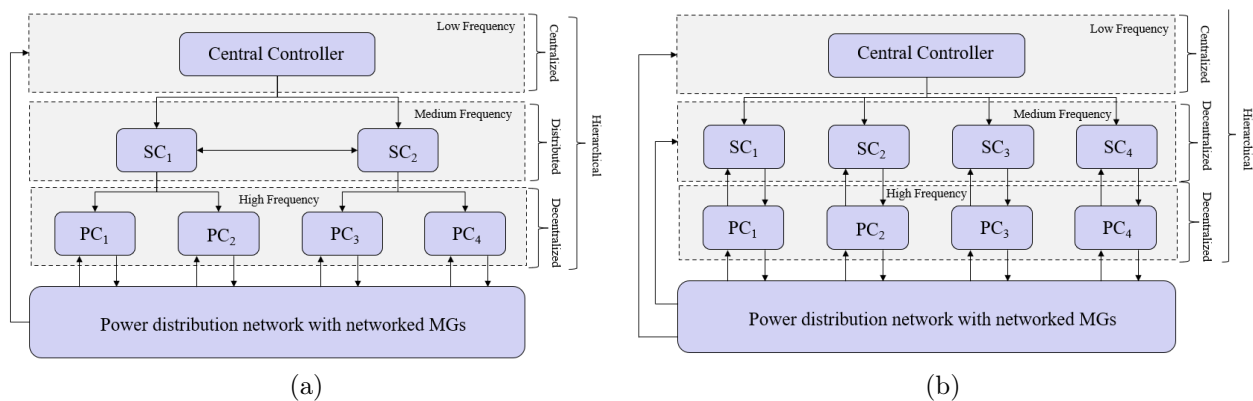


Figure 2.5: Three-layer (primary, secondary, tertiary) distribution network control framework. (a) A centralized, distributed, decentralized hierarchical architecture. (b) A centralized, decentralized, decentralized hierarchical architecture.

### 2.3 Review of Discrete-time Control Methods

Control systems play a key role in achieving the safe and economic operation of the power grid. Hierarchical control utilizes various spatiotemporal control methods collectively working towards a common objective. For practical purposes, PI and PR control methods are preferred at the device level, and model predictive control (MPC) and reinforcement learning (RL)-based control are preferred at the system or network level. At any level, a particular set of grid parameters such as voltage and frequency are continuously monitored and specific actions such as power injection or absorption are performed to maintain the grid parameters at the required set points. In this section background of the control methods that are used in this dissertation is provided.

#### 2.3.1 PI Control

PI controllers are very common in industrial hierarchical control applications [13, 82]. To achieve decentralized control, various PI control strategies are attempted in the literature [64, 83, 84]. The proportional gain term attempts to penalize the present error term while the integral term considers the history of the error. The integral term also aids in mitigating the steady-state error which may not be possible with just proportional gain. As integral term continuous to accumulate error, under certain conditions, this accumulation even exceeds

the physical capabilities of the plant. Hence, appropriate anti-wind-up logic is adopted [85]. An anti-windup included PI controller using the backward Euler discretization method is described by:

$$u_k = \left( k_p + \left( k_i + k_w du_k \right) \frac{T_s z}{z-1} \right) e_k \quad (2.20)$$

where  $u_k$  is the controller output signal,  $k_p$  is the proportional gain coefficient,  $k_i$  is the integral gain coefficient,  $k_w$  is the anti-windup gain coefficient,  $T_s$  is the sampling period,  $e_k$  is the error signal which is the difference between the measured signal and the reference signal,  $du_k$ , the difference between the saturated control signal,  $usat_k$ , and the calculated unsaturated control signal  $u_k$ .

### 2.3.2 PR Control

PR controllers are primarily designed for systems with sinusoidal reference signals, hence preferred for AC voltage and current control. The PR controller contains a proportional and resonant term with independent gain terms which can be tuned. PR controllers do not need coordination transformation to  $dq$  frame. Moreover, the resonant term offers finite high gain around the system AC frequency, hence achieving better reference/set-point tracking and disturbance rejection capability in comparison to the PI control loops of the  $dq$ -frame. [86]

PI controllers are more suitable for the control of DC signals. Hence, predominantly used in  $dq$ -frame-based IBR control. However, they may lead to steady-state errors resulting in inaccurate tracking of IBR set-points. On the other side, PR controllers can mitigate this steady-state error as they can be directly applied on  $abc$ -frame signals [58]. A PR controller designed using the backward Euler discretization method is described by:

$$u_k = \left( k_p + k_i \frac{2\omega_o}{\frac{z-1}{T_s z} + 2\omega_o + \frac{T_s \omega_g^2 z}{z-1}} \right) e_k \quad (2.21)$$

where  $u_k$  is the controller output signal,  $k_p$  is the proportional gain coefficient,  $k_i$  is the integral gain coefficient,  $T_s$  is the sampling period,  $e_k$  is the error signal which is the difference between the measured signal and the reference signal,  $\omega_o$  is the bandwidth surrounding the grid frequency of  $\omega_g$ .

### 2.3.3 LTI MPC

MPC is usually designed based on the state-space mathematical model of the plant [87]. The state-space model facilitates the prediction of future state variables based on the current information and model parameters. A state-space model of a plant is given by:

$$\begin{aligned}
x_{k+1} &= Ax_k + Bu_k + v_k \\
y_k &= Cx_k + w_k
\end{aligned}
\tag{2.22}$$

where  $k$  is the discrete sample,  $u$  is the input vector,  $x$  is the state vector,  $y$  is the output vector,  $A \in \mathbb{R}^{m \times m}$  is the system matrix,  $B \in \mathbb{R}^{m \times n}$  is the control input matrix,  $C \in \mathbb{R}^{r \times m}$  is the output measurement matrix, unknown  $v_k$  and  $w_k$  are system disturbances and measurement noises respectively. In the MPC formulation, input vectors can not directly influence the output vectors hence  $D$  matrix is zero. This is due to the requirement of a prediction model that utilizes current system information to predict future state behavior.

By considering  $\Delta x_k = x_k - x_{k-1}$ ,  $\Delta u_k = u_k - u_{k-1}$ , the generalized augmented incremental state space model that is not influenced by system disturbances and measurement noise is described by (2.23)

$$\begin{aligned}
\overbrace{\begin{bmatrix} \Delta x_{k+1} \\ y_{k+1} \end{bmatrix}}^{\tilde{x}_{k+1}} &= \overbrace{\begin{bmatrix} A & 0 \\ CA & 1 \end{bmatrix}}^{\tilde{A}} \overbrace{\begin{bmatrix} \Delta x_k \\ y_k \end{bmatrix}}^{\tilde{x}_k} + \overbrace{\begin{bmatrix} B \\ CB \end{bmatrix}}^{\tilde{B}} \overbrace{\begin{bmatrix} \Delta u_k \end{bmatrix}}^{\tilde{u}_k} \\
\overbrace{\begin{bmatrix} y_k \end{bmatrix}}^{y_k} &= \overbrace{\begin{bmatrix} 0 & 1 \end{bmatrix}}^{\tilde{C}} \overbrace{\begin{bmatrix} \Delta x_k \\ y_k \end{bmatrix}}^{\tilde{x}_k}
\end{aligned}
\tag{2.23}$$

where  $\tilde{A}$ ,  $\tilde{B}$ ,  $\tilde{C}$  are the parameters of the augmented model which are the building blocks for the prediction model given by:

$$y_{k+1|M} = p_M + F_M \tilde{u}_{k|M}, \tag{2.24}$$

$$p_M = O_M \tilde{A} \tilde{x}_k^c, \tag{2.25}$$

$$F_M = [ O_M \tilde{B} \quad H_M ]$$

where  $M$  is the prediction horizon, and the extended observability matrix ( $O_M$ ) is computed based on  $\tilde{A}$ , and  $\tilde{C}$ , and  $H_M \in \mathbb{R}^{rM \times (M-1)m}$  is the standard Toeplitz matrix of the form [88]. The MPC is designed subjecting to the performance index [89]:

$$\min_{\tilde{u}} J_k = \sum_{i=1}^M (\tilde{y}_{k+i})^T Q_i (\tilde{y}_{k+i}) + (\tilde{u}_{k+i})^T R_i (\tilde{u}_{k+i}) \tag{2.26}$$

where  $Q \in \mathbb{R}^{Mm \times Mm}$  is the positive semi-definite symmetric weight matrix for the future predicted states with  $Q_i \forall i = 1, 2, \dots, M$  being on the diagonal block, and  $R \in \mathbb{R}^{Mn \times Mn}$  is the positive semi-definite symmetric weight matrix for the future predicted control action with

$R_i \forall i = 1, 2, \dots, M$  being on the diagonal block.

### 2.3.4 Q-learning-based Control

Q-learning is one of the model-free RL methods wherein the agent directly interacts with the environment (network) with no prior knowledge of the network model [90]. Q-learning is an off-policy temporal-difference (TD) learning, wherein value estimates are updated by bootstrapping without waiting for the result of an episode. Bootstrapping provisions TD learning to converge faster and the agent attempts to find the optimal policy ( $\pi^*$ ) by maximizing the cumulative discounted reward [91] as given by (2.27)

$$\pi^* = \pi \mathbb{E}_\pi \left[ \sum_{t=0}^T \gamma^t R_{t+1} | S_k = s, A_k = a \right] \quad (2.27)$$

where  $S_k \in \mathcal{S}$  is the network state,  $A_k \in \mathcal{A}$  is agent's action at the iteration  $t$ ,  $R_{t+1} \in \mathcal{R} = \mathbb{R}$  is the reward obtained at the  $t + 1$  iteration,  $\gamma \in [0, 1]$  is the discount factor used to control the influence of future rewards. The Q-learning agent has the objective to find the optimal policy by learning the optimal action-value function as given by (2.28)

$$Q(S_k, A_k) \leftarrow Q(S_k, A_k) + \alpha \left( R_{k+1} + \gamma \max_a Q(S_{k+1}, a) - Q(S_k, A_k) \right) \quad (2.28)$$

where  $\alpha$  is the learning rate. As per (2.28), the TD between predicted and the present Q-values is calculated and for every state  $S$ , the true action value related to policy  $\pi$  is given by  $Q(S_k, A_k) = \mathbb{E}_\pi(R_k + \gamma R_{k+1} \dots | S_k = s, A_k = a)$ . Since in every state, the optimal value is obtained by considering the highest action value, thereby optimal policy ( $\pi^*$ ) is derived as represented in (2.27).

### 2.3.5 Comparison of the Control Methods

The aforementioned control methods can be applied at different hierarchical layers in network control. A comparison based on the features offered by the control methods is provided in Table 2.1. PI and PR methods are feasible for the design of single input single output (SISO) systems while MPC [92, 93] and RL [94–96] methods can be extended to multiple input multiple outputs (MIMO) systems. The major advantage of the MPC method is its capability to achieve constraint handling. Control methods such as PI and PR do not offer such capability while RL methods can be extended to achieve constraint handling [97, 97, 98]. The PI and PR controllers to operate, the model of the system is not required, however, MPC needs a high-fidelity known model, or a system identification technique to compute the model parameters [99]. On the other hand, RL algorithms can be both model-based and model-free [91]. In this dissertation, PR/PI control methods are used to achieve the primary control layer objectives, MPC with constraints is formulated at the secondary control layer (both model-based and system identification-based) to solve the regulation

problem, and the model-free q-learning algorithm is extended to achieve the underlying reconfiguration goal at the network layer.

TABLE 2.1: Comparison between different control methods.

Features	PI	PR	MPC	RL
I/O system	SISO	SISO	MIMO	MIMO
Constraints	No	No	Yes	Yes
Model required	No	No	Yes	Yes & No
AC/DC system	DC	AC	AC & DC	AC & DC

Though the PR control method can be applied directly to AC systems to achieve device-level control, it has significant limitations in extension to the system level. At the system level, MIMO handling along with the constraints is a typical requirement. MPC methods are predominantly used in the literature to handle reference tracking in MIMO systems under constraints [89]. Furthermore, the nature of the reference can be any trajectory including AC signal [100]. The RL algorithms are readily applicable to the formulation of the agent and environment as a Markov decision process, leading to discrete sequential control actions [101, 102]. However, RL methods can be extended to provide continuous action control such as load-frequency control [103], robot control [104], and linear quadratic tracking [105].

## 2.4 Scope of the Dissertation

From Section 1.1 the context of the dissertation is the transition towards 100% sustainable energy resource-based power grid operation. Though this transition in broader terms is highly optimistic, it rather offers numerous research questions that need to be addressed immediately and near future. The increase in penetration of DERs, variable generation, bi-directional power flow, and increased controllability and observability have led to the development of various applications at multiple spatiotemporal scales. Research challenges in this regard can be classified primarily into planning and operational categories for the distribution network. In this dissertation subset of operational challenges are identified and systematically classified at the device, system, and network levels.

Firstly, device-level challenges include immediate attention to unifying various applications that can enable multiple operating modes in the power network. The device-level applications are inherently decentralized and operate at a faster timescale with high controller bandwidth. Device level controller design is performed by extending PI/PR control strategy discussed in Section 2.3. Furthermore, the design of the application and stability analysis are critically addressed utilizing the principles of the linear control system theory. Understanding the

injection of PNS components for different types of devices, and designing dedicated control strategies to achieve the respective control objective, are the major challenges at the device level.

Secondly, system-level challenges include the formulation of decentralized control techniques to achieve system-level control goals. As distribution networks offer observability mainly at the nodes where DERs are coupled to the power grid line, and the controllability is associated with the same nodes. Thus with large-scale integration of DERs, achieving system-level control goals get cumbersome. This necessitates the scalable controller design and is computationally simpler to deploy on the grid edge devices. With the recent development of inter-operable system standards such as IEC 61850 and MESA for DER integration, the system can encompass devices from multiple vendors. This leads to the exploration of data-driven approaches to serve the use case of an interoperable system. The advent of learning-based techniques, and state estimation methods have aided the development of low-order high fidelity system models. Furthermore, controller behavior needs to be optimal and in this dissertation, MPC control strategy is extended to achieve efficient operation at the system level including the stability analysis.

Lastly, network-level reconfiguration is more of a futuristic research challenge that includes connected multiple MGs. With large-scale DER integration, a feeder network can be upgraded to include multiple MGs operating as island and grid-connected modes. The business case for utilities with the such upgrade is to increase resilience during extreme events. The such case requires an event-driven communication-based real-time executable approach preserving network stability and offering power quality to the end users. In the dissertation, optimal network reconfiguration is approached as a routing problem and RL techniques are utilized to offer topology-agnostic, scalable, optimal solutions. Furthermore, devising a systematic layered architecture is necessary to deliver the developed applications to the end users. The roles and responsibilities of utilities, aggregators, and prosumers to achieve 100% sustainable generation are as well highlighted in this dissertation.

## 2.5 Summary

This chapter presents characteristics and challenges in the DER-integrated modern distribution grid. The analysis and comparison of various aspects of the distribution grid application, such as control architecture, control methods, and time scale of operation are provided. Furthermore, two major power-sharing strategies have been carefully analyzed, and droop based method has been applied to the case of unbalanced distribution grids. The need for a decentralized control strategy is discussed in maintaining the nominal system voltage and frequency during steady-state operating conditions. Lastly, in alignment with broader topics and the outline discussed in Chapter 1, the scope of the dissertation is provided.

## CHAPTER 3: A Sequence-based Unified Control Architecture for Multiple IBR Modes of Operation

*There is no unique picture of reality.*

---

Stephen Hawking

Control of multiple inverter-based resources (IBR) in the distribution grid can be achieved by adopting appropriate droop laws. However, in an unbalanced power distribution system with single-phase and two-phase laterals, droop-based control methods fail thus requiring dedicated IBR control methods that can supply the required positive and negative sequence (PNS) components. In this chapter, a unified control architecture is proposed for stable multiple IBR operations that can improve the accuracy of active and reactive power sharing alongside maintaining the voltage and frequency of the system close to the nominal values. The proposed control strategy ensures the supply of required negative sequence components to maintain balanced system voltage and mitigate the active power ripples during unbalanced faults. The unified control architecture is devised through a systematic definition of steady-state operating modes and the interaction among hierarchical entities in the grid. The results are verified using a real-time simulator-based multi-rate model-in-the-loop set-up. Furthermore, appropriate communication network latency is considered for the verification of the performance of the proposed PNS controller. The verification of test cases for various grid events confirms the capability and effectiveness of the proposed control architecture, and suitability for 100% IBR-based grid operation.

### 3.1 Introduction

The power distribution system has a lower  $X/R$  ratio in comparison to the bulk-power grid and is generally unbalanced in nature with unequal phase-wise loading levels due to the common use of single- and two-phase laterals [106]. For normal operating conditions and during outages or islanded operations, in the presence of several IBRs, the distribution system needs to operate in different scenarios, a) grid-following type of IBRs supply power as per the provided set-points in presence of the main grid source, b) grid-forming type of IBRs maintain desired balanced grid voltage and frequency and share the power demand among the other grid-following IBRs in absence of the main grid source, and c) perform smooth transitioning with acceptable transients when the main grid source connects and disconnects [107]. Grid-forming IBRs using dedicated controllers can generate PNS components dur-

ing unbalanced scenarios and are capable of supplying continuous negative sequence (NS) currents to maintain balanced voltage in the system [108, 109].

Typically, the grid-following IBR is designed to incorporate the negative sequence current blocking control (NSCB) and supply only positive sequence (PS) currents [58]. During unbalanced voltage conditions, the IBR supplying only PS currents result in the second harmonic component in DC-link voltage and the injected active power. This may lead to the disconnection of the IBR from the grid to safeguard IBR components [110]. By accurately extracting the PNS voltages and currents, compensation for the ripples in the DC-link and active power is possible [108, 111]. Moreover, IEEE P 2800 [37], and recent European grid codes [112] have updated the requirement of negative-sequence current injection performance from IBR-based DER. This requirement is also in alignment with the research roadmap for IBRs [113]. Alongside, the current limiting feature of the IBRs plays a critical role in providing fault ride-through capabilities [114] and can be a concern in providing enough unbalanced current. In this regard, strategies proposed in previous works ([108, 115–117]) suffer from complexity and lack generality.

In [108], a methodology for ride-through along with PNS control is proposed which is generic to different types of IBRs. However, this method has two main drawbacks. First, multiple signal transformation (such as from  $dq$  to  $abc$  frame and vice-versa) is required for the controller operation during current limiting which may not be computationally efficient and may lead to high transient currents during grid fault conditions. Second, in that architecture, the controller does not consider grid-following IBRs which share the load power with the grid-forming IBR in the islanded system. The approach proposed in [115] requires computation and systematic selection of the power ratios ( $P^+/P$  and  $Q^+/Q$ ) to meet the current limiting requirement. Approaches that require switching between the synchronous reference frame and natural reference frame, and current clipping until the computation of RMS value (such as in [116]) add complexities to the current limiting strategy. Ref. [117] have proposed a synchronous reference frame sequence-based control, wherein current limiting is achieved by dynamically calculating PNS  $dq$ -frame current signals. The dynamic calculation requires the computation of phasors which in turn incur delays.

Advanced droop control is a well-established power-sharing method for stable multiple IBR operations without the need for communication [28, 30, 118]. In this method, the local controller is designed with droop laws considering the network characteristics and IBR output impedances. Since the distribution system has a low  $X/R$ , the correlation of the form  $P \sim V$  and  $Q \sim \omega$  is valid for the IBRs with any type of output impedance [28]. However, these droop laws lead to the deviation of system frequency and voltage from the nominal values [75]. By adopting the angle droop law, the system frequency can be maintained close to the

nominal value further improving the accuracy of power-sharing [119]. And, to minimize the system voltage deviation from the nominal value, a robust droop controller can be designed as presented in [29].

When the main grid source maintains the system voltage, the voltage penalty of the robust droop law is insignificant as the system voltage deviation is negligible. Furthermore, to improve the power tracking accuracy of the IBRs in presence of the main grid source, it is possible to add an integral action to the droop law [120]. However, in the absence of the main grid source, as the total load in the system does not match the injected power by the IBR pure integrators fail to perform [121]. Though proportional gain-based robust droop control penalizes the voltage deviation arising from the load changes, the system steady-state voltage errors are still not negligible. Thus there is a necessity to improve the robust droop law to maintain system voltage close to the nominal values.

While connecting the main grid to the islanded system, the internal reference voltage of the IBRs needs to be corrected such that the voltage magnitude and angle difference between the main grid and islanded system is within the tolerance band before closing the breaker [65]. ANSI code A25A provides requirements for dispatching and synchronizing multiple DERs for seamless transitioning between the modes of operation [122]. Droop-based seamless transitioning approaches require a centralized algorithm to modify droop parameters in real-time [123] and inertia emulation of the system [124]. Hierarchical control approaches [125, 126] are expensive when there is a scope to unify the controller layers of different timescales [127]. Phase-locked loop (PLL) based grid synchronization and seamless transitioning techniques have demonstrated an improved performance under different dynamic conditions of the system [65, 107]. However, such PLL-based approaches did not verify the control strategy that involves droop laws in an unbalanced system.

### 3.2 Research Contributions

In this chapter, a unified control architecture is proposed for the stable multiple IBR operation in an unbalanced distribution system alongside maintaining system voltage and frequency close to the nominal values. The authors have worked to address the key research challenges mentioned in the research road-map of the IBR-based power grid operation [113] and in alignment to which the key contributions of the proposed architecture are:

- Improved positive sequence IBR power control method for maintaining system parameters such as voltage magnitude and frequency close to the nominal values
- Negative sequence IBR power control mechanism for mitigating the power ripples occurring during unbalanced faults, thereby assuring the ride-through capability of the IBR.

- A straightforward generalized PNS-scaling-based current limiter (CL) to achieve the required ride-through capability in different modes of operation.
- Real-time model-based verification for various grid events such as linear and nonlinear load changes, ride-through during unbalanced faults, seamless transitioning between the proposed modes of operation, and dynamic role change of IBRs.
- Verification of the architecture with underlying communication network latency.

### 3.3 Control Architecture for IBRs in an Unbalanced System

In this section control architecture for a given IBR operation in an unbalanced system is described. A PNS-based architecture is designed using the linear system theory principles.

#### 3.3.1 System Description in terms of PNS Components

Fig. 3.1 depicts the system overview and the cascaded controller configuration of the three-phase IBR with a constant DC link voltage. IBR system including  $LCL$  filter is connected to the grid through a smart switch (SS) for the grid-tied or islanded mode of operation. Smart switches are controllable circuit breakers with communication capabilities that aid in network reconfiguration [6]. Dominant switching harmonics of the power electronic switches of the IBR are attenuated by designing an appropriate  $LCL$  filter and a passive damping method is used in series with a filter capacitor [128] to mitigate the resonant peak issues.

The control system consists of a current control loop followed by a voltage control loop that gets reference signals from the PNS power control loop. The power reference signals for the power control loop are usually provided by the DER management system (DERMS) based on the system-level requirements. The PNS components of three-phase  $abc$  frame voltage and current signals are extracted using the delayed signal cancellation (DSC) method [129] using (3.1).

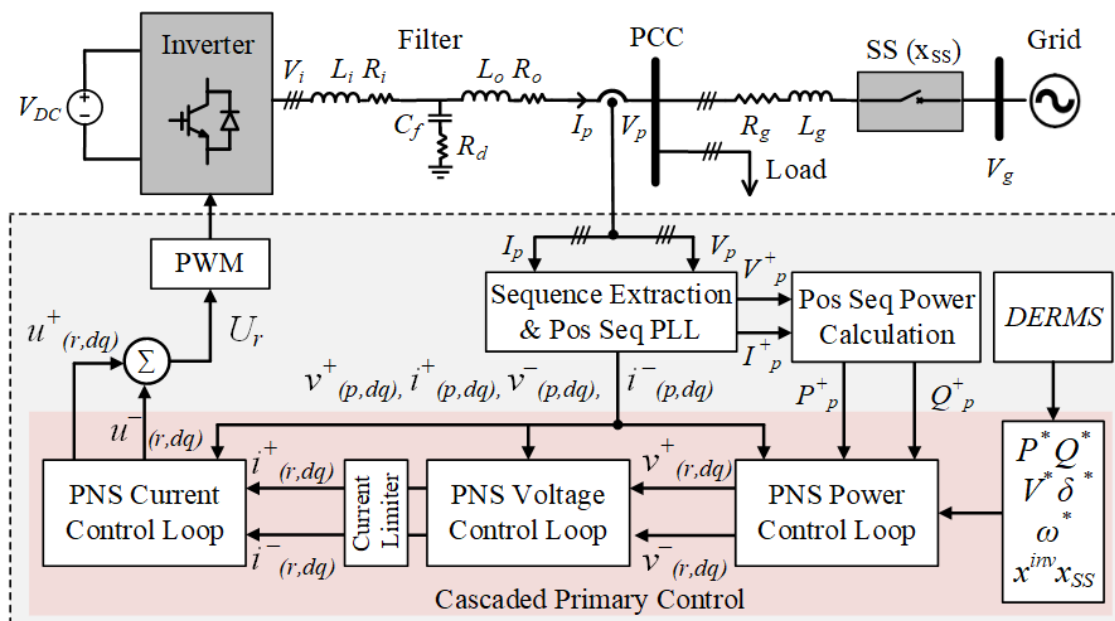


Figure 3.1: IBR PNS controller overview along with the CL in an unbalanced system.

An unbalanced signal  $V_p$  with the phase of  $\delta$  can be decomposed into positive  $V_p^+$  and negative  $V_p^-$  sequence balanced space vector as described in Fig. 3.2. The PS space vector rotates in a counter-clockwise direction, with an angular velocity of  $\omega$  and the NS space vector rotates in a clockwise-rotation direction with the same angular velocity. Considering the ideal discretization process and accurate knowledge of the grid frequency, the method can be used for online detection of PNS components [129].

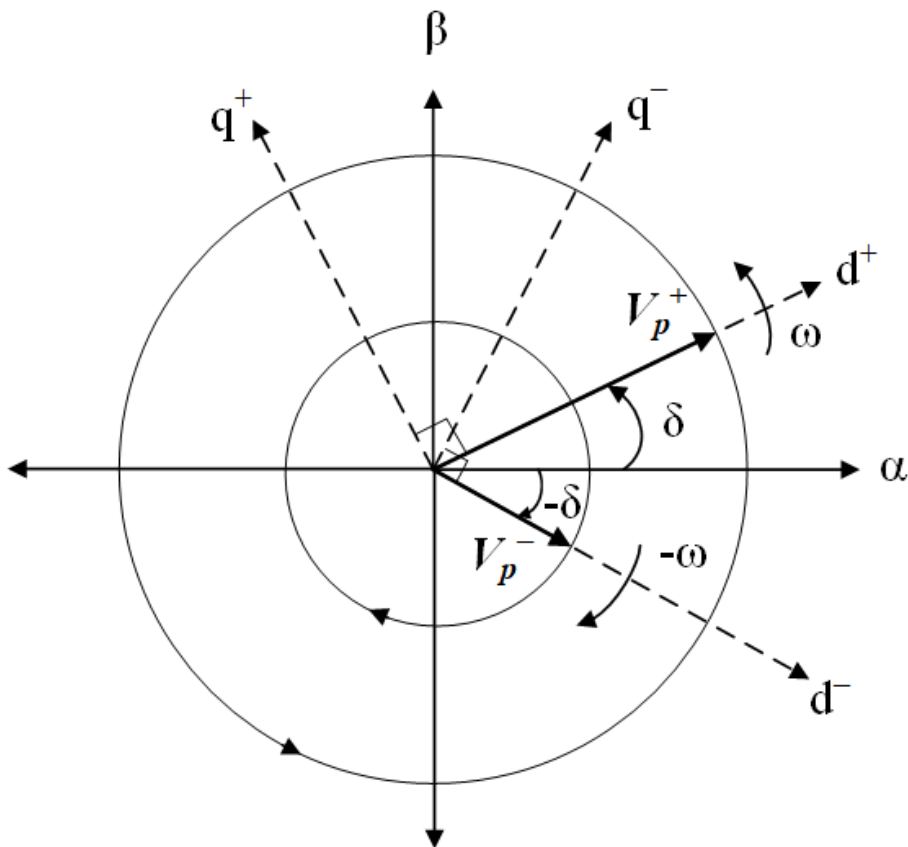


Figure 3.2: Decomposition of an unbalanced PCC voltage in terms of positive ( $V_p^+$ ) and negative ( $V_p^-$ ) sequence space vector, in stationary ( $\alpha\beta$ ) and rotating ( $dq$ ) reference frames.

The DSC method applied in the  $abc$  frame is described by (3.1) for the extraction of PNS components of the PCC voltage ( $V_p$ ) and current ( $I_p$ ). Here  $T_g$  is the period of measured PCC signals.

$$\begin{aligned} V_p^\pm(t) &= \frac{1}{2} \left( V_p(t) \pm jV_p\left(t - \frac{T_g}{4}\right) \right) \\ I_p^\pm(t) &= \frac{1}{2} \left( I_p(t) \pm jI_p\left(t - \frac{T_g}{4}\right) \right) \end{aligned} \quad (3.1)$$

According to (3.1), while decomposing the voltage/current signal, DSC block will introduce a time delay of a quarter of the grid frequency period [66]. *Pade* approximation is used to obtain the rational transfer function of delays in terms of poles and zeros [130] as shown in (3.2). This DSC transfer function is further used in the design of PNS controllers and the PLL.

$$G_{DSC}(s) = \frac{X^\pm(s)}{X(s)} = e^{-\frac{sT_g}{4}} \approx \left( \frac{1 - 0.5\frac{T_g}{4}s}{1 + 0.5\frac{T_g}{4}s} \right) \quad (3.2)$$

### 3.3.2 Design Approach for the PNS Controller

The block diagram representation of the described system for the design and analysis of control loops is depicted in Fig. 3.3. The diagram is a multi-variable linear continuous-time system representation in terms of input  $U(s)$  to output  $Y(s)$  transfer matrices of the form:  $Y(s) = G(s)U(s)$ . For the controller design, the representation of transfer matrix  $G(s)$  for a given set of  $dq$ -frame inputs ( $[u_{(i,d)}^\pm, u_{(i,q)}^\pm]^T$ ) and outputs ( $[y_{(o,d)}^\pm, y_{(o,q)}^\pm]^T$ ) is given by (3.3). The cross-coupling elements (off-diagonal terms in  $G(s)$ ) are relatively small and therefore are neglected in the controller design. Furthermore, their effect can be eliminated by including the feed-forward compensation in the controller design [131].

$$\begin{bmatrix} y_{(o,d)}^\pm \\ y_{(o,q)}^\pm \end{bmatrix} = \begin{bmatrix} G_{(io,dd)}^\pm(s) & 0 \\ 0 & G_{(io,qq)}^\pm(s) \end{bmatrix} \begin{bmatrix} u_{(i,d)}^\pm \\ u_{(i,q)}^\pm \end{bmatrix} \quad (3.3)$$

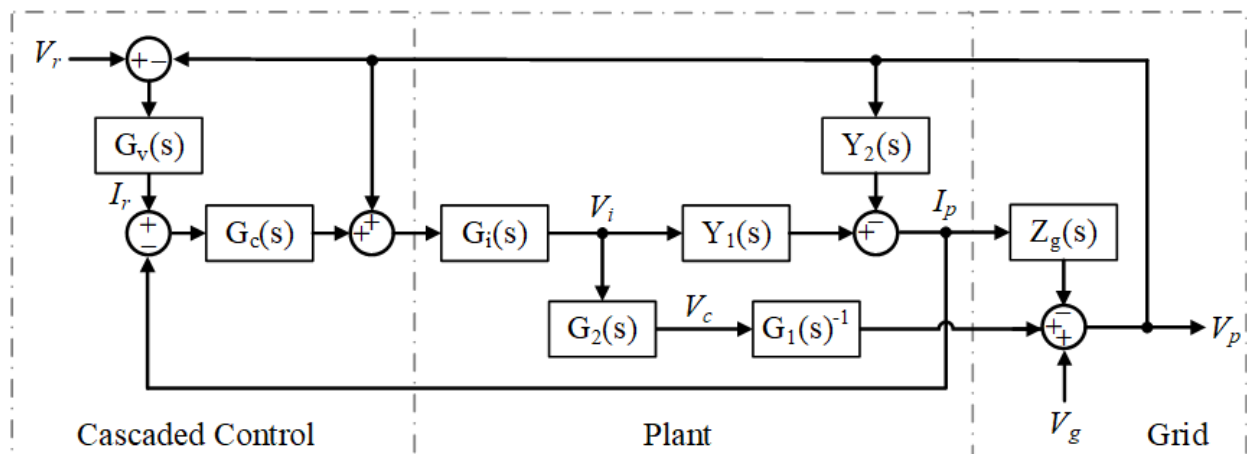


Figure 3.3: Block diagram of the cascaded current control followed by a voltage control loop, LCL plant, and the grid.

### 3.3.3 Description of *LCL* Plant Representation

Digitally controlled IBRs have a time delay of one sampling period ( $T_s$ ) due to the computational time of micro-controllers and half-sampling period ( $\frac{T_s}{2}$ ) delay of the pulse width modulator, represented as  $G_i(s)$ . The transfer function in terms of poles and zeros for  $G_i(s)$  is given by [130],

$$G_i(s) = e^{-1.5T_s s} \approx \frac{1 - 0.5T_s s}{(1 + 0.5T_s s)^2} \quad (3.4)$$

The transfer function from input to output variables can be identified by solving (3.5) and by considering 6x6 identity matrix for C. The solution for the same is described by (3.6).

$$Y(s) = G(s)U(s) = [C(sI - A)^{-1}B]U(s) \quad (3.5)$$

$$\begin{bmatrix} i_{(p,d)}^\pm & i_{(p,q)}^\pm & i_{(i,d)}^\pm & i_{(i,q)}^\pm & v_{(c,d)}^\pm & v_{(c,q)}^\pm \end{bmatrix}^T = \begin{bmatrix} Y_{(pp,dd)}^\pm(s) & Y_{(pp,qd)}^\pm(s) & Y_{(ip,dd)}^\pm(s) & Y_{(ip,qd)}^\pm(s) \\ Y_{(pp,dq)}^\pm(s) & Y_{(pp,qq)}^\pm(s) & Y_{(ip,dq)}^\pm(s) & Y_{(ip,qq)}^\pm(s) \\ Y_{(pi,dd)}^\pm(s) & Y_{(pi,qd)}^\pm(s) & Y_{(ii,dd)}^\pm(s) & Y_{(ii,qd)}^\pm(s) \\ Y_{(pi,dq)}^\pm(s) & Y_{(pi,qq)}^\pm(s) & Y_{(ii,dq)}^\pm(s) & Y_{(ii,qq)}^\pm(s) \\ G_{(pc,dd)}^\pm(s) & G_{(pc,qd)}^\pm(s) & G_{(ic,dd)}^\pm(s) & G_{(ic,qd)}^\pm(s) \\ G_{(pc,dq)}^\pm(s) & G_{(pc,qq)}^\pm(s) & G_{(ic,dq)}^\pm(s) & G_{(ic,qq)}^\pm(s) \end{bmatrix} \begin{bmatrix} v_{(p,d)}^\pm & v_{(p,q)}^\pm & v_{(i,d)}^\pm & v_{(i,q)}^\pm \end{bmatrix}^T \quad (3.6)$$

By ignoring the cross-coupling transfer functions as per (3.3), transfer matrices of the open-loop system are represented by (3.7). These transfer matrices capture the dynamics of the open-loop system for both positive and negative sequence components.

$$\begin{bmatrix} I_p(s) \\ I_i(s) \\ V_c(s) \end{bmatrix} = \begin{bmatrix} Y_1(s) & Y_2(s) \\ Y_3(s) & Y_4(s) \\ G_1(s) & G_2(s) \end{bmatrix} \begin{bmatrix} V_p(s) \\ V_i(s) \end{bmatrix} \quad (3.7)$$

### 3.3.4 PS Voltage-based PLL

PLL is used to track the grid voltage angle for the grid-following type of operation and generate an internal voltage angle with a fixed frequency of 60 Hz for the grid-forming type of IBRs. However, in an unbalanced system, the challenge in PLL design is to tackle the double grid frequency ripple caused by a three-phase unbalance voltage transformation to  $dq$ -frame. Moreover, the voltage signal could be distorted by the voltage sag/swell and harmonics; thus, the detection of the positive-sequence voltage component is critical for improving the tracking of the voltage phase as depicted in Fig. 3.4.

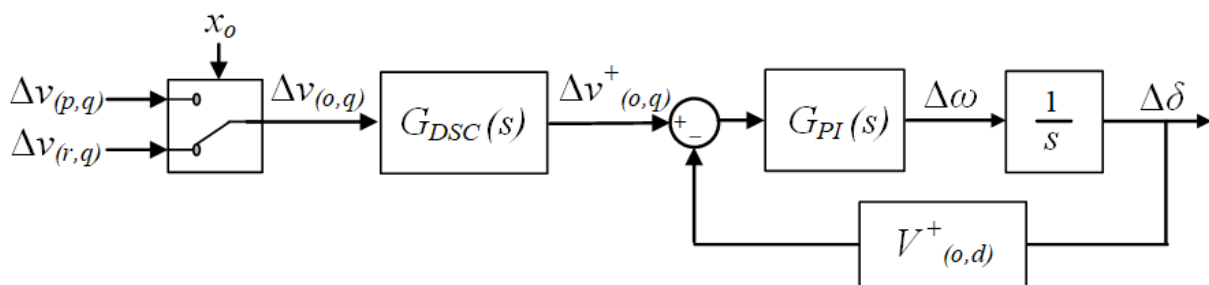


Figure 3.4: Linearized small signal model of PS voltage-based PLL that facilitates the seamless transition between grid-connected and islanded operating modes.

Since the DSC block can decompose the measured and reference signals into PNS components in real-time, a PS voltage component ( $V_o^+$ ) can be further utilized to track the voltage angle accurately. Based on the  $x^{inv}$  (see Section 3.4), the relevant input voltage signal ( $V_o^+$ ) is used to track the voltage phase as given by (3.8). Second-order linearized small-signal expression for PLL (PI loop filter and integrator) in terms of the feedback of  $V_{(o,d)}^+$  is given

by [80] (3.9). The  $dq$ -frame signals are generated by using the PS voltage angle tracked by the PLL.

$$V_o^+ = !x^{inv}V_p^+ + x^{inv}V_r^+ \quad (3.8)$$

$$\Delta\dot{\delta} = k_p^{pll}(v_{(o,q)}^+ - V_{(o,d)}^+\Delta\delta) + k_i^{pll} \int (v_{(o,q)}^+ - V_{(o,d)}^+\Delta\delta) dt \quad (3.9)$$

From (3.2) and (3.9), the representation of the PS voltage-based PLL in transfer function form is described as:

$$\frac{\Delta\delta(s)}{\Delta v_{(o,q)}(s)} = G_{DSC}(s) \left( \frac{k_p^{pll}s + k_i^{pll}}{s^2 + V_{(o,d)}^+k_p^{pll}s + V_{(o,d)}^+k_i^{pll}} \right) \quad (3.10)$$

From (3.2) and (3.9), the Bode plot with  $V_{(o,d)}^+ = 1$  and different damping coefficients ( $\zeta$ ) is depicted in Fig. 3.5. The plots showcase that the PLL design is stable with positive phase and gain margins, and has good PLL bandwidth to perform better when the voltage signal has harmonics and dc offsets. The loop filter gain coefficients ( $k_p^{pll} = 70, k_i^{pll} = 2500$ ) have a damping coefficient of 0.7, and the voltage angle tracking settling time of less than 100 *ms*. These parameters offer a gain margin of 17.2 dB, phase margin of 110 degrees, and bandwidth of 15 Hz.

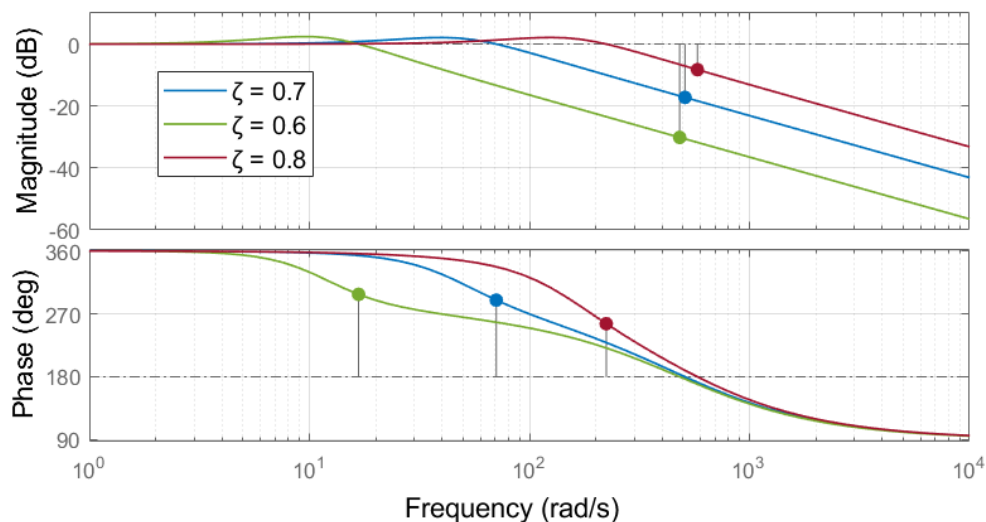


Figure 3.5: Bode plot of the linearized PS voltage-based PLL for different  $\zeta$  values.

### 3.3.5 Design of PNS Current Control Loop

When the IBR is connected to the grid through a closed SS, the current injected at PCC ( $I_p$ ) can be expressed as a function of LCL plant input voltage ( $V_i$ ) and the PCC voltage ( $V_p$ ):

$$I_p(s) = Y_1(s)V_i(s) - Y_2(s)V_p(s) \quad (3.11)$$

In this scenario, PCC voltage ( $V_p$ ) maintained by the grid source acts as a disturbance in the system represented as an impedance concerning the current control loop. Thus the open-loop transfer function, including digitally controlled IBR emulation, is identified as:

$$G_{(c,ol)}(s) = \frac{I_p(s)}{V_i(s)} = G_i(s)Y_1(s) \quad (3.12)$$

The closed loop CC is designed considering the transfer matrix representation as:

$$G_{(c,cl)}(s) = \frac{G_i(s)Y_1(s)G_c(s)}{1 + G_i(s)Y_1(s)G_c(s)} \quad (3.13)$$

where  $G_c(s)$  is the transfer matrix that accommodates PNS current PI controllers in  $dq$ -frame:

$$G_c(s) = \begin{bmatrix} \frac{k_{(p,d)}^{cc\pm}s + k_{(i,d)}^{cc\pm}}{s} & 0 \\ 0 & \frac{k_{(p,q)}^{cc\pm}s + k_{(i,q)}^{cc\pm}}{s} \end{bmatrix} \quad (3.14)$$

Fig. 3.6 depicts the Bode plots for  $G_{(c,ol)}(s)$  and  $G_{(c,cl)}(s)$  at  $k_{(p,d)}^{cc} = 0.08$ ,  $k_{(i,d)}^{cc} = 55$ . CC gain parameters are tuned to provide better response time within the stability margins. It can be seen that the closed-loop system is stable with positive gain and phase margin. Moreover, after adding the PI controller increase in gain margin from 6.29 dB to 27.9 dB and an increase in phase margin from 65.6 degrees to 117 degrees, greatly improves the stability margin of the system.

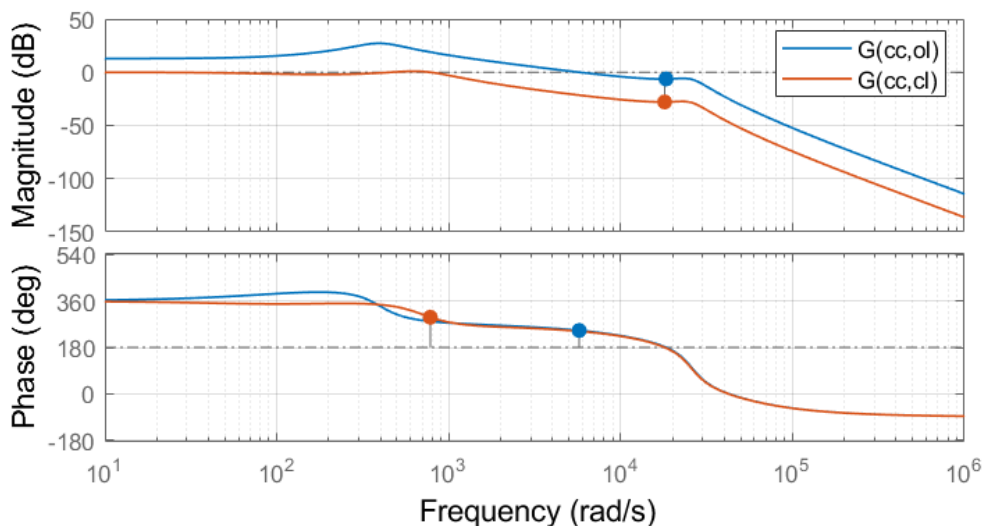


Figure 3.6: Bode plot of the open loop system and corresponding current control applied closed loop.

### 3.3.6 Design of PNS Voltage Control Loop

During the islanded mode of operation, the SS is opened, and the IBR regulates the voltage at the PCC. Therefore, the open-loop transfer function as a ratio of voltage at PCC ( $V_p$ ) and LCL filter input voltage ( $V_i$ ) can be expressed as:

$$G_{(v,ol_{sys})}(s) = \frac{V_p(s)}{V_i(s)} = \frac{G_2(s)}{G_1(s)} \quad (3.15)$$

where  $G_1(s) = \frac{V_c(s)}{V_p(s)}$ ,  $G_2(s) = \frac{V_c(s)}{V_i(s)}$  are obtained from (3.7) Since the CC is already designed to meet its objective, the open loop model for voltage control is updated as:

$$G_{(v,ol)}(s) = \frac{V_p(s)}{I_r(s)} = \frac{G_2(s)G_i(s)G_c(s)}{G_1(s)} \quad (3.16)$$

The closed loop VC is designed considering the transfer matrix representation as:

$$G_{(v,cl)}(s) = \frac{G_2(s)G_i(s)G_c(s)G_v(s)}{G_1(s) + G_2(s)G_i(s)G_c(s)G_v(s)} \quad (3.17)$$

where  $G_v(s)$  is the transfer matrix that accommodates PNS voltage PI controllers in  $dq$ -frame:

$$G_v(s) = \begin{bmatrix} \frac{k_{(p,d)}^{vc\pm}s + k_{(i,d)}^{vc\pm}}{s} & 0 \\ 0 & \frac{k_{(p,q)}^{vc\pm}s + k_{(i,q)}^{vc\pm}}{s} \end{bmatrix} \quad (3.18)$$

Fig. 3.7 depicts the Bode plots for  $G_{(v,ol)}(s)$  and  $G_{(v,cl)}(s)$  at  $k_{(p,d)}^{vc} = 85$ ,  $k_{(i,d)}^{vc} = 1546$ . VC gain parameters are tuned to meet the stability margins. It can be seen that the closed-loop system is stable with positive gain and phase margins. The gain margin of the closed loop system reduces to 18.7 dB, from 36.4 dB of the open loop system at 67.3 krad/s. Moreover, the closed loop system with voltage control retains the 132-degree phase margin of the open loop system. The designed current and voltage control loop gain parameters are used across both PNS controllers in  $d$  as well as  $q$  axis due to the symmetrical nature of sequence components and  $dq$ -frame.

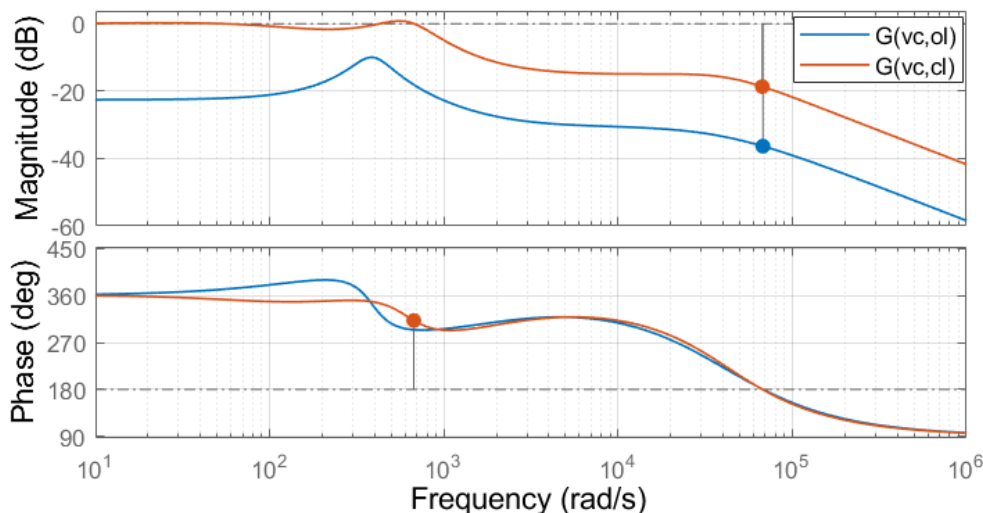


Figure 3.7: Bode plot of the open-loop system and corresponding cascaded voltage-current control applied closed loop

### 3.3.7 Strategy for PNS Current Limiting in $dq$ -frame

During the fault scenarios, the IBR output current should be limited to protect the underlying power electronic components and provide ride-through capabilities. Typically, grid-following IBRs are configured to supply 1.1 p.u. to 1.2 p.u. of current during the fault, while grid-forming IBRs can supply up to 2 p.u. of current [109]. The proposed current limiter for both types of IBRs is described in Fig. 3.8. In unbalanced fault scenarios, the current limiting method should ensure  $abc$  frame current reference signal amplitude ( $I_r$ ) is limited to a predetermined value  $I_{lim}$ . In the proposed limiter, first, ( $I_r$ ) is calculated based on the output of the PNS VC as shown in (3.19).

$$I_r^\pm = \sqrt{(i_{(r,d)}^{\pm ul})^2 + (i_{(r,q)}^{\pm ul})^2}, \quad I_r = I_r^+ + I_r^- \quad (3.19)$$

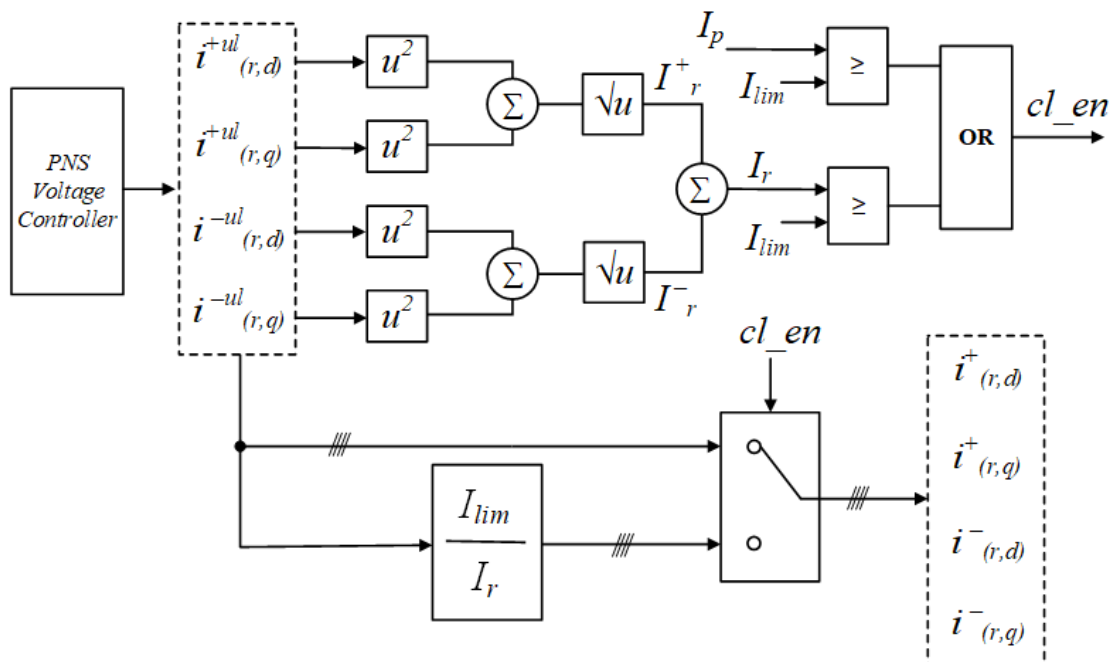


Figure 3.8: Proposed Sequence Component based Current Limiter in  $dq$ -frame

To limit  $I_r$  to  $I_{lim}$  during fault scenarios (when  $I_r$  or  $I_p$  is greater than  $I_{lim}$ ), let there be a common scaling factor  $k_s$ , which leads to regulating the reference current amplitude to  $I_{lim}$ , then  $k_s$  is identified by (3.20) and (3.21):

$$I_{lim}^{\pm} = \sqrt{(k_s i_{(r,d)}^{\pm ul})^2 + (k_s i_{(r,q)}^{\pm ul})^2} \implies I_{lim} = k_s I_r \quad (3.20)$$

$$k_s = \begin{cases} \frac{I_{lim}}{I_r} & \text{if } (I_r | I_p) \geq I_{lim} \\ 1 & \text{otherwise} \end{cases} \quad (3.21)$$

The proposed method is generic and is applicable in balanced scenarios ( $I_r^- = 0$ ) and all type of faults as the scaling factor proportionally reduces the PNS  $dq$  components. The scaling-based approach is more efficient than the latching-based approach as during transients, the individual PNS  $dq$  signals may latch at wrong values. This incorrect latching may lead to unexpected wind-ups, thereby leading to violation of the current limiting after the clearance of the fault signal [53]. Moreover, due to current limitations, the integrators of PNS VCs would face a wind-up challenge. To overcome this, a tracking integration method (with a gain value of 1) is applied to prevent the wind-up evolved from [85].

### 3.4 Unified Architecture for Multiple IBR Operation with Seamless Transition

A unified control methodology is proposed in this section to achieve the seamless operation of parallel IBRs in an unbalanced system. The methodology involves the unification of power-sharing, and power-tracking approaches for PS controllers and the choice of NS voltage controller (NSVC) depending on the state of the IBR ( $x_i^{inv}$ ) as described in Fig. 3.9. A communication delay of  $T_{d1}$  is modeled to demonstrate the interaction between time-critical messages (such as IEC 61850 compliant trip signals) between the relay and the IBRs [132]. A delay of  $T_{d2}$  that is applicable for the IP-based networks is modeled for the communication

between DERMS and IBRs.

*Definition 1:* For a group of IBRs ( $i = 1, 2, \dots, n$ ) in a section of the network, let  $inv_i^t = 0$  and  $inv_i^t = 1$  represent the grid-following and grid-forming type of an IBR respectively. Furthermore, let  $x_{SS} = 0$  represent the presence of the main grid source with SS being closed, and  $x_{SS} = 1$  represents the disconnection of the main grid source with SS being open. At any given point of time, there exists a unique state  $x_i^{inv} = (x_{SS} \ \& \ inv_i^t)$  that dictates IBR to operate with the grid-following role ( $x_i^{inv} = 0$ ) or grid-forming role ( $x_i^{inv} = 1$ ).

Based on *Definition 1*, the steady-state operating modes of the proposed unified controller are described below:

1. Type 0 PS mode, Type 0 NSVC ( $x_{SS} = 0, x_i^{inv} = 0$ ): network voltage is balanced by the main grid source, all the IBRs are in grid-following role, delivering power as per the given set-points, and supply NS currents only when there is an unbalanced scenario.
2. Type 1 PS mode, Type 0 NSVC ( $x_{SS} = 1, x_i^{inv} = 0$ ): as the main grid source is unavailable, network voltage is balanced by the grid-forming IBR, rest of the grid-following IBRs share the load power and supply NS currents only when there is an unbalanced scenario.
3. Type 1 PS mode, Type 1 NSVC ( $x_{SS} = 1, x_i^{inv} = 1$ ): as the main grid source is unavailable, network voltage is balanced by the grid-forming IBR through the continuous supply of NS currents, and perform load power sharing with the rest of the grid-following IBRs

In this section, details of the operating modes and the underlying control methods are described. The configuration details for different operating modes of the IBR are provided in Table 3.1.

TABLE 3.1: Variable and parameter configuration for multiple IBR operations based on the proposed unified control

Mode/Control	$x_{SS}$	$v_{(r,i)}^+$	$P_i^*$	$Q_i^*$	$x_i^{inv}$	$v_{(r,i)}^-$	$\delta(PLL)$
Type 0 PS mode / Type 0 NSVC	0	droop Type 0	$P_r^i$	$Q_r^i$	0	$v_{(p,i)}^-$	$\delta_p^i$
Type 1 PS mode / Type 0 NSVC	1	droop Type 1	1	0	0	$v_{(p,i)}^-$	$\delta_p^i$
Type 1 PS mode / Type 1 NSVC	1	droop Type 1	1	0	1	0	$\delta_r^i$

### 3.4.1 PS Power Control Methodology

From the universal and robust droop laws [28] [29], and by the adoption of angle droop [119], droop correlations that are valid for a low  $X/R$  distribution system are given by (3.22) and (3.23).

$$v_{(r,i)}^+ = V_i^* - k_p^P \Delta P_i^+ + k_p^V \Delta V_i \quad (3.22)$$

$$\delta_{(r,i)}^+ = \delta_i^* + k_p^Q \Delta Q_i^+ \quad (3.23)$$

where  $\Delta P_i^+ = (P_{(p,i)}^+ - P_i^*)$ ,  $\Delta Q_i^+ = (Q_{(p,i)}^+ - Q_i^*)$ , and  $\Delta V_i = (V_i^* - V_{(p,i)})$ .

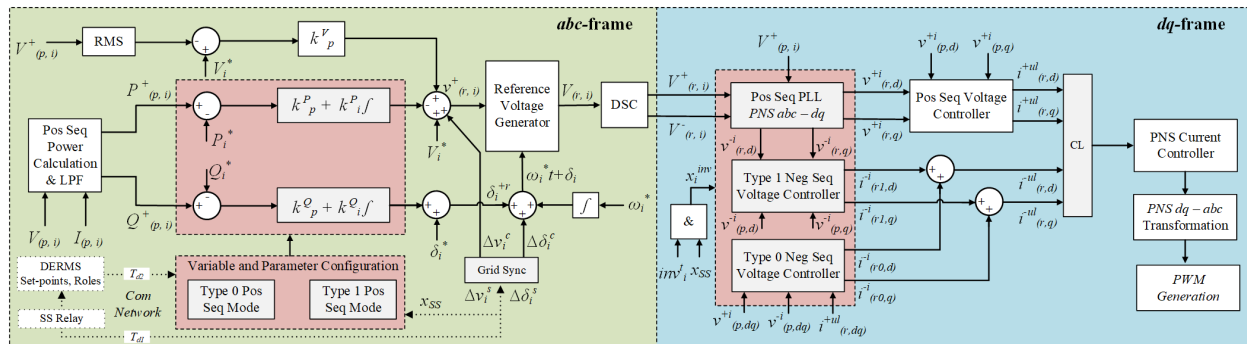


Figure 3.9: Proposed unified PNS control that can seamlessly operate irrespective of the type of IBRs. When  $x_i^{inv} = 0$ , PLL tracks the voltage angle at the PCC of respective IBR and when  $x_i^{inv} = 1$ , PLL tracks the IBR internal voltage angle.

**Type 0 PS mode** ( $x_{SS} = 0$ ): In this mode, PCC voltage angle is tracked by the IBRs as  $x_i^{inv} = 0$ . In the proposed approach, utilizing the robust droop control laws of (3.22) and (3.23), active and reactive power reference tracking ( $P_i^* = P_r^i$ ,  $Q_i^* = Q_r^i$ ) is achieved by introducing the integral error loop as shown in (3.24) and (3.25). Since  $\Delta V_i$  is close to zero in healthy grid operating conditions, the voltage drop penalty factor  $k_p^V$  does not influence the power tracking capability. The introduced integral error term guarantees power tracking with no steady-state error which may not possible with (6.7) and (6.8).

$$v_{(r,i)}^+ = V_i^* + k_p^V \Delta V_i - k_p^P \Delta P_i^+ - k_i^P \int \Delta P_i^+ dt \quad (3.24)$$

$$\delta_{(r,i)}^+ = \delta_i^* + k_p^Q \Delta Q_i^+ + k_i^Q \int \Delta Q_i^+ dt \quad (3.25)$$

In this mode, the main grid source maintains the voltage and frequency close to the nominal values, and DERMS issues  $P_r^i$ , and  $Q_r^i$  power reference set-points to the respective DERs as described in Table 3.1.

**Type 1 PS mode** ( $x_{SS} = 1$ ): In this mode, for the transformation of the signals from *abc*-frame to *dq*-frame, the PCC voltage angle is considered when  $x_i^{inv} = 0$ , and the internal voltage angle is considered when  $x_i^{inv} = 1$ . The integral terms of (3.24) and (3.25) that facilitate accurate power tracking in Type 0 PS mode can not be applied in Type 1 PS mode as the power delivered by the IBR is never equal to the total load in the system. Let  $\hat{P}_{(p,i)}^+$  be the estimated power to be delivered by the  $i^{th}$  IBR, then error in power sharing is represented by  $\Delta \hat{P}_i^+ = \hat{P}_{(p,i)}^+ - P_{(p,i)}^+$ . An integral component is added to the (3.22) as described by (3.26) to minimize this steady state power-sharing error  $\Delta \hat{P}_i^+$ . This minimization of power-sharing error proportionally minimizes the voltage deviation error occurring from (3.22).

$$v_{(r,i)}^+ = V_i^* + k_p^V \Delta V_i - k_p^P \Delta P_i^+ - k_i^P \int \Delta \hat{P}_i^+ dt \quad (3.26)$$

In the steady-state operation,  $\hat{P}_{(p,i)}^+$  and  $\hat{Q}_{(p,i)}^+$  are obtained as the ratio of the respective estimated active and reactive power demand and the aggregated available power supply.

However, integral of the term  $\Delta\hat{Q}_i^+$  in reactive power droop law ( $Q \sim \delta$ ) is not controllable and hence (3.23) is used in Type 1 PS mode by setting  $k_i^Q$  to zero in (3.25). Moreover, the adoption of angle droop ensures the system frequency close to the nominal value. The power-sharing set-point signal ( $\hat{P}_{(p,i)}^+$ ) is communicated to the respective DERs from the DERMS.  $P_i^*$ , and  $Q_i^*$  set-points are set to 1 and 0 respectively in Type 1 PS mode as mentioned in Table 3.1.

### 3.4.2 NS Power Control Methodology

**Type 1 NSVC ( $x_i^{inv} = 1$ ):** when the SS is closed ( $x_{SS} = 0$ ), the grid source maintains the balanced voltage in the system by supplying the required NS currents. When the SS is open ( $x_{SS} = 1$ ), grid-forming IBR is expected to perform a similar job to the main grid source. As depicted in Fig. 3.9 NS voltage reference  $V_{(r,i)}^-$  extraction from  $V_{(r,i)}$  is ideally zero as  $V_{(r,i)}$  calculated from PS droop laws is a balanced signal. Furthermore, the operating state of a given IBR ( $x_i^{inv} = 1$ ) dictates the NS reference voltages ( $v_{(r,d)}^{-i}, v_{(r,q)}^{-i}$ ) to be set to zero as  $V_{(r,i)}^- = 0$ . This approach results in the providing required NS reference currents ( $i_{(r1,d)}^{-i}, i_{(r1,q)}^{-i}$ ) to maintain the balanced voltage in the system during the steady state operation.

**Type 0 NSVC ( $x_i^{inv} = 0$ ):** IBRs that are operating as grid-following type witness balanced voltage at their respective PCCs maintained by either grid source or grid-forming IBRs (with Type 1 NSVC when  $x_i^{inv} = 1$ ). However, PCC voltage could still be unbalanced during unbalanced faults. In such unbalanced scenarios, for all the grid-following IBRs in the system ( $x_i^{inv} = 0$ ), an appropriate NS current reference needs to be calculated to mitigate the second harmonic power ripples in the system [133].

IBR operating state  $x_i^{inv} = 0$  dictates NS reference voltages ( $v_{(r,d)}^{-i}, v_{(r,q)}^{-i}$ ) to be set to NS PCC voltage values ( $v_{(p,d)}^{-i}, v_{(p,q)}^{-i}$ ) so that Type 1 NSVC becomes void. When the PCC voltages are unbalanced, IBR active and reactive power at PCC in terms of time domain signal ( $p_{(p,i)}(t), q_{(p,i)}(t)$ ) are given by (3.27) and (3.28) respectively.

$$p_{(p,i)}(t) = p_{(p,i)} + p_{(p,i)}^1 \cos(2\omega t) + p_{(p,i)}^2 \sin(2\omega t) \quad (3.27)$$

$$q_{(p,i)}(t) = q_{(p,i)} + q_{(p,i)}^1 \cos(2\omega t) + q_{(p,i)}^2 \sin(2\omega t) \quad (3.28)$$

where

$$p_{(p,i)} = p_{(p,i)}^+ + p_{(p,i)}^- = \frac{3}{2}(v_{(p,d)}^{+i} i_{(r,d)}^{+i} + v_{(p,q)}^{+i} i_{(r,q)}^{+i} + v_{(p,d)}^{-i} i_{(r,d)}^{-i} + v_{(p,q)}^{-i} i_{(r,q)}^{-i}) \quad (3.29)$$

$$q_{(p,i)} = q_{(p,i)}^+ + q_{(p,i)}^- = \frac{3}{2}(v_{(p,q)}^{+i} i_{(r,d)}^{+i} - v_{(p,d)}^{+i} i_{(r,q)}^{+i} + v_{(p,q)}^{-i} i_{(r,d)}^{-i} - v_{(p,d)}^{-i} i_{(r,q)}^{-i})$$

$$p_{(p,i)}^1 = \frac{3}{2}(v_{(p,d)}^{-i} i_{(r,d)}^{+i} + v_{(p,q)}^{-i} i_{(r,q)}^{+i} + v_{(p,d)}^{+i} i_{(r,d)}^{-i} + v_{(p,q)}^{+i} i_{(r,q)}^{-i}) \quad (3.30)$$

$$p_{(p,i)}^2 = \frac{3}{2}(v_{(p,q)}^{-i} i_{(r,d)}^{+i} - v_{(p,d)}^{-i} i_{(r,q)}^{+i} - v_{(p,q)}^{+i} i_{(r,d)}^{-i} + v_{(p,d)}^{+i} i_{(r,q)}^{-i})$$

In presence of the main grid source (Type 0 PS mode), the IBR is expected to deliver reference values of active power ( $P_i^*$ ) and reactive power ( $Q_i^*$ ) that would reflect in measured

DC components:  $p_{(p,i)}^+$  and  $q_{(p,i)}^+$  at PCC. In absence of main grid source (Type 1 PS mode), power-sharing droop laws dictate the  $p_{(p,i)}^+$  and  $q_{(p,i)}^+$  at PCC. Given an unbalanced scenario, in both cases,  $p_{(p,i)}^1$  and  $p_{(p,i)}^2$  are oscillatory in nature (twice the grid frequency) and there is a need of dedicated controller to reduce these oscillations.

The objective of Type 0 NSVC is to mitigate the power ripples (set  $p_{(p,i)}^1$  and  $p_{(p,i)}^2$  to 0) by computing appropriate NS reference currents ( $i_{(r0,d)}^{-i}, i_{(r0,q)}^{-i}$ ). Cascaded power and voltage loop PS controllers provide the PS CC reference values ( $i_{(r,d)}^{+ul}, i_{(r,q)}^{+ul}$ ).  $dq$ -frame PNS components of measured PCC voltage are available after signal decomposition using DSC method and  $abc-dq$  transformation. The aforementioned known signals are utilized to compute the NS current reference values ( $i_{(r0,d)}^{-i}, i_{(r0,q)}^{-i}$ ) by solving (3.30) in terms of unknown variables as given by (3.31). Calculated NS current reference values are added to Type 1 NSVC output (before the current limiter) as shown in Fig. 3.9, so that in closed-loop, grid-following IBRs deliver NS currents only during unbalanced scenarios.

$$\begin{bmatrix} i_{(r0,d)}^{-ul} \\ i_{(r0,q)}^{-ul} \end{bmatrix} = \begin{bmatrix} v_{(p,d)}^{+i} & v_{(p,q)}^{+i} \\ -v_{(p,q)}^{+i} & v_{(p,d)}^{+i} \end{bmatrix}^{-1} \begin{bmatrix} -v_{(p,d)}^{-i} i_{(r,d)}^{+ul} - v_{(p,q)}^{-i} i_{(r,q)}^{+ul} \\ -v_{(p,q)}^{-i} i_{(r,d)}^{+ul} + v_{(p,d)}^{-i} i_{(r,q)}^{+ul} \end{bmatrix} \quad (3.31)$$

### 3.4.3 Mode Transitioning and Synchronization Mechanism

The proposed architecture ensures a smooth transition of IBR operation to Type 1 PS mode during intentional or unintentional islanding scenarios. When the grid is healthy, and there is an intention to re-connect the grid source, both  $\Delta v^s$  and  $\Delta \delta^s$  need to be within the acceptable range [114]. As depicted in Fig. 3.10, Relay communicates these differences to all the IBRs in the system. The consecutive steps to achieve synchronization and transition to Type 0 PS mode are mentioned below:

1. Relay issues  $en_{sy}$  signal which enables grid sync logic in the respective IBR control.
2.  $v_i^c$  is added to the IBR reference voltage in  $abc$ -frame for the voltage magnitude correction. This addition reflects in PS  $d$ -axis voltage reference signal ( $v_{(r,d)}^{+i}$ ).
3. A PI controller is used to generate voltage angle correction  $\delta_i^c$  in all of the IBR control.
4. When both side voltage parameters of SS are within the acceptable range (verified by Sync-check program), the relay operates to close SS and communicates the SS close status  $x_{SS} = 0$ .
5. After reading SS close status, IBRs transition to the Type 0 PS mode/Type 0 NSVC.

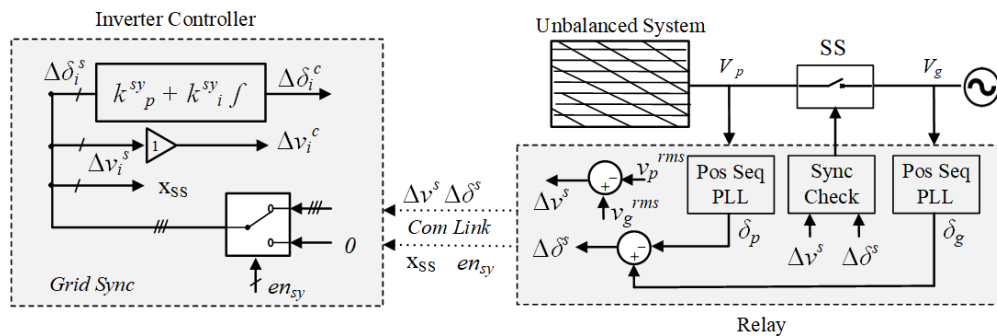


Figure 3.10: PS PLL-based synchronized grid connection for IBRs.

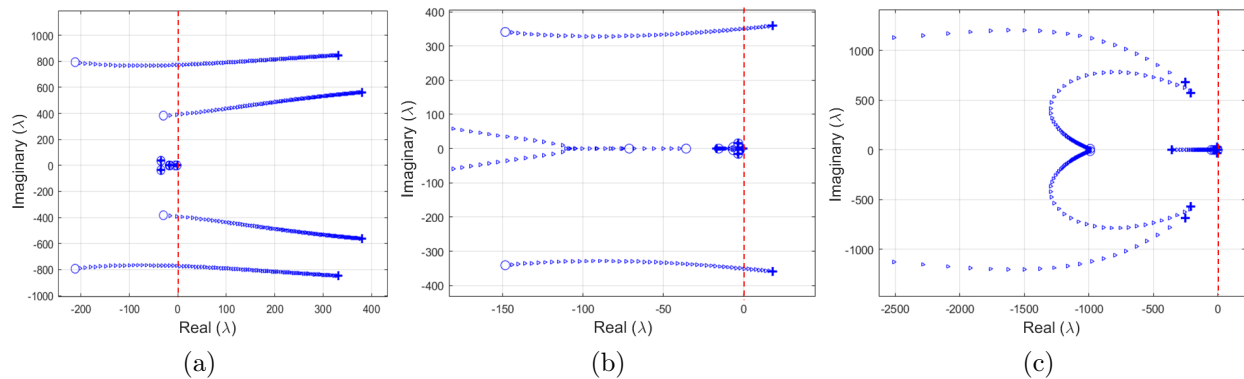


Figure 3.11: Eigenvalue analysis performed using the system matrix of the proposed closed-loop controller. The mode sensitivity for the droop law design parameters and the movement of eigenvalues for a given perturbation (voltage sag) is analyzed. (a) The trajectory of the eigenvalues as a function of the droop parameters in Type 0 PS mode, (b) Trajectory of the eigenvalues as a function of the droop parameters in Type 1 PS mode, (c) Medium and low-frequency eigenvalue trace for the PCC voltage sag due to faults.

### 3.4.4 Stability Analysis

The PS power calculation block (see Fig. 3.1) averages the computed instantaneous power using a low pass filter (LPF). Time domain representation of averaged active and reactive power after an LPF with a cut-off frequency of  $\omega_c$  on their respective instantaneous values is given by:

$$\dot{P}_{p,i}^+ = \omega_c (p_{p,i}^+ - P_{p,i}^+) \quad (3.32)$$

$$\dot{Q}_{p,i}^+ = \omega_c (q_{p,i}^+ - Q_{p,i}^+) \quad (3.33)$$

Based on the  $dq$  transformation of  $abc$  frame reference voltage signal as shown in (3.24) and (3.25), small signal voltage reference signal for VC can be represented as:

$$\Delta v_{(r,d)}^+ = k_p^V \Delta v_{(p,d)}^+ - k_p^P \Delta P^+ - k_i^P \int \Delta P^+ dt \quad (3.34)$$

$$\Delta v_{(r,q)}^+ = 0 \implies \Delta \delta^+ = k_p^Q \Delta Q^+ + k_i^Q \int \Delta Q^+ dt \quad (3.35)$$

The small-signal stability analysis is performed with a linearized dynamic model of closed-loop IBR control loops in  $dq$ -frame. Eigenvalue analysis is performed separately for design parameters of Type 0 and Type 1 PS mode and the voltage sag scenario arising from the faults. To perform such studies the respective steady-state values from the simulation are used in the stability analysis. System and per unitized controller parameters provided in Table 3.2 are utilized for the initialization of the linear model.

In a cascaded control system, outer loops are designed with a bandwidth that is at least four times slower than that of inner loops to achieve good tracking resolution and to avoid disturbances from the inner loop propagating to the outer loops. Droop laws along with the LPF are designed with low bandwidths (1-10 Hz) so that power control is slower than the voltage control, thereby ensuring the power quality. While designing the droop proportional parameters,  $(k_p^P, k_p^Q)$ , it is necessary to address the trade-off between the load power sharing accuracy and the overall closed-loop stability conditions. Integral droop parameters  $(k_i^P, k_i^Q)$  are designed to mitigate the steady-state errors with reasonable transients. The proportional parameters are varied from  $(0.1 \leq k_p^{P/Q} \leq 1.1)$  with an increment of 0.01 (100 values). Similarly, integral droop parameters are varied from  $(2 \leq k_i^{P/Q} \leq 3)$  with an increment of 0.01, and the trajectory of eigenvalues is observed.

Fig. 3.11a and Fig. 3.11b depict the trajectory of the dominant low-frequency eigenvalues ( $\lambda$ ) as a function of the droop parameters in Type 0 and Type 1 PS operating mode respectively. Since in the distribution grid, the line resistance can not be ignored, coupling of active and reactive power exists. This is justified by the observation in both modes of operation, as eigenvalues (shown as trajectory) are sensitive to both active and reactive power state variables. Moreover, a gradual increase in the droop parameter values leads to the movement of the sensitive eigenvalues towards the instability region causing oscillations in the system. Thus the choice of droop parameter values is performed based on the trade-off between improved transient response and system stability. For Type 1 operating mode as per the design rule,  $k_i^Q$  is set to zero and  $\Delta P^+$  is substituted by  $\Delta \hat{P}^+$  before performing the stability analysis.

Fig. 3.11c shows the trace of the medium and low-frequency modes for the PCC voltage sag occurring due to the faults in the system. The initial system is stable as the eigenvalues ( $\lambda$ ) are on the left half of the plane. When the voltage sag as a perturbation is included in the system dynamics, eigenvalues move in the direction of the right-half plane. However, eigenvalues are observed to be still in the stable region even when the voltage drop is considered. This analysis proves that the proposed controller and the design parameters are capable to operate the IBR in the stable region during faults in the system.

### 3.5 Real-time Multi-rate MIL Set-Up and Results

For the validation of the proposed architecture, 500 KVA and 200 KVA detailed IBR models are integrated into the section of the IEEE 123 node system at node 1 and node 13 respectively, as depicted in Fig. 3.12. Detailed IBR models are required to analyze the performance of ride-through capability during transients. *SS2* is always open, and part of the network that is upstream to node 13 is disconnected. Based on the status of *SS1*, IBRs operate in the respective modes. Initially, IBR 1 is configured as a grid-forming type with

a current limit of 1.4 p.u., and IBR 2 is configured as a grid-following type with a 1.1 p.u. current limit. The detailed switching model of IBRs is connected at node 1 and node 13 over a  $\Delta$ - $Y_g$  transformer with 480 V on the low voltage side and 4.16 kV on the grid side. System and per unitized controller parameters are provided in Table 3.2.

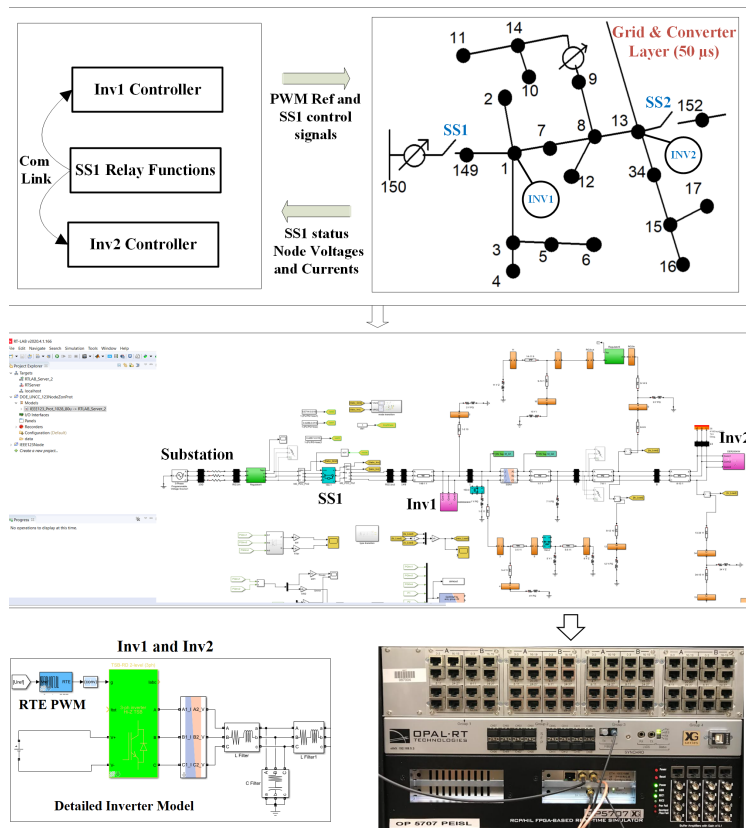


Figure 3.12: A section of IEEE 123 node system along with the detailed IBR models (TSB-RD 2-level) and control methods is used for system-level validation using real-time Opal-RT simulator.

The described system executes in the real-time (RT) simulator as per the Model-in-the-loop (MIL) test set up in the OPAL-RT eMEGASIM platform. RT simulator model is divided into two layers: the grid and converter layer executes with the sample time of 50  $\mu$ s and the controller layer is executed at 100  $\mu$ s. Such a multi-rate model is essential for the effective utilization of computational resources and the deployability of applications in a chosen target hardware [134].

TABLE 3.2: Summary of system and controller parameters

System Parameters	Values	Controller Parameters	Values (p.u.)
$(L_i^1, R_i^1)$	$(176 \mu H, 26.4 m\Omega)$	$(k_{(p,dq)}^{cc}, k_{(i,dq)}^{cc})$	(0.08, 55)
$(L_o^1, R_o^1)$	$(5.28 \mu H, 1 m\Omega)$	$(k_{(p,dq)}^{vc}, k_{(i,dq)}^{vc})$	(85, 1546)
$(C_f^1, R_d^1)$	$(287.8 \mu F, 44.5 m\Omega)$	$(k_p^{pll}, k_i^{pll})$	(70, 2500)
$(L_i^2, R_i^2)$	$(441 \mu H, 32.7 m\Omega)$	$(K_p^P, K_i^P)$	(0.3, 2.23)
$(L_o^2, R_o^2)$	$(13.2 \mu H, 1.5 m\Omega)$	$(K_p^Q, K_i^Q)$	(0.5, 2.23)
$(C_f^2, R_d^2)$	$(115.1 \mu F, 112 m\Omega)$	$K_p^V$	0.85
$V_{DC}$	900 V	$(k_p^{sy}, k_i^{sy})$	(0.04, 17.6)
$\omega_s$	377 rad/s	$F_{sw}$	10 kHz

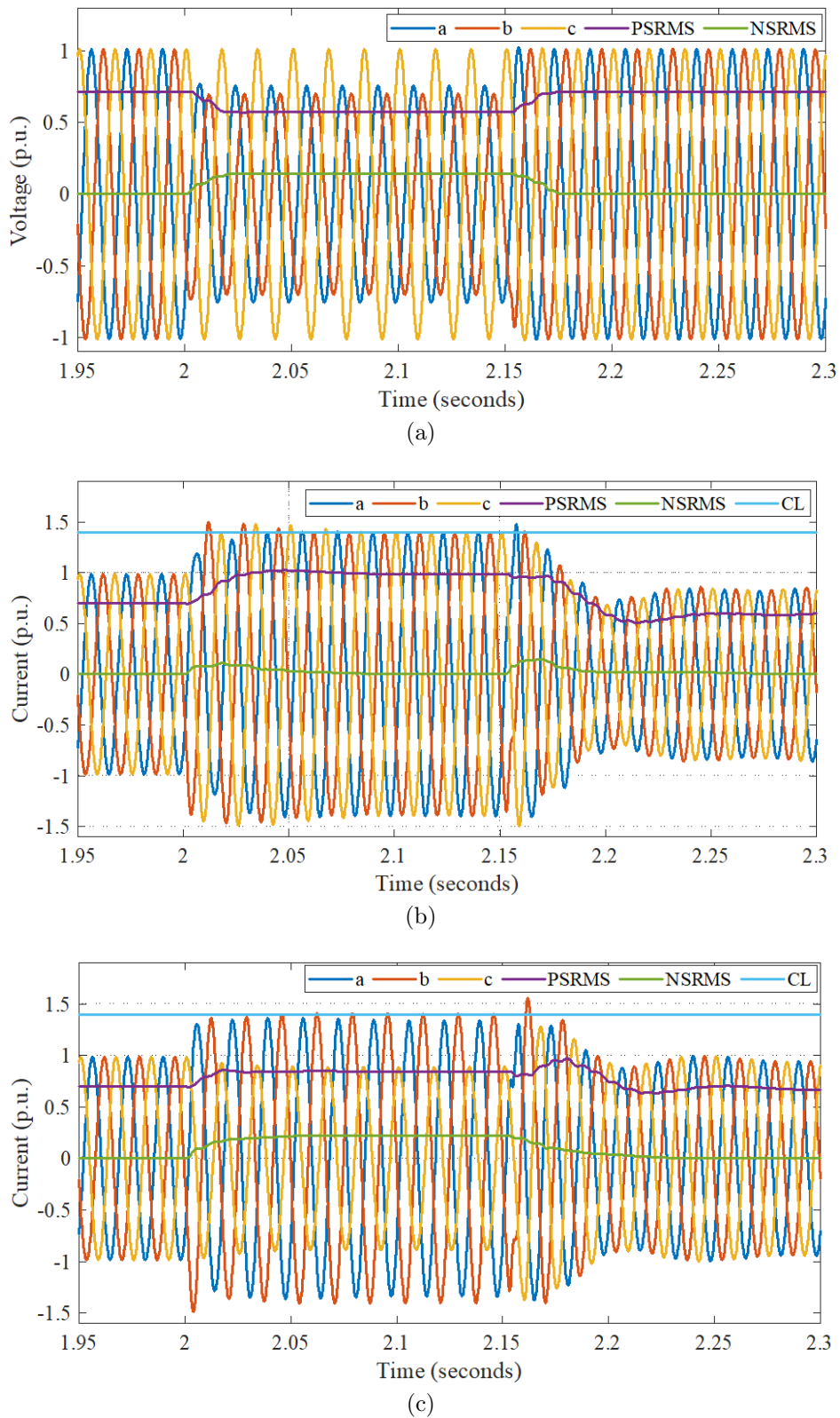


Figure 3.13: IBR 1 response to an unbalanced fault (AG) for the duration of 150 ms with fault resistance of  $0.5 \Omega$  at node 7 during Type 0 PS mode of operation. (a) Three-phase PCC (node 1) voltages and corresponding PNS RMS values. Three phase currents and corresponding PNS RMS values are injected by IBR 1 when (b) NSCB control is applied. (c) Type 0 NSVC is applied.

### 3.5.1 Unbalanced Fault in Type 0 PS Mode

In this mode, the voltage balance in the grid is maintained by substation (node 150) by supplying negative sequence currents, and IBRs deliver reference power by tracking the respective PCC voltage angle. Fig. 3.13 shows the MIL set-up results for the IBR response to an unbalanced fault in the Type 0 PS mode of operation. IBR 1 is operating in unity power factor mode with an active power reference of 1 p.u. An unbalanced fault (AG) of  $0.5 \Omega$  is introduced on node 8 at 2 s for the duration of 150 ms. During the fault, the voltage at

PCC (node 1 and node 13) would have positive as well as negative sequence components as seen in Fig. 3.13a. During the AG fault, 71% voltage sag on phase  $a$ , and 67% voltage sag on phase  $b$ , leading to 23 % sag on PS RMS voltage and 16 % swell on NSRMS voltage.

The IBR injects only PS current as shown in Fig. 3.13b with NSCB control and the NSRMS current value is observed to be zero. This leads to ripples of twice the grid frequency in the power delivered by IBR 1. With the NSVC, IBR 1 injects only PS currents up to 2 s as shown in Fig. 3.13c. However, from 2 s to 2.15 s, due to unbalance voltage at PCC, the IBR injects NS currents as calculated from (3.31). In comparison to the NSCB strategy, the proposed approach is effective in improving power quality by minimizing the 120 Hz oscillations in the active power signal from 21% to 0.1% as depicted in Fig 3.14 Type 0 PS mode graph. During a fault, a pre-determined fault current of 1.4 p.u. is delivered by the IBR validating the current limit design.

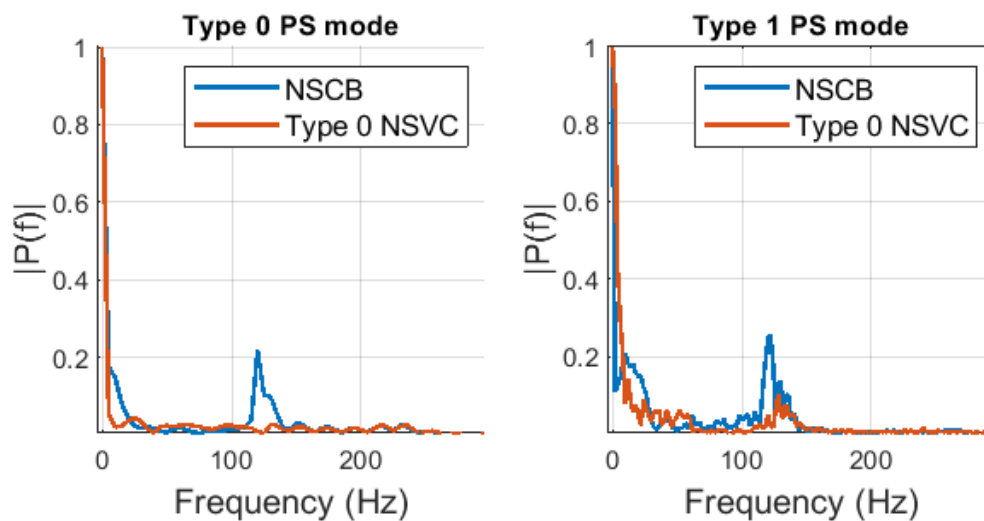


Figure 3.14: Normalized power spectrum of unbalanced fault responses for active power signal from the grid-following IBRs in Type 0 and Type 1 PS mode.

### 3.5.2 Unbalanced Fault in Type 1 PS Mode

Fig. 3.15 shows the MIL set-up results for the IBR response to an unbalanced fault in the Type 1 PS mode of operation. Upon islanding (SS1 is open), IBR 1 operates as a grid-forming type, IBR 2 operates in a grid-following type, and they collectively share the grid load as per the droop laws. IBR 1 is configured as a grid-forming type that supplies the required NS currents (refer Fig. 3.15b 3.95 s to 4 s) to maintain balanced grid voltage (refer Fig. 3.15a 3.95 s to 4 s) as per Type 1 NSVC. Contrary to this, IBR 2 is configured as a grid-following type that supplies no NS currents as seen in Fig. 3.15c. A pre-determined current limit of 1.4 p.u. and 1.1 p.u. is applied on IBR 1 and IBR 2, respectively. At node 7, an unbalanced fault (AG) with fault resistance of  $1 \Omega$  is introduced at 4 s for a duration of 150 ms resulting in voltage characteristics as shown in Fig. 3.15a. The AG fault results in 59% voltage sag on phase  $a$ , 59% voltage sag on phase  $b$ , and 22% voltage sag on phase  $c$  leading to 45 % sag on PS RMS voltage and 25 % swell on NSRMS voltage.

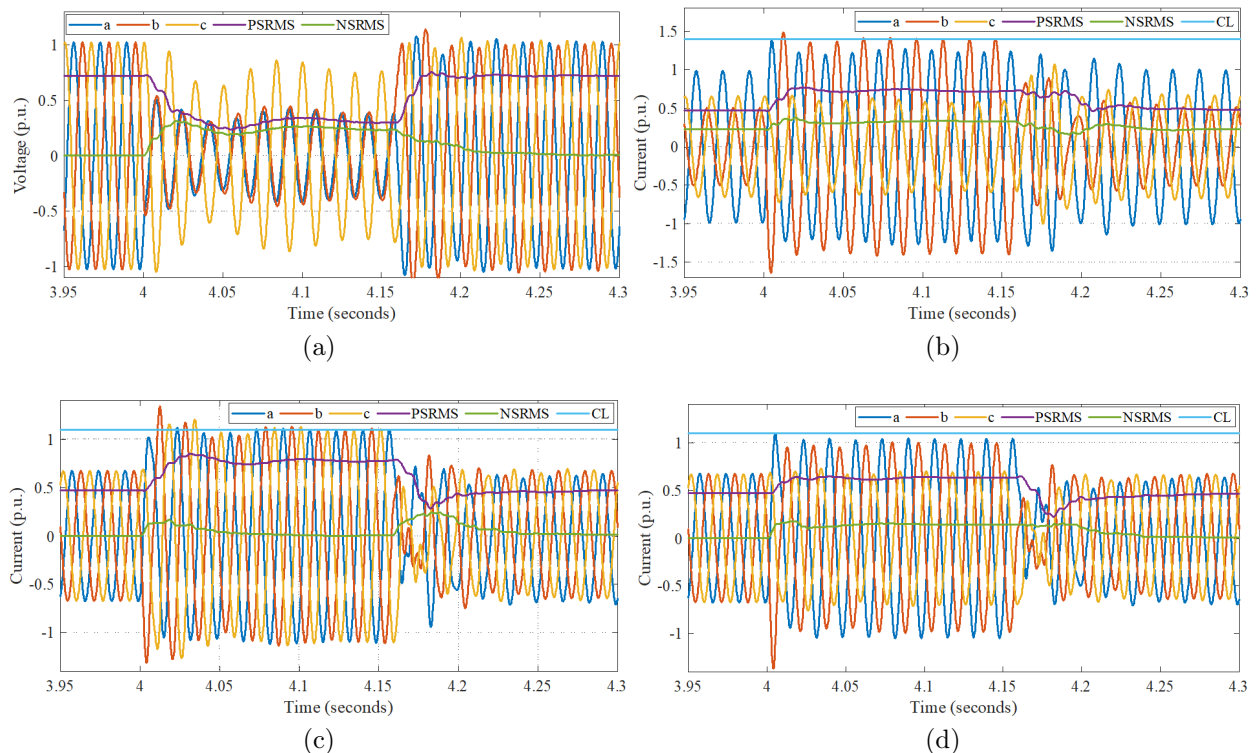


Figure 3.15: Unbalanced fault (AG) for the duration of 150 ms with fault resistance of  $1 \Omega$  at node 7 during Type 1 PS mode. (a) Three-phase PCC (node 1) voltages and corresponding PNS RMS values. (b) Three phase currents and corresponding PNS RMS values injected by IBR 1. Three phase currents and corresponding PNS RMS values are injected by IBR 2 when (c) NSCB control is applied. (d) Type 0 NSVC, is applied.

During the fault, an increase in PNS current is observed for the IBR 1, and current phases are limited to 1.4 p.u. as seen from Fig. 3.15b. When the IBR 2 is controlled with NSCB control, there is no NS injection from the IBR during unbalanced fault as seen from Fig. 3.15c. By applying the proposed Type 0 NSVC, IBR 2 can deliver appropriate NS currents in Type 1 PS mode as well. IBR 2 injects NS currents from 4 s to 4.15 s as calculated from (3.31) along with the pre-determined fault current of 1.1 p.u. as shown in Fig. 3.15d. In comparison to the NSCB strategy, the proposed approach is effective in improving the power quality by minimizing the 120 Hz oscillations in the active power signal from 26% to 2% as depicted in Fig 3.14 Type 1 PS mode.

### 3.5.3 Type 1 PS Mode Power Sharing Analysis

In another MIL configuration, faults in the system are disabled and the proposed Type 1 PS mode control method is validated. The total unbalanced active and reactive load power on the described section of the IEEE 123 node system is 400 kW, and 200 kVar, respectively. Phase-wise load distribution is given by: 160 kW, 80 kVar in phase A, 40 kW, 20 kVar in phase B, and 200 kW, 100 kVar in phase C. As shown in Fig. 3.16a, up to 3 s, IBR 1 and IBR 2 are operating in unity power factor mode by tracking the respective active power references: 500 kW (1 p.u.) for Inv1 and 160 kW (0.8 p.u.) for Inv2. Three different events such as islanding scenario (at 3 s), load decrease (at 4 s), and load increase (at 5 s) are tested in a Type 1 PS mode of operation. During all three events, reasonable transients

for around 200 ms are observed from Fig. 3.16. The PQ demand in the system is the sum of load demand and losses. This PQ demand of the network is obtained from the power measurements at node 149 in absence of DERs and the presence of the main grid source at node 150. Power-sharing error (PSE) is computed as a percentage value of  $\Delta\hat{P}_i^+$  and  $\Delta\hat{Q}_i^+$  as described in Section 3.4.1 Type 1 PS mode. Since angle droop is used in both methods, system frequency is observed to be close to the nominal value (60 Hz).

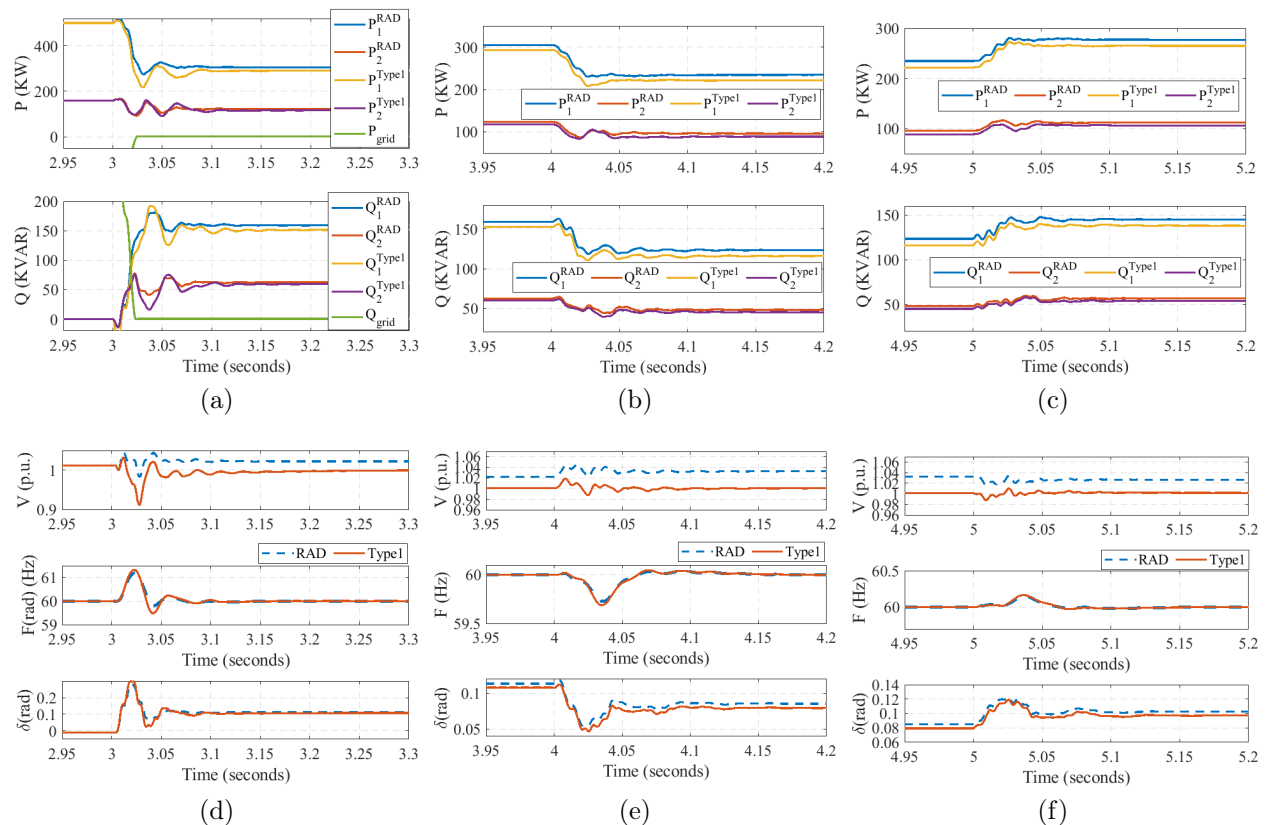


Figure 3.16: IBR 1 and IBR 2 active and reactive power sharing and system parameters (voltage magnitude, frequency, and voltage angle at node 149) in Type 1 operating model in the islanded system. (a) PQ sharing after Type 1 PS mode transition. (b) Load decrease in Type 1 PS mode. (c) Load increase in Type 1 PS mode. (d) System parameters after Type 1 PS mode transition. (e) System parameters after load decrease. (f) System parameters after load increase.

Power-sharing and system parameter values are compiled in Table 3.3 to highlight the significance of the proposed Type 1 PS mode droop law against the RAD law. Due to the integral action of the proposed Type 1 droop law, PSE for active power for both of the IBRs is around 0.07% to 1% whereas the RAD law leads to a PSE of 4.4% to 9.6%. Moreover, with the proposed approach system voltage is close to 1 p.u., while RAD law leads the system voltage up to 1.033 p.u. Thus the proposed method is highly effective in improving the accuracy of active power-sharing along with maintaining system voltage magnitude close to nominal values. Furthermore, in the case of reactive power-sharing, in comparison to RAD law (PSE of 6.5% to 12.3%), the proposed method showcases the improvement (PSE of 1.7% to 5.6%).

In Type 1 PS mode, a nonlinear load of 90 kW is connected and disconnected at 4 s and 5 s respectively as shown in Fig. 3.17. Fig. 3.17a depicts the increase in the PS current injection of grid forming IBR as the balanced nonlinear load is connected in the system.

TABLE 3.3: Comparison between proposed droop law and robust angle droop law for power sharing between the IBRs and the regulation of system parameters in Type 1 PS mode of operation.

Event and PQ demand(kW, kVar)	Control Method	Inv 1 Sharing		Inv1: PSE		Inv 2 Sharing		Inv2: PSE		System (node 149)		
		P(kW)	Q(kVar)	$\Delta P(\%)$	$\Delta Q(\%)$	P(kW)	Q(kVar)	$\Delta P(\%)$	$\Delta Q(\%)$	V(p.u.)	F (Hz)	$\delta(\text{rad})$
Islanding (408.83 205.23)	RAD	304.9	159	4.41	8.46	123.3	62.5	5.55	6.58	1.022	60.027	0.113
	Type 1	291.8	151.7	0.07	3.38	116.8	59.67	0.007	1.76	0.999	60.021	0.107
Load decrease (307.23, 153.86)	RAD	234.5	123.5	6.85	12.37	95.8	48.22	9.13	9.69	1.033	60.035	0.085
	Type 1	221.5	116.1	0.93	5.64	88.66	45.11	1.002	2.61	1.001	60.037	0.079
Load increase (368.07, 184.66)	RAD	277	144.89	3.82	9.84	112.3	56.88	6.78	7.80	1.026	60.026	0.102
	Type 1	264.8	138.1	0.71	4.7	106	54.17	0.79	2.67	1.002	60.024	0.097

Nonlinear load power-sharing among the IBRs and the system parameter regulation to the nominal values are observed to be stable as shown in Fig. 3.17b and Fig. 3.17c respectively.

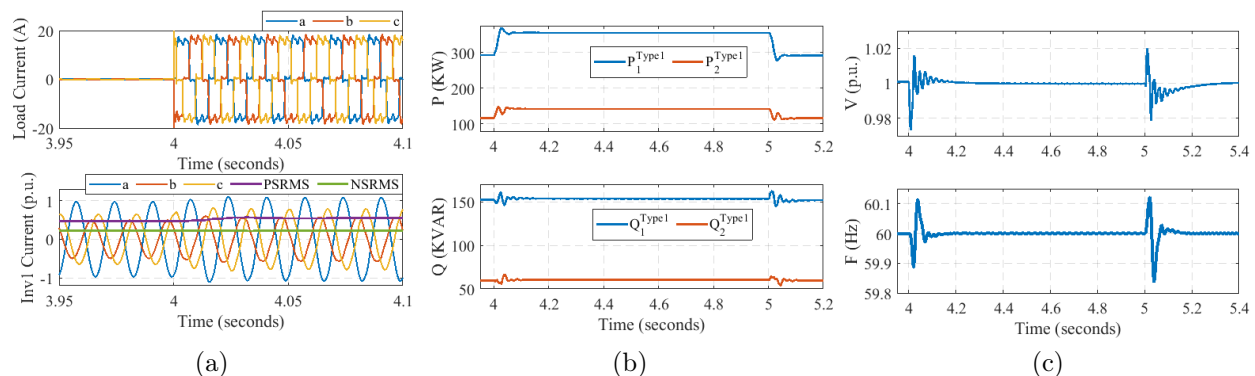


Figure 3.17: At node 8, a nonlinear load of 90 kW is connected and disconnected at 4 s and 5 s respectively in the Type 1 mode of operation. (a) Grid-forming IBR continues to supply sinusoidal currents. (b) Active power-sharing of the IBRs. (c) Regulation of System voltage and frequency changes.

### 3.5.4 Impact of Communication Network Latency

IEC 61850 network is considered for communication between the SS1 relay and IBRs [135]. The status/control messages are exchanged using the GOOSE protocol. To replicate the allowed maximum transfer time of the trip category GOOSE messages, a delay ( $T_{d1}$ ) of 4 ms is simulated. An unbalanced fault (AG) at the grid side is simulated for 1 s duration when IBRs are operating in Type 0 PS mode. The relay function is programmed with ride-through conditions such as: if the voltage sag in any of the phases is between 0.6 p.u. and 0.7 p.u. for at least 0.5 s, SS1 open command should be issued and the SS1 status is communicated to the IBRs after 4 ms of delay ( $T_{d1}$ ). From Fig. 3.18a both IBR 1 and IBR 2 successfully limit the current within the respective thresholds during ride-through. SS1 open status ( $x_{SS} = 1$ ) is communicated to IBRs after a 4 ms delay and IBRs inject current as per their roles in Type 1 PS mode. Fig. 3.18b depicts the system voltage and frequency (node 149) response during and post-ride-through. Once the system is islanded after the ride-through voltage is brought back to the nominal values by the Type 1 mode of operation.

The communication between DERMS and IBRs is assumed to occur over an IP-based network. A communication delay ( $T_{d2}$ ) of 10 ms, 50 ms, and 100 ms are simulated for the load active power-sharing set-point provided by DERMS to the IBRs operating in Type 1 PS mode. System voltage and the active power-sharing of the grid forming (P1) and grid

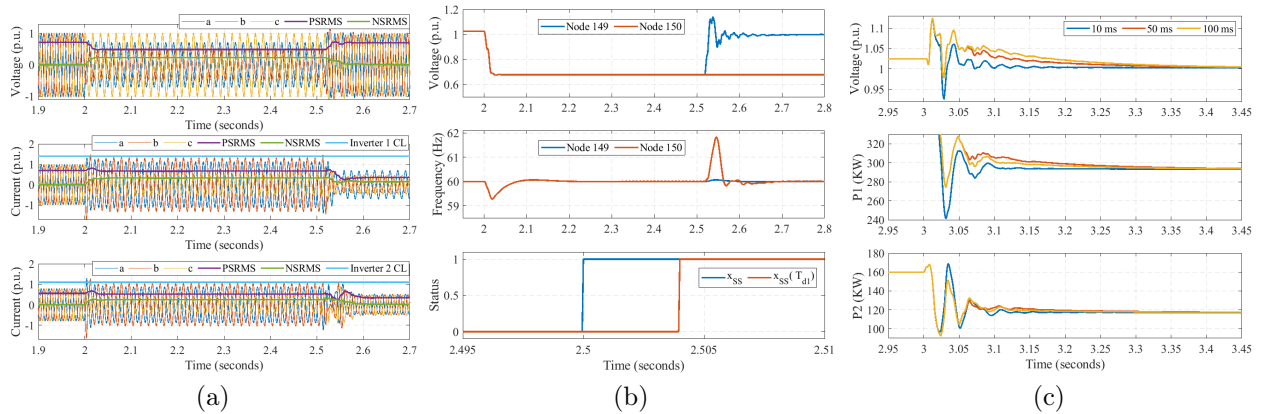


Figure 3.18: (Fig. (a) and (b)) Transition to Type 1 PS mode of operation after rid-through. (a) Node 149 voltage and IBR currents (b) System parameter response including  $T_{d1}$  Fig. (c) DERMS issues power-sharing set-point, IBR power, and system voltage (node 149) response plotted for various  $T_{d2}$ .

following (P2) IBR are shown in Fig. 3.18c. With the increase in latency, the settling time of voltage regulation and the IBR power-sharing increases. However, the system is observed to be stable proving the proposed design is effective in achieving control objectives even when the latency factors are considered.

### 3.5.5 Dynamic Change in the IBR Roles

To validate the stable operation and power-sharing of IBRs even after dynamically changing their roles, the pre-determined current limit of IBR 2 is increased to 1.5 p.u. This increase in the current limit facilitates the supply of the required NS current in the network. In Type 1 operating mode, grid-forming type IBR 1 (up to 6 s) supplies the required NS current to maintain the balanced voltage in the network as shown in Fig. 3.19a while grid-following IBR 2 supplies only PS currents as shown in Fig. 3.19b. At 6 s, DERMS issues a signal to swap the role of IBRs ( $T_{d2} = 50$  ms is considered), and after 6.05 s IBR 1 supplies only PS current, and IBR 2 starts supplying the required NS currents. From Fig. 3.19c, it is inferred that the power-sharing is the same and stable with acceptable transients after swapping the IBR roles and system voltage at node 149 is balanced and stable.

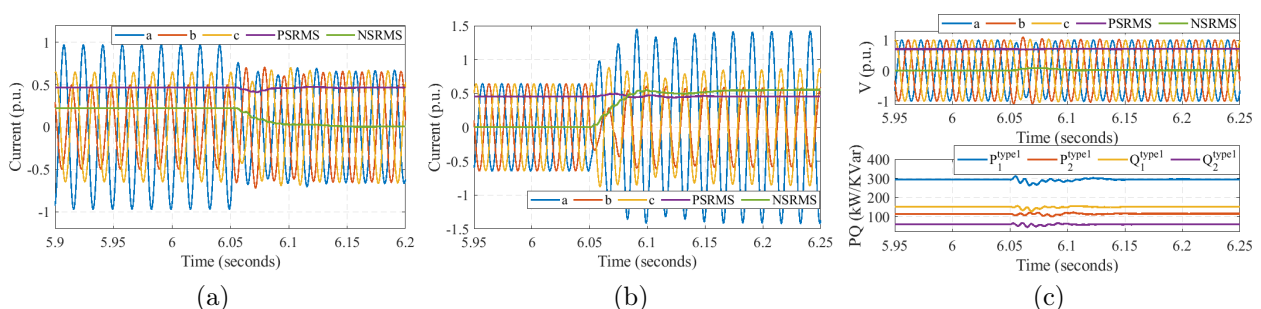


Figure 3.19: IBR roles are dynamically changed at 6 s based on the signal from DERMS. System voltage at node 149 is balanced, the same PQ sharing continues after the role change and both IBRs switch to the required control methods. (a) IBR 1: grid-forming to following at 6 s (b) IBR 2: grid-following to forming at 6 s (c) IBR PQ sharing and system voltage

### 3.5.6 CL Estimation with % Grid Unbalance

When IBR 2 transitions to the grid-forming role, it is responsible for balancing the network voltage by supplying required NS currents. It is critical to identify the CL value for the IBR 2 as unbalance in the network can lead to higher phase currents (beyond 1 p.u.) even if power-sharing is much less than the rated value. Per phase Thevenin equivalent impedance ( $Z_{a/b/c}^{th}$ ) seen at the PCC (node 13) of IBR 2 is calculated by varying the unbalance in loads of the network (Fig. 3.12) maintaining the same total load (400 kW, 200 kVar). The impedance unbalance is calculated as maximum deviation of per-phase impedance from the average impedance:  $\left(\frac{\max(\Delta Z_{a/b/c}^{th})}{Z_{avg}^{th}}\right)$ , where  $\Delta Z_{a/b/c}^{th} = Z_{a/b/c}^{th} - Z_{avg}^{th}$ . For each impedance unbalance (%) scenario, the model is executed to obtain the IBR 2 phase-wise peak currents. Fig. 3.20 depicts the relation between the impedance unbalance (%) observed at the PCC of IBR 2 and the phase-wise peak currents injected by the IBR 2 operating in a grid-forming role. For the loading scenario discussed in Section 3.5.3, an impedance unbalances of around 70 % is observed. From Fig. 3.20, 70 % impedance unbalance corresponds to 1.46 p.u. maximum phase current, hence 1.5 p.u. CL is chosen to facilitate stable steady-state operation. It is worth noting that this design can work for any existing load and power rating of the IBR irrespective of the micro grid location.

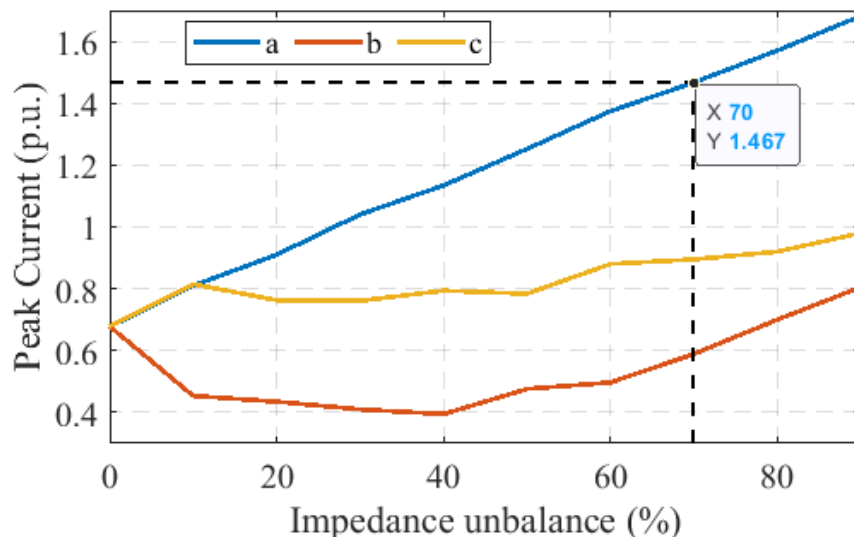


Figure 3.20: IBR 2 per phase peak current plotted against the Thevenin impedance unbalance seen at the PCC (node 13).

### 3.5.7 Transition from Type 1 to Type 0 PS Mode

Fig. 3.21 shows the MIL set-up results for the transition from Type 1 PS mode to Type 1 PS mode of operation. As shown in Fig.3.21a, Sync check signal is issued from the relay at 6.95 s, along with the  $en_{sy}$ ,  $\Delta\delta$  and  $\Delta v$  signals communicated to each of the IBRs reach after  $T_{d1} = 4ms$ . IBR controller regulates voltage magnitude and angle at node 149 such that  $\Delta v^s$  and  $\Delta\delta^s$  gets closer to zero in 6 cycles (Fig. 3.21b) and 100 ms (Fig. 3.21a) respectively. When grid and islanded system voltage magnitude and the angle is close enough as per

ANSI code A25A requirement, the SS1 close command is issued. The voltage phase and the magnitude of the islanded system are thus matched to the grid voltage without leaving any distortions on the system voltage as seen in Fig. 3.21c. Once the SS1 is closed, both the IBRs switch to Type 1 PS mode of operation seamlessly with acceptable transients of around 200 ms, and the additional power generated from the IBRs is injected into the grid as depicted in Fig. 3.21c.

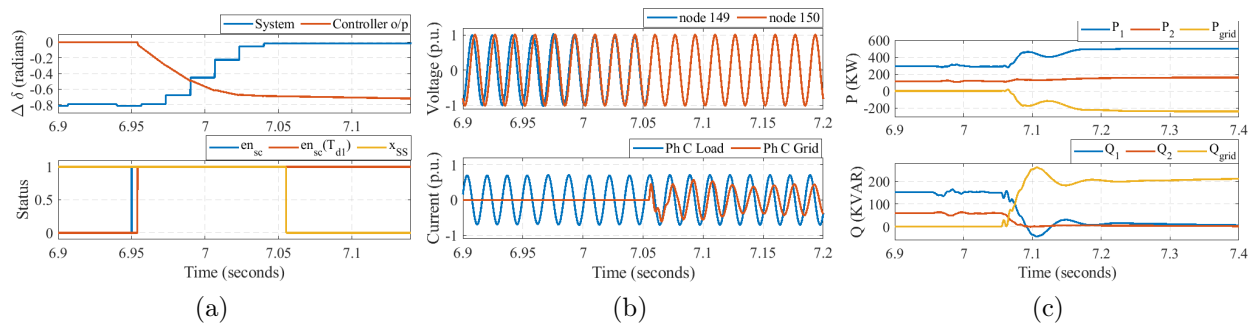


Figure 3.21: Grid synchronization and transitioning to Type 0 PS mode based on the relay function signals (derived from the measurements at SS1) communicated to all the IBRs in the system (IEC 61850 communication network is assumed). (a) IBR control response for sync enable (b) Sync enable to grid-connect period (c) PQ sharing and reference tracking

### 3.6 Summary

In this chapter, a unified control architecture for multiple IBR operations is validated in an unbalanced system using the detailed real-time IBR model. The generalized PNS current limiter is successful in limiting the IBR currents to the pre-determined values for different types of IBRs in different operating modes. Furthermore, with the dedicated NS power control techniques, mitigation of power ripples with 20% improvement is showcased during unbalanced fault scenarios. The quantitative analysis in comparison to the RAD law, confirms the effectiveness of the proposed PS power controller for power-sharing accuracy and maintaining the nominal system voltage magnitude. With the real-time MIL verification, the authors claim that the proposed architecture is effective in operating a stable power grid during load change, fault scenarios, mode transitions, and 100% IBR-based operation with the designated roles.

## CHAPTER 4: Decentralized State Estimation-based Optimal Integral Model Predictive Control of Voltage and Frequency

*Experimental confirmation of a prediction is merely a measurement. An experiment disproving a prediction is a discovery.*

---

Enrico Fermi

The power distribution system is undergoing a shift from centralized to decentralized operation due to the large-scale integration of distributed energy resources (DER). To increase the scalability and reduce the dependency on communication networks, there is a strong need for a decentralized control framework that can maintain the nominal voltage and frequency in a microgrid (MG). In this chapter, a novel decentralized state estimation-based optimal voltage and frequency restoration strategy is proposed. The framework computes the optimal integral model predicted control reference signal to the primary controller, which is unaffected by the local measurement noise, hence, ensuring stable power-sharing among the DERs. The proposed framework is built on a first-order DER model and a local/global measurements-based local state estimation technique, facilitating deployability to the grid edge devices. The capabilities of the proposed framework are tested and validated on a real-time simulator with a full system dynamic model considering an islanded section of the IEEE 123 node distribution network for the various grid events. It is observed that the framework offers significant transient performance improvement in comparison to the Linear Quadratic Regulator method, with around 70% faster voltage restoration when the communication latency is considered.

### 4.1 Introduction

The integration of photo-voltaic and battery energy storage-based DERs in the power distribution grid has increased drastically in recent years. DERs are interfaced with the power distribution network through the IBRs. The IBRs play an important role in coupling the DC side of the DERs to the power grid, enabling distributed generation, and improving the utilization of local renewable energy-based resources. In a distribution network, when the electric grid (through substation) is available, the DERs operate in grid-connected mode. During the unavailability of the substation, DERs can operate in an islanded mode forming an MG [136] and most importantly DERs possess the ability to operate each local area

independently.

Efficient and stable operation of MG requires a hierarchical control system with a time-scale separation between the primary, secondary, and tertiary control layers [5]. To improve the reliability of MG operation, reduction of dependency on the communication infrastructure at each of the layers is necessary [13, 82]. Furthermore, shifting the decision-making and control capability to the grid-edge through a decentralized hierarchical architecture has multiple benefits such as, a) reduction in the computational load on the central controller [137], b) improved scalability facilitating large-scale DER integration [138], c) reduced design complexity for the MG operation [139].

Decentralized primary control (PC) techniques are typically utilized to achieve stable and efficient autonomous operation of DERs in an MG without the need for communication [52, 53]. The design of the PC for multiple DER operations in an unbalanced distribution system requires dedicated positive and negative sequence (PNS) control loops. The PC of a DER consists of inner PNS current and voltage loops, and an outer power loop that deploys appropriate droop laws [53]. Droop law as a part of primary control is a key strategy to enable stable power-sharing among DERs in an MG without the need for communication. Droop correlations typically mimic the synchronous machines chosen depending on the type of the power network [140, 141]. For the low  $X/R$  ratio distribution network, a universal droop law with the correlations  $P \sim V$  and  $Q \sim \omega$  is proven valid even for the DERs with the different output impedance [28]. Furthermore, a robust droop controller is demonstrated to minimize the voltage variations arising due to droop laws and changing loads [29]. In this work, the authors adopt a robust droop controller for designing the PC of DERs.

While the PC enables stable power-sharing, voltage and frequency in the MG deviate from the nominal values due to the inherent nature of droop laws. This necessitates the introduction of a secondary controller (SC) to regulate voltage and frequency to the nominal values [52, 142]. SCs are broadly classified under centralized, distributed, and decentralized frameworks. The *centralized frameworks* serves the use case of controlling the distribution network with fewer DERs without adding to the cost and complexity of the prevailing network [9]. However, these frameworks pose a limitation on scalability, offer low reliability, and are vulnerable to the single point of failure and cyber-attacks [7, 8]. Whereas in *Distributed frameworks*, devices have complete access to the system states based on which they can conduct local control decisions utilizing a sparse communication network [10, 11]. Nevertheless, with the large-scale integration of DERs, distributed frameworks face various challenges such as design complexities, scalability issues, and lack of robustness of sparse communication networks [14, 15]. Moreover, the *decentralized frameworks* are typically local to the DERs, therefore, offering scalability and demand minimal or no communication

infrastructure [13, 138].

Decentralized frameworks with classical PI regulator-based approaches utilize the local measurements to meet the SC objective [64, 83, 84]. Controller performance presented in [83] is highly affected by the balanced/unbalanced load mix and voltage ranges. The schemes that are robust against load mix are validated only for parallel DER operation not considering the power network and its impedance [64, 84]. A band-pass washout filter-based scheme that is equivalent to a PI controller is presented in [143] for voltage and frequency restoration. However, though the washout filter approach considers distribution line impedance, it offers compromised dynamic performance and leads to a longer restoration time.

In all of the PI controller-based approaches (from classical to advanced control techniques) the integral component of each of the DER controllers may accumulate the system disturbance and the measurement noise local to the respective PCCs leading to gradual deterioration of the power-sharing. A switched control design method proposed in [144] transitions between P and PI controller based on the time-dependent protocol. Though the approach does not deteriorate power sharing, the improvement in the controller transient performance is necessary. Furthermore, switched control mainly depends on event detection strategy, failure of which may alleviate controller performance and may lead to oscillations. In [12], an LQR frequency control technique along with the stability analysis is presented based on the first-order model of the DER. The study is limited to optimally computing the controller gain parameters of the PI controller. Hence there is a need to build a model-based control approach that includes integral behavior and is not sensitive to system disturbances and measurement noise.

In large-scale power networks, decentralized estimation techniques typically utilize local measurements and dynamic models to reduce the dependency on the communication networks [145–148]. In [145] a Kalman-Bucy filter is applied to achieve fast terminal sliding mode control for the distributed voltage regulation. This work requires feedback linearization of the detailed DER model that depends on the exact knowledge of all the parameters hence leading to design complexity. A non-linear state estimation method presented in [146] utilizes the detailed source and network model, requiring expensive computational resources and model accuracy, thus infeasible for deployment with the grid-edge controllers. A decentralized load frequency control using a dynamic state estimation method is proposed in [147]. The approach has the potential for frequency estimation in MGs, likewise, the work presented in [148]. However, these works may not be suitable for voltage estimation as the estimator utilizes the local measurements only, and since the voltage is a local state, system-level synchronization cannot be achieved.

## 4.2 Research Contributions

Several distributed model predictive control (MPC) approaches such as a finite-time observer for the voltage control [149], frequency control with voltage constraints [150], and secondary control of DC MG [151] are proposed in the literature. Major drawbacks of these approaches include coupled frequency and voltage restorations, disturbance accumulation due to segregated integral action, and communication requirements between the subsystems. Motivated by the aforementioned limitations of the existing MPC and other control frameworks, a generic integral MPC (IMPC)-based secondary control framework for both frequency and voltage restoration is presented in this chapter. The salient contributions of the proposed control framework are as follows.

- At the control layer, the formulation of voltage and frequency restoration is decoupled, hence the transient responses are independently achieved. Furthermore, the cost function of the proposed optimal control is formulated to incorporate the integral action on the estimated states along the prediction horizon. This predictive integral action mechanism accelerates the restoration of voltage and frequency, especially advantageous when communication latency is considered.
- First order augmented incremental model decentralized extended Kalman filter (AIM-DEKF)-based state estimation facilitates the dynamic synchronization of system states locally, thereby offering a balance between the communication requirement and the computational complexity. The proposed estimator can be deployed in the grid-edge devices assuring frequency synchronization without communication and voltage synchronization based on the global measurement. The estimator does not require communication among the subsystems and from the controller perspective, the subsystems are completely decoupled, hence offering design scalability. The scalable nature of the proposed control framework improves the overall scalability of the MGs.
- The IMPC framework utilizes the AIM model that has an inherent integral action on the outputs and the AIM is insensitive to the system disturbance and measurement noise. Therefore, the local measurement noise is not accumulated by the integral action and thus the droop laws of PC are not affected, ensuring stable power sharing among the DERs.
- Optimal control is formulated to incorporate constraints such that the control signal is accounted for explicit amplitude and rate constraints. Thus during short-term grid faults, SC assists the PC in performing ride-through activity by providing the constrained references.

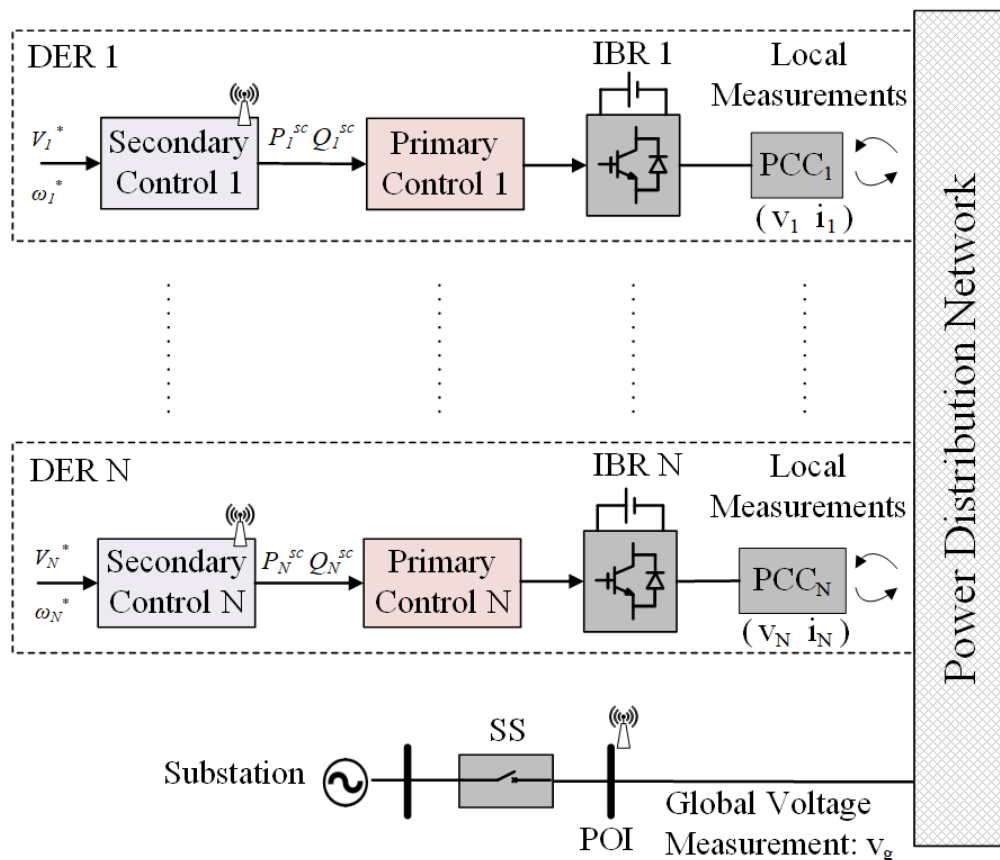


Figure 4.1: Overview of the decentralized secondary control architecture for the islanded power distribution network.

- The framework is foolproof against various grid events such as islanding, load change, generation loss, and grid faults, and robust against communication latency and the measurement noise as validated by the real-time (RT) model-in-the-loop (MIL) simulation of the DER integrated unbalanced distribution network.

### 4.3 Overview of Hierarchical PC and SC

Fig. 4.1 represents the DER integrated distribution network acting as an islanded MG when the substation is disconnected from the rest of the system operating a smart switch (SS) at the POI. In this section, the primary controller and the control problem to be solved by the secondary controller are discussed.

#### 4.3.1 Description of Control Architecture

The DERs along with the associated primary controller are connected to the distribution grid at the respective Point of Common Coupling (PCC). The primary controller architecture applicable to the distribution network is shown in Fig. 4.1. The DC side voltage ( $V_{DC}$ ) is assumed to be fixed considering the ideal characteristics of DER. The IBR is equipped with a  $LCL$  output filter including a passive damping resistor ( $R_d$ ) to ensure stable interaction with the grid. The primary control loops typically utilize the local current and voltage measurements to ensure the reference values are tracked with acceptable transients. Since distribution networks are unbalanced, dedicated PNS current and voltage control loops are designed to maintain the balanced voltage when the substation node is disconnected [53].

The current reference limiter is used to achieve the IBR ride-through capabilities during the fault scenarios. Droop laws are typically designed as an outer power control loop to the voltage control loop, and they ensure stable power-sharing among the multiple IBRs. To achieve the closed-loop stable operation of the IBRs, the inner current and voltage control loop dynamics are designed to be faster in comparison to the outer droop control loop by including low-pass filtered (LPF) power measurements. Thus, to capture the primary controller dynamics, it is sufficient to consider the droop loop behavior including the LPF dynamics [12].

Droop laws enable stable power-sharing among IBRs depending on the power network type (resistive or inductive) [28]. Since the distribution grid has a low  $X/R$ , robust droop law is considered to achieve the power-sharing [29]. This law illustrates the positive correlation between active power ( $P_i^p$ ) and the voltage magnitude ( $V_i^p$ ), and the negative correlation between reactive power ( $Q_i^p$ ) and the frequency ( $\omega_i^p$ ). Based on this law, the corresponding voltage and frequency at the PCC of  $i^{th}$  IBR are given by (4.1a) and (4.1b).

$$V_i = V_i^* + k_i^V (V_i^* - V_i) - k_i^P (P_i - P_i^*) \quad (4.1a)$$

$$\omega_i = \omega_i^* + k_i^Q (Q_i - Q_i^*) \quad (4.1b)$$

where  $V_i^*$ ,  $\omega_i^*$ ,  $P_i^*$ ,  $Q_i^*$  are the voltage, frequency, active power, and reactive power set-points respectively,  $V_i^p$  is the measured PCC voltage magnitude,  $P_i^*$ ,  $Q_i^*$ , are the filtered active and reactive power signals,  $k_i^P$ ,  $k_i^Q$ , are the droop coefficients, and  $k_i^V$  is the penalty parameter for voltage deviation.

It is evident from (4.1), during power-sharing IBRs steady-state voltage and frequency deviate from nominal values. To restore the network voltage and frequency, a secondary controller that provides appropriate active ( $P_i^{sc}$ ) and reactive ( $Q_i^{sc}$ ) power set-points is necessary. A decentralized secondary control approach is described in Fig. 4.1, which utilizes local PCC measurements for frequency restoration and additional global voltage measurements for voltage restoration.

#### 4.3.2 Review of the Problem Description

Fig. 4.2 describes the generalized droop characteristic for a low  $X/R$  distribution system given by (4.1). As per the proportional droop laws, the rated power delivered ( $P_i^* = P_i^p$  and  $Q_i^* = Q_i^p$ ) from the IBRs would maintain the nominal voltage and frequency at PCC (point A). When there is a change in the system operating condition, the power delivered is usually at the value  $P_i$  and  $Q_i$  (point B) depending on the load power demand. As a result, voltage and frequency deviate from their respective nominal values. Though the robust droop law has an additional proportional voltage error penalty, unlike in the conventional droop law,

the required voltage restoration is still not achieved as the active and reactive power reference set-points are fixed ( $P^* = 1$  p.u. and  $Q^* = 0$  p.u. respectively). Secondary control requires

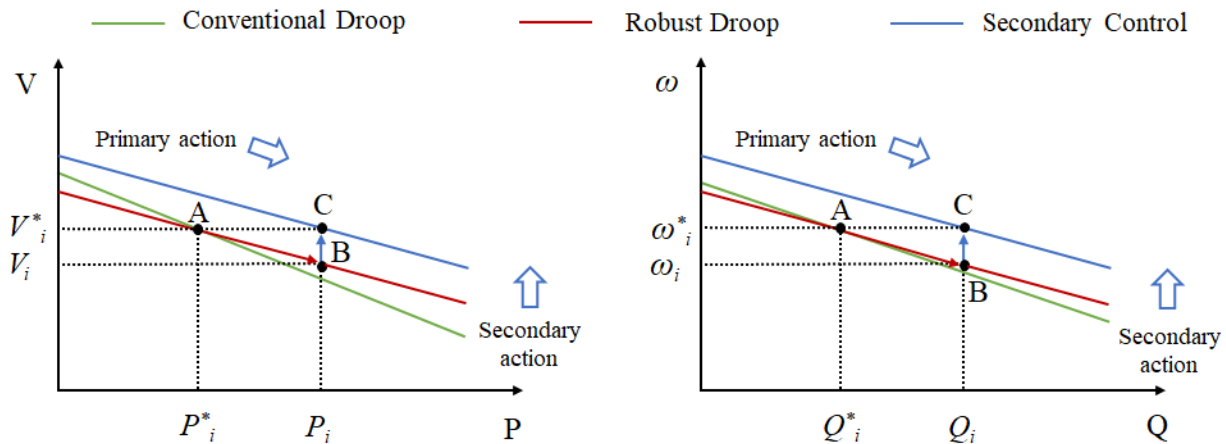


Figure 4.2: Shift in the droop behavior as an act of the secondary controller.

performing corrective action and restoring the voltage and frequency to nominal values, along with the stable power-sharing in the MG. Thus underlying secondary controller would modify the primary controller power reference values [73] such that the droop characteristics would be shifted to restore the voltage and frequency (point C). The measured frequency at any node of the system is a global state [152], and the measured voltage at a given node is a local state [75] due to the mismatch in the line impedance. Depending on the nature of these states, a systematic approach is required for the design of an optimal decentralized secondary controller.

### 4.3.3 DER - MG Interaction Model

In the cascaded PC loops, LPF slows the dynamics of the power control loop, hence segregating from faster dynamics-based voltage and current control loops. Thus, the transients of voltage and current controllers are not propagated to the power control loop, ensuring higher power quality. The time-domain representation of the filtered power signals is given by,

$$\dot{P}_i = \omega_i^c (p_i - P_i) \quad (4.2a)$$

$$\dot{Q}_i = \omega_i^c (q_i - Q_i) \quad (4.2b)$$

where  $\omega_i^c$  is usually in the range of 2 Hz to 10 Hz. Representing droop laws of (4.1) in terms of  $(P_i, Q_i)$  and substituting them in (4.2) would lead to the first order DER model:

$$\dot{v}_i^\epsilon = -\omega_i^c \hat{v}_i^\epsilon + \frac{k_i^P \omega_i^c}{1 + k_i^V} \delta p_i \quad (4.3a)$$

$$\dot{\hat{\omega}}_i^\epsilon = -\omega_i^c \hat{\omega}_i^\epsilon - k_i^Q \omega_i^c \delta q_i \quad (4.3b)$$

where  $\hat{v}_i^\epsilon \cong V_i^* - \hat{v}_i$ ,  $\hat{\omega}_i^\epsilon \cong \omega_i^* - \hat{\omega}_i$ ,  $\delta p_i = P_i^* - p_i$  and  $\delta q_i = Q_i^* - q_i$ . For an islanded system as shown in Fig. 4.1, utilizing the distribution network physics, active and reactive power injected at the  $i^{\text{th}}$  DER node can be represented as:

$$p_i = \sum_{l=1, l \neq i}^L V_i V_l |Y_{il}| \cos(\delta_i - \delta_l - \theta_{il}) \quad (4.4a)$$

$$q_i = \sum_{l=1, l \neq i}^L V_i V_l |Y_{il}| \sin(\delta_i - \delta_l - \theta_{il}) \quad (4.4b)$$

where  $\delta_i$  is the voltage angle at the  $i^{\text{th}}$  DER node,  $L$  are the total nodes in the network (DER and load nodes),  $\mathbf{Y} \in \mathbb{C}^{L \times L}$  is the admittance matrix with the magnitude  $|Y_{il}| = \|\mathbf{Y}_{il}\|_2$ , and the phase angle  $\theta_{il} = \angle \mathbf{Y}_{il}$ . Due to the DER dynamics of (4.3), voltage and frequency at the  $i^{\text{th}}$  DER node are controllable. Thus from the network perspective, behind every DER node, there is a controllable voltage source. However, the local voltage at a given load node  $V_l$ , ( $\forall l \in 1, 2, \dots, L, l \neq i$ ) may be uncertain. In this work constant power or constant impedance loads are considered such that the assumption  $\hat{v}_l^\epsilon \leq \kappa \hat{v}_i^\epsilon$  holds good, where  $v_l^\epsilon$  is the deviation of load node voltage from the nominal value, and  $\kappa > 0$  is a constant related to the load properties and network topology [153].

The islanded distribution network ( $\mathcal{S}$ ) can be represented as a composition of  $N$  connected dynamic linear subsystems ( $\mathcal{S} = [\mathcal{S}_1, \mathcal{S}_2, \dots, \mathcal{S}_i, \dots, \mathcal{S}_N]$ ),  $i \in \{1, 2, \dots, N\}$ ,  $N \geq 2$ . The dynamics of each  $\mathcal{S}_i$  is represented by (4.3), where the  $\hat{v}_i^\epsilon$  and  $\hat{\omega}_i^\epsilon$  are predicted based on the local measurements  $p_i$  and  $q_i$ . From this representation of  $\mathcal{S}_i$  dynamics, it is evident that subsystems do not interact with one another, and hence are dynamically decoupled in nature. However, as per (4.4), every  $\mathcal{S}_i$  dynamics is affected by the network characteristics, and that would be captured in the inputs to the  $\mathcal{S}_i$  dynamics. Let  $\mathcal{S}_j$  be the unique subsystem with unknown dynamics (such as POI) in the network where the measurements are available. So for each  $\mathcal{S}_i$ , there exists a unique  $\mathcal{S}_j$  with coupled network constraints, therefore a coupled objective function. Hence the synergy between  $\mathcal{S}_i$  and  $\mathcal{S}_j$  is utilized to define a decentralized network dynamics  $\tilde{\mathcal{S}}_i$  and the corresponding local optimal control problem  $\tilde{\mathcal{P}}_i$  is formulated. Thus the system ( $\mathcal{S}$ ) level global performance objective is accomplished by formulating and solving the local  $\tilde{\mathcal{P}}_i$  at each subsystem. Precise definition of  $\tilde{\mathcal{S}}_i$  and  $\tilde{\mathcal{P}}_i$  are provided in the Section 4.4.1.

#### 4.3.4 Synthesis of Decentralized Secondary Controller

When the reference to the primary controller is provided by the secondary controller, the updated robust droop laws will then be:

$$V_i = V_i^* + k_i^V (V_i^* - V_i) - k_i^P (P_i - P_i^{sc}) \quad (4.5a)$$

$$\omega_i = \omega_i^* + k_i^Q (Q_i - Q_i^{sc}) \quad (4.5b)$$

where SC corrected active and reactive power references are given by  $P_i^{sc} = P_i^* + \delta P_i^{sc}$  and  $Q_i^{sc} = Q_i^* - \delta Q_i^{sc}$  respectively. The expansion of (4.5) leads to:

$$V_i = V_i^* + k_i^V (V_i^* - V_i) - k_i^P (P_i - P_i^*) - k_i^P \delta P_i^{sc} \quad (4.6a)$$

$$\omega_i = \omega_i^* + k_i^Q (Q_i - Q_i^*) + k_i^Q \delta Q_i^{sc} \quad (4.6b)$$

The voltage and frequency restoration terms:  $k_i^P \delta P_i^{sc}$  and  $k_i^Q \delta Q_i^{sc}$  can be termed as  $\delta V_i^{sc}$  and  $\delta \omega_i^{sc}$  respectively. Thus, with the retention of droop slope secondary controller shifts the droop characteristic as discussed in Fig. 4.2. This synchronized shift is performed at each subsystem by solving the respective  $\tilde{\mathcal{P}}_i$ , leading to the restoration of voltage and frequency to the nominal values at POI. This chapter proposes a decentralized predictive optimal secondary control framework to compute  $\delta P_i^{sc}$  and  $\delta Q_i^{sc}$  signals in the coming section.

### 4.4 Decentralized IMPC Framework

The local PCC voltage/current measurements, and the global POI voltage measurements-based decentralized IMPC-DEKF framework are described in Fig. 4.3. For the frequency restoration at POI, local PCC measurements are sufficient and the grid frequency is computed based on the positive sequence PCC voltage-based PLL. Voltage restoration at the POI in the distribution network requires the measured voltage to be communicated to the DER nodes. To achieve a realistic design, a common communication latency is modeled in terms of measurement delay. A similar delay is assumed between  $\mathcal{S}_i$  and  $\mathcal{S}_j$  such that  $Td_1 \cong Td_i \cong Td_N \cong Td$ . In the proposed framework, SCs at each of  $\mathcal{S}_i$  take control decisions independent of each other. The detailed design of the proposed framework is described in this section.

#### 4.4.1 Formulation of Decentralized Optimal Control

The first order model of  $\mathcal{S}_i$  represented in (4.3) is converted into a discrete form state equation given by:

$$\hat{v}_i^\epsilon(k+1) = a_i^v \hat{v}_i^\epsilon(k) + b_i^v \delta p_i(k) + v_i^v(k) \quad (4.7a)$$

$$\hat{\omega}_i^\epsilon(k+1) = a_i^f \hat{\omega}_i^\epsilon(k) + b_i^f \delta q_i(k) + v_i^f(k) \quad (4.7b)$$

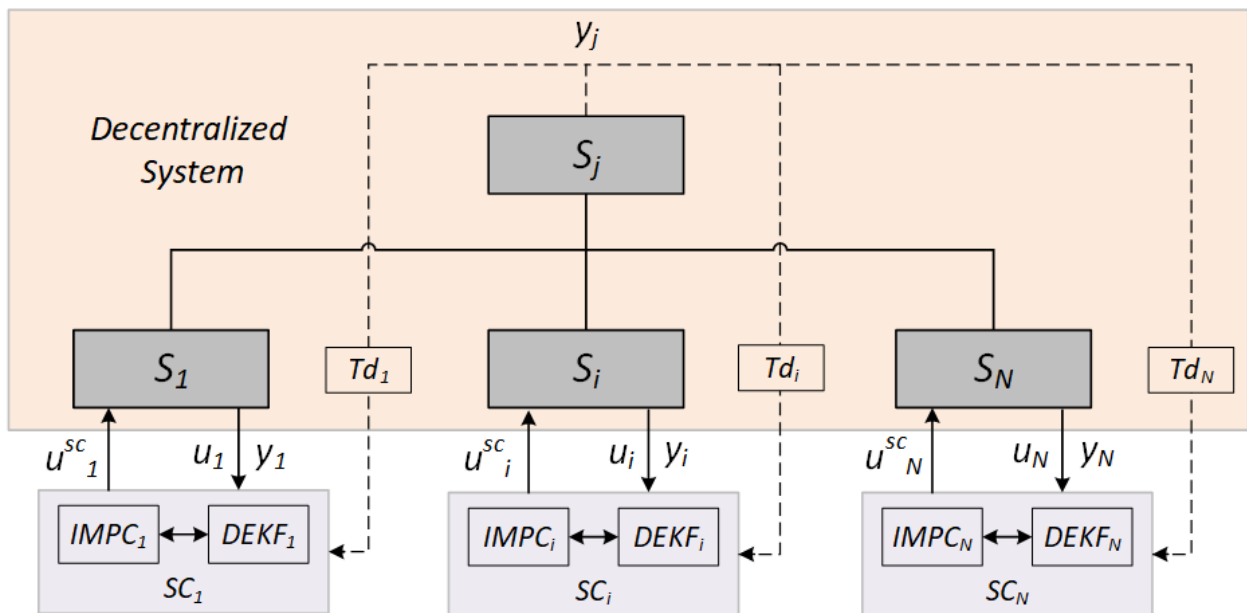


Figure 4.3: Proposed IMPC-DEKF framework that is applicable for both frequency and voltage restoration.

where  $a_i^v = a_i^f = e^{-\omega_i^c T_s^{sc}}$ ,  $b_i^v = \frac{k_i^P(1-a_i^v)}{1+k_i^V}$ ,  $b_i^f = k_i^Q(1-a_i^f)$ , and  $k \in \mathbb{N}$  such that  $t = kT_s^{sc}$ .

Furthermore, the unknown plant disturbances affecting voltage and frequency deviation prediction are given by  $v_i^v(k)$  and  $v_i^f(k)$  respectively. Output equations of  $\mathcal{S}_i$  are given by:

$$v_i^e(k) = c_i^v \hat{v}_i^e(k) + w_i^v(k) \quad (4.8a)$$

$$\omega_i^e(k) = c_i^f \hat{\omega}_i^e(k) + w_i^f(k) \quad (4.8b)$$

where  $c_i^v, c_i^f$  are state-to-output relation coefficients defined based on the observability of the states, and  $w_i^v(k), w_i^f(k)$  are the respective unknown measurement noises affecting the voltage and frequency measurements respectively. The generalized  $\mathcal{S}_i = f(\hat{x}_i^e(k), u_i(k), y_i^e(k))$  dynamics in state-space form is given by:

$$\mathcal{S}_i = \begin{cases} \hat{x}_i^e(k+1) = A_i \hat{x}_i^e(k) + B_i u_i(k) + v_i(k) \\ y_i^e(k) = C_i \hat{x}_i^e(k) + w_i(k) \end{cases} \quad (4.9)$$

where  $\hat{x}_i^e(k) \in \mathcal{X}_i := [\hat{v}_i^e(k) \ \hat{\omega}_i^e(k)]^T \subseteq \mathbb{R}$ ,  $u_i(k) \in \mathcal{U}_i := [\delta p_i(k) \ \delta q_i(k)]^T \subseteq \mathbb{R}$ ,  $y_i^e(k) \in \mathcal{Y}_i := [v_i^e(k) \ \omega_i^e(k)]^T \subseteq \mathbb{R}$ ,  $v_i(k) \in [v_i^v(k) \ v_i^f(k)]^T \subseteq \mathbb{R}$ ,  $w_i(k) \in [w_i^v(k) \ w_i^f(k)]^T \subseteq \mathbb{R}$ ,  $A_i := \text{diag}(a_i^v, a_i^f)$ ,  $B_i := \text{diag}(b_i^v, b_i^f)$ ,  $C_i := \text{diag}(c_i^v, c_i^f)$ . Let  $\mathcal{X} := \mathcal{X}_1 \times \dots \times \mathcal{X}_i \times \dots \times \mathcal{X}_N$ ,  $\mathcal{U} := \mathcal{U}_1 \times \dots \times \mathcal{U}_i \times \dots \times \mathcal{U}_N$ , and  $\mathcal{Y} := \mathcal{Y}_1 \times \dots \times \mathcal{Y}_i \times \dots \times \mathcal{Y}_N$ , then the overall system dynamics is defined as:  $\mathcal{S} = f(\hat{x}^e(k), u(k), y^e(k))$ .

Let  $\mathcal{S}_j$  be the unique measurement node in the system ( $\mathcal{S}$ ) defined as  $\mathcal{S}_j = y_j^e(k) \in [v_j^e(k) \ \omega_j^e(k)]^T$ . It is assumed that the measured states at  $\mathcal{S}_j$  are available at  $\mathcal{S}_i$  to achieve a system-level objective that is commonly shared among all subsystems, simultaneously satisfying the coupling constraints. The formulation of  $\mathcal{S}_i$  dynamics needs to be improved such

that the closed-loop system shall witness an offset-free steady-state response even in the presence of external disturbance and/or model mismatch. An appropriate state estimation technique would improve the accuracy of predicted system states utilizing the measurements. Thus with the combination of the model and the state estimator, local dynamics is represented as  $\tilde{\mathcal{S}}_i = f(\hat{x}_i^\epsilon(k), u_i(k), y_i^\epsilon(k), y_j^\epsilon(k))$ . Considering the  $\tilde{\mathcal{S}}_i$  dynamics,  $\tilde{\mathcal{P}}_i$  with optimal value function  $\tilde{J}_i(\tilde{y}_i(k|M), \tilde{u}_i(k|M))$  associated with the  $i^{th}$  subsystem is given by:

$$\begin{aligned} \tilde{\mathcal{P}}_i := \min_{\tilde{u}_i} \tilde{J}_i(k) = & \sum_{p=1}^M \tilde{y}_i(k+p)^T Q_i \tilde{y}_i(k+p) + \\ & \tilde{u}_i(k+p)^T R_i \tilde{u}_i(k+p) \end{aligned} \quad (4.10)$$

where  $\hat{Q}_i := \hat{Q}_i^v \times \hat{Q}_i^\omega \in \mathbb{R}$  is the positive definite symmetric weighting matrix for the future predicted states with  $(\hat{Q}_p^v, \hat{Q}_p^\omega) \forall p = 1, 2, \dots, M$  being on the diagonal block, and  $\hat{R}_i := \hat{R}_i^v \times \hat{R}_i^\omega \in \mathbb{R}$  is the positive definite symmetric weighting matrix for the future predicted control action with  $(\hat{R}_p^v, \hat{R}_p^\omega) \forall p = 1, 2, \dots, M$  being on the diagonal block. The problem  $\tilde{\mathcal{P}}_i$  for  $\tilde{\mathcal{S}}_i$  dynamics ensures the controller predicted outputs of  $\tilde{\mathcal{S}}_i$  will depend on the estimated outputs. As the estimated output from the state estimator reaches the measured output during the steady-state, elimination of steady-state error is guaranteed by solving  $\tilde{\mathcal{P}}_i$ . Components needed to build  $\tilde{\mathcal{P}}_i$  such as  $(\tilde{y}_i(k|M), \tilde{u}_i(k|M))$  are discussed in the subsequent subsections.

#### 4.4.2 AIM Incorporating the Output Integral Action

To formulate the  $\tilde{\mathcal{S}}_i$  dynamics in the IMPC framework, firstly an AIM is developed. The model representation from (4.7a) through (4.8b) that is insensitive to the unknown system disturbances and measurement noise variables is described in terms of AIM form as:

$$\begin{aligned} \Delta \hat{v}_i^\epsilon(k+1) &= a_i^v \Delta \hat{v}_i^\epsilon(k) + b_i^v \Delta p_i(k) \\ v_i^\epsilon(k) &= v_i^\epsilon(k-1) + c_i^v \Delta \hat{v}_i^\epsilon(k) \end{aligned} \quad (4.11)$$

$$\begin{aligned} \Delta \hat{\omega}_i^\epsilon(k+1) &= a_i^f \Delta \hat{\omega}_i^\epsilon(k) + b_i^f \Delta q_i(k) \\ \omega_i^\epsilon(k) &= \omega_i^\epsilon(k-1) + c_i^f \Delta \hat{\omega}_i^\epsilon(k) \end{aligned} \quad (4.12)$$

Thus the AIM states are obtained by augmenting the currently predicted state deviation with the previously measured output. From (4.11), and (4.12), generalized AIM is described by (4.13)

$$\begin{aligned}
\overbrace{\begin{bmatrix} \Delta \hat{x}_i^\epsilon(k+1) \\ y_i^\epsilon(k) \end{bmatrix}}^{\tilde{x}_i(k+1)} &= \overbrace{\begin{bmatrix} a_i & 0 \\ c_i & 1 \end{bmatrix}}^{\tilde{A}_i} \overbrace{\begin{bmatrix} \Delta \hat{x}_i^\epsilon(k) \\ y_i^\epsilon(k-1) \end{bmatrix}}^{\tilde{x}_i(k)} + \overbrace{\begin{bmatrix} b_i \\ 0 \end{bmatrix}}^{\tilde{B}_i} \overbrace{\begin{bmatrix} \Delta u_i(k) \end{bmatrix}}^{\tilde{u}_i(k)} \\
\overbrace{\begin{bmatrix} y_i^\epsilon(k) \end{bmatrix}}^{y_i(k)} &= \overbrace{\begin{bmatrix} c_i & 1 \end{bmatrix}}^{\tilde{C}_i} \overbrace{\begin{bmatrix} \Delta \hat{x}_i^\epsilon(k) \\ y_i^\epsilon(k-1) \end{bmatrix}}^{\tilde{x}_i(k)}
\end{aligned} \tag{4.13}$$

where  $\tilde{A}_i \in \mathbb{R}^{m \times m}$  is the system matrix,  $\tilde{B}_i \in \mathbb{R}^{m \times n}$  is the control input matrix,  $\tilde{C}_i \in \mathbb{R}^{r \times m}$  is the output measurement matrix. For the voltage restoration problem:  $\tilde{x}_i(k) \in \left[ \Delta \hat{v}_i^\epsilon(k) \ v_i^\epsilon(k-1) \right]^T$ ,  $\tilde{u}_i(k) \in \Delta p_i(k)$ ,  $y_i(k) \in v_i^\epsilon(k)$ , and for the frequency restoration problem:  $\tilde{x}_i(k) \in \left[ \Delta \hat{\omega}_i^\epsilon(k) \ \omega_i^\epsilon(k-1) \right]^T$ ,  $\tilde{u}_i(k) \in \Delta q_i(k)$ ,  $y_i(k) \in \omega_i^\epsilon(k)$ . The AIM incorporates the discrete-time deviation of the system states and inputs to introduce an integral action on the output in the closed-loop control.

*Remark:* To eliminate the voltage and frequency steady-state errors occurring from droop characteristics of (4.1), SC is required to incorporate an integral component [75]. The representation (4.13) is in agreement with the first-order model (4.3) including the integral action on the estimated output.

*Proof:* Integral action on state deviation in the discrete form at the  $k^{\text{th}}$  sample is given by:

$$\begin{aligned}
y_i^\epsilon(k) &= T_s^{\text{sc}} y_i^\epsilon(k) + y_i^\epsilon(k-1) \implies T_s^{\text{sc}} y_i^\epsilon(k) \\
&= y_i^\epsilon(k) - y_i^\epsilon(k-1) = c \Delta x_i^\epsilon(k)
\end{aligned} \tag{4.14}$$

This leads to the definition of integral action as:  $y_i^\epsilon(k) = c \Delta x_i^\epsilon(k) + y_i^\epsilon(k-1)$ . However, the resultant representation of (4.13) is:  $y_i^\epsilon(k) = c \Delta \hat{x}_i^\epsilon(k) + y_i^\epsilon(k-1)$ . Thus the necessary condition to incorporate the correct integral action in the AIM is to have the predicted state deviation equal and similar to the actual state deviation ( $\hat{x}_i^\epsilon \simeq x_i^\epsilon$ ). Here  $c = 1$  is considered as both voltage and frequency states are observable at the respective PCCs.

#### 4.4.3 Dynamic Synchronization of the AIM states

The representation of  $\mathcal{S}_i$  dynamics is a low-order high-fidelity model that accurately provides the steady-state representation of the system frequency. Since the frequency is a global state [152], for the measured frequency at a given node  $j, j \neq i$ :  $\omega_j^\epsilon \simeq \omega_i^\epsilon, \forall i \in 1, 2, \dots, N$ . As the influence of network impedance on frequency is negligible, the model represented in (4.12) provides sufficient frequency prediction.

*Definition 1:* For the local observation-based global state prediction, the error between the model predicted state deviation ( $\hat{x}_i^\epsilon$ ) and the observed global steady-state deviation ( $\bar{x}_j^\epsilon$ ) can

be verified by:

$$\lim_{k \rightarrow \infty} \|\hat{x}_i^\epsilon(k) - \bar{x}_j^\epsilon\| = 0 \implies \hat{x}_i^\epsilon \simeq \bar{x}_j^\epsilon$$

Thus, as per *Definition 1*, further synchronization of the AIM predicted frequency states of every  $\mathcal{S}_i$  is not required. However, when a DER is disconnected from the network, as it supplies no power into the network ( $\delta q_i(k) = 0 \implies \hat{\omega}_i^\epsilon(k) = 0, \forall k$ , see (4.7b)), model-based state prediction fails. To accomplish the plug-and-play feature, in frequency restoration case, the model predicted frequency deviation ( $\hat{\omega}_i^\epsilon(k)$ ) needs to be synchronized based on the local measurements ( $y_i^\epsilon(k) := \omega_i^\epsilon(k)$ ) before utilizing it in the prediction model. The representation of  $\mathcal{S}_i$  dynamics does not provide an accurate steady-state representation of the measured voltage at a given node  $j$ : ( $v_j^\epsilon \neq v_i^\epsilon, \forall i \in 1, 2, \dots, N$ ). Since the voltage is a local state [75], the measured voltages at different nodes in the network are different. As the influence of network impedance on the voltage cannot be ignored, the model in (4.11) provides an inaccurate voltage prediction.

*Definition 2:* For the local observation based local state prediction, the error between the model predicted state deviation ( $\hat{x}_i^\epsilon$ ) and the observed global steady-state state deviation ( $\bar{x}_j^\epsilon$ ) is verified by:

$$\lim_{k \rightarrow \infty} \|\hat{x}_i^\epsilon(k) - \bar{x}_j^\epsilon\| \leq \epsilon$$

Thus, as per *Definition 2*, synchronization of the the AIM predicted voltage states of every  $\mathcal{S}_i$  based on the global measurements ( $y_j^\epsilon(k) := v_j^\epsilon(k)$ ) is required. A generic DEKF for the dynamic synchronization of the AIM states that applies to both frequency and voltage restoration is represented by,

$$\tilde{x}_i^c(k+1) = \tilde{x}_i(k) + \tilde{K}_i(k) \left( y_i^\epsilon(k) + \Delta y_{ij}^\epsilon(k) - \tilde{C}_i \tilde{x}_i(k) \right) \quad (4.15)$$

where  $\Delta y_{ij}^\epsilon(k) = y_j^\epsilon(k) - y_i^\epsilon(k)$ , the DEKF gain matrix  $\tilde{K}_i(k) = \tilde{P}_i(k) \tilde{C}_i^T (\tilde{C}_i \tilde{P}_i(k) \tilde{C}_i^T + \tilde{R}_i(k))^{-1}$ , and the prediction error co-variance matrix computed recursively as  $\tilde{P}_i(k+1) = \tilde{A}_i(\tilde{P}_i(k) - \tilde{K}_i(k) \tilde{C}_i \tilde{P}_i(k)) \tilde{A}_i^T + \tilde{Q}_i(k)$ .

Since DEKF is effective for the noisy measurements that follow Gaussian distribution, the AIM-DEKF estimator is suitable for the systems with the Gaussian noise only even though AIM models is insensitive to the unknown noise. The convergence of Kalman gains is proved due to the convergence of the recursive  $\tilde{P}_i(k)$  computation. Since the AIM is insensitive to the process noise, the convergence of  $\tilde{P}_i(k)$  is guaranteed [154]. The AIM and DEKF together (4.15) lead to the local dynamic synchronization of the system states defined as  $\tilde{\mathcal{S}}_i$  and the corresponding local optimal control problem  $\tilde{\mathcal{P}}_i$  (4.10). In case of frequency restoration  $\Delta y_{ij}^\epsilon(k) \simeq 0$ , hence no communication is needed between  $\mathcal{S}_j$  and  $\mathcal{S}_i$ .

#### 4.4.4 Prediction Model

With the knowledge of the current states of the representation (4.13), the prediction model for the finite horizon of the next  $M$  time steps has the form:

$$\tilde{y}_i(k+1|M) = p_M + F_M \tilde{u}_i(k|M), \quad (4.16)$$

where

$$\begin{aligned} p_M &= O_M \tilde{A}_i \tilde{x}_i^c(k), \\ F_M &= [ O_M \tilde{B}_i \quad H_M ] \end{aligned} \quad (4.17)$$

The extended observability matrix ( $O_M$ ) is computed based on  $\tilde{A}_i$ , and  $\tilde{C}_i$ , represented as:

$$O_t \stackrel{\text{def}}{=} \begin{bmatrix} \tilde{C}_i \\ \tilde{C}_i \tilde{A}_i \\ \vdots \\ \tilde{C}_i \tilde{A}_i^{i-1} \end{bmatrix} \in \mathbb{R}^{tr \times m}$$

and  $H_M \in \mathbb{R}^{rM \times (M-1)m}$  is the standard Toeplitz matrix of the form:

$$H_i \stackrel{\text{def}}{=} \begin{bmatrix} \tilde{C}_i \tilde{B}_i & 0 & 0 & \cdots & 0 \\ \tilde{C}_i \tilde{A}_i \tilde{B}_i & \tilde{C}_i \tilde{B}_i & 0 & \cdots & 0 \\ \vdots & \vdots & \vdots & \ddots & \vdots \\ \tilde{C}_i \tilde{A}_i^{i-2} \tilde{B}_i & \tilde{C}_i \tilde{A}_i^{i-3} \tilde{B}_i & \tilde{C}_i \tilde{A}_i^{i-4} \tilde{B}_i & \cdots & 0 \end{bmatrix}$$

#### 4.4.5 Formulation of Optimal Control with the Constraints

One of the objectives of the proposed IMPC framework is to enhance the voltage and frequency restoration performance by utilizing the inequality constraint handling property. The IMPC framework is designed to achieve input constraints such that the SC-generated signal can be limited within the range of  $[u_{min}, u_{max}]$ . This aids in accomplishing the power reference saturation, especially during abnormal situations such as system faults, thereby resulting in the stable operation of DERs during ride-through.

The inequality constraints as a linear inequality matrix are obtained by specifying the rate of change of input as in (4.18a) and the input magnitude constraint as in (4.18b).

$$\tilde{u}_{min} \leq \tilde{u}_i(k|M) \leq \tilde{u}_{max} \quad (4.18a)$$

$$u_{min} \leq u_i(k|M) \leq u_{max} \quad (4.18b)$$

The constraint conditions of (4.18) need to be represented only in terms of optimization variable, hence reformulated as per the requirements of quadratic programming [88]. Thus, the optimization variable can be represented as (4.19),

$$u_i(k|M) = S\tilde{u}_i(k|M) + cu_i(k-1) \quad (4.19)$$

where

$$S = \begin{bmatrix} I_n & 0_n & \cdots & 0_n \\ I_n & I_n & \cdots & 0_n \\ \vdots & \vdots & \ddots & \vdots \\ I_n & I_n & \cdots & I_n \end{bmatrix}, \quad c = \begin{bmatrix} I_n \\ I_n \\ \vdots \\ I_n \end{bmatrix}$$

$I_n$  is the  $n \times n$  identity matrix and  $0_n$  is the  $n \times n$  zero matrix. The performance index (4.10) along with the constraints (4.19) is applied to the prediction model (4.16) resulting in a quadratic function of the standard form:

$$\begin{aligned} \min_{\tilde{u}_i} J_i(k) &= \sum_{p=1}^M (\tilde{u}_i(k+p))^T H_i(\tilde{u}_i(k+p)) \\ &\quad + 2(f_i(k))^T (\tilde{u}_i(k+p)) \end{aligned} \quad (4.20a)$$

$$\text{s.t. } \tilde{x}_i(k+1) = \tilde{A}_i \tilde{x}_i(k) + \tilde{B}_i \tilde{u}_i(k) \quad (4.20b)$$

$$\tilde{x}_i^c(k) = \tilde{x}_i(k) + \tilde{K}_i(k) (y_i^\epsilon(k) + \Delta y_{ij}^\epsilon(k) - \tilde{C}_i \tilde{x}_i(k)) \quad (4.20c)$$

$$y_i^\epsilon(k) = \tilde{C}_i \tilde{x}_i^c(k) \quad (4.20d)$$

$$\mathcal{A} \tilde{u}_i(k) \leq b_i(k) \quad (4.20e)$$

where

$$\begin{aligned} H_M &= F_M^T \hat{Q}_M F_M + \hat{R}_M, \\ f_i(k) &= F_M^T \hat{Q}_M p_M, \\ \mathcal{A} &= \begin{bmatrix} I_{(nM, nM)} & -I_{(nM, nM)} & S & -S \end{bmatrix}^T, \\ u_{lim} &= (u_{max} - cu_i(k-1)), \\ b_i(k) &= \begin{bmatrix} \tilde{u}_{max} & -\tilde{u}_{min} & u_{lim} & -u_{lim} \end{bmatrix}^T, \end{aligned} \quad (4.21)$$

In this formulation, the specified objective function (4.20a) is convex as the obtained  $H_M$  is positive-semidefinite. The objective function is the result of setting the reference signal to zero as the state deviations have to be mitigated. The system dynamics, including the integral of state deviation, are presented by the constraint (4.20b). The corrections to the predicted state based on the measurements are expressed by (4.20c) and (4.20d). Also,

---

**Algorithm 1:** Proposed decentralized SC approach for voltage and frequency restoration applied at each  $\mathcal{S}_i$ .

---

```

1 Inputs:  $u_i(k), y_i(k), 1 \leq i \leq N, N \geq 2, y_j(k)$ 
2 Output:  $u_i^{sc}(k), 1 \leq i \leq N$ 
3 if  $\mathcal{S}_i$  is islanded then
4   Initialize  $\tilde{A}_i, \tilde{B}_i, \tilde{C}_i$  as per the AIM (4.13)
5   Initialize:  $\tilde{x}_i = X_0, \tilde{P}_i = P_0, u_i^{sc} = U_0^{sc}, k = 1$ 
6   for  $k = 1, 2, \dots$  do
7     Apply the first sample of the previous iteration control update vector
        $u_i^{sc}(k-1)$  to the  $\mathcal{S}_i$ 
8     Compute the model inputs using PCC current and voltage measurements
       ( $u_i := (\delta p_i, \delta q_i)$ )
9     AIM-based initial prediction of the states:
        $\tilde{x}_i(k+1) = \tilde{A}_i \tilde{x}_i(k) + \tilde{B}_i(\tilde{u}_i(k) + \Delta u_i^{sc}(k))$ 
10    Extrapolate the error co-variance matrix:
        $\tilde{P}_i(k) = \tilde{A}_i \tilde{P}_i(k-1) \tilde{A}_i^T + w_i(k) \tilde{Q}_i(k) w_i(k)^T$ 
11    Dynamically synchronize AIM states based on the local ( $y_i^\epsilon := (v_i^\epsilon, \omega_i^\epsilon)$ ) and
       global ( $y_j^\epsilon := v_j^\epsilon$ ) measurements (4.15)
12    Compute prediction model utilizing the AIM and the synchronized states
       (4.16)
13    Obtain new optimal solution vector  $\tilde{u}_i^{sc}(k|M_u)$  over the horizon  $M_u$  by solving
        $\tilde{\mathcal{P}}_i(4.20)$ 
14    Compute the current control update vector as:
        $u_i^{sc}(k|M_u) = \tilde{u}_i^{sc}(k|M_u) + \tilde{u}_i^{sc}(k-1|M_u)$ 
15  end
16 end

```

---

the ramp rate and the saturation for the DER power reference are represented by (4.20e). The optimization variable  $\tilde{u}_i(k|M)$  is solved for every discrete sample ( $k$ ), and the first control value is used to generate the power reference signal for the PC, thus repeating in a receding horizon fashion. The  $M$  is chosen such that the controller is internally stable and offers reasonable transient performance for the identified  $T_s^{sc}$ . For the RT implementation  $M_u \ll M$  is used to reduce the computational complexity. The detailed steps for the closed-loop control are described in Algorithm 1. The controller update sample  $u_i^{sc}(k)$  is  $\delta P_i^{sc}$  and  $\delta Q_i^{sc}$  for voltage and frequency restoration respectively.

#### 4.4.6 Communication Network Performance

As the proposed architecture is decentralized, the frequency restoration that is based on local PCC measurements is highly scalable to the larger distribution networks. However, since voltage restoration requires global measurements, communication network performance plays a major role in deciding the scalability of the proposed framework. Communication network performance parameters such as packet latency and packet losses highly affect the performance of the control application. During the packet loss, the proposed framework facilitates two options. Firstly, previously received packet data can still be used for the state deviation correction. Secondly, using the model predicted state deviation based on the PCC power measurements can be used as an input to the prediction model. Thus, the framework

TABLE 4.1: Electrical parameters of DERs and loading in the islanded section of IEEE 123 node system

DER Ratings and corresponding <i>LCL</i> filter parameters					
Parameters	Symbols	DER 1 (node 1)	DER 2 (node 13)	DER 3 (node 21)	DER 4 (node 25)
Rated active and reactive power	$P, Q$	500 kW, 200 kVar	200 kW, 80 kVar	400 kW, 160 kVar	150 kW, 60 kVar
Filter input inductor	$L_i, R_i$	352.7 $\mu$ H, 2 m $\Omega$	881.2 $\mu$ H, 3 m $\Omega$	440.9 $\mu$ H, 2 m $\Omega$	1200 $\mu$ H, 3 m $\Omega$
Filter output inductor	$L_o, R_o$	5.3 $\mu$ H, 1 m $\Omega$	13.3 $\mu$ H, 1 m $\Omega$	6.6 $\mu$ H, 1 m $\Omega$	17.6 $\mu$ H, 1 m $\Omega$
Filter capacitor, damping resistor	$C_f, R_d$	287.8 $\mu$ F, 45 m $\Omega$	115.1 $\mu$ F, 112 m $\Omega$	230.2 $\mu$ F, 55.6 m $\Omega$	86.3 $\mu$ F, 148 m $\Omega$
Phase-wise and total loading in the identified section of IEEE 123 node system					
Parameters	Symbols	Phase A	Phase B	Phase C	Total
Active power load	$P_L$	360 kW	80 kW	320 kW	760 kW
Reactive power load	$Q_L$	180 kVar	40 kVar	160 kVar	380 kVar

is tolerant against packet losses. To consider the impact of packet latency on the proposed framework, metrics for NDN-based and IP-based networks [155] are utilized. According to this, a default of 10 ms of communication latency is considered between  $\mathcal{S}_i$  and  $\mathcal{S}_j$ . Nevertheless, to assess the scalability of voltage restoration for larger distribution networks with higher DER integration that may lead to traffic congestion, higher communication latency test scenarios are performed.

#### 4.5 RT multi-core multi-rate MIL set up and Results

The proposed secondary controller is validated utilizing an island-able section of the IEEE 123 node system as shown in Fig. 4.4. The SS between node 18 and node 135, and between node 13 and node 152 is always in an open state, while the one at node 149 (SS1) is controllable. When SS1 is closed, all the DERs operate in the grid-following mode, tracking the provided PQ set-points. When SS1 is open, the DERs share the load in the islanded system using the primary droop controller given by (4.1a) and (4.1b). All four DERs are connected to the distribution network through a  $\Delta$ - $Yg$  transformer.

The hierarchical primary and secondary control systems along with the IEEE 123 node system, including DER models are implemented in RTLAB software and executed in the RT simulator utilizing the OPAL-RT eMEGASIM platform. The selected IEEE 123 node feeder along with the DER model is split across two cores and is executed with a sample time of 50  $\mu$ s. The Artemis stub line is used to perform the three-phase distributed parameter line model for the optimized RT simulation of Core 1 and Core 2. The hierarchical controller layer is implemented with the time-scale separation of the primary (100  $\mu$ s) and secondary controllers (1 ms) with associated DERs. A software-based interrupt handler facilitates this multi-rate hierarchical control execution. To achieve stable closed-loop operation, the secondary controller needs to be executed at a much slower sample time in comparison to the primary controller. Appropriate choice of the sample time is essential for the deployability of control application in a chosen target hardware [156].

RTLAB OpComm blocks are used to communicate messages between different cores. The controller layer gets the respective PCC voltage and current measurements and computes the PWM signals for the IBRs of the DER models. The global voltage measurement from

the measurement unit (MU) at node 149 is delayed by 10 ms (default communication latency) before being utilized in the secondary controller. The proposed secondary controller computes  $\delta P_i^{sc}$  and  $\delta Q_i^{sc}$  signals for the primary controller droop laws represented in (4.6). The IMPC quadratic problem (4.20) is solved using the MATLAB *quadprog* function. The results of the proposed controller are compared against the decentralized optimal PI controller proposed in the literature [12]. Phase-wise and total load in the islanded section and the DER sizes and *LCL* filter parameters are mentioned in Tables 4.1. The system and controller parameters are described in Tables 4.2.

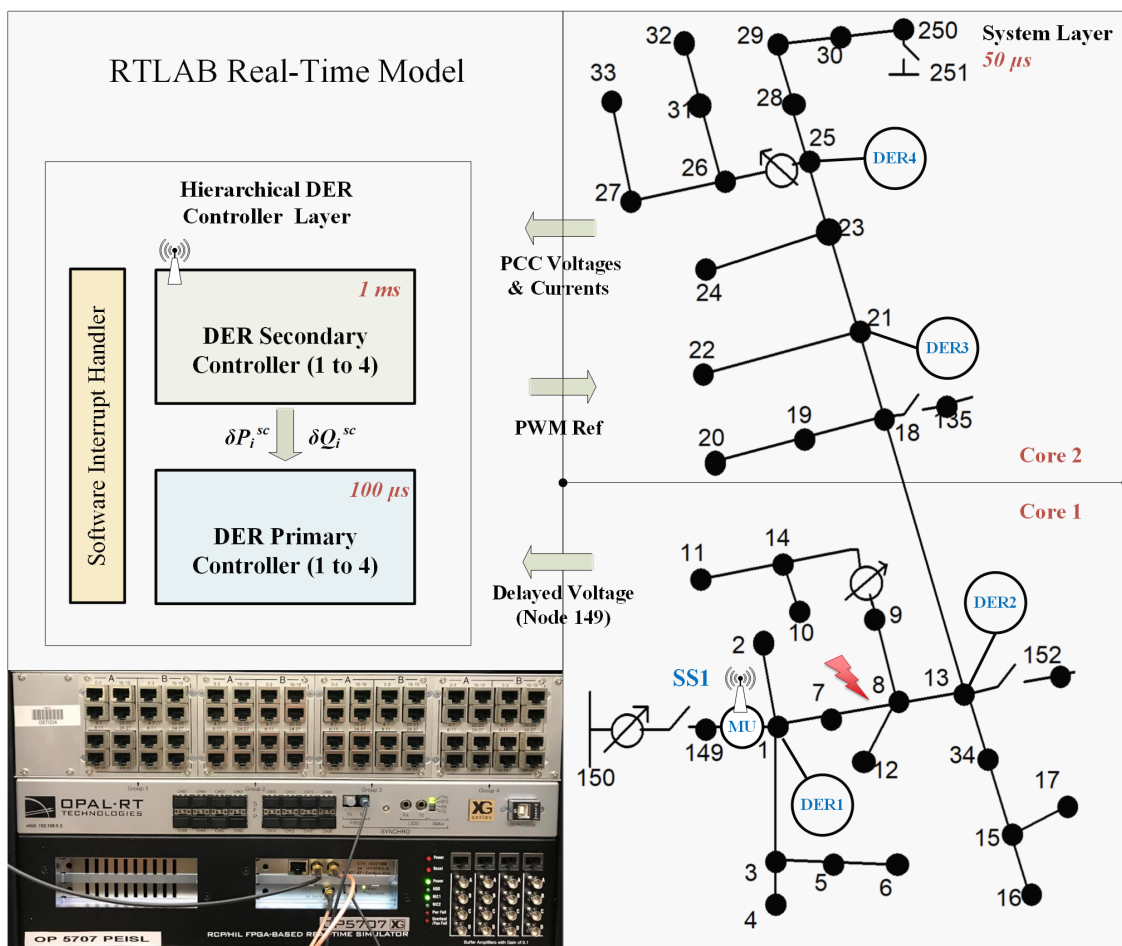


Figure 4.4: RT set-up to validate the functionality of proposed secondary controller framework.

#### 4.5.1 Discrete-time AIM-based Stability Analysis

AIM model for each of the DER subsystem ( $\mathcal{S}_i$ ) is built utilizing the control parameters provided in Table 4.2. The unconstrained IMPC has the analytical solution given by:

$$\tilde{u}_i^{sc}(k|M) = -H_i^{-1} f_i(k) = K_i^{mpc} x_i^c(k) \quad (4.22)$$

The impact of the IMPC controller gains on the closed loop system is assessed utilizing the discrete root locus of  $(\tilde{A}_i - \tilde{B}_i K_i^{mpc})$ . To achieve the closed-loop stability of the predictive controller,  $\hat{Q}_i$  and  $\hat{R}_i$  weight matrix values are varied to understand the stability margin. Fig 4.5a depicts the root locus of an  $\mathcal{S}_i$ , as the  $\hat{Q}_i$  weight matrix of voltage and frequency restoration is varied (0.001 to 5), keeping other parameters in consistent with Table 4.2. The

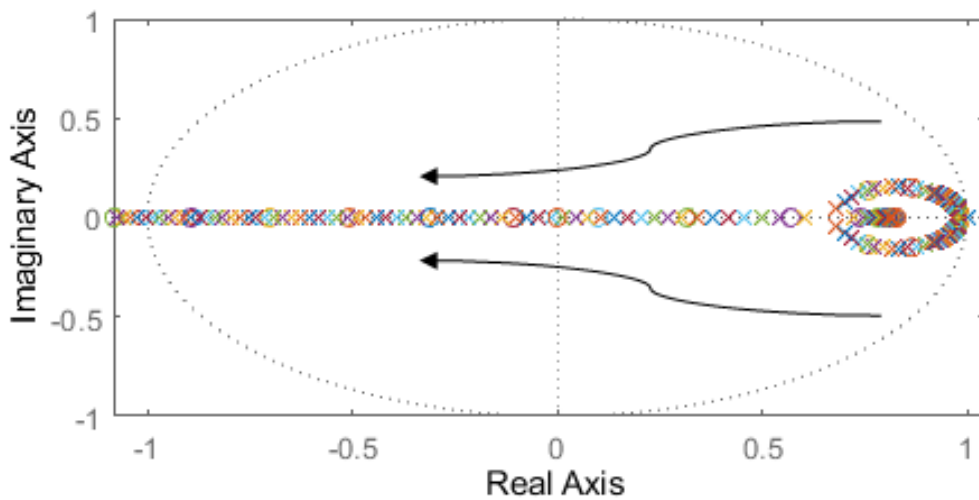
TABLE 4.2: System and controller parameters

System Parameters		
Parameters	Symbol	Value
DER DC link voltage	$V_{DC}$	900 VDC
IBR Voltage	$V_p$	480 V (RMS)
Grid Voltage	$V_{149}$	4.16 kV (RMS)
Grid Frequency	$\omega_p$	60 Hz
Primary Controller Parameters (p.u.)		
$P - V$ droop coefficient	$K^P$	0.8
$Q - \omega$ droop coefficient	$K^Q$	0.5
Robust droop coefficient	$K^V$	1
Voltage controller gains	$(k_p^v, k_i^v)$	(2.8, 205.3)
Current controller gains	$(k_p^c, k_i^c)$	(0.37, 19.3)
PLL gains	$(k_p^{pll}, k_i^{pll})$	(0.19, 6.6)
Secondary Controller Parameters		
Voltage deviation penalty	$Q^{v^\epsilon}$	0.1
Frequency deviation penalty	$Q^{\omega^\epsilon}$	0.1
Active power deviation penalty	$R^{\Delta p}$	0.5
Reactive power deviation penalty	$R^{\Delta q}$	5
Prediction horizon	$M$	10
Covariance of the process noise	$\tilde{Q}$	1
Covariance of the measurement noise	$\tilde{R}$	0.1

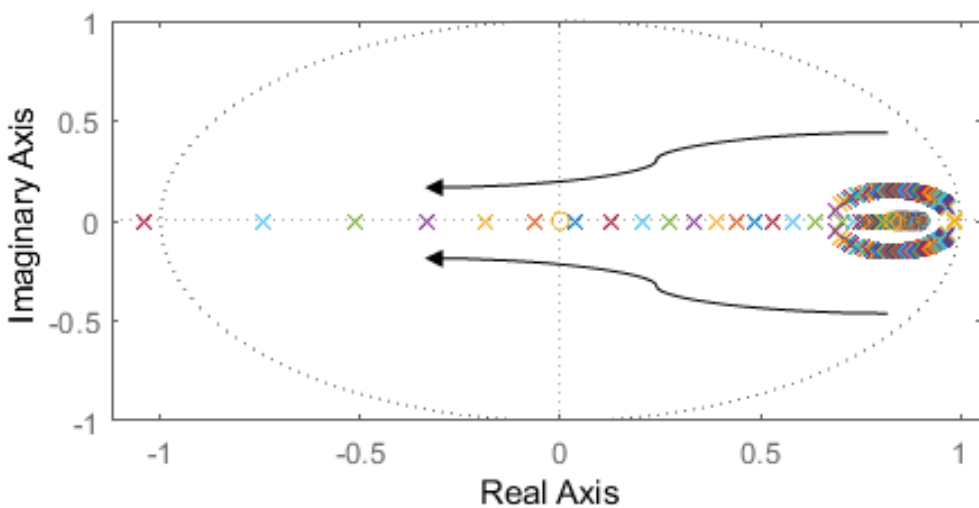
eigenvalues are within the unit circle until the  $\hat{Q}_i$  values are less than 2.14 maintaining a stable system. Similarly, Fig. 4.5b is obtained by varying the  $\hat{R}_i$  values from 0.0001 to 10 while other parameters are kept constant as per Table 4.2. The eigenvalues are observed to be within the unit circle until  $\hat{R}_i$  values are more than 0.0014. When  $\hat{Q}_i$  and  $\hat{R}_i$  values are varied some of the eigenvalues change from real to complex conjugate and vice-versa affecting the damping of the system. Appropriate selection of values for  $\hat{Q}_i$  and  $\hat{R}_i$  that provide good stability margin and faster transient response are mentioned in Table 4.2. From both root locus plots, it is evident that the controller design is stable for the larger parameter range ensuring the stability and robustness of the IMPC controller.

#### 4.5.2 Analysis of Primary Controller and State Estimation

After islanding the network, Fig. 4.6a depicts the frequency and voltage observations at the nodes where DERs are connected and at node 149 (node of interest) without enabling the secondary controller. At 4 s, 100 kW, 50 kVar load is disconnected from the network, and at 6 s the same load is added back. Both voltage and frequency are deviating from the nominal values due to the effect of droop laws. Furthermore, voltages at different nodes are at slightly different values due to the effect of line impedance while frequencies synchronize to a common value. In Fig. 4.6, verification of state estimation is showcased. In the case of frequency, steady-state values of model prediction ( $\hat{\omega}^\epsilon$ ) and measured values ( $\omega^\epsilon$ ) match (as per *Definition 1*) unlike in the case of voltage (as per *Definition 2*). Kalman filter based correction yields in  $(\hat{\omega}_c^\epsilon, \hat{v}_c^\epsilon)$ , matching the model prediction  $(\hat{\omega}^\epsilon, \hat{v}^\epsilon)$  to the measurements



(a)



(b)

Figure 4.5: Stability analysis of decentralized IMPC control by varying weight matrices. (a) Eigenvalue trajectory for the variation of  $\hat{Q}_i$  (0.001 to 5) (b) Eigenvalue trajectory for the variation of  $\hat{R}_i$  (0.0001 to 10)

$(\omega^e, v^e)$ , even during the transients.

#### 4.5.3 Voltage and Frequency Restoration Post Islanding

As observed from Fig. 4.7a, until 2 s, in the presence of the substation node (150), DERs are tracking their respective active power set-points in unity power factor mode. The substation node absorbs the excess generation from the DERs and supplies the required reactive power for the network. After the opening of the SS1, DERs in the network achieve stable active and reactive power-sharing with the secondary controller being enabled. The reasonable transients for around 200 ms are observed and all the four DERs share the total load of 760 KW, 380 KVar, and the line losses in the system. From Fig. 4.7d, it is observed that the proposed secondary controller regulates the system frequency and voltages (observed at node 149) to the nominal values. Table 4.3 quantifies the proposed controller performance. In the case of frequency restoration, the settling time for both methods is close enough, however, the PI method leads to higher over/undershoots. In the case of voltage restoration, the settling time of the proposed method showcases significant improvement even in presence

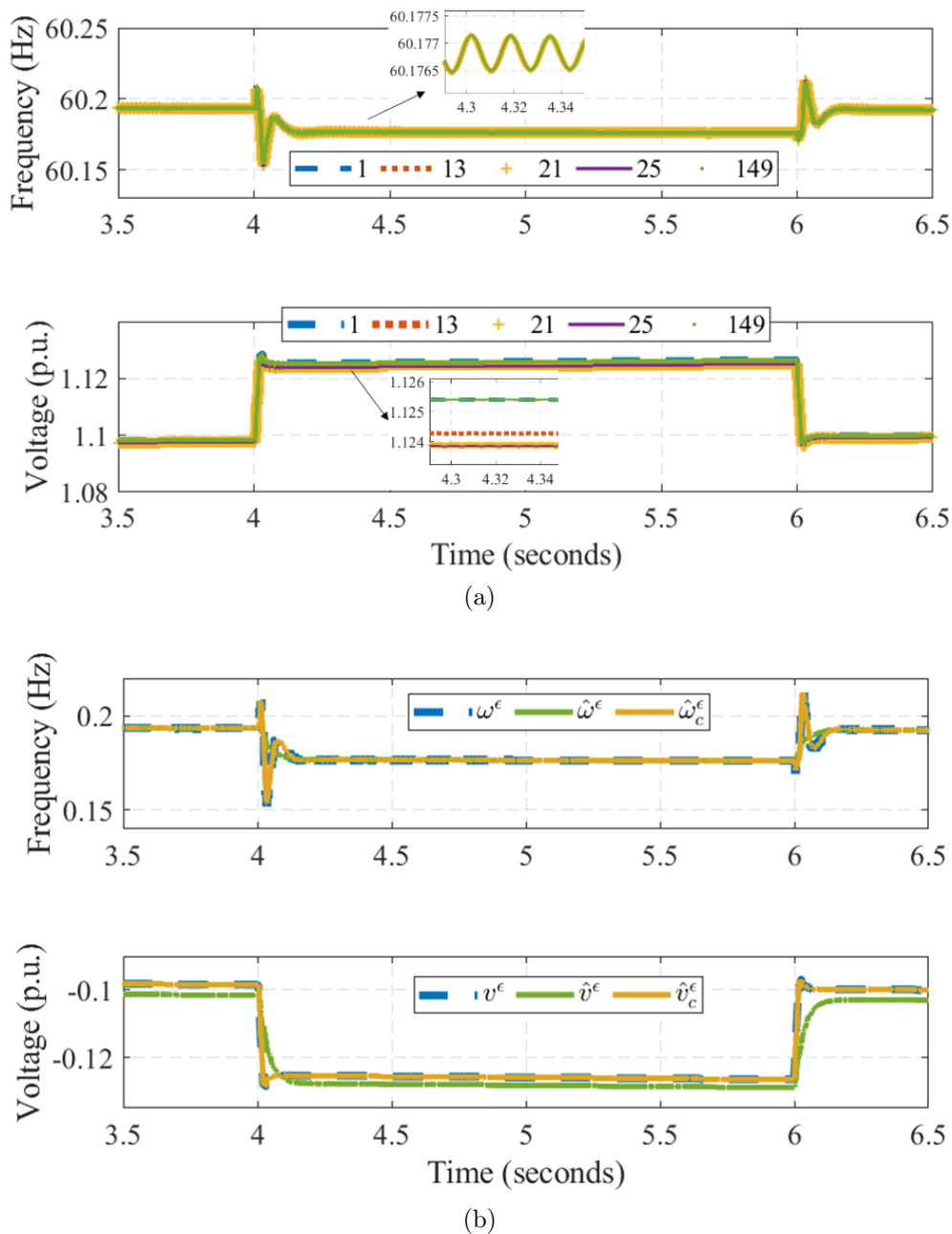


Figure 4.6: Voltage and frequency without secondary controller (a) Primary Controller Responses (b) Verification of the state estimation

of communication latency (10 ms).

#### 4.5.4 Voltage and Frequency Restoration during Load Change

In the islanded system, at 4 s, 100 kW, 50 kVar load is disconnected from the network, and at 6 s it is connected back. Fig. 4.7b and Fig. 4.7c depict the stable power-sharing among the DERs during load decrease and load increase respectively. Fig. 4.7e and Fig. 4.7f showcase the voltage and frequency restoration comparison between the proposed method and the optimal PI controller-based method for load change events. As quantified in Table 4.3, the over/undershoots are lower for frequency restoration and faster voltage restoration is achieved. From these test scenarios, it can be inferred that the predictive mechanism facilitates faster restoration in comparison to the optimal PI control strategy.

#### 4.5.5 Controller Performance during Fault Scenario

Three-phase short-term fault (ABCG) of  $1 \Omega$  resistance for 200 ms (from 5 s to 5.2 s) is simulated at node 8 as shown in Fig. 4.7g. The fault leads to a voltage sag of 0.5 p.u.

TABLE 4.3: Comparison of the proposed IMPC-based controller performance against the optimal PI controller [12].

Application:	Frequency and Voltage Restoration (FR, VR)								
Performance:	Settling time (s)			Overshoot (%)			Undershoot (%)		
Test Scenario	PI	IMPC	Improvement	PI	IMPC	Improvement	PI	IMPC	Improvement
Islanding	(0.26, 0.65)	(0.255, 0.2)	(2%, 70%)	(3.5, 12.3)	(3.5, 12.3)	(0%, 0%)	(4.5, 12)	(2, 10)	(55%, 16%)
Load decrease	(0.28, 0.6)	(0.275, 0.15)	(2%, 75%)	(0.07, 2.5)	(0.02, 2.5)	(74.6%, 0%)	(0.08, 0)	(0.07, 0)	(14.3%, 0%)
Load increase	(0.25, 0.58)	(0.245, 0.12)	(2%, 80%)	(0.08, 0)	(0.07, 0)	(14%, 0%)	(0.07, 2.2)	(0.02, 2.2)	(74%, 0%)

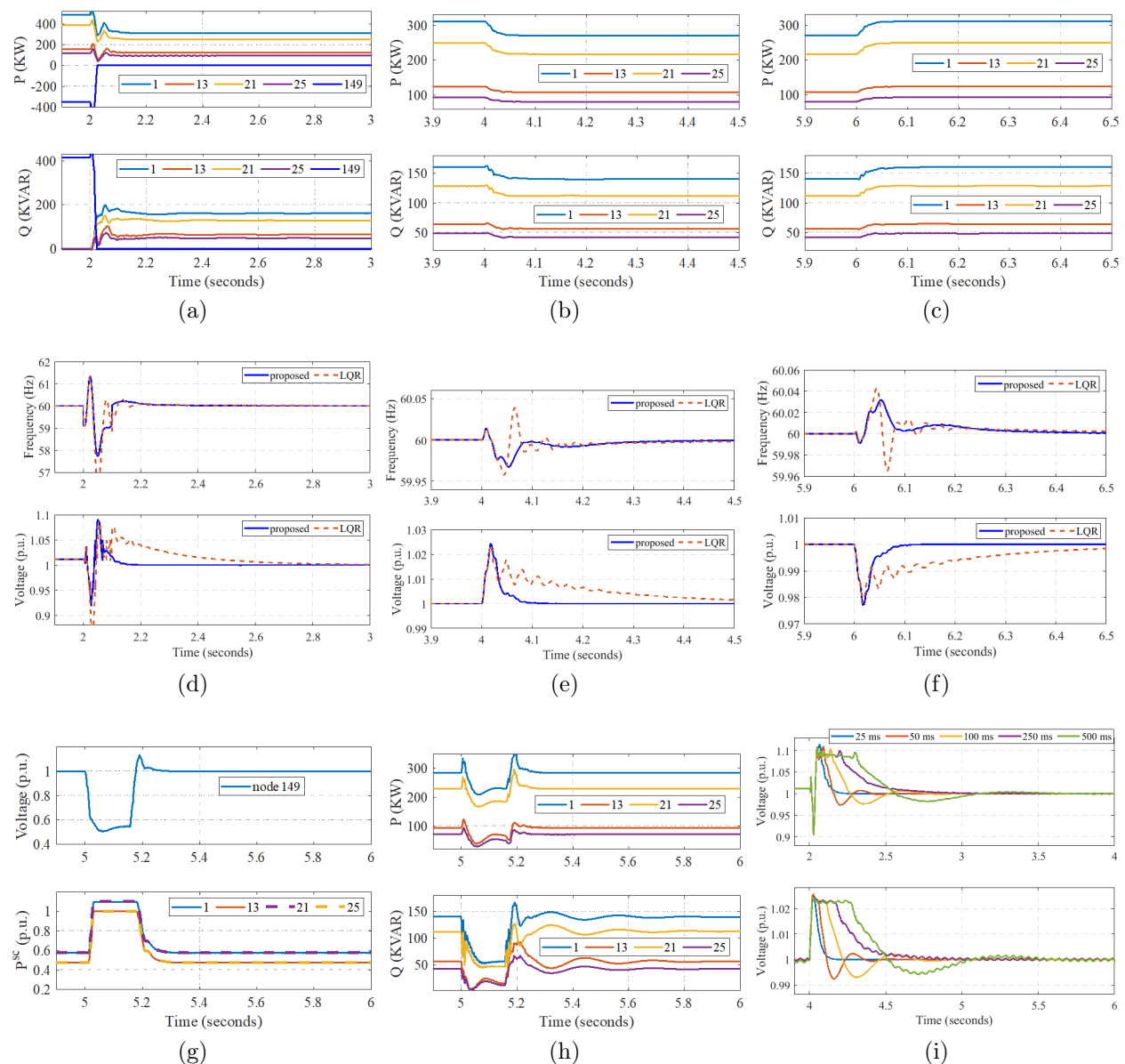


Figure 4.7: DER active and reactive power sharing and system parameters (voltage magnitude, and frequency at node 149) in the secondary controller enabled islanded distribution system. (a) PQ sharing after islanded (b) Load decrease in islanded system (c) Load increase in islanded system (d) System parameters after islanding (e) System parameters after load decrease (f) System parameters after load increase (g) Controller performance during a fault (h) Power sharing during and post fault (i) Impact of communication latency

at node 149. In the IMPC framework, the constraints ( $u_{min}, u_{max}$ ) for DER 1 and DER 3 are configured as 0, and 1.1 p.u., and for DER 2 and DER 4 are configured as 0 and 1 p.u. As depicted in Fig. 4.7g, the IMPC framework generated an active power reference signal ( $P^{sc}$ ) for the primary controller as per the terms of the mentioned constraints, and after fault clearance, the framework generates the power reference signals same as the pre-fault duration. Fig. 4.7h confirms the stable power-sharing of the DERs after the clearance of the fault, and power-sharing continues to be the same as the pre-fault values. This test scenario confirms that the proposed framework is robust and stable during the short-term faults in

TABLE 4.4: Controller performance during grid events in presence of communication latency for the voltage restoration.

Latency (ms)	Settling time (s)	
	Islanding	Load change
25	0.24	0.17
50	0.52	0.46
100	0.89	0.76
250	1.01	0.83
500	1.1	1.0

the grid, and the IBR ride-through capability is accomplished.

#### 4.5.6 Impact of Latency on Voltage Restoration

Since frequency restoration depends on local PCC measurements, the solution is communication free. In the case of voltage restoration, various communication latency is considered, and the results for the same are depicted in Fig. 4.7i. With the increase in latency, it is observed that voltage restoration time is increased during the islanding event (at 2 s) and the load change (at 4 s) as shown in Table 4.4. However, the framework is effective in achieving stable voltage restoration. This test scenario confirms the scalability of the proposed framework for larger distribution networks with a higher number of DER integration even during unusual network traffic congestion.

#### 4.5.7 Plug-and-Play Capability Performance Analysis

In this test scenario, as shown in Fig. 4.8, at 8 s DER 4 is disconnected from the network, and it is connected back at 9 s. Before the DER 4 disconnection, all 4 DERs are sharing the load in the network, and post 8 s, DER 4 active and reactive power reached zero as seen from Fig. 4.8a. Since DER 4 is unavailable, the remaining 3 DERs increase the power-sharing as per the droop law to meet the load demand. When DER4 is reconnected at 9 s, the remaining 3 DERs reduce power-sharing.

Fig. 4.8b demonstrates the restoration of system voltage and frequency (measured at node 149) to their respective nominal values during plug-in and plug-out of DER 4. Thus, using the proposed method, stable power-sharing is achieved and system voltage and frequency are restored even when one of the DERs is seamlessly plugged in/out from the network with acceptable transients. From Fig. 4.8 it is observed that the transients during plug-in are different from those during plug-out. During plug-out, DER 4 disconnection leads to a step-change in the load of the system. However, during plug-in, DER 4 connects to the network with the initial dynamics of the primary controller. And, these dynamics influence the power-sharing of the other DERs and the voltage/frequency restoration.

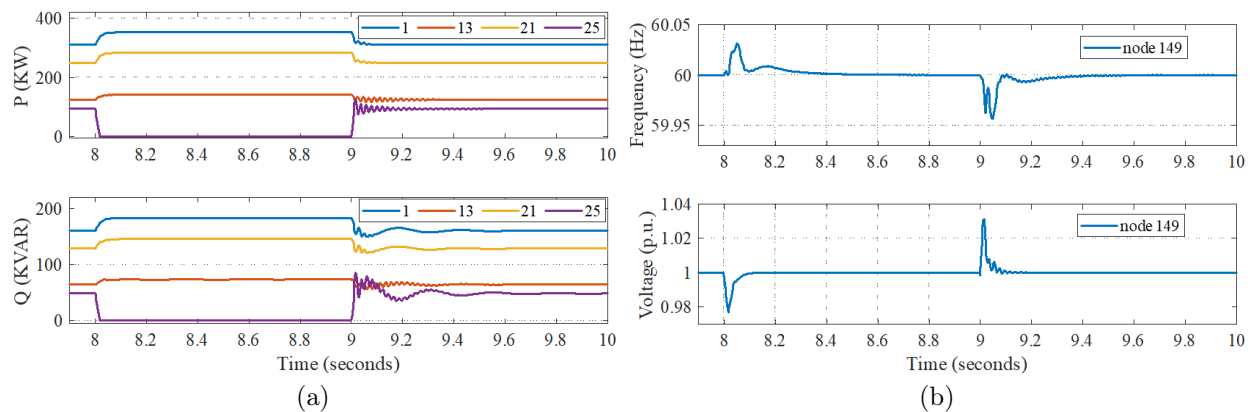


Figure 4.8: Validation of plug-and-play feature with the proposed framework. DER4 at node 25 is plugged-out at 8 s and plugged in at 9 s. (a) Power sharing with the plug-out and plug-in of DER 4. (b) Voltage and frequency restoration with the plug-out and plug-in of DER 4.

#### 4.5.8 Controller Performance with Noisy Measurements

To demonstrate the performance of the proposed controller when the measurements are noisy, a white Gaussian noise level of  $\sigma^2 = 1$  is applied to the actual voltage ( $V_p$ ) measurement at all the PCC nodes where DERs are connected. For the simple illustration, in Fig. 4.9a, the noisy measurement at node 1 is shown and the proposed SCs collectively restore the voltage and frequency at POI without degradation. Fig. 4.9b depicts the reference signal generated by the proposed SC is noise-free in comparison to the LQR method (no estimator). Thus the approach without an estimator leads to the much-degraded system voltage and frequency restoration as seen from Fig. 4.9a.

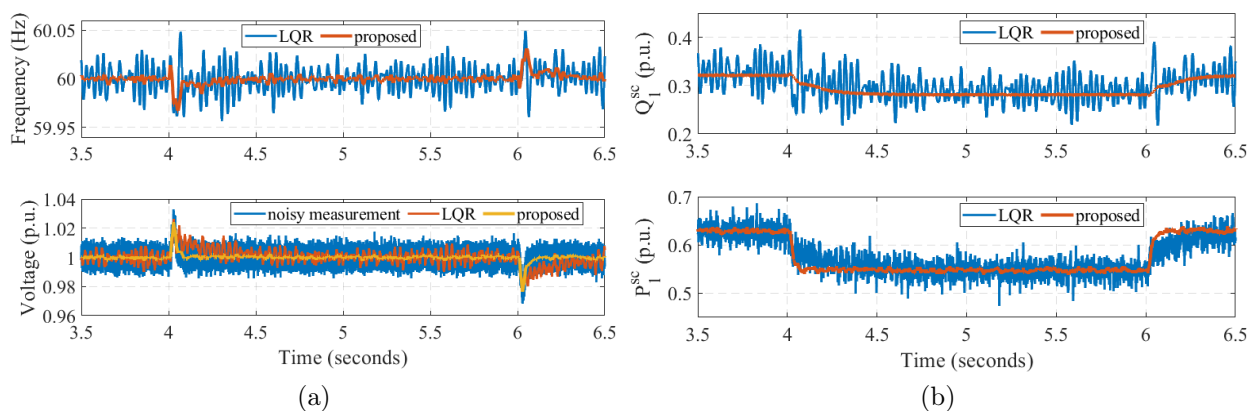


Figure 4.9: The controller performance analysis for the measurements with the white Gaussian noise ( $\sigma^2 = 1$ ) during the load change event. (a) Voltage and frequency restoration at the POI. (b) The secondary controller generated a reference signal for the primary controller.

## 4.6 Summary

In this chapter, a decentralized secondary frequency and voltage control of MGs in the distribution network is introduced. The proposed generic framework utilizes the AIM and local state estimation techniques to solve the quadratic optimal control problem using IMPC methodology. The frequency restoration solution is showcased without the need for communication, and the design is robust against measurement noise and system disturbances. Though voltage restoration requires a communication network, scalability and tolerance to

wards traffic congestion are showcased considering higher communication latency. Through the MIL RT setup, it is shown that the proposed IMPC framework performs better than the LQR control by delivering better transient performance and faster restoration. A generic straightforward design that is insensitive to measurement noise, robustness against system faults using the constraint IMPC framework, and plug-and-play capability enables stable operation of 100% DER-based autonomous MGs in the distribution grid.

## CHAPTER 5: Data-driven Decentralized Online System Identification-based Integral Model Predictive Control of Voltage and Frequency

*If you cannot measure it, you cannot improve it.*

---

Lord Kelvin

This chapter proposes a decentralized online system identification-based integral model predictive control strategy for the voltage and frequency regulation in the Microgrids (MG). The main advantage of the proposed architecture is that the approach is inherently adaptive to changing system conditions and does not require the knowledge of system parameters. In addition, as the decentralized system parameters are identified online utilizing local/global measurements, the controller is robust against unknown system disturbances. The decentralized nature of the proposed architecture evolved from an extended Kalman filter that is utilized to synchronize the decentralized states of the identified model thereby enabling a plug-and-play capability. The proposed controller is constructed utilizing the identified augmented incremental model that incorporates optimal integral action required to mitigate the steady-state errors in the MG voltage and frequency. Furthermore, controller formulation as a quadratic optimization problem including the constraints limits the control inputs within the bounds during electric faults thus assisting the downstream primary controller in accomplishing ride-through capability. The proposed framework is validated utilizing a section of the IEEE 123 bus distribution network for the different grid events including the effect of communication latency. Model-in-the-loop real-time simulation results demonstrate that the proposed framework offers significant transient performance improvement compared to the optimal PI strategy, especially around 50% faster regulation, when the communication latency is considered.

### 5.1 Introduction

The integration of distributed energy resources (DERs) into the power grid has rapidly increased in recent years. A group of DERs in the network can form a microgrid (MG) that can be operated as grid-connected or as an island [142]. A DER is usually interfaced with the power grid through the inverter-based resource (IBR) that couples the DC energy resources to the AC power grid. To share the load power among the multiple IBRs in an islanded MG, the droop technique is commonly adopted as a part of the IBR primary controller [81]. However, voltage and frequency in the MG are not maintained at the respective nominal values due

to the nature of the droop laws [52, 142]. This is the requirement for the development of secondary control layer that can provide appropriate power reference signals to the primary controller to regulate the voltage and frequency.

Conventional *centralized* secondary control frameworks are highly dependent on the data availability and are prone to a single point of failure [7, 8]. The *distributed* secondary control frameworks utilize sparse communication structures to share the critical state information among the neighboring nodes, and hence are less prone to operational failure. However, with the high penetration of DERs, distributed frameworks pose design complexities and scalability concerns [14, 15]. *Decentralized* secondary control frameworks require minimum or no communication infrastructure and are scalable with large-scale DER integration [12, 146, 157]. Detailed network model-based decentralized solution approaches require expensive computational resources at the grid edge leading to deployability challenges [146, 157]. In Ref. [12], optimal PI control parameters are identified from the quadratic cost function to achieve the frequency regulation. Though the control strategy utilizes a lower-order model, the droop control-associated parameters may not be available from the various IBR manufacturers, and the formulation can not be extended to accommodate the system constraints. Moreover, system model mismatch and uncertainties in large-scale networks may lead to unstable controller behavior [40]. Therefore, decentralized data-driven optimal control approaches have the potential applicability in the case of large network-based MGs.

To meet the various MG level control objectives in the distribution network, different data-driven strategies are proposed in the literature utilizing machine learning techniques [103, 158–160]. The strategies adopt deep reinforcement learning and deep neural network techniques to model the distribution system dynamics [103, 158, 159]. These methods require intensive training (learning) and thus are not feasible for decentralized control in several instances. However, it is showcased that the voltage/frequency regulation and power-sharing can be achieved using the online tuned neural network avoiding the training phase [160]. The feasibility of such architecture is poor as it cannot work in an unbalanced distribution grid wherein dedicated positive and negative sequence (PNS) IBR controllers are required to maintain the network voltage balance. Moreover, the methodology requires interaction among DERs, thus posing design challenges for large-scale DER integration.

Another body of work offers a data-driven solution based on the identification of the underlying system dynamics by learning the relationship between the system states and control inputs [40–42, 161]. For example, in [40], linear time-varying dynamics are learned and optimal power injection from the DERs to minimize generation cost is achieved through the design of an estimator and controller. However, a major drawback of the design is the performance degradation of the estimation process during significant load variability. The authors

in [41] utilize a measurement-based partial form dynamic linearization technique to develop an adaptive dual-droop primary control scheme. However, the cooperative secondary control for voltage and frequency regulation has a dependency on the communication network. In [42], the radial distribution network parameters are learned based on the limited measurement data to achieve voltage regulation. The work does not consider the DER dynamics and is not suitable for DER-based meshed MGs. Moreover, both works [41, 42] need further research investigation to make them feasible for unbalanced distribution networks. The  $H_2$  optimization method is proposed in [161], which combines primary and secondary controllers in an MG without performing system identification. The method however fails to account for the nonlinearities in the network dynamics at different operating points.

In the aforementioned works, the data-driven optimal control methods do not formulate the predictive model and the system constraints. This would deteriorate the controller's performance during electric faults and communication delays. A distributed model predictive control (MPC) approach proposed in Ref. [149] does not depend on droop and network parameters. However, the method has a communication dependency on neighboring control subsystems that may lead to scalability issues. Furthermore, the formulation does not make use of the constraint capability of the MPC method. Recent work on robust MPC to perform reference tracking subject to state/input constraints and uncertainties is proposed in [162]. The control scheme utilizes a centralized approach thus infeasible for large-scale DER-integrated distribution networks. In another recent work, a time-varying reference tracking control with system constraints and unknown additive disturbances is proposed [163]. The method uses a robust feedback law with certain degrees of conservativeness, leading to the compromised optimal solution. Such methods may not be suitable for decentralized applications as the aggregated effect of the compromised optimality at every subsystem can be a threat to the overall system behavior.

## 5.2 Research Contributions

In summary, the primary limitation of the existing data-driven optimal control methods are the need to have interactions among the subsystems, performance degradation due to nonlinear network dynamics, and their inability to utilize the MPC constraints effectively. With this motivation, a novel decentralized system identification-based integral MPC (IIMPC) technique to achieve the secondary control objectives of the islanded MG is proposed in this chapter. The main contributions of the proposed framework in comparison to the previous implementations in the literature are:

- The control framework harnesses an identified low order high fidelity grid characterization model and estimator to meet the MG level control objective. The decentralized controller offers a computationally less expensive solution hence feasible for deployment

in grid-edge devices.

- IIMPC input constraints are formulated to assist the primary controller in achieving ride-through thereby assuring the IBR ride-through capability during electric faults.
- The framework is a communication-free solution for frequency regulation and a global measurement-based solution for voltage regulation. Since the decentralized control subsystems do not exchange data, design scalability is achieved.
- The proposed optimal control ensures stable active and reactive power sharing among the IBRs. The augmented model incorporates an integral effect on outputs and the predictive control mechanism speeds up the regulation of MG frequency and voltage.
- The architecture is inherently adaptive to the changing system conditions and foolproof against generation loss, communication latency, and electric faults as verified by the real-time (RT) model-in-the-loop (MIL) simulation.

*Notation:*  $\mathbb{R}$  and  $\mathbb{R}^r$  stands for the real space and  $r$  dimensional Euclidean space, respectively. A diagonal matrix is represented as  $diag(x_1, \dots, x_n)$ , where  $x_1, \dots, x_n$  are the diagonal entries. The representation  $\sum_{i=0}^{M-1} y_{k+i}^T Q_i y_{k+i}$  is written in compact form as  $y_{k|M}^T Q y_{k|M}$  where  $y_k \in \mathbb{R}^r$ ,  $Q \in \mathbb{R}^{Mr \times Mr}$  and  $Q := diag(Q_i) \quad \forall i = 0, 1, \dots, M$ . The vector  $\mathbf{y}$  of length  $M$  at  $k^{th}$  instance is represented as:  $\mathbf{y}_{k|M} = [y_{k|k}, y_{k+1|k}, \dots, y_{k+M-1|k}]$ .

### 5.3 System Overview

In this section, details of the power distribution network, and primary controller followed by a secondary controller associated with DERs are provided.

#### 5.3.1 Distribution Network Characteristics

Fig. 4.1 depicts the high-level architecture of the power distribution system with the DER integration. The DERs are asynchronously coupled to the AC power grid at the point of common coupling (PCC) through power electronic converters and *LCL* filter with a damping resistor ( $R_d$ ), termed as IBRs. Usually, an IBR output AC voltage is less than the network line voltage. Hence, a  $\Delta - Y_g$  transformer interfaces an IBR to the network line. A smart switch (SS) is a controllable breaker that can be tripped or closed to isolate or reconnect a part of the network to a substation node or to another MG at a point of interconnection (POI).

To design the primary controllers of IBRs, network characteristics play a critical role [28]. Major characteristics of the distribution network are, a) they have low  $X/R$  compared to the bulk power grid, b) due to many single-phase and two-phase laterals, the network is unbalanced [50]. There are two types of IBRs designed by considering the aforementioned network characteristics, viz., grid-forming IBRs to supply negative sequence currents to

balance the network voltage and grid-following IBRs to track voltage angle at PCC thereby delivering or sharing power along with other IBRs. The control strategy for such IBRs must enable efficient operation in the presence and absence of the substation node, basically forming an MG [81]. Details of the control architecture including primary and secondary loop design are discussed next.

### 5.3.2 Description of Primary Controller

Typically, the primary controller has inner current and voltage control loops followed by a power control loop. Sophisticated positive and negative sequence-based current and voltage loops are designed for the IBRs with different objectives. For a grid-forming IBR, these control loops enable the supply of negative sequence currents to maintain the network voltage balance. For the grid-following inverters, these control loops suppress the supply of negative sequence currents [136]. Both IBRs have a current limiter to facilitate the ride-through capability in case of faults [81].

The power control loop incorporates a low pass filter (LPF), and a robust droop law [29] with overall closed-loop dynamics slower than the inner current and voltage loops. The droop correlation for a low  $X/R$  network is of the form  $P - v$ ,  $Q - \omega$  [28] as given in (5.1):

$$v_i = v^* - n_i(P_i - P_i^*) + K_i^e(v^* - v_i) \quad (5.1a)$$

$$\omega_i = \omega^* + m_i(Q_i - Q_i^*) \quad (5.1b)$$

where  $v^*, \omega^*, P_i^*, Q_i^*$  are voltage, frequency, active power, and reactive power set-points respectively,  $n_i, m_i, K_i^e$  are the droop coefficients, and LPFed active ( $P_i$ ) and reactive power ( $Q_i$ ) at PCC is given by:

$$\dot{P}_i = \omega_i^c(p_i - P_i) \quad (5.2a)$$

$$\dot{Q}_i = \omega_i^c(q_i - Q_i) \quad (5.2b)$$

where  $\omega_i^c$  is the corner frequency of LPF,  $p_i$  and  $q_i$  are the measured active and reactive power shared by  $i^{th}$  IBR. Since the power control loop dominates the overall dynamics of the IBR, it can be used to represent the reduced-order IBR model for the design of the secondary controller [12].

### 5.3.3 Description of Secondary Controller

From (5.1), it is evident that the change in the power-sharing leads to a deviation of voltage and frequency from the nominal values. To design an MPC controller that can mitigate steady-state voltage and frequency errors, a high-fidelity model capturing the IBR dynamics is necessary. By substituting (5.1) in (5.2), for LPFed active and reactive power, droop

parameter and LPF parameter-based first order voltage and frequency dynamics equations are obtained [12, 149].

Since it is assumed that the IBR parameters are unavailable, a data-driven representation for the voltage and frequency dynamics at  $PCC_i$  can be represented as:

$$\dot{v}_i^\epsilon = a_i^v v_i^\epsilon + b_i^v p_i \quad (5.3a)$$

$$\dot{\omega}_i^\epsilon = a_i^\omega \omega_i^\epsilon - b_i^\omega q_i \quad (5.3b)$$

where  $v_i^\epsilon \cong v_i^* - v_i$  and  $\omega_i^\epsilon \cong \omega_i^* - \omega_i$  are the measured PCC voltage and frequency steady-state errors respectively due to the droop laws of the primary controller;  $a_i^v, a_i^\omega, b_i^v, b_i^\omega$ , are the time-varying parameters to be identified. Voltage and frequency measurements are used to estimate model parameters, and states accurately, before utilizing them in the IIMPC controller. IIMPC controller computes new active ( $P_i^{sc}$ ) and reactive ( $Q_i^{sc}$ ) power references for the primary controller (applied to (5.1),  $P_i^* := P_i^{sc}, Q_i^* := Q_i^{sc}$ ) such that voltage and frequency are maintained at the respective nominal values ( $v^*, \omega^*$ ), at the POI in the network.

#### 5.4 Mathematical Preliminaries and Problem Formulation

In this section, the decentralization approach for the large-scale islanded MG is discussed. The approach will provide a platform to devise a data-driven IIMPC methodology discussed in Section 5.5.

##### 5.4.1 Large Signal Dynamic Model of an Islanded MG

While (5.3) provides the IBR dynamics, the power delivered by the IBRs at the system level is governed by the network flow represented in terms of power flow equation (5.4a) and (5.4b).

$$p_i = v_i^2 G_{ii} - \sum_{j=1, j \neq i}^N v_i v_j |Y_{ij}| \cos(\delta_i - \delta_j - \theta_{ij}) \quad (5.4a)$$

$$q_i = -v_i^2 B_{ii} - \sum_{j=1, j \neq i}^N v_i v_j |Y_{ij}| \sin(\delta_i - \delta_j - \theta_{ij}) \quad (5.4b)$$

where  $|Y_{ij}| = \sqrt{G_{ij}^2 + B_{ij}^2}$ , admittance angle  $\theta_{ij} = \arctan(B_{ij}/G_{ij})$ . For distribution networks with low  $X/R$  ratio, closed-loop dynamics from (5.3) and (5.4) is obtained as:

$$\dot{v}_i = b_i^v G_{ii} v_i^2 + a_i^v v_i - b_i^v \sum_{j=1, j \neq i}^N v_i v_j |Y_{ij}| \cos(\delta_i - \delta_j - \theta_{ij}) \quad (5.5a)$$

$$\dot{\omega}_i = b_i^\omega B_{ii} v_i^2 + a_i^\omega \omega_i + b_i^\omega \sum_{j=1, j \neq i}^N v_i v_j |Y_{ij}| \sin(\delta_i - \delta_j - \theta_{ij}) \quad (5.5b)$$

The model in (5.5) is the nonlinear representation of voltage and frequency dynamics at the respective  $PCC_i$  that depends on DER and network parameters. Thus generic nonlinear dynamics at a given  $PCC_i$  is represented as:

$$\dot{x}_i(t) = f(x_i(t), x_j(t), u_i(t), \xi_i(t)) \quad (5.6)$$

where  $x_i(t) := [v_i, \omega_i]_{i \in \mathcal{N}}^T$ ,  $x_j(t) := [v_j]_{j \in \mathcal{N}}^T$  are the fully observable states of the MG available at  $PCC_i$ ,  $u_i(t) := [p_i, q_i]_{i \in \mathcal{N}}^T$  are the control inputs, and  $\xi_i(t) \in [\mathbb{R}_i]_{i \in \mathcal{N}}$  are the exogenous system disturbances observed at  $PCC_i$ , due to load changes, IBR losses, electric line faults or such similar events.

#### 5.4.2 Synchronization of Local and Global States

A decentralized controller is formulated through a system characteristic identification, based on the local measurements and correcting the necessary states as per the global measurements. A generic nonlinear model for predicting the  $PCC_i$  state deviation from the nominal values ( $\hat{x}_i(t) := [\hat{v}_i^\epsilon, \hat{\omega}_i^\epsilon]_{i \in \mathcal{N}}^T$ ) given the power delivered ( $u_i(t) := [p_i, q_i]_{i \in \mathcal{N}}^T$ ) by the DERs can be represented as a decentralized function:

$$\dot{\hat{x}}_i(t) = \hat{f}(\hat{x}_i(t), u_i(t)) \quad \forall i \in \mathcal{N} \quad (5.7)$$

The model (5.7) is obtained as a result of the least-square estimation applied on the known input ( $u_i(t)$ ) and the observed output samples ( $y_i(t)$ ). This leads to the identification of time-varying model parameters  $\hat{\theta}_i(t) := [A_i(t) B_i(t)]^T$ .

Let there be a global unique point such as POI in the MG at which voltage ( $v_g^\epsilon$ ) and frequency ( $\omega_g^\epsilon$ ) need to be regulated to the nominal values. In the case of frequency, observations at various PCCs synchronize to the same value since the network impedance between PCCs does not influence the frequency. Therefore, for a global state such as frequency, the model defined in (5.7) offers a high-fidelity prediction.

*Definition 1: For a local observation of the global state deviation such as frequency ( $\omega_i^\epsilon$ ), the steady state error between the predicted deviation with the identified model ( $\hat{\theta}_i$ ) and the observed state deviation at the POI ( $\omega_g^\epsilon$ ) is verified by:*

$$\lim_{t \rightarrow \infty} |\omega_g^\epsilon(t) - \hat{\omega}_i^\epsilon(t)| = 0 \implies \hat{\omega}_i^\epsilon(t) \simeq \omega_g^\epsilon(t)$$

In the case of voltage, observations at various PCCs do not synchronize to the same value since the network impedance between PCCs does influence the voltage. Therefore, for a local state such as voltage, the model defined in (5.7) offers a low-fidelity prediction.

*Definition 2: For a global observation of a local state deviation such as voltage ( $v_i^\epsilon$ ), the*

steady-state error in the predicted voltage deviation with the identified model ( $\hat{\theta}_i$ ) and the observed state deviation at the POI ( $v_g^\epsilon$ ) is verified by:

$$\lim_{t \rightarrow \infty} |v_g^\epsilon(t) - \hat{v}_i^\epsilon(t)| \leq \epsilon_i(t) \implies \hat{v}_i^\epsilon(t) \neq v_g^\epsilon(t)$$

Thus, further correction to the local state prediction is required based on the observation of the voltage at the POI. The Kalman filter estimation is extended to achieve the required correction (5.8). The design framework is discussed in Section 5.5.2.

$$\dot{\hat{x}}_i(t) = \hat{f}(\hat{x}_i(t), y_g^\epsilon(t), u_i(t)) \quad \forall i \in \mathcal{N} \quad (5.8)$$

Both model (5.6) and (5.7) have  $O(n)$  computation complexity. The model (5.7) requires no communication and the model (5.8) requires sparse communication (local node interacts only with the global node - POI), in comparison to the model (5.6) that requires dense communication infrastructure with  $O(Nn)$  complexity.

#### 5.4.3 Formulation of Data-driven Decentralized System Dynamics

A set of  $N$  IBR-based DERs are interfaced to an unbalanced, low  $X/R$  distribution network at spatially different nodes termed as PCCs. The decentralized system dynamics that has to be identified can be defined as a set of subsystems at PCCs  $\hat{\mathcal{S}} := [\hat{\mathcal{S}}_1, \hat{\mathcal{S}}_2, \dots, \hat{\mathcal{S}}_i, \dots, \hat{\mathcal{S}}_N] \forall i \in \mathcal{N}$ . Furthermore, the unique global measurement point at POI is represented as  $\mathcal{S}_g$ , at which voltage and frequency have to be regulated to nominal values. With the assumption of availability of measured POI states ( $\mathcal{S}_g$ ) at each of the decentralized system  $\hat{\mathcal{S}}_i$  all the estimated states of  $\hat{\mathcal{S}}_i$  can be synchronized using extended Kalman filter (EKF). Autoregressive with exogenous input (ARX) model incorporating EKF for the identified discrete-time decentralized system dynamics is represented as  $\hat{\mathcal{S}}_i = f(\hat{x}_k^\epsilon, u_k, y_k^\epsilon, y_k^{g\epsilon})$  and its state-space model as in (5.9) ( $i$  is omitted on the right-hand side for simplified representation).

$$\hat{\mathcal{S}}_i = \begin{cases} \hat{x}_{k+1}^\epsilon = \hat{A}_k \hat{x}_k^\epsilon + \hat{B}_k u_k + \hat{K}_k e_k \\ y_k^{g\epsilon} = C_k \hat{x}_k^\epsilon + e_k \end{cases} \quad (5.9)$$

where  $k$  is the discrete-time sample,  $\hat{x}_k^\epsilon \in \hat{\mathcal{X}}_i := [\hat{v}_k^\epsilon \ \hat{\omega}_k^\epsilon]^T \subseteq \mathbb{R}$ ,  $u_k \in \mathcal{U}_i := [p_k \ q_k]^T \subseteq \mathbb{R}$ ,  $y_k^\epsilon := C_k \hat{x}_k^\epsilon = [v_k^\epsilon \ \omega_k^\epsilon]^T \subseteq \mathbb{R}$ ,  $y_k^{g\epsilon} \in \mathcal{Y}_i := [v_k^{g\epsilon} \ \omega_k^{g\epsilon}]^T \subseteq \mathbb{R}$ ,  $\hat{A}_k := \text{diag}(\hat{a}_k^v, \hat{a}_k^f)$ ,  $\hat{B}_k := \text{diag}(\hat{b}_k^v, \hat{b}_k^f)$ ,  $C_k := \text{diag}(c_k^v, c_k^f)$ ,  $e_k = y_k^{g\epsilon} - y_k^\epsilon$  and  $\hat{K}_k$  is the estimated Kalman gain matrix. The  $\hat{\mathcal{S}}_i$  representation in (5.9) compensates for any steady-state error arising from the network disturbance and estimated model mismatch.

### 5.5 Decentralized IIMPC Framework

Fig. 5.1 depicts the scheme of the proposed data-driven controller. In this formulation,

controller subsystems ( $\mathcal{S}_1 \dots \mathcal{S}_i \dots \mathcal{S}_N$ ) independently generate control signals ( $u_i^{sc}$ ) without requiring communication between subsystems. The observed voltage at POI ( $\mathcal{S}_g$ ) is communicated to the respective subsystems ( $\mathcal{S}_i$ ) at PCCs. The global measurement is  $y_g^\epsilon$  represented as the function of latency and a common latency value is assumed ( $d_1 = d_i = d_N = d_0$ ). In this section details of the proposed framework are discussed (to reduce the notational burden, subscript  $i$  as a DER number is omitted).

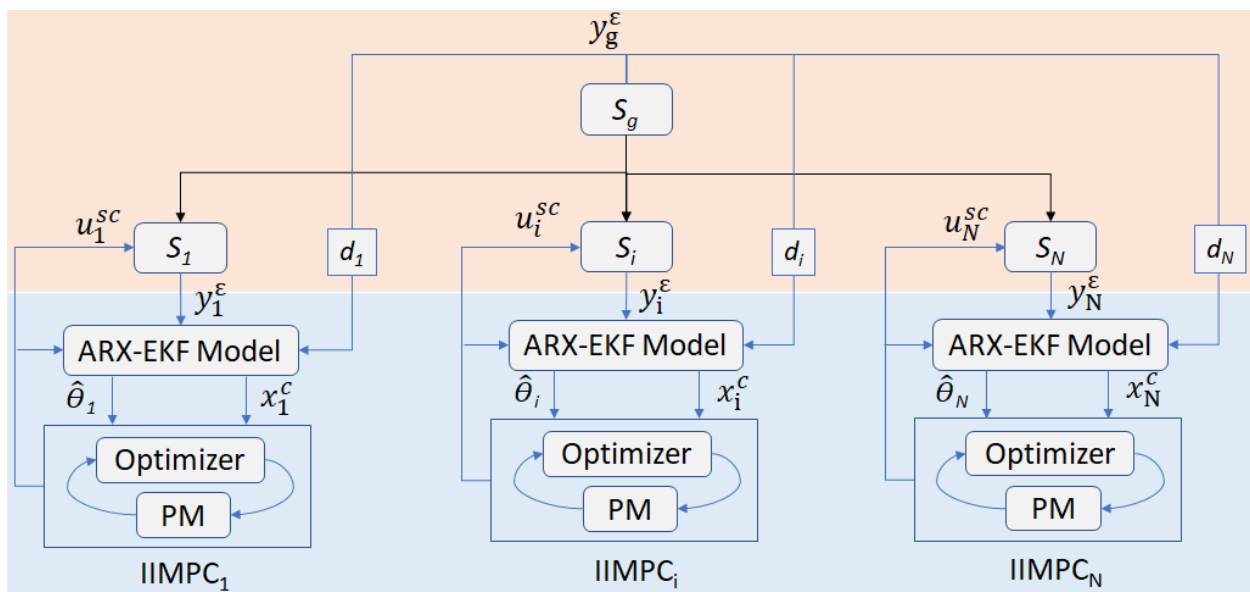


Figure 5.1: Proposed data-driven hierarchical decentralized IIMPC framework suitable for frequency and voltage regulation.

### 5.5.1 Online Identification of the Subsystem Dynamics

Let the  $(p_k, q_k) \in u_k$  are the inputs and  $(v_k^\epsilon, v_k^{g\epsilon}, \omega_k^\epsilon) \in y_k$  are the outputs of the system to be identified. As the IBR droop control is typically designed with low bandwidth, the measured outputs and inputs are passed through LPF with corner frequency  $\omega_c$ , as represented in (5.10),

$$\bar{y}_k = \alpha \bar{y}_{k-1} + (1 - \alpha) y_k, \quad \bar{u}_k = \alpha \bar{u}_{k-1} + (1 - \alpha) u_k \quad (5.10)$$

where  $\alpha = e^{(-\omega_c T_s^{sc})}$ , with  $T_s^{sc}$  as sampling rate, filtered output and inputs are given by  $(\bar{v}_k^\epsilon, \bar{v}_k^{g\epsilon}, \bar{\omega}_k^\epsilon) \in \bar{y}_k$ , and  $(\bar{p}_k, \bar{q}_k) \in \bar{u}_k$  respectively.

To obtain the IBR-grid interaction model of (5.3), the decoupled characteristics between  $\bar{v}_k^\epsilon$  and  $\bar{p}_k$ , and  $\bar{\omega}_k^\epsilon$  and  $\bar{q}_k$  are independently identified online based on the recursive least square (RLS) estimation given by (5.11),

$$\min V(\hat{\theta}_k) = \sum_{i=1}^k \lambda^{k-i} (\bar{y}_k - \phi_k^T \hat{\theta}_k) + \gamma \Delta \bar{y}_k \quad (5.11)$$

where  $\gamma := \{0, 1\}$  is the parameter that defines the nature of the state, (1 for global state and 0 for local state),  $\Delta \bar{y}_k = (\bar{y}_k^{g\epsilon} - \bar{y}_k)$  is the observed error between the global and local state,  $\phi$  holds the observed data based on the order of identification, and the  $\lambda \in (0, 1]$  is the forgetting factor.

The RLS scheme with exponential forgetting estimates the parameters ( $\hat{\theta}_k$ ) based on the observations ( $\bar{y}_k$ ) recursively using the update rule (5.12) by computing  $K_k$  and  $P_k$  at every time-step given in (5.13).

$$\hat{\theta}_k = \hat{\theta}_{k-1} + K_k(\bar{y}_k + \gamma\Delta\bar{y}_k - \phi_k^T\hat{\theta}_k) \quad (5.12)$$

$$K_k = \frac{P_{k-1}\phi_k}{\lambda + \phi_{k-1}^T P_{k-1} \phi_{k-1}}, \quad P_k = \frac{1}{\lambda}(1 - K_k\phi_k^T)P_{k-1} \quad (5.13)$$

The first order estimated parameters ( $[a_k, b_k] \in \hat{\theta}_k$ ) are used to represent the discrete-time linear time variant (LTV) system as given by the ARX model (5.14),

$$\hat{x}_{k+1} = a_k\hat{x}_k + b_k\bar{u}_k + w_k \quad (5.14)$$

where the predicted states are ( $[\hat{v}_k^\epsilon, \hat{\omega}_k^\epsilon] \in \hat{x}_k$ ), the inputs as ( $[\bar{p}_k, \bar{q}_k] \in \bar{u}_k$ ), and  $w_k$  is the unknown measurement noise.

### 5.5.2 Augmented Model Incorporating the Integral Action

The first order model of (5.14) is converted into an augmented incremental state space model that is insensitive to disturbances and noise as described by (5.15),

$$\begin{aligned} \underbrace{\begin{bmatrix} \Delta\hat{x}_{k+1}^\epsilon \\ \bar{y}_k^\epsilon \\ \bar{u}_k \end{bmatrix}}_{\tilde{x}_{k+1}} &= \underbrace{\begin{bmatrix} a_k & \Delta a_k & \Delta b_k \\ c & 1 & 0 \\ 0 & 0 & 1 \end{bmatrix}}_{\tilde{A}_k} \underbrace{\begin{bmatrix} \Delta\hat{x}_k^\epsilon \\ \bar{y}_{k-1}^\epsilon \\ \bar{u}_{k-1} \end{bmatrix}}_{\tilde{x}_k} + \underbrace{\begin{bmatrix} b_k \\ 0 \\ 1 \end{bmatrix}}_{\tilde{B}_k} \underbrace{\begin{bmatrix} \bar{u}_k \\ \Delta\bar{u}_k \end{bmatrix}}_{\tilde{u}_k} \\ & \underbrace{\begin{bmatrix} \bar{y}_k^\epsilon \end{bmatrix}}_{\tilde{y}_k} = \underbrace{\begin{bmatrix} c & 1 & 0 \end{bmatrix}}_{\tilde{C}} \underbrace{\begin{bmatrix} \Delta\hat{x}_k^\epsilon \\ \bar{y}_{k-1}^\epsilon \\ \bar{u}_{k-1} \end{bmatrix}}_{\tilde{x}_k} \end{aligned} \quad (5.15)$$

where  $\tilde{A}_k \in \mathbb{R}^{m \times m}$  is the system matrix,  $\tilde{B}_k \in \mathbb{R}^{m \times n}$  is the control input matrix,  $\tilde{C} \in \mathbb{R}^{r \times m}$  is the output measurement matrix.

The model states, inputs, and outputs are identified as follows. In the case of voltage regulation problem:  $\tilde{x}_k := \begin{bmatrix} \Delta\hat{v}_k^\epsilon & \bar{v}_{k-1}^\epsilon & \bar{p}_{k-1} \end{bmatrix}^T$ ,  $\tilde{u}_k := \Delta\bar{p}_k$ ,  $\tilde{y}_k := \bar{v}_k^\epsilon$ , and for the frequency regulation problem:  $\tilde{x}_k := \begin{bmatrix} \Delta\hat{\omega}_k^\epsilon & \bar{\omega}_{k-1}^\epsilon & \bar{q}_{k-1} \end{bmatrix}^T$ ,  $\tilde{u}_k := \Delta\bar{q}_k$ ,  $\tilde{y}_k := \bar{\omega}_k^\epsilon$ . The incremental state-space model of (5.15) is obtained from (5.14) as per the principles of the LTV system, where for all time-varying signals ( $\hat{x}_k^\epsilon, \bar{y}_k^\epsilon, \bar{u}_k, a_k, b_k$ )  $\in s$  are represented in the form:  $s_k = s_{k-1} + \Delta s_k$ .

*Remark:* Droop laws lead to the deviation of voltage and frequency, and the integral action on voltage and frequency errors is necessary to regulate them to nominal values [75]. The augmented incremental model in (5.15) derived from LTV first-order model (5.14) inherits

the integral action on the model output.

*Proof:* For the measured state deviation signal ( $\bar{y}^\epsilon$ ), at the sample  $k$ , the integral action is given by:

$$\bar{y}_k^\epsilon = T_s^{sc} \bar{y}_k^\epsilon + \bar{y}_{k-1}^\epsilon \implies T_s^{sc} \bar{y}_k^\epsilon = \bar{y}_k^\epsilon - \bar{y}_{k-1}^\epsilon = \Delta \bar{y}_k^\epsilon = c \Delta x_k^\epsilon \quad (5.16)$$

Thus the representation of integral action is given by:  $\bar{y}_k^\epsilon = c \Delta x_k^\epsilon + \bar{y}_{k-1}^\epsilon$ . However, the resultant representation of (5.15) is:  $\bar{y}_k^\epsilon = c \Delta \hat{x}_k^\epsilon + \bar{y}_{k-1}^\epsilon$ . Therefore, to incorporate the valid output integral action in the incremental model, the necessary condition is: ( $\hat{x}^\epsilon \simeq \bar{x}^\epsilon$ ). Since the respective frequency and voltage, measurements are available to all the subsystems at PCCs,  $c = 1$  is considered in this proof.  $\square$

As per *Definition 2*, further correction to the local state prediction is required based on the global observation of the voltage ( $\bar{y}_k^{g\epsilon}$ ) at the POI. The Kalman estimation technique is extended to correct the predicted state deviation by calculating appropriate Kalman gain ( $\tilde{K}$ ). Kalman gains dictate how much the model predicted state values need to be corrected for as per the given observation represented in (5.15),

$$\tilde{x}_k^c = \tilde{x}_k + \gamma \tilde{K}_k (\bar{y}_k^{g\epsilon} - \tilde{C} \tilde{x}_k) \quad (5.17)$$

where  $\tilde{K}_k \in \mathbb{R}^{m \times 1}$  is the Kalman filter gain matrix computed as  $\tilde{K}_k = \frac{\tilde{P}_k \tilde{C}^T}{\tilde{C} \tilde{P}_k \tilde{C}^T + \tilde{R}}$ , and the extrapolation of the error co-variance matrix  $\tilde{P}_k = \tilde{A} \tilde{P}_{k-1} \tilde{A}^T + \tilde{Q}$ . If  $\tilde{x}_k$  are global states, then  $\gamma = 0$ , and no further correction is necessary. The corrected state estimation ( $\tilde{x}_k^c$ ) is further used in the prediction and optimization module.

### 5.5.3 Formulation of Optimal Control with the Constraints

Utilizing the estimated states from (5.15) and (5.17), the prediction model (PM) [88] for the finite prediction horizon of next  $M$  time steps is given by:

$$\tilde{\mathbf{y}}_{k+1|M} = p_M + F_u \tilde{\mathbf{u}}_{k|M_u}, \quad (5.18)$$

where  $p_M = O_M \tilde{A}_k \tilde{x}_k^c$ ,  $F_M = [O_M \tilde{B}_k \quad T_M]$ , and  $F_u$  is defined from all rows in  $F_M$  and the first  $nM_u$  columns ( $F_u \in \mathbb{R}^{rM \times M_u n}$ ). The extended observability matrix ( $O_M$ ) is computed based on  $\tilde{A}_k$ , and  $\tilde{C}$  and  $T_M \in \mathbb{R}^{rM \times (M-1)m}$  is the standard Toeplitz matrix.

The decentralized control problem  $\tilde{\mathcal{P}}_i$  formulated with a value function  $\tilde{J}_k(\tilde{\mathbf{y}}_{k+1|M}, \tilde{\mathbf{u}}_{k|M_u})$  associated with the  $i^{th}$  subsystem  $\tilde{\mathcal{S}}_i$  is given by:

$$\tilde{\mathcal{P}}_i := \min_{\tilde{\mathbf{u}}} \tilde{J}_k = \tilde{y}_{k+1|M}^T Q \tilde{y}_{k+1|M} + \tilde{u}_{k|M_u}^T R_u \tilde{u}_{k|M_u} \quad (5.19)$$

where  $M_u$  is a control horizon such that  $1 \leq M_u \leq M$ ,  $Q \in \mathbb{R}^{rM \times Mr}$  and  $R_u \in \mathbb{R}^{nM_u \times M_u n}$  are the positive definite symmetric weighting matrices,  $\tilde{y}_{k|M}$  and  $\tilde{u}_{k|M_u}$  are the PM (5.18) outputs and inputs respectively. Since  $\tilde{\mathcal{P}}_i$  is a regulation problem, reference values are zero in the value function. The solution of  $\tilde{\mathcal{P}}_i$  generates reference signals to the respective primary controller such that steady-state voltage and frequency errors are eliminated.

During extreme events such as faults in the system, output variables  $\bar{y}_k$  may experience sag or swell. This may lead the IIMPC controller to generate an unrealistic power reference signal to the primary controller leading to unstable operation. Therefore it is necessary to design the control variable constraints with the range of  $[u_{min}, u_{max}]$ , such that the IIMPC controller generates the bounded power reference. This is achieved by designing appropriate inequality constraints for the control variable by specifying the rate of change of the control variable as in (5.20a) and the control variable magnitude constraint as in (5.20b).

$$\tilde{u}_{min} \leq \Delta \tilde{\mathbf{u}}_{k|M_u} \leq \tilde{u}_{max} \quad (5.20a)$$

$$u_{min} \leq \tilde{\mathbf{u}}_{k|M_u} \leq u_{max} \quad (5.20b)$$

The inequality constraints in (5.20) must be reduced to a form to include only the optimization control variable ( $\tilde{u}_k$ ), hence the representation is reduced as in (5.21) [88].

$$\tilde{\mathbf{u}}_{k|M_u} = S_u \Delta \tilde{\mathbf{u}}_{k|M_u} + c_u \tilde{u}_{k-1} \quad (5.21)$$

where  $S_u \in \mathbb{R}^{M_u n \times M_u n}$ ,  $c_u \in \mathbb{R}^{M_u n \times n}$

$$S_u \triangleq \begin{bmatrix} I_n & 0_n & \cdots & 0_n \\ I_n & I_n & \cdots & 0_n \\ \vdots & \vdots & \ddots & \vdots \\ I_n & I_n & \cdots & I_n \end{bmatrix}, \quad c_u \triangleq \begin{bmatrix} I_n \\ I_n \\ \vdots \\ I_n \end{bmatrix}$$

$I_n$  is the  $n \times n$  identity matrix and  $0_n$  is the  $n \times n$  zero matrix. The performance index (5.19) along with the constraints (5.21) is applied on the PM (5.18) resulting in a quadratic function of the standard form:

$$\min_{\tilde{\mathbf{u}}} \tilde{J}_k = (\tilde{u}_{k|M_u})^T H_k (\tilde{u}_{k|M_u}) + 2(f_k)^T (\tilde{u}_{k|M_u}) \quad (5.22a)$$

$$\text{s.t. } \tilde{x}_{k+1} = \tilde{A}_k \tilde{x}_k + \tilde{B}_k \tilde{u}_k \quad \forall k = 1, 2, \dots, M-1 \quad (5.22b)$$

$$\tilde{x}_k^c = \tilde{x}_k + \gamma \tilde{K} (\bar{y}_k^{ge} - \tilde{C} \tilde{x}_k) \quad \forall k = 1, 2, \dots, M-1 \quad (5.22c)$$

$$\tilde{\mathbf{y}}_{k+1|M} = p_M + F_u \tilde{\mathbf{u}}_{k|M_u} \quad \forall k = 1, 2, \dots, M-1 \quad (5.22d)$$

$$\mathcal{A} \tilde{\mathbf{u}}_{k|M_u} \leq b_k \quad \forall k = 1, 2, \dots, M_u - 1 \quad (5.22e)$$

---

**Algorithm 2:** Data-driven closed-loop controller using IIMPC scheme executed in each of the subsystem  $\mathcal{S}_i$ .

---

**1 Input:**  $u_k, y_k^\epsilon, y_k^{g\epsilon}, \forall k = 1, 2, \dots, M$ , initial state  $x_0$   
**2 Output:**  $u_k^{sc}, \forall k = 1, 2, \dots, M$   
**3 Initialize:**  $\tilde{x}_k = X_0, \tilde{P}_k = P_0, u_k^{sc} = U_0^{sc}, k = 1$   
**4 for**  $k = 1, 2, \dots$  **do**  
**5**     Calculate the inputs to the model using PCC current and voltage measurements  
 $u_k := (p_k, q_k)$   
**6**     Calculate the outputs of the model using PCC and POI voltage measurements  
 $y_k^\epsilon := (v_k^\epsilon, \omega_k^\epsilon), y_k^{g\epsilon} := (v_k^{g\epsilon}, \omega_k^{g\epsilon})$  respectively  
**7**     Use LPFed model I/Os to estimate the model parameters solving (5.11)  
recursively through (5.12)  
**8**     Compute the augmented model matrices:  $\tilde{A}_k, \tilde{B}_k, \tilde{C}$  using identified model  
parameters of (5.14)  
**9**     Predict the states of the augmented model in the closed loop as:  
 $\tilde{x}_{k+1} = \tilde{A}_k \tilde{x}_k + \tilde{B}_k (\tilde{u}_k + u_k^{sc})$   
**10**    **if**  $\gamma = 1$  **then**  
**11**     | Correct the states of the augmented model through EKF using (5.17)  
**12**    **end**  
**13**     Compute  $p_M$  and  $F_u$  as per the prediction model represented in (5.18)  
**14**     Calculate  $H_k, f_k, \mathcal{A}$  and  $b_k$  according to (5.23)  
**15**     Solve (5.22) to get optimal control solution vector  $\tilde{\mathbf{u}}_{k|M_u}^{sc}$  over the prediction  
horizon  $M$   
**16**     Compute the control update variable using the first sample  $\tilde{u}_{k|k}^{sc}$  of the solution  
vector ( $\tilde{\mathbf{u}}_{k|M_u}^{sc}$ ) as:  $u_k^{sc} = \tilde{u}_{k|k}^{sc} + u_{k-1}^{sc}$   
**17 end**

---

where

$$\begin{aligned}
 H_k &= F_u^T Q F_u + R_u, \quad \forall k = 1, 2, \dots, M_u - 1 \\
 f_k &= F_u^T Q p_M, \quad \forall k = 1, 2, \dots, M_u - 1 \\
 \mathcal{A} &= \begin{bmatrix} I_{(nM_u, nM_u)} & -I_{(nM_u, nM_u)} & S_u & -S_u \end{bmatrix}^T, \\
 b_k &= \begin{bmatrix} \tilde{u}_{max} & -\tilde{u}_{min} & u_{max} - c_u u_{k-1} & -u_{min} + c_u u_{k-1} \end{bmatrix}^T \quad \forall k = 1, 2, \dots, M_u - 1
 \end{aligned} \tag{5.23}$$

The aforementioned objective function (5.22a) is convex since the Hessian matrix  $H_k \in \mathbb{R}^{nM_u \times M_u n}$  is positive-semidefinite. State prediction based on identified system parameters and the inputs is given by the constraint (5.22b). The constraint (5.22c) describes the correction to the local state prediction based on the global measurement. The PM based on the corrected states is provided in (5.22d). The linearized inequality matrix form of (5.22e) limits the ramp rate and power reference amplitude before sending them to the primary controller. The IIMPC controller solves the optimization variable vector  $\tilde{\mathbf{u}}_{k|M_u}$  every time step ( $k$ ), and the first value is used to generate reference signals to the downstream primary controller. The computation of  $P_k^{sc}$  and  $Q_k^{sc}$  is thus carried as  $u_k^{sc} = \tilde{u}_{k|k}^{sc} + u_{k-1}^{sc}$  for the respective voltage and frequency regulation. The complete flow of the control scheme is provided in Algorithm 2.

### 5.5.4 Controller Feasibility and Stability Analysis

The theoretical properties of the proposed IIMPC are analyzed in this section. Initially, the recursive feasibility is established for the IIMPC control scheme followed by guaranteed regulation of the system outputs under Lyapunov criteria. The core question of recursive feasibility is when (5.22a) has a solution at  $k$ , then after a discrete time update  $k := k + 1$ , with different initial state and control variable value, still (5.22a) has the feasible solution? The analytical solution to (5.22a) without considering (5.22e) is:

$$\tilde{u}_{k|k}^{sc} = \Delta \bar{u}_{k|k}^{sc} = -H_k^{-1} f_k = K_k^{mpc} x_k^c \quad \forall k = 1, 2, \dots \quad (5.24)$$

where  $K_k^{mpc} = -H_k^{-1} F_u^T Q O_M \tilde{A}_k$ . Recursive feasibility is validated by proving the feasibility of the constraint (5.22e) for  $k := k + 1$  as per Farkasâ lemma [164].

*Lemma 1:* Let  $\mathcal{A} \in \mathbb{R}$ , and  $b \in \mathbb{R}$  then either there is  $\tilde{u} \in \mathbb{R}$ , such that  $\mathcal{A}\tilde{u} \leq b$  or there is  $y \in \mathbb{R}$  such that  $y \geq 0$ ,  $y^T \mathcal{A} = 0$  and  $y^T b < 0$ .

*Proof:* Given the  $x_k^c$  and  $u_k^{sc}$ , the question of feasibility is given by:

$$\exists u_{k+1}^{sc} \ni \mathcal{A} \tilde{u}_{k+1}^{sc} \leq b \implies \mathcal{A} K_{k+1}^{mpc} x_{k+1}^c \leq b \quad (5.25)$$

By substituting the state equation of (5.9) in (5.25),

$$\exists u_{k+1}^{sc} \ni \mathcal{A} K_{k+1}^{mpc} \hat{B}_k u_k \leq b - \mathcal{A} K_{k+1}^{mpc} (\hat{A}_k \hat{x}_k^\epsilon + \hat{K}_k e_k) \quad (5.26)$$

Let  $F := \mathcal{A} K_{k+1}^{mpc} \hat{B}_k$ , then according to Farkasâ lemma, infeasibility to (5.26) is equivalent to satisfying vector  $y$  with below constraints:

$$y \geq 0, y^T F = 0, y^T (b - \mathcal{A} K_{k+1}^{mpc} (\hat{A}_k \hat{x}_k^\epsilon + \hat{K}_k e_k)) < 0 \quad (5.27)$$

Since  $R_u$  is positive definite,  $F > 0$ , hence  $y = 0$  must be true. So the third constraint of (5.27) is not satisfied. Therefore, (5.22a) is recursively feasible.  $\square$

*Lemma 2:* If the solution to optimization problem (5.19), subject to the constraint (5.25) is feasible at the initial time  $\tilde{u}_{k|k}^{sc}$ , then the predicted control variable  $\tilde{u}_{k+1|k}^{sc}$ , for the closed loop identified system (5.12) with the state correction as per (5.9), is bounded and asymptotically converges to zero.

*Proof:* The assumption for this proof is that the optimization problem (5.19) in *Lemma 1* is recursively feasible. Without the loss of generality, the length of prediction and control horizon is assumed to be the same ( $M$ ). The stability is analyzed by considering the optimal cost of  $\tilde{J}_k$  in (5.19) as a Lyapunov candidate function  $V_k := \tilde{J}_k^{sc}$ . Let the optimal control

sequence at instance  $k$  is:  $\tilde{\mathbf{u}}_k^{sc} = [u_{k|k}^{sc}, u_{k+1|k}^{sc}, \dots, u_{k+M|k}^{sc}]$ , then let candidate control sequence at  $(k+1)^{th}$  instance is:  $\tilde{\mathbf{u}}_{k+1}^{sc} = [u_{k+1|k}^{sc}, u_{k+2|k}^{sc}, \dots, u_{k+M|k}^{sc}, K_{k+M}^{mpc} x_{k+M|k}^c]$ , where  $K_{k+M}^{mpc} x_{k+M|k}^c$  is the state feedback element. Now the Lyapunov candidate function at  $(k+1)^{th}$  instance is the optimal cost of  $\tilde{J}_{k+1}$  represented as  $V_{k+1} := \tilde{J}_{k+1}^{sc}$ . The cost function  $\tilde{J}_{k+1}$  including terminal cost ( $\forall k = M, M+1, \dots, \infty$ ) is given by,

$$\tilde{J}_{k+1} = \tilde{y}_{k+1|\infty}^T Q \tilde{y}_{k+1|\infty} + \tilde{u}_{k+1|\infty}^{scT} R \tilde{u}_{k+1|\infty}^{sc} \quad (5.28)$$

The representation of (5.28) can be arranged as (5.29), by adding and subtracting the initial cost,

$$\tilde{J}_{k+1} = \tilde{y}_{k|\infty}^T Q \tilde{y}_{k|\infty} + \tilde{u}_{k|\infty}^{scT} R \tilde{u}_{k|\infty}^{sc} - \left( \tilde{y}_k^T Q \tilde{y}_k + \tilde{u}_k^{scT} R \tilde{u}_k^{sc} \right) \quad (5.29)$$

$$\tilde{J}_{k+1} = J_k^{sc} - \left( \tilde{y}_k^T Q \tilde{y}_k + \tilde{u}_k^{scT} R \tilde{u}_k^{sc} \right) \implies \tilde{J}_{k+1}^{sc} \leq \tilde{J}_{k+1} \quad (5.30)$$

From (5.30), the Lyapunov inequality of condition for asymptotic stability ( $\Delta V_k \leq 0$ ) is reached. The feasibility of the terminal constraint of the cost function is obvious from the recursive feasibility of *Lemma 1*. This completes the stability proof.  $\square$

#### 5.5.5 Impact of Communication Latency

The global voltage measurement ( $v_g^e \in y_g^e$ ) is a function of communication latency when utilized at each of  $\tilde{\mathcal{S}}_i$ . In the case of decentralized frequency regulation, local PCC frequency measurement is sufficient to achieve POI frequency regulation ( $\omega_i^e \notin y_g^e$ ) as per *Definition 1*, hence communication latency has no impact. In the case of decentralized voltage regulation, a fixed communication delay of  $d_0$  is modeled before utilizing the voltage value at each of  $\tilde{\mathcal{S}}_i$ . The constant latency of  $d_0 = 10$  ms is assumed based on the verified metrics from the literature applicable to IP-based and NDN-based networks [155]. Moreover, since large-scale networks with higher DER penetration may lead to higher latency, the suitability of the proposed framework for higher latency is verified through latency up to 100 ms.

### 5.6 Real-Time (RT) multi-rate Model-in-the-Loop (MIL) Test-Bed and Results

Fig. 4.4 depicts the IEEE 123 node network with four DERs integrated at different nodes. DERs in the network operate in grid-connected mode when SS1 at node 149 is closed. However, when SS1 is tripped (open state), DERs operate in islanded mode. The primary controller of the DERs performs power tracking based on the provided set points in the grid-connected model. The same primary controller ensures load power-sharing among the DERs in the network in islanded mode. The proposed secondary controller is tested in the islanded mode of operation when SS1 is in the open state. Since the IBR corresponding to each DER terminal voltage at PCC ( $V_i$ ) is lower compared to the network line voltage, a  $\Delta$ - $Yg$  transformer is modeled to step up the voltage. The test set-up contains an RT-

LAB<sup>®</sup> real-time multi-core model of the IEEE 123 node network, IBR-LCL filter connected to a transformer at PCCs, primary controller, secondary controller, and software interrupt handler to facilitate the multi-rate execution of different subsystems. The entire model is executed in two separate CPUs of OPAL-RT machine utilizing eMEGASIM platform [165]. The distributed line parameter network model across two CPUs is achieved through the appropriate design of state-space nodal and Artemis stub line blocks from the RTLAB library.

The sample time of the DER integrated network model, primary controller, and secondary controller are 50  $\mu$ s, 100  $\mu$ s, and 1 ms respectively. Such multi-rate modeling facilitates the effective utilization of computational resources while porting the application to the target hardware. The primary controller inputs include the three-phase current and voltage from the respective PCCs. Based on the measured power and reference power, the primary controller generates PWM signals for the IBR switches. Inputs to the secondary controller include the respective voltage magnitude and frequency measurements from PCCs, POI voltage magnitude measurements (with a delay of 10 ms), and voltage/frequency nominal reference values. Voltage magnitudes are computed using true RMS block, and frequency measurements using a positive sequence voltage-based PLL model. The secondary controller implements the proposed IIMPC and generates active and reactive power reference signals for the downstream primary controller. The formulated constrained quadratic optimization problem is solved through *quadprog* function from MATLAB. Prediction horizon  $M$  is chosen such that the controller is internally stable and offers reasonable transient performance for the identified sample time of the secondary controller. For RT implementation, a lower value of control horizon ( $M_u < M$ ) is used to reduce the computational complexity. DER sizing and LCL filter parameters that are provided in Table 4.1 of the previous chapter are valid for the test setup of this chapter too. System and controller parameters are tabulated in Table 5.1.

### 5.6.1 Verification of Primary Controller Response

Without enabling the secondary controller, the frequency and voltage deviations at one of the PCCs (node 25) and at node 149 (POI) is showcased in Fig. 5.2a. The network is operated in islanded mode post 2 s. An active and reactive power load of 100 kW, 50 kVar is removed at 3 s and added back at 4 s. In islanded mode, due to different loading instances, the voltage and frequency deviate from the respective nominal values as seen in Fig. 5.2a. Due to the influence of line impedance, the voltage observed at different nodes such as POI (node 149), and PCC (node 25) are different. However, the observed frequencies are similar. In case of frequency, the model predicted signal and the measured signal match (see *Definition 1*) ( $\hat{\omega}_{25}^\epsilon \cong \hat{\omega}_{149}^\epsilon$ ). In the case of voltage, (see *Definition 2*) ( $\hat{v}_{25}^\epsilon \neq \hat{v}_{149}^\epsilon$ ),

TABLE 5.1: The parameter details of the electric system and the controllers

System Parameters		
Parameters	Symbol	Value
DER DC link voltage	$V_{DC}$	900 VDC
IBR Voltage at PCC	$V_i$	480 V (RMS)
Grid Voltage	$V_{149}$	4.16 kV (RMS)
Grid Frequency	$\omega_{149}$	60 Hz
Primary Controller Parameters (p.u.)		
Voltage droop coefficient	$n$	0.5
Frequency droop coefficient	$m$	2
Robust droop coefficient	$K^V$	1
Voltage controller gains	$(k_p^v, k_i^v)$	(2.8, 205.3)
Current controller gains	$(k_p^c, k_i^c)$	(0.37, 19.3)
PLL gains	$(k_p^{pll}, k_i^{pll})$	(0.19, 6.6)
Secondary Controller Parameters		
LPF corner frequency	$\omega_c$	10 Hz
Forgetting factor	$\lambda$	0.99
Voltage deviation penalty	$Q^{v\epsilon}$	0.05
Frequency deviation penalty	$Q^{\omega\epsilon}$	0.5
Active power deviation penalty	$R^p$	1
Reactive power deviation penalty	$R^q$	1
Prediction horizon	$M$	10
Control horizon	$M_u$	4
Covariance of the process noise	$\tilde{Q}$	1
Covariance of the measurement noise	$\tilde{R}$	0.1

Kalman method-based correction yields in matching the corrected model prediction to the measurements ( $\hat{v}_{25}^c \cong \bar{v}_{149}^c$ ), even during the transients. The estimated model parameters (5.14) and the Kalman gain coefficients that enable accurate voltage estimation are depicted in Fig. 5.2b.

### 5.6.2 Analysis of Voltage and Frequency Regulation

Initially, all four DERs are connected to the grid and inject power as per the set points. At 2 s, islanding is detected due to the opening of SS1, and DERs perform network load sharing. A pre-identified load of 100 kW and 50 kVar is removed and added back at 3 s and 4 s respectively. Fig. 5.3a showcases post-islanding DER powers stabilize after 500 ms with reasonable transients and during load change the power sharing is observed to be stable. Fig. 5.3d depicts the voltage and frequency regulation to the nominal values during the events. after islanding and during load changes. Fig. 5.3d also compares the performance of the proposed controller with the optimal PI controller. The IIMPC controller offers faster settling time (from 600 ms to 300 ms - 50 % improvement) in case of voltage/frequency regulation, and better transient performance during islanding events. Quantitative analysis of the performance comparison for these events is presented in Table 5.2. Fig. 5.3g showcases the per unitized control signals generated by the proposed controller for the primary controllers of the respective DERs. It is worth noting that the IBRs of similar sizes generate

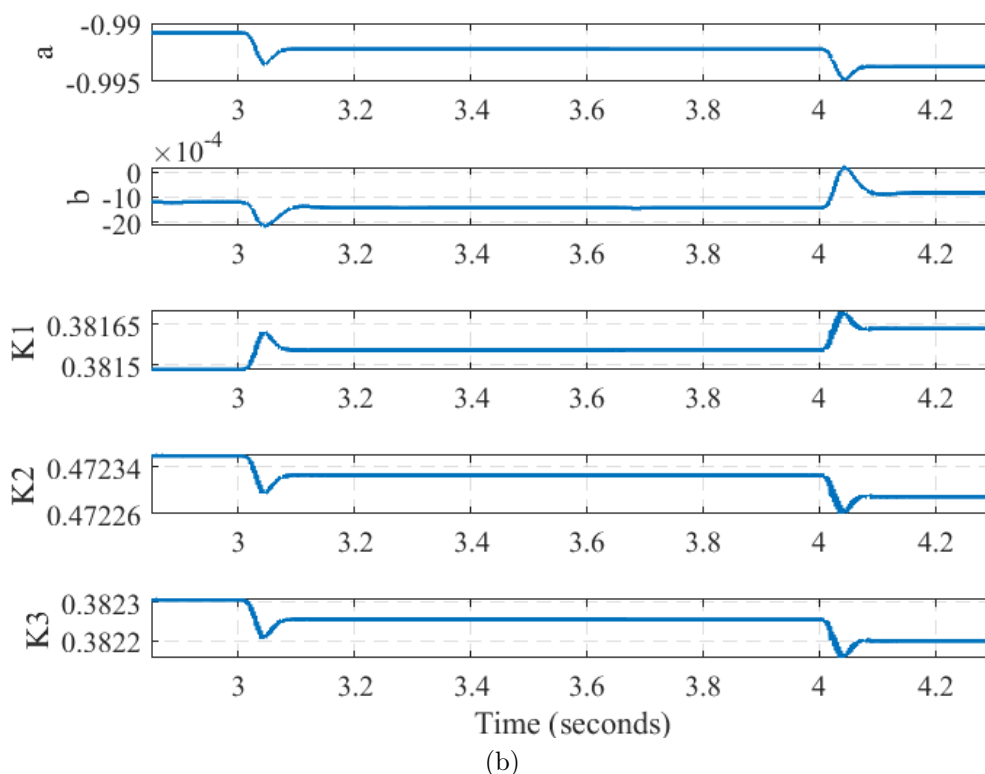
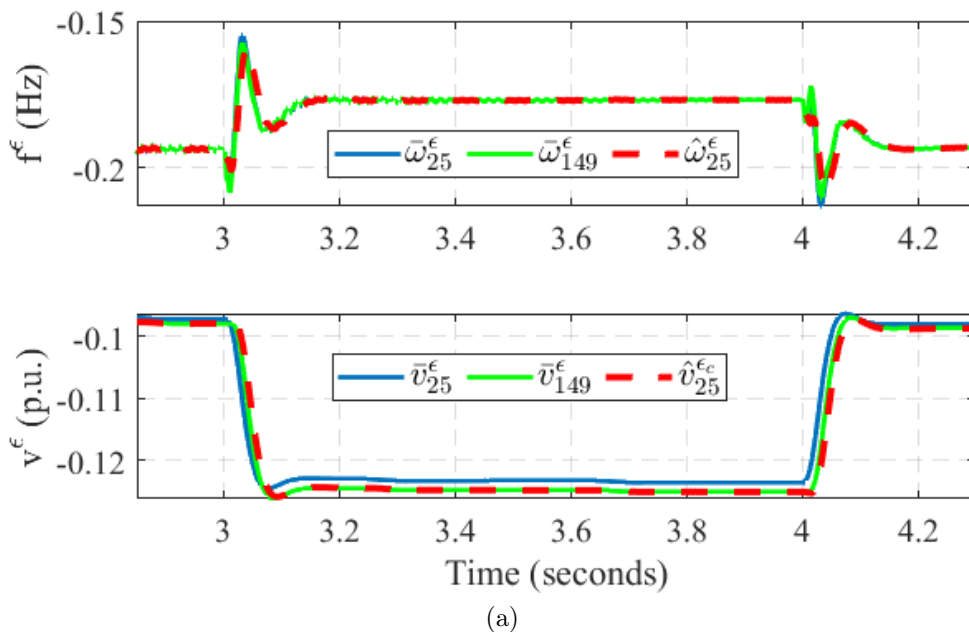


Figure 5.2: Voltage and frequency deviation without the secondary controller, verification of system identification and state correction at remote node 25 for load change in the system. (a) Decentralized frequency and voltage estimation at node 25. (b) Online computed RLS parameters and Kalman gains to estimate node 149 (POI) states at node 25 (PCC).

similar power reference values. The three-phase POI voltage measurements during islanding are shown in Fig. 5.3j, and the transients during 100 ms are within reasonable bounds.

### 5.6.3 Plug-and-Play Capability Performance Analysis

As shown in Fig. 5.3b, DER 4 is disconnected from the MG at 7 s and connected back at 8 s to demonstrate the effectiveness of the proposed framework for generation loss. When the DER 4 power goes to zero, the remaining DER power-sharing increases, and when DER 4 is back it resumes sharing its part of the load. The rest of the DERs reduce their power-sharing when DER 4 is connected back. Fig. 5.3e depicts the voltage and frequency restoration during a plug-and-play scenario with DER4. The performance of the IIMPC

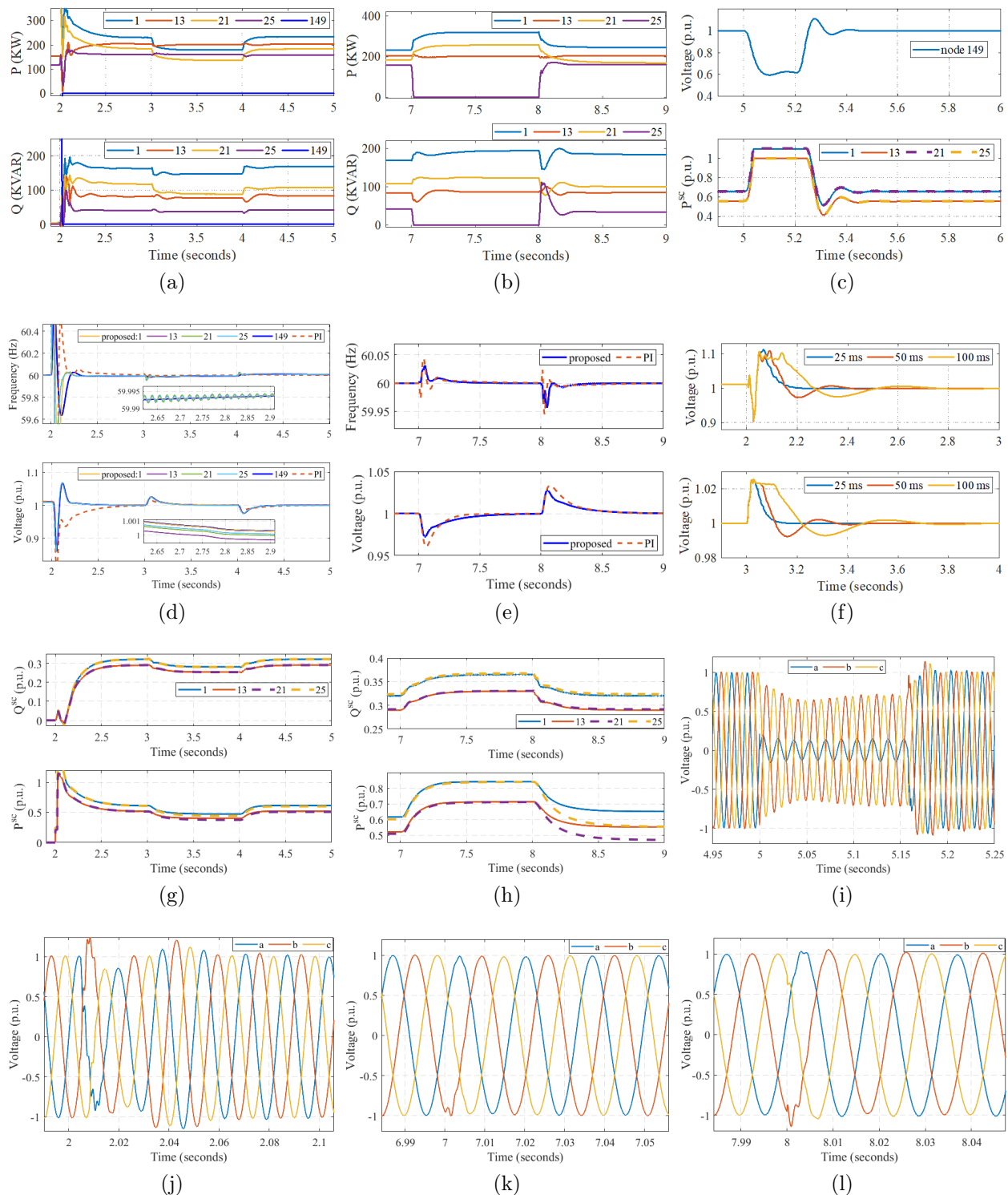


Figure 5.3: Real-time simulator results showcasing stable power sharing, voltage and frequency regulation at POI, control signals from the proposed framework, and three-phase voltage signals at the POI for various simulated events. All the graphs are plotted based on real-time data logging in the target Opal-RT hardware. Logged data resolution for voltage and power signals is  $50 \mu\text{s}$ , and data resolution for control signals ( $P_i^{sc}$ ,  $Q_i^{sc}$ ) is 1 ms. (a) PQ sharing after the islanding (b) PQ sharing for plug-and-play of DER 4 (c) Controller performance during fault case (d) System states during events (e) V/f response for plug-and-play of DER 4 (f) Communication latency influence (g) Controller response during events (h) Controller response for plug-out/ plug-in (i) Voltage response during fault (j) Voltage response during islanding (k) DER plug-in voltage response (l) DER plug-out voltage response.

framework is compared with the optimal PI controller except that the PI controller leads to higher over/undershoots. Fig. 5.3h showcases the per-unitized control signals for the primary controllers of the respective DERs. It is worth noting the adaptive behavior of the framework, which generates different reference values after DER 4 plug-in, yet maintains stable power sharing and regulating voltage and frequency. Fig. 5.3k and Fig. 5.3l showcase

TABLE 5.2: Voltage and frequency regulation performance comparison for various events between IIMPC and optimal PI [12].

Applications:	Frequency regulation (FR) and voltage regulation (VR) performance analysis (FR, VR)								
Criteria:	Settling time (s)			Overshoot (%)			Undershoot (%)		
Events	Optimal PI	IIMPC	Improvement	Optimal PI	IIMPC	Improvement	Optimal PI	IIMPC	Improvement
Islanding	(0.5, 0.6)	(0.31, 0.3)	(38%, 50%)	(0.84, 0)	(1, 5)	(-19%, NA)	(0.7, 24)	(0.6, 18)	(14%, 25%)
Load decrease	(0.12, 0.28)	(0.1, 0.28)	(17%, 0%)	(0, 2)	(0, 2.2)	(0, -10%)	(0.07, 0)	(0.08, 0)	(-14.3%, 0%)
Load increase	(0.1, 0.48)	(0.1, 0.3)	(0%, 37%)	(0.08, 0)	(0.07, 0)	(14%, 0%)	(0, 1)	(0, 1)	(0%, 0%)
Plug-out	(0.21, 0.4)	(0.21, 0.5)	(0%, -25%)	(0.08, 0)	(0.065, 0)	(18.75%, 0%)	(0.07, 3.5)	(0.065, 2.5)	(7.6%, 40%)
Plug-in	(0.35, 0.55)	(0.35, 0.55)	(0%, 0%)	(0.04, 3)	(0, 2.5)	(100%, 16.6%)	(0.083, 0)	(0.08, 0)	(3.6%, 0%)

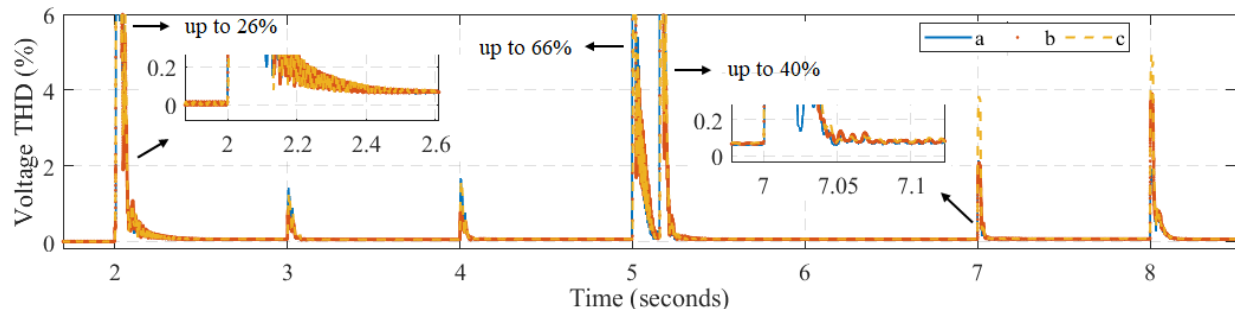


Figure 5.4: THD of the voltage profile at the POI during steady state and events. The THD spikes during events last 50-100 ms.

reasonable 1-2 cycle transients for the POI three-phase voltages during plug-out and plug-in respectively. Quantitative analysis of the performance comparison is presented in Table 5.2. Out of 30 scenarios, in 13 scenarios proposed controller performs better than PI controller, 4 scenarios PI controller performs better and in another 13 scenarios performance is neutral.

#### 5.6.4 Controller Performance during Fault Scenario

An unbalanced fault of AG is simulated at 5 s for 150 ms at node 8 with a fault impedance of  $1 \Omega$ . The three-phase voltage at POI due to fault is depicted in 5.3i. A higher voltage sag is observed in comparison to the other two phases as this is an unbalanced fault. The averaged RMS voltage value of POI is depicted in 5.3c, according to which an average sag of 0.6 p.u. occurs during the fault time. The control variable minimum value ( $u_{min}$ ) in the proposed IIMPC framework is 0 for all the DERs while the maximum value ( $u_{max}$ ) is

TABLE 5.3: Voltage THD during steady-state and events

Mode (steady state)	Average THD (%)		
	Phase A	Phase B	Phase C
Grid-connected	0.015	0.015	0.015
Islanded	0.06	0.066	0.07
Events (transients)	Maximum THD (%)		
Islanding (2s)	20.3	26.7	17.1
Load decrease (3s)	1.42	0.81	1.23
Load increase (4s)	1.61	0.87	1.58
Fault (5s)	26.2	66.1	13.7
Fault recovery (5.015s)	40.1	35.2	15.1
Plug-out (7s)	2.71	2.73	3.82
Plug-in (8s)	2.3	3.87	4.92

1.1 p.u. for DER 1 and DER 3, 1 p.u. for DER 2 and DER 4. During the voltage sag, the IIMPC active power control variable ( $P_i^{sc}$ ) for the primary controller is saturating at the defined constraints. After the fault, the controller continues to provide an appropriate power reference signal to keep the MG voltage at 1 p.u. Through this case study, the capability to handle the designed constraints of the IIMPC framework during electric faults is showcased, due to which voltage at POI is regulated to the nominal value after the short-term fault.

#### 5.6.5 Influence of Communication Delay

Frequency regulation at POI is accomplished just based on the PCC measurements, hence, communication delay  $d_0$  does not influence the frequency response. However, for various delays, the different voltage response is observed in Fig. 5.3f. Increasing delay leads to increasing voltage settling time, and stable voltage regulation is observed. For a delay of 25 ms, 50 ms, 100 ms, the voltage settling time of 0.24 s 0.52 s 0.85 s during islanding and 0.17 s, 0.46 s, 0.76 s during load change is observed respectively. Therefore, in this case, the stability of the proposed controller is verified for possible higher communication delays in large-scale networks with high DER penetration. In case of communication failure, if the MG voltage is outside 0.88 p.u. - 1.1 p.u. range, DERs will be disconnected in accordance with the IEEE 1547-2018 standards [114].

#### 5.6.6 Voltage Signal Quality at POI

In the grid-connected mode, the substation node (modeled as a voltage source) maintains the voltage in the network while in islanded mode, grid forming inverter (at node 1), maintains the voltage in the network. Fig. 5.3i through Fig. 5.3l illustrates the three-phase voltage graphs at POI during various events. The total harmonic distortion (THD) of the POI AC voltage is computed and presented in Fig. 5.4. The quantitative analysis of THD is presented in Table. 5.3. As per the IEEE 519-2022 standard for harmonic control, for a network voltage of 4.16 kV, up to 5% THD is allowed [166]. Clearly, steady state THDs are very low (0.1%) and during regular events such as load change and DER plugin/out THD less than 5% is achieved.

### 5.7 Summary

In this chapter, decentralized online system identification, and estimation-based IIMPC controller for voltage and frequency regulation in an islanded network are verified in a real-time test environment. The frequency regulation is demonstrated without the impact of communication delay, and the robustness of voltage regulation for higher latency is demonstrated. In comparison to the optimal PI controller, the proposed controller offers better transient performance during the majority of the scenarios, especially better settling time (by 50%) when communication delays are included. Moreover, IIMPC capability to handle

constraints is showcased through an electric fault scenario and post-fault voltage is stable and regulated to the nominal values. Lastly, network voltage quality is quantitatively analyzed, and THD levels are less than 5% (as per the IEEE 519-2022 standard) during steady-state operation, load change, and plug-in/out. The IIMPC framework is developed based on a low-order high-fidelity model and estimator, thus feasible for deployment in grid-edge devices. Through the various test scenarios, the robustness of the framework is showcased during various events with the consideration of communication latency.

## CHAPTER 6: An Extended Q-routing-based Event-driven Dynamic Reconfiguration of Networked MGs

*All modern revolutions have ended in a reinforcement of the power of the State.*

---

Albert Camus

The operation of networked MGs enables the availability of local distributed energy resources (DER) at the network level. During grid events such as electric faults, part of the power distribution network needs to be isolated such that the healthy part of the network can operate generally through optimal reconfiguration. Most of the topology agnostic reconfiguration schemes are complicated, computationally expensive, and offer a single optimal path. To overcome these disadvantages, a reinforcement learning-based extended Q-routing method is proposed in this chapter to achieve optimal network reconfiguration. The proposed method utilizes a model-free adaptive learning technique, thus efficiently discovering optimal paths in a dynamically changing network. To validate the proposed method in a real-time environment, a detailed dynamic distribution network model is developed, including primary and secondary control of integrated DERs and the protection functions. Furthermore, event-driven communication is designed to exchange data between the dynamic network model and the reconfiguration agent. The real-time results obtained from the IEEE 123 node dynamic model showcase the effectiveness of the proposed method.

### 6.1 Introduction

The rapid integration of distributed energy resources (DER) in the distribution network has paved a way for the modernization of the grid. DERs such as photovoltaic and battery energy storage, are interfaced with the power distribution network through inverter-based resources (IBRs). A cluster of DERs forms an MG that can be operated in a grid-connected or islanded mode of operation utilizing a hierarchical control structure [4]. The distribution network is usually unbalanced due to the uneven loading per phase. Therefore, for the stable operation of the IBRs, the primary controller requires dedicated positive and negative sequence (PNS) control loops [53]. Droop control strategy as a part of primary control enables power tracking and power sharing of multiple IBRs in the grid-connected and islanded mode of MG operation. A robust droop control mechanism which is applicable for low  $X/R$  networks is adopted in this work as a part of the primary controller.

The substation in the distribution network maintains the balanced network voltage usually close to nominal values. However, in absence of a substation, grid-forming IBR maintains the balanced network voltage [53]. Moreover, due to the droop strategy, voltage and frequency deviate from the nominal values during islanded operation of MGs. This necessitates the introduction of the secondary controller to provide appropriate power set-points to the primary controller such that network voltage and frequency are near nominal values [99]. A decentralized PI controller is used in this work to meet the secondary controller objective [13].

In a power network, the neighboring MGs can be connected to improve the overall network performance in terms of economic viability, reliability, and resiliency during extreme events and cyber attacks [167–169]. Specifically, it is feasible to group the MGs under the same feeder and caters to the critical loads outside the respective electric boundaries [170, 171]. MG reconfiguration studies are performed from the capability [172, 173] and stability [174, 175] perspective and its effect on the power losses, topology, voltage profile, the reactive power reserves, and the stability margin are investigated. The studies showcased that optimal network reconfiguration is necessary for minimizing power losses and improving the voltage profile. With this motivation, in this chapter, a learning-based optimal network reconfiguration is formulated that is adaptive to the dynamically changing power network.

A networked MG is a cluster of interconnected MGs whose boundaries can change dynamically to provide improved service during grid events such as short/long-term faults, generation loss, and various others. The various traditional reconfiguration approaches are improved to achieve the MG capacity enhancement [176, 177], minimize switching operation costs [178], and achieve radiality constraints [179]. However, such approaches are feasible during the planning phase of DER integration or slower time-scale control operation during the operational phase. Genetic algorithm-based real-time optimal MG reconfiguration that is sensitive to grid events is proposed in [180]. This work may not be applicable to radial distribution networks, as it assumes voltage violation and line overloading constraints that are designed during the bulk-grid planning and operational control criterion. Moreover, the distributed generators are not modeled as IBRs, hence feasibility for 100% IBR-based operation cannot be guaranteed.

For a radial network reconfiguration, a mixed integer nonlinear optimization problem is formulated to maximize the load support using the backup DERs in [181]. In this work, a simple network topology is considered, and the influence of IBR protection and control on the reconfiguration is not considered. Furthermore, a closed-loop real-time verification of the algorithm is not performed. In [136], IBR models along with the control and protection features are modeled that aid in the stable reconfiguration of the network. When the fault

is identified in a zone, it is isolated from the rest of the network, and a breadth-first search (BFS) based automated reconfiguration scheme reconnects the healthy zones back to the network. This approach leads to minimal islands in a network, thus adding the self-healing feature to enhance grid resiliency. The real-time co-simulation results of the same work are presented in [16], further proving the smooth flow of data between the cyber and physical parts in the system. However, there are two major limitations of the works provided in [16,136]. Firstly, though droop control is used for power-sharing among the IBRs, a secondary voltage and frequency control is not designed as a part of the model. Droop loops are sensitive to the parameters and without secondary control, voltage and frequency in the zone may deviate such that the load-shedding scheme may get enabled inappropriately. This may in turn lead to instability in the zone. Secondly, since the network reconfiguration is an event-driven application, a thorough investigation of the communication design and closed-loop cycle time performance details are not provided.

From another perspective, network reconfiguration can be perceived as an environment-agent interaction. The dynamic network model with IBR control and protection can be treated as an environment. An agent incorporates an intelligent algorithm that takes actions based on the states of the environment. Reinforcement learning (RL) is one of the machine learning paradigms that work based on the agent with the state-action-reward mechanism in interaction with the environment. The objective of an agent is to take actions that will maximize rewards through the exploration and exploitation of the environment [91,182]. RL is applied for the routing problems as it offers important benefits such as: being agnostic to network models, computationally less expensive, and providing near-optimal solution [90,183]. Without the knowledge of network topology, the RL-based routing method is capable of finding the shortest path between the pair of source and destination nodes based on the defined optimization criteria. Q-learning is used to find the optimal policy for a given finite Markov decision process (MDP) when the state transition matrix is not available [184]. Furthermore, Q-routing is similar to Q-learning except that 1) it does not use the discount rate, 2) it chooses minimum future cost for every state instead of maximum future reward. Q-routing is predominantly used in networking applications wherein it has showcased promising improvements in prediction and exploration [185].

## 6.2 Research Contributions

In this chapter, an RL-based optimal reconfiguration framework is proposed using an extended Q-learning approach. In the proposed approach, when an extreme event occurs in an MG, the status of boundary SSs is communicated to the reconfiguration framework. The framework ensures cascaded islanding situation is avoided, and the healthy MGs are connected back to the grid through the shortest path. Unlike the conventional breadth-first

search reconfiguration approach [136], in the proposed approach, a group of boundary SSs of an MG is identified as a node, and the source node to the destination node's end-to-end shortest path is computed using Q-routing. The major contributions of this chapter are as follows.

- A detailed dynamic model of the environment is developed including IBR primary control, secondary control, protection, synchronization, and load-shedding schemes. The design is optimized for real-time operation using distributed modeling and is capable of communicating its states to the agent at a millisecond timescale post-event.
- Proposed dynamic reconfiguration is formulated as an MDP, and the extended Q-routing-based reconfiguration method efficiently discovers the optimal path between the source and destination nodes. The extended Q-routing algorithm utilizes the edge weights to compute the optimal path and the approach is capable of finding multiple optimum paths, unlike the BFS method.
- Real-time agent-in-the-loop validation of the proposed method showcases the optimal network reconfiguration, including stable power sharing, and nominal voltage in respective MGs. Furthermore, duplex-event-driven communication is developed between the agent and the environment to minimize the closed loop cycle time of the network reconfiguration.

### 6.3 Components of MG Control and Protection

An overview of the hierarchical control applicable for IBR operation in the distribution network is depicted in Fig. 6.1. A brief description of the components utilized in modeling the network operation dynamics is presented in this Section.

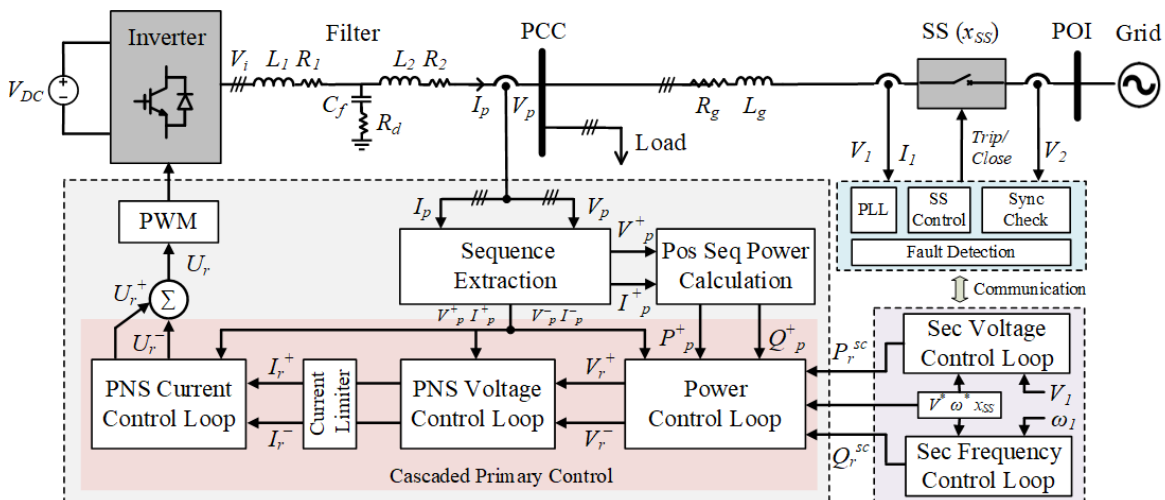


Figure 6.1: Hierarchical IBR control including primary and secondary controller layers applicable for the unbalanced distribution network.

### 6.3.1 Overview of the IBR control

The IBR system and its hierarchical controller overview are depicted in the Fig. 6.1. The DC link voltage of the IBR is assumed to be constant and IBR is interfaced with the distribution network at the PCC. The switching harmonics of the power electronic components of IBR are attenuated by designing the appropriate *LCL* filter. *LCL* filter poses the challenge of the resonant peak which is mitigated by incorporating a passive damping resistor [128].  $R_g$  and  $L_g$  represent the equivalent impedance of the low  $X/R$  distribution grid. The SS is situated at the point of interconnection (POI), and the tripping of the SS leads to the islanded mode of operation supporting the load in the distribution network.

The IBR hierarchical control system consists of a primary controller followed by a secondary controller. The objective of the primary controller is to achieve power tracking and power sharing in grid-connected and islanded modes of operation respectively, by utilizing the PCC measurements. The secondary controller aims at maintaining the nominal voltage and frequency in the islanded MG by utilizing the measurements at POI. The operation of SS is controlled through an intelligent electronic device (IED), with built-in fault identification and MG isolation (to open the SS) and grid synchronization (to close the SS) functions. In a given MG at least one grid-forming IBR is designed and the rest of the IBRs are designed as grid following. IBRs deliver the power based on the set points provided to them during grid-connected MG operation, thereby all IBRs are grid-following. In the islanded MG, grid-forming IBR maintains the balanced voltage in the network, while grid-following IBRs along with the grid-forming IBR share the load.

### 6.3.2 Primary Controller

The distribution network is usually unbalanced in nature. To achieve stable power tracking and power sharing, dedicated PNS controllers are designed. The *abc* frame voltage and current measurements are decomposed into PNS components utilizing the delayed signal cancellation technique [129].

$$V_p^\pm(k) = \frac{1}{2} \left( V_p(k) \pm V_p(k) z^{\frac{T_g}{4}} \right) \quad (6.1)$$

$$I_p^\pm(k) = \frac{1}{2} \left( I_p(k) \pm I_p(k) z^{\frac{T_g}{4}} \right) \quad (6.2)$$

PI controllers are more suitable for the control of DC signals. Hence, predominantly used in *dq*-frame-based IBR control. However, they may lead to steady-state errors resulting in inaccurate tracking of IBR set-points. On the other side, PR controllers can mitigate this steady-state error as they can be applied on *abc*-frame signals [186]. The primary controller is designed as a PNS proportional resonant (PR) cascaded current control (CC) loop followed by the voltage control (VC) loop given by (6.3) and (6.4) respectively.

$$U_r^\pm(k) = V_p^\pm(k) \pm \left( k_p^{cc} + k_i^{cc} \frac{2\omega_o}{\frac{z-1}{T_s^{pc}z} + 2\omega_o + \frac{T_s^{pc}\omega_g^2z}{z-1}} \right) \Delta I_e^\pm(k) \quad (6.3)$$

$$I_r^\pm(k) = \left( k_p^{vc} + k_i^{vc} \frac{2\omega_o}{\frac{z-1}{T_s^{pc}z} + 2\omega_o + \frac{T_s^{pc}\omega_g^2z}{z-1}} \right) \Delta V_r^\pm(k) \quad (6.4)$$

where the PR controller is discretized using backward Euler method,  $\Delta I_e^\pm(k) = (I_r^\pm(k) - I_p^\pm(k))$   $k_i$  is the error feedback of the CC,  $\Delta V_r^\pm(k) = (V_r^\pm(k) - V_p^\pm(k))$  is the error feedback of the VC,  $k_p^{cc}$  and  $k_p^{vc}$ , are the proportional gain coefficient of the CC and VC respectively,  $k_i^{cc}$  and  $k_i^{vc}$ , are the integral gain coefficient of the CC and VC respectively,  $T_s^{pc}$  is the primary control sample time,  $\omega_o$  is the bandwidth around the grid frequency of  $\omega_g$ .

Grid-forming IBRs require negative sequence voltage and current controllers to balance the voltage in the distribution grid while the grid following IBRs utilizes a negative sequence current blocking control strategy. To assist IBR in ride-through, the current limiter is implemented with a pre-determined limiting value of  $I_{lim}$ . To avoid the propagation of the transients of high bandwidth CC and VC, droop laws are implemented with relatively lower bandwidth. This is accomplished by utilizing the digital low pass filter (LPF) to process the computed active ( $p_i$ ) and reactive power ( $q_i$ ). The time domain representation of the LPFed active ( $P_i$ ) and reactive ( $Q_i$ ) power is given by (6.5) and (6.6),

$$P_i(k) = \alpha P_i(k-1) + (1-\alpha)p_i(k) \quad (6.5)$$

$$Q_i(k) = \alpha Q_i(k-1) + (1-\alpha)q_i(k) \quad (6.6)$$

where  $\alpha = e^{(-\omega_c T_s^{pc})}$  with the  $\omega_c$  as the corner frequency of the LPF, usually in the range of 2 Hz to 10 Hz. Robust droop laws that are applicable for a low  $X/R$  network are adopted to design the outermost power control loop [81, 187] as given by (6.7) and (6.8),

$$V_i^r(k) = V^* - \left( k_p^P - x_{MG} k_i^P \frac{T_s^{pc}}{z-1} \right) \Delta P_i(k) + k_p^V \Delta V_i(k) \quad (6.7)$$

$$\omega_i^r(k) = \omega^* + \left( k_p^Q + x_{MG} k_i^Q \frac{T_s^{pc}}{z-1} \right) \Delta Q_i(k) \quad (6.8)$$

where  $\Delta P_i = P_i - P_i^{sc}$ ,  $\Delta Q_i = Q_i - Q_i^{sc}$ ,  $\Delta V_i = V^* - V_i^p$ ,  $P_i^{sc}$ ,  $Q_i^{sc}$  are active and reactive power set-points issued by the secondary controller,  $V^* = 1$  and  $\omega^* = 377$  rad/s are the voltage magnitude and angular frequency set-point values,  $k_p^P$ ,  $k_p^Q$  are droop coefficients,  $k_p^V$  is the voltage deviation penalty factor,  $k_i^P$ ,  $k_i^Q$  are the integral gain coefficients for mitigating power tracking error during the grid-connected mode of operation ( $x_{MG} = 1$ ). During islanded mode of operation ( $x_{MG} = 0$ ), integral gains are disabled and droop gains facilitate power sharing among multiple IBRs.

### 6.3.3 Secondary Controller

During grid-connected mode ( $x_{MG}^m = 1$ ) of operation of an MG, secondary controller issues set-points ( $P_i^{sc} = P_i^{MPP}, Q_i^{sc} = 0$ ) to the primary controller. Thus all IBRs are operated in unity power factor mode, injecting active power as per the maximum power point. During islanded mode of operation ( $x_{MG}^m = 0$ ), droop laws lead to the deviation of voltage and frequency of MG at POI from its nominal values [99]. So, a decentralized secondary PI controller is used to generate ( $P_i^{sc}, Q_i^{sc}$ ) such that the voltage and frequency of the MG are close to the nominal values. The integral term in the secondary controller aids in mitigating the steady-state error which may not be possible with just proportional gain. As integral term continuous to accumulate error, under certain conditions such as fault scenarios, this accumulation even exceeds the physical capabilities of the inverter. Hence, appropriate anti-wind-up logic is adopted, and the controller using the backward Euler discretization method is described by:

$$P_i^{sc}(k) = \left( k_p^v + \left( k_i^v + k_w^v dV(k) \right) \frac{T_s^{sc} z}{z-1} \right) \Delta V_i^1(k) \quad (6.9)$$

$$Q_i^{sc}(k) = \left( k_p^\omega + \left( k_i^\omega + k_w^\omega d\omega(k) \right) \frac{T_s^{sc} z}{z-1} \right) \Delta \omega_i^1(k) \quad (6.10)$$

where  $\Delta \omega_i^1(k) = \omega^* - \omega_i^1$ , and  $\Delta V_i^1(k) = V^* - V_i^1$  are PI controller input error signal that is the difference between measured and reference values,  $k_p^v, k_p^\omega$  are the proportional gain coefficient,  $k_i^v, k_i^\omega$  are the integral gain coefficient,  $k_w^v, k_w^\omega$  are the anti-windup gain coefficients of the voltage and frequency controllers, respectively,  $T_s^{sc}$  is the sampling time of the secondary controller,  $dV(k), d\omega(k)$  are the difference between the saturated and unsaturated control signals.

### 6.3.4 Protection Functions

Protections functions are modeled to realistically capture the dynamics and delays incurred from the field intelligent electronic devices (IED) responses. When the faults occur in the network, from the first principles, it is evident that at least one phase current will flow in the direction of the fault location. Therefore, computing the current direction at the boundary SS of the MGs assists in the identification of the unhealthy MG. To identify and isolate unhealthy MG from the rest of the network, a 90-45 direction scheme [188] is implemented at the boundary SS. Fault identification logic issues the boundary SSs to be tripped when the network voltage sag reaches below 0.88 p.u. and the fault sustains for at least 3 cycles (50 ms). After isolating the unhealthy MG, the voltage in the other MGs may still remain below 0.88 p.u. for a longer time. Hence, a fault-detection flag logic to compute sustenance of the voltage sag up to 6 cycles (100 ms) is adopted not to trip the boundary SSs of healthy MGs [136].

When an MG is islanded, an appropriate load-shedding scheme is enabled to ensure the stable operation of MG by attaining generation-load balance. Post islanding, if MG frequency is outside 57 Hz - 62 Hz range, and if MG voltage is outside 0.88 p.u. - 1.1 p.u. range, a pre-identified non-critical load is shed. The aforementioned ranges are in accordance with the IEEE 1547-2018 standards. To connect MG back to the grid, SSs are assumed capable of reclosing actions with the support of IEDs. The IED fetches the voltage and currents from either side of the SS to verify the synchronization conditions before closing the SS. The synchronization IEDs are compliant with the ANSI/IEEE device 25 standards and are typically used to perform SS closure. Synchronization conditions are met when the phase-wise voltage magnitude, phase-wise voltage angle, and network frequency difference are below 0.13 p.u., 0.0175 rad, and 2 Hz respectively. SS close command is issued only if the aforementioned conditions are satisfied.

#### 6.4 Event Driven Dynamic Optimal Reconfiguration Framework

The RL agents learn from the experience through the interaction with the environment in terms of states, actions, and rewards [91]. Q-learning is a widely used model-free RL method that utilizes a look-up table to store the values of each state-action pair. This look-up table tends to grow as the states in the environment increase. For the real-time closed-loop interaction between the agent and the environment, simplification of the learning process and improvements to computational efficiency are necessary. In this section, the details of the proposed computationally efficient reconfiguration framework and the extended Q-routing algorithm used to construct the RL agent are discussed.

##### 6.4.1 Graph Theory-based Dynamic Networked MG Model

An example networked MG model is illustrated in Fig. 6.2. Standard IEEE 123 node system is modified to comprise seven independently islandable MGs. Each of the MG has the boundary SSs opening which leads to the islanded operation. Each of the MGs contains one grid-forming IBR and the rest can be grid-following IBRs. The default network is connected to the substation node (G1) and the alternate substation node (G2) is as well provided. While one of the substation nodes is connected to the network, the entire network is operated by maintaining the radial topology. The operation of SSs (open or close) is considered a discrete event leading to the dynamic sectionalization of the network.

The distribution network is considered as an environment that is modeled using the graph theory principles as shown in Fig. 6.3. The network model of  $N$  connected MGs is represented as an undirected cost graph  $\mathcal{G} = (\mathcal{V}, \mathcal{E}, \mathcal{C})$ , where  $\mathcal{V} := [v_1, v_2, \dots, v_i, \dots, v_N]$ ,  $\forall i \in \{1, 2, \dots, N\}$ ,  $N \geq 2$  is the finite set of MG nodes in the network,  $\mathcal{E} := e_{ij} \in \{0, 1\}$ ,  $\forall j \in \{1, 2, \dots, N\}$  is the finite set of edges connecting the pair of MG nodes, and  $\mathcal{C} := c_{ij}$  is the set

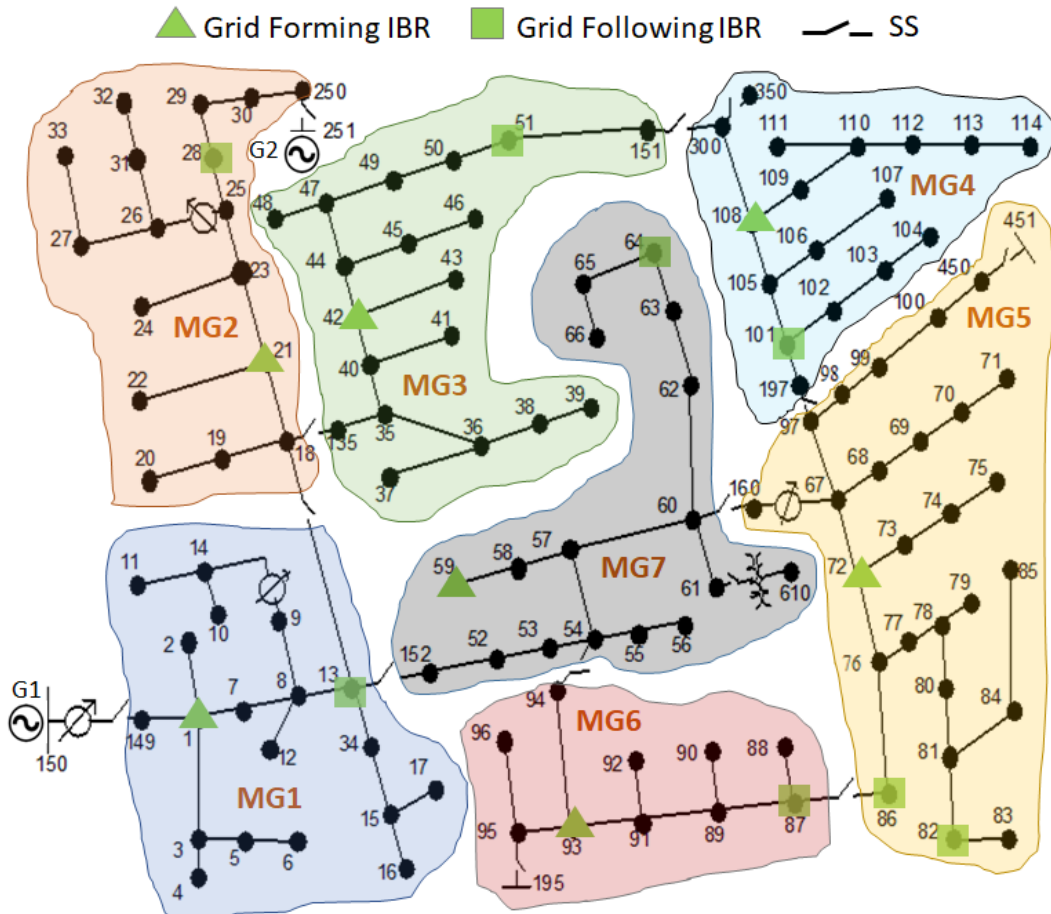


Figure 6.2: Modified IEEE 123 node system consisting of pre-identified atomic MGs with a stipulated electric boundary. Each of the MGs have at least one grid-forming inverter.

of real number costs assigned to the edges. Let states at the discrete-time  $k$  of the network be represented as  $\mathcal{S} := [\mathcal{E}, \mathcal{F}]$ , where  $\mathcal{F} := [f_1, f_2, \dots, f_i, \dots, f_N] \in \{0, 1\}$ , is the fault state set of the MGs. Let the states at the discrete time  $k$  be represented as  $\mathcal{S}(k)$ . An event ( $e_l$ ) is said to have occurred in the environment when  $\mathcal{S}(k) \neq \mathcal{S}(k-1)$ . The event space is defined as,  $e := [e_1, e_2, \dots, e_l, \dots]$ ,  $\forall l \in \{1, 2, \dots\}$ . Thus the dynamic event-driven networked MG model is represented as:

$$\mathcal{G}_l = (\mathcal{V}, \mathcal{S}, \mathcal{C}, e) \quad (6.11)$$

The event-driven model of networked MG is represented as a 3-tuple sequence:  $(\mathcal{G}_{l-1}, \mathcal{G}_l, \mathcal{G}_{l+1})$ , where  $(\mathcal{G}_{l-1})$  is the initial network topology that is operated optimally,  $(\mathcal{G}_l)$  is the post-event network topology that is operated ensuring the stability (not necessarily optimal), and  $(\mathcal{G}_{l+1})$  is the optimally reconfigured networked topology through the actions of the RL agent. Thus, after every event ( $e_l$ ), states ( $\mathcal{S}_k$ ) are communicated to an external RL agent which in turn offers optimal actions to achieve the network reconfiguration.

#### 6.4.2 Formulation of RL-based Optimal Reconfiguration

The network with the default state is modeled in the RL agent. Every time event occurs in the environment, the change in state information is communicated to the RL agent and the network model in the RL agent is updated. The reconfiguration framework is modeled

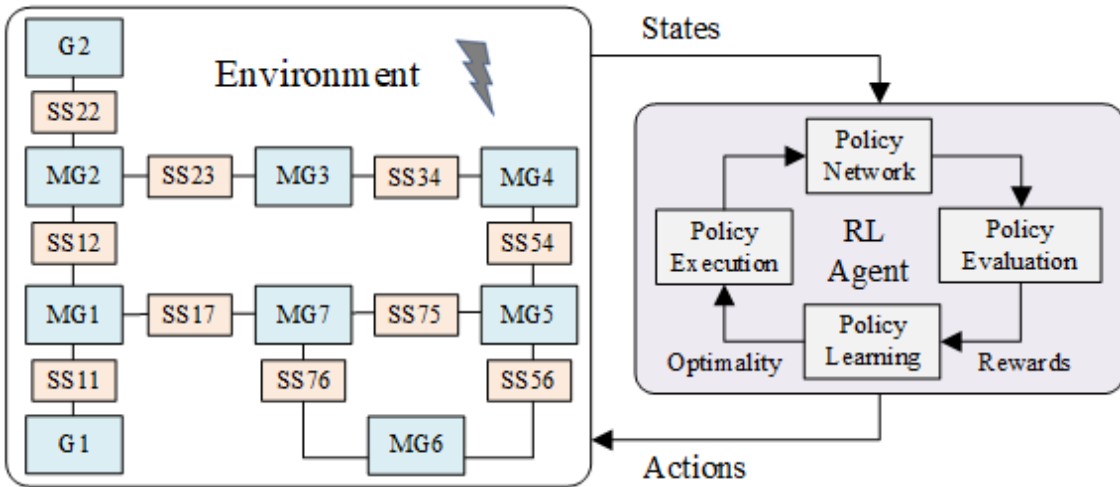


Figure 6.3: Proposed event-driven dynamic reconfiguration framework showcasing the interaction between the environment and the RL agent [189].

as a Markov decision process (MDP), represented as a tuple  $\mathcal{M} = \langle \mathcal{S}, \bar{s}, \mathcal{A}, \mathcal{P}, \mathcal{R} \rangle$ , where  $\mathcal{S}$  is the finite set of observable states of the environment,  $\bar{s} \in \mathcal{S}$  is the initial state,  $\mathcal{A}$  is the finite set of actions taken by the RL agent,  $\mathcal{P}$  represents the probability of transitioning from the current state to the next state after taking an action;  $\mathcal{R} : \mathcal{S} \times \mathcal{A} \rightarrow \mathbb{R}_{\geq 0}$  is the reward obtained when the system transitions from current state to the next state after implementing an action. Reward function is represented as  $r = \mathcal{R}(s, a, s')$ , where  $s, s' \in \mathcal{S}; a \in \mathcal{A}$ .

Every time an event occurs in the environment, the reconfiguration framework states are initialized such that  $\bar{s} = \mathcal{S}_k$ . thereby updating the *policy network*. With an initial state  $\bar{s}$ , a path through the MDP is the sequence of  $(\mathcal{S}_t, \mathcal{A}_t, \mathcal{R}_t)$ . MDP transitions into the next state by a choice of action and this choice is made by a policy. A deterministic stationary policy is defined as  $\pi : \mathcal{S} \rightarrow \mathcal{A}$ , that maps the states and actions. The *policy evaluation* involves transitioning to a set of possible states while avoiding forbidden states ( $\mathcal{H}$ ) with an objective of minimizing the cumulative costs. Forbidden states ( $\mathcal{H}$ ) are updated in two stages. Firstly, knowing the network topology ( $\mathcal{G}$ ),  $\forall e_{ij} \in \mathcal{E}$ , if there exists no direct path between  $v_i$  and  $v_j$ , then  $e_{ij} \in \mathcal{H}$ . This is a kind of static update performed during the initialization of the RL agent. Secondly, when an event occurs, ( $\mathcal{H}$ ) is updated dynamically such that all the edges belonging to the faulty node are forbidden. For instance, if  $f_i = 1$ ,  $v_i$  has a fault and needs to be isolated, hence all the  $e_{ij}$  of  $v_i$  are accounted towards the  $\mathcal{H}$ . The construction of  $\mathcal{H}$  is thus represented as in (6.12).

$$\mathcal{H} = \begin{cases} v_i \rightarrow v_j, \exists e_{ij} \notin \mathcal{E}, \forall i, j \in \mathbb{N} \\ v_i \rightarrow v_j, \exists e_{ij} \in \mathcal{E} \ni v_i \in \mathcal{F}, \forall i, j \in \mathbb{N} \end{cases} \quad (6.12)$$

*Policy learning* is performed using a Q-learning technique, which is a type of off-policy temporal-difference learning method. In this technique, the state-action values are updated through bootstrapping. Hence, the agent does not wait for the result until the end of the episode. Bootstrapping and utilization of  $\mathcal{H}$  for the reward mechanism facilitates faster

convergence. The RL agent attempts to find the optimal policy ( $\pi^*$ ) by maximizing the cumulative discounted reward as given by (6.13)

$$\pi^* =_{\pi} \mathbb{E}_{\pi} \left[ \sum_{t=0}^T \gamma^k \mathcal{R}_{t+1} | \mathcal{S}_t = s, \mathcal{A}_t = a \right] \quad (6.13)$$

where  $t$  is the current iteration,  $\gamma \in [0, 1]$  is the discount factor used to weigh the rewards of the near future to the one in the distant future.

Rewards for the RL agent action are calculated based on the mechanism given by (6.14), where costs associated with the forbidden states and allowed states play a critical role in finding the optimal path between source and destination vertices.

$$\mathcal{R}_t := \mathcal{C}_t = \begin{cases} c_d & \text{if } e_{ij} \notin \mathcal{H} \\ c_{max} & \text{if } e_{ij} \in \mathcal{H} \end{cases} \quad (6.14)$$

By using the reward mechanism (6.14), the Q-routing representation for path discovery in the network is formulated as (6.15),

$$Q(\mathcal{S}_t, \mathcal{A}_t) \leftarrow Q(\mathcal{S}_t, \mathcal{A}_t) + \alpha \left( \mathcal{R}_{t+1} + \gamma \min_a Q(\mathcal{S}_{t+1}, a) - Q(\mathcal{S}_t, \mathcal{A}_t) \right) \quad (6.15)$$

where  $\alpha$  is the learning rate. As per (6.15), the TD between predicted and the present Q-values is calculated and for every state  $S$ , the true action value related to policy  $\pi$  is given by  $Q(\mathcal{S}_t, \mathcal{A}_t) = \mathbb{E}_{\pi}(R_t + \gamma R_{t+1} \dots | \mathcal{S}_t = s, \mathcal{A}_t = a)$  and the discount factor is set to 1. Choice of the action is derived from the  $\epsilon$ -greedy policy as given by:

$$\mathcal{A}_t = \begin{cases} \min Q_t(\mathcal{S}, \mathcal{A}; \mathcal{R}) & \text{with probability } (1 - \epsilon) \\ \text{random } \mathcal{A}_t \notin \mathcal{H} & \text{with probability } \epsilon \end{cases} \quad (6.16)$$

Once the optimal policy is learned, in *policy execution* phase, the learned optimal policy is used to compute the required actions to traverse a path from the source to destination vertices as given by,

$$reach_{-H} = \{v_i \rightarrow v_j \in Path_{\mathcal{M}, \bar{s}} \ni e_{ij} \notin \mathcal{H}, \forall i, j \in \mathbb{N}\} \quad (6.17)$$

wherein the traversed path within the MDP avoiding the edges of  $\mathcal{H}$  is optimal. This leads to the construction of the optimally reconfigured network  $\mathcal{G}_{l+1}$ . The change in the states between the  $\mathcal{G}_l$  and  $\mathcal{G}_{l+1}$  are computed and communicated back to the environment as actions. To summarize, each of the MGs in the network can autonomously island, and connect back to the grid with reasonable transients, and stably operate in either mode performing designated roles.

---

**Algorithm 3:** Event-driven extended Q-routing algorithm for the optimal path discovery.

---

```

1 Communication Data:  $\mathcal{S}_l := [\mathcal{E}_l, \mathcal{F}]$ 
2 Inputs:  $\mathcal{G}_{l-1}, \mathcal{H}_{l-1}$ 
3 Outputs:  $\mathcal{G}_{l+1}, \mathcal{A}_T \in \mathcal{E}$ 
4 Initial network model  $\mathcal{G}_{l-1} = (\bar{v}_i \in \mathcal{V}, \bar{e}_{ij} \in \mathcal{E}, \bar{c}_{ij} \in \mathcal{C})$ 
5 Initialize  $Q(s, a) \forall s \in \mathcal{S}, \forall a \in \mathcal{A}(s)$  arbitrarily
6 Initialize  $\alpha \in (0, 1], \gamma, \epsilon, \text{episodes}$ 
7 Initialize  $\mathcal{R} :=$  using (6.14) for  $\mathcal{G}_{l-1}$ 
8 if Event  $e_l$  occurs in the environment then
9   Update  $\mathcal{G}_l \leftarrow \mathcal{G}_{l-1}$ , given  $\mathcal{S}_l$ 
10  Update  $\mathcal{H}_l \leftarrow \mathcal{H}_{l-1}$ , given  $\mathcal{S}_l$ 
11  for each episode do
12    Define empty set for tracing  $\mathcal{E}_t$ 
13    Chose random source-destination pair  $(x, y) \in \mathcal{V}_l$ 
14    for each step of episode do
15      Get valid action set  $\mathcal{E}_v, \forall e_{ij} \notin \mathcal{H}_l$ 
16      Choose  $\mathcal{A}_t$  for  $\mathcal{S}_t$  using policy (6.16)
17       $\forall A_t \in \mathcal{E}_v$ , take action  $A$ , get  $R$  using (6.14)
18       $\forall A_t \notin \mathcal{E}_v$ , get  $R$  using (6.14)
19      Update  $Q_t(\mathcal{S}_t, A_t)$  using (6.15)
20      Update traced path  $v_i \rightarrow v_j \in \text{Path}_{\mathcal{M}, \bar{s}}, \exists e_{ij} \in \mathcal{E}_t$ 
21      Choose  $y = z, z \in \mathcal{V}_l$ 
22       $\mathcal{S}_{t+1} \leftarrow \mathcal{S}_t$  until  $\mathcal{S}_t$  is not terminal
23    end
24  end
25  Update the network model  $\mathcal{G}_{l+1} = (\mathcal{V}_{l+1}, \mathcal{E}_{l+1}, \mathcal{C}_{l+1})$  using the optimal actions
26     $\mathcal{E}_t \leftarrow \mathcal{A}_t$ 
27  Identify SS state changing from open to close due to RL agent action  $\mathcal{G}_{l+1} \leftarrow \mathcal{G}_l$ 
28  Communicate SSs to be closed:  $e_{ij} := 1 \in \mathcal{E}_{l+1}$ 
29 end

```

---

### 6.4.3 Proposed Q-routing based Optimal Path Identification

Algorithm 3, describes the detailed steps to achieve event-driven reconfiguration with extended Q-routing. The shortest path discovery is simplified by the introduction of  $\mathcal{H}$ . The set  $\mathcal{H}$  provides prior knowledge to the learning algorithm to avoid edges that return maximum costs. Unlike, the BFS method, for a given network topology  $\mathcal{G}_l$  along with  $\mathcal{H}$ , the proposed algorithm can provide multiple optimum paths if they exist. Once the optimal reconfigured network  $\mathcal{G}_{l+1}$  is provided by the algorithm, the edges of  $\mathcal{E}_{l+1}$  are compared with the  $\mathcal{E}_l$ , and set of edges that have to be closed on the optimal path is identified. Finally, RL agent sends *close* signal to the SSs on the optimal path in the environment. Actual closure of SS is subject to the synchronization conditions as discussed in Section 6.3.4.

## 6.5 RT Set-up and Discussion of Results

In the real-time simulation, the IEEE 123 node distribution network with DERs, communication, and protection functionalities is distributed among seven cores of the OP5707 RT simulator. During the islanded mode of operation of MGs, to ensure generation load balance, a load shedding scheme as per Table 6.1 is applied. The total IBR capacity and

TABLE 6.1: Load shedding nodes in the islanded mode.

MGs	Load shedding nodes
MG3	35, 36, 37, 38, 39, 41, 43, 45, 46, 49, 50, 51
MG5	68, 69, 70, 71, 73, 74, 75, 77, 80, 82, 84, 85, 98
MG7	52, 53, 58, 59, 62, 66

TABLE 6.2: Total IBR capacity and loading per MGs including load shedding in MG3, MG5, and MG7 (see Table 6.1).

MGs:	MG1	MG2	MG3	MG4	MG5	MG6	MG7
IBRs(kVA)	510	450	390	390	710	300	390
Load(kVA)	447	403	379	358	481	224	365

the total active load (after considering load shedding) in each of the MGs are given in Table 6.2. IBR models interface the DER DC side to the AC distribution grid through a  $\Delta$ - $Yg$  transformer with 480 V on the low voltage side and 4.16 kV on the grid side. IBR electrical parameters, system parameters and control parameters are listed in Table 6.3 and Table 6.4 respectively. The entire IBR-integrated IEEE 123 node network is distributed among four CPU cores. Protection, grid synchronization, and associated functions are split among two CPU cores. Lastly, one CPU core of Opal-RT is used for the communication functions. Such a systematic distribution of the environment ensures real-time execution without overruns. The event-related data is sent from the RT model to the Python server when the change in the states is observed in the environment. Python server is running in the host computer which reads, processes, and sends data every time an event occurs. In this section, closed-loop RT results are analyzed. All the RT graphs are based on the data logged by the RT simulator.

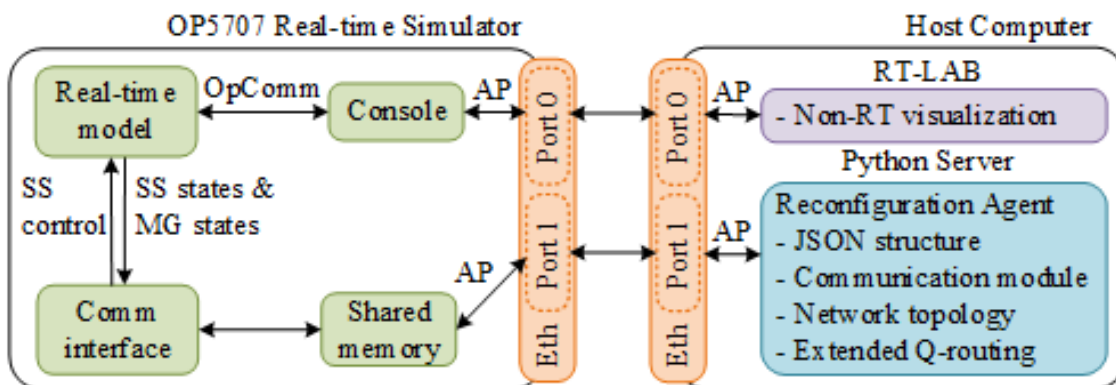


Figure 6.4: Real-time set-up to verify the dynamic reconfiguration framework based on event-driven communication. The event-driven communication platform is provided by OPAL-RT.

RT-LAB software from OPAL-RT, running in the host computer provides the interface between the user and the real-time simulator. During the simulation, RT-LAB shows the Console which establishes the communication with the real-time model by using an *OpComm* block as shown in Fig. 6.4. The Console shows the simulated results from the real-time

TABLE 6.3: Electrical parameters of the IBRs in the modified IEEE 123 node system. Five different sizes of IBRs are developed and placed at 15 various nodes in the modified IEEE 123 node distribution network.

IBR ratings, placements, and corresponding <i>LCL</i> filter parameters					
Symbols	node: 1	node: 21	node: 13, 28, 42, 59, 72, 108	node: 51, 64, 93, 86, 101	node: 82, 87
$P_i, Q_i$	300 kW, 200 kVar	240 kW, 130 kVar	210 kW, 120 kVar	180 kW, 100 kVar	120 kW, 60 kVar
$L_1, R_1$	293.9 $\mu$ H, 2 m $\Omega$	367.4 $\mu$ H, 2 m $\Omega$	420.1 $\mu$ H, 2 m $\Omega$	489.9 $\mu$ H, 2 m $\Omega$	734.8 $\mu$ H, 2 m $\Omega$
$L_2, R_2$	8.8 $\mu$ H, 1 m $\Omega$	11.1 $\mu$ H, 1 m $\Omega$	12.57 $\mu$ H, 1 m $\Omega$	14.6 $\mu$ H, 1 m $\Omega$	22 $\mu$ H, 1 m $\Omega$
$C_f, R_d$	172.6 $\mu$ F, 74.1 m $\Omega$	138.1 $\mu$ F, 92.7 m $\Omega$	120.9 $\mu$ F, 105.9 m $\Omega$	103.6 $\mu$ F, 123.6 m $\Omega$	69.07 $\mu$ F, 184.4 m $\Omega$

TABLE 6.4: System and controller parameters

System parameters		PC parameters (p.u.)		SC/RL parameters	
Symbol	Value	Symbol	Value	Symbol	Value
$V_{DC}$	900 V	$(k_p^P, k_i^P)$	(0.9,10)	$(k_p^v, k_i^v)$	(2,25)
$V_p$	480 V	$(k_p^Q, k_i^Q)$	(0.45,15)	$(k_p^\omega, k_i^\omega)$	(2,15)
$V_g$	4.16 kV	$k^V$	1	$(k_w^v, k_w^\omega)$	(1,1)
$\omega_g$	60 Hz	$(k_p^{vc}, k_i^{vc})$	(0.5,50)	$\gamma$	1
$N$	15	$(k_p^{cc}, k_i^{cc})$	(1,100)	$\epsilon$	0.1
$T_s^{pc}$	62.5 $\mu$ s	$I_{lim}$	1.5 p.u.	$\alpha$	0.98
$T_s^{sc}$	1 ms	$\omega_c$	63 rad/s	<i>episode</i>	1000
$T_r^{ss}$	40 ms	$\omega_o$	0.5 rad/s	$(c_d, c_{max})$	(1,10)

model and lets the user send the control signals to the real-time model. The communication for the reconfiguration uses the same Ethernet port as the communication of the Console but a different TCP port to establish the connection with the reconfiguration agent. The reconfiguration agent is developed in Python running from a Python server that is on the host computer of the RT simulator.

### 6.5.1 Implementation of Event-driven Communication

To implement the event-driven communication in the RT model of the IEEE 123 node distribution network, the TCP/IP-based Asynchronous Ethernet process is added. This communication is set as the TCP client which is initiating a connection with the Python server running on the host computer. According to the JSON template, which is a format of data defined in the Python server, the protocol of the communications in the RT model is modified to be compatible with this data format. Based on the design, this communication exchanges event-related data with the Python server when it is triggered by certain events in the RT model. From the RT model, all the required voltage and current measurements and active and reactive power calculations from transformers/regulators, capacitors, loads, SSs, and IBR are sent to the Python server. The data from the measurements and calculations are mapped based on the JSON template. The received data from the Python server to the RT model is also mapped according to the JSON template and sent to the corresponding elements in the RT model. After integrating the communication, the IEEE 123 node distribution model is tested in RT with the Python server. The event-driven data communication between the RT model and the Python server is verified as per the JSON template.

Modified IEEE 123 node network running in RT simulator, reconfiguration agent running in the host computer, and the communication between these two entities through port 1 are depicted in Fig. 6.4. The network model is run in RT, and when any fault is detected in the network, the TCP/IP-based communication is triggered by the event that sends new states to the reconfiguration agent. The default state of the network model is tied to Substation G1, and SS22, SS34, and SS76 are in *open* state maintaining the radial topology of the power distribution network.

### 6.5.2 Comparison Between the Q-routing and BFS Methods

For the performance evaluation, the proposed method and BFS-based method are executed in a Python Server with the Intel Xeon CPU clock frequency of 3.4 GHz and 32 GB RAM. The environment of Fig. 6.3 is considered and the path between a given grid node (G1 or G2) and an MG node is computed. Furthermore, the optimal path from Q-routing and BFS methods are recorded as shown in Table 6.5. BFS method computes static/dynamic adjacency matrix and node incidence matrix [136], implying the weights of the edges are the same. However, Q-routing considers the weights of the edges as per the formulation of Section 6.4.2. Hence, from Table 6.5, it is evident that when there exist multiple optimal paths, unlike BFS, the proposed method successfully detects them. However, the execution time of the proposed method is clearly higher than the BFS method. Improving the execution time of the proposed method is not in the scope of this work.

TABLE 6.5: Optimal paths from BFS and Q-routing methods, and comparison of execution times.

Grid Node	MG Node	Paths			Time (ms)	
		All	Q-routing	BFS	RL	BFS
G1	MG2	SS12 → SS11	SS12 → SS11	SS12 → SS11	36.7	4.8
		SS12 → SS23 → SS34 → SS54 → SS75 → SS17 → SS11				
		SS12 → SS23 → SS34 → SS54 → SS56 → SS76 → SS17 → SS11				
G1	MG3	SS23 → SS12 → SS11	SS23 → SS12 → SS11	SS23 → SS12 → SS11	45.8	7.4
		SS34 → SS54 → SS75 → SS17 → SS11				
		SS34 → SS54 → SS56 → SS76 → SS17 → SS11				
G1	MG4	SS34 → SS23 → SS12 → SS11	SS34 → SS23 → SS12 → SS11	SS54 → SS75 → SS17 → SS11	58.3	7.6
		SS54 → SS75 → SS17 → SS11				
		SS54 → SS56 → SS76 → SS17 → SS11				
G1	MG5	SS75 → SS17 → SS11	SS75 → SS17 → SS11	SS75 → SS17 → SS11	73.9	3.5
		SS56 → SS76 → SS17 → SS11				
		SS54 → SS34 → SS23 → SS12 → SS11				
G1	MG6	SS76 → SS17 → SS11	SS76 → SS17 → SS11	SS76 → SS17 → SS11	38.3	4.8
		SS56 → SS75 → SS17 → SS11				
		SS56 → SS54 → SS34 → SS23 → SS12 → SS11				
G1	MG7	SS17 → SS11	SS17 → SS11	SS17 → SS11	28.4	6.5
		SS57 → SS54 → SS34 → SS23 → SS12 → SS11				
		SS76 → SS56 → SS54 → SS34 → SS23 → SS12 → SS11				
G2	MG1	SS12 → SS22	SS12 → SS22	SS12 → SS22	54.2	7.1
		SS17 → SS57 → SS54 → SS34 → SS23 → SS22				
		SS17 → SS76 → SS56 → SS54 → SS34 → SS23 → SS22				
G2	MG3	SS23 → SS22	SS23 → SS22	SS23 → SS22	86.2	6.8
		SS34 → SS54 → SS57 → SS17 → SS12 → SS22				
		SS34 → SS54 → SS56 → SS76 → SS17 → SS12 → SS22				
G2	MG4	SS34 → SS23 → SS22	SS34 → SS23 → SS22	SS34 → SS23 → SS22	25.4	8.1
		SS54 → SS75 → SS17 → SS12 → SS22				
		SS54 → SS56 → SS76 → SS17 → SS12 → SS22				
G2	MG5	SS54 → SS34 → SS23 → SS22	SS54 → SS34 → SS23 → SS22	SS54 → SS34 → SS23 → SS22	76.8	5.1
		SS75 → SS17 → SS12 → SS22				
		SS56 → SS76 → SS17 → SS12 → SS22				
G2	MG6	SS76 → SS17 → SS12 → SS22	SS76 → SS17 → SS12 → SS22	SS76 → SS17 → SS12 → SS22	61.8	4.8
		SS56 → SS57 → SS17 → SS12 → SS22				
		SS56 → SS54 → SS34 → SS23 → SS22				
G2	MG7	SS17 → SS12 → SS22	SS17 → SS12 → SS22	SS17 → SS12 → SS22	26.9	6.1
		SS57 → SS54 → SS34 → SS23 → SS22				
		SS76 → SS56 → SS54 → SS34 → SS23 → SS22				

### 6.5.3 Sequence of Events

The sequence of events detected to evaluate the proposed reconfiguration method is shown in Fig. 6.5. In *case 1*, the fault event ( $e_1$ ) is simulated at 2 s in MG2 and the fault flag is cleared ( $e_2$ ) at 10 s. In *case 2*, fault event ( $e_3$ ) is simulated in MG1 at 22 s and the fault flag is cleared ( $e_4$ ) at 30 s. Lastly, in *case 3*, the fault ( $e_5$ ) is simulated in MG4 at 40 s, and the fault flag is cleared ( $e_6$ ) at 45 s. Each of the faults is an ABCG-type fault, with a fault impedance of  $1 \Omega$ , and a fault duration of 200 ms. Fig. 6.5 further verify the fault detection algorithms as the faults are detected only in the respective MGs where they are configured. A typical fault detection time is around 60 ms post the simulated time, as depicted in Fig. 6.7. This delay in detection is related to how fast the voltage drops below the threshold (0.88 p.u.), and a wait time of three grid cycles to avoid false fault detection due to the short-term transients.

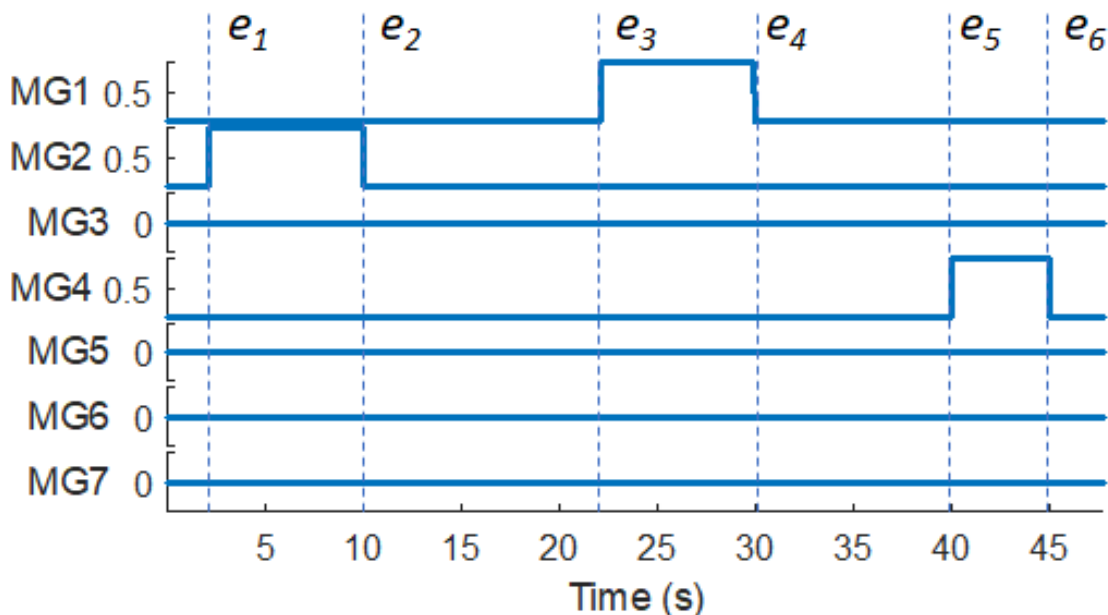


Figure 6.5: Fault event detection in the respective MGs. At every instance of the event, the data is communicated between the environment and the RL agent.

### 6.5.4 Behavior of the Environment and RL Agent Actions

The Behavior of the environment during events and the RL agent actions for optimal reconfiguration are graphically represented in Fig. 6.8. In *Case 1*, where the fault is simulated in MG2, post-fault detection boundary SSs open as shown in Fig. 6.8b. Once the RL agent receives the data from the environment due to the change in the state, the optimal path to connect back the healthy MG3 is computed as the closing of SS34 (see Fig. 6.8c). Once the fault flag in MG2 is cleared, MG2 is connected back to the network by closing SS12 (see Fig. 6.8d). From Fig. 6.6 it can be seen that fault in MG2 leads to the opening of SS12, and SS23 at 2.06 s resulting in islanding of MG2 and MG3 (see Fig. 6.9a). Detecting the event ( $e_1$ ), RL agent issues SS34 *close* signal received in the environment at 2.125 s and SS34 is closed at 3.265 s when grid synchronization conditions are met (see Fig. 6.6). Thus healthy

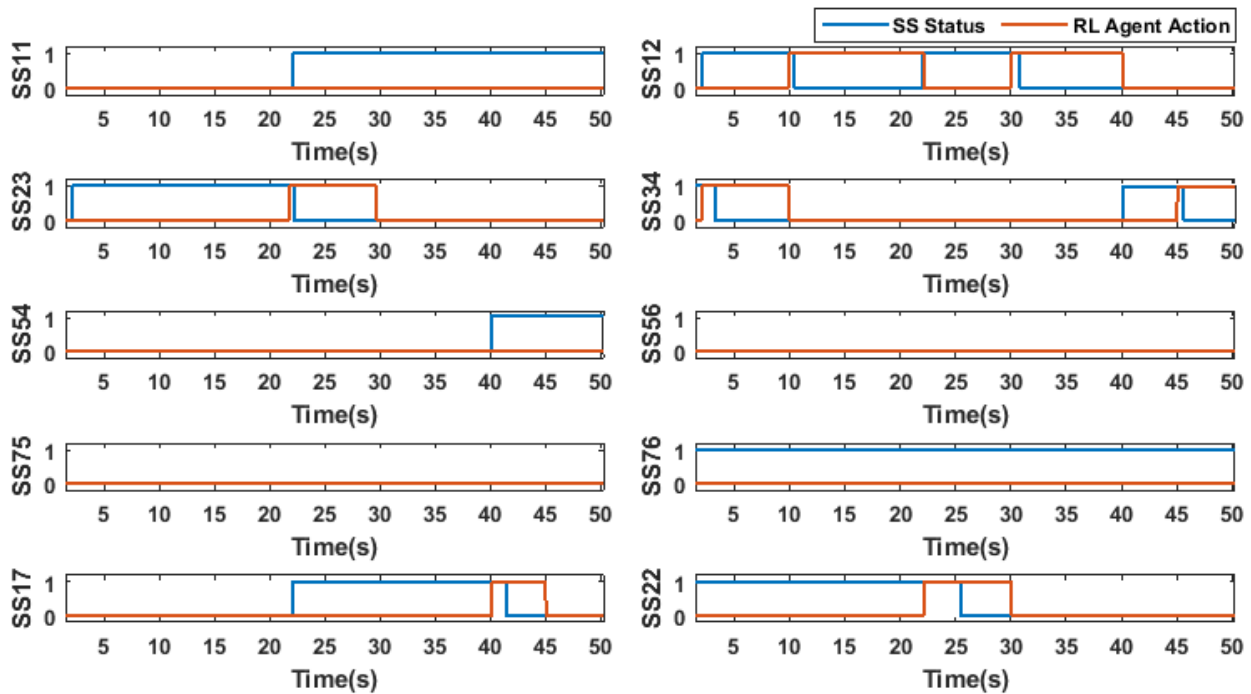


Figure 6.6: RL agent actions received at the environment, and closing of the corresponding SSs only after the grid synchronization conditions are satisfied.

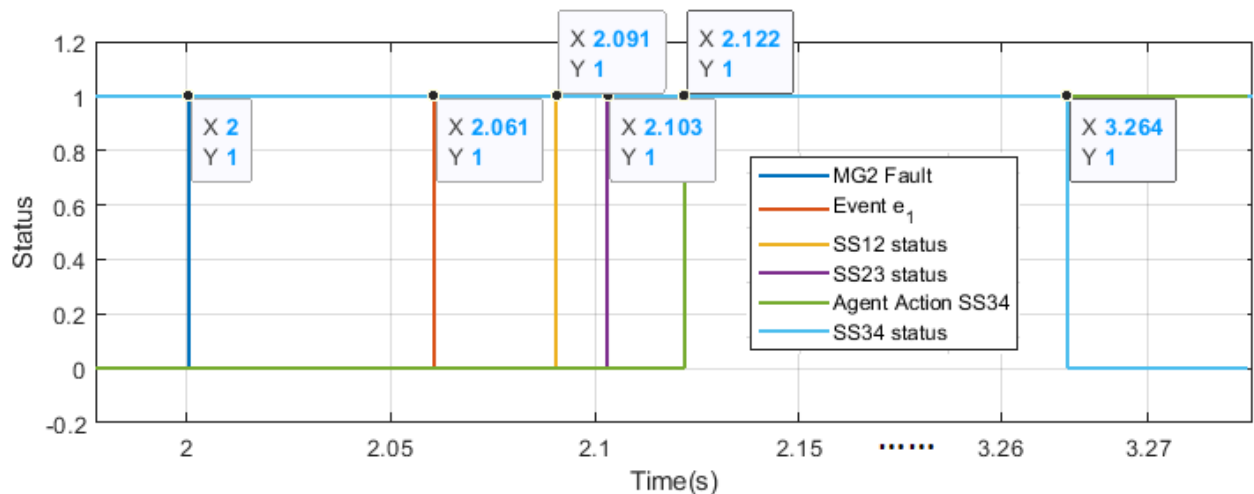


Figure 6.7: Timing analysis of fault detection (event), SS *opening*, closed-loop delay of RL agent actions, and *closing* of SS post grid synchronization.

MG3 connects back to grid post ( $e_1$ ). Once the fault flag is cleared ( $e_2$ ), MG2 connects back to the grid through the closure of SS12 (see Fig. 6.6 and Fig. 6.9a) at 10.6 s.

In *Case 2*, where the fault is simulated in MG1, post-fault detection boundary SSs open as shown in Fig. 6.8e. Once the RL agent receives the data from the environment due to the change in the state, the optimal path to connect back the healthy MGs is computed as the closing of SS22 and SS23 (see Fig. 6.8f). Once the fault flag in MG1 is cleared, MG1 is connected back to the network by closing SS12 (see Fig. 6.8g). From Fig. 6.6 it can be seen that fault in MG1 leads to the opening of SS11, SS12, and SS17 at 22.06 s resulting in islanding of all the MGs as the grid node is disconnected (see Fig. 6.9b). Detecting the event ( $e_3$ ), the RL agent issues SS22 and SS23 *close* signal received in the environment at 22.2 s. SS23 closes at 22.4 s and SS22 is closed at 25.45 s when grid synchronization conditions are met (see Fig. 6.6). Thus all the healthy MGs connect back to grid post ( $e_1$ ) at 25.45 s (see Fig. 6.9b). Once the fault flag is cleared ( $e_4$ ), MG1 connects back to the grid through the

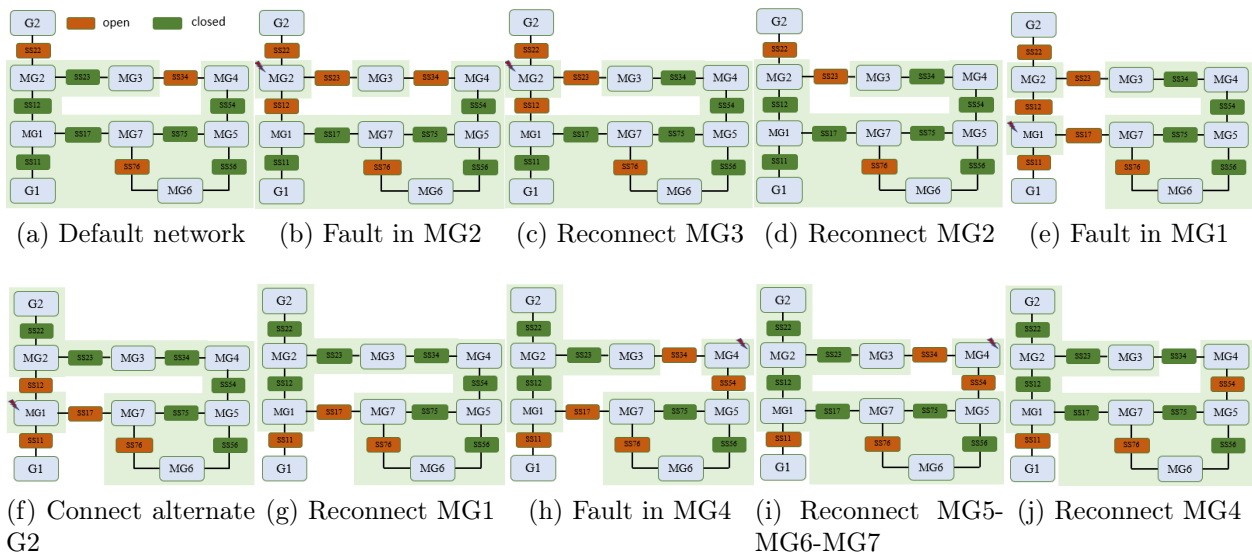


Figure 6.8: Graphical representation of the sequence of events, isolating faulty MG, reconnecting healthy MGs through the optimal action of the RL agent.

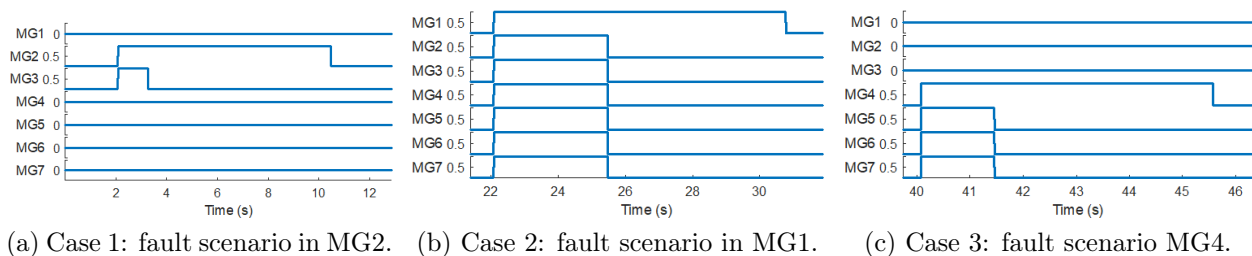


Figure 6.9: Islanding and grid connection of the MG nodes in the environment due to the simulated fault events and the action of RL agent respectively.

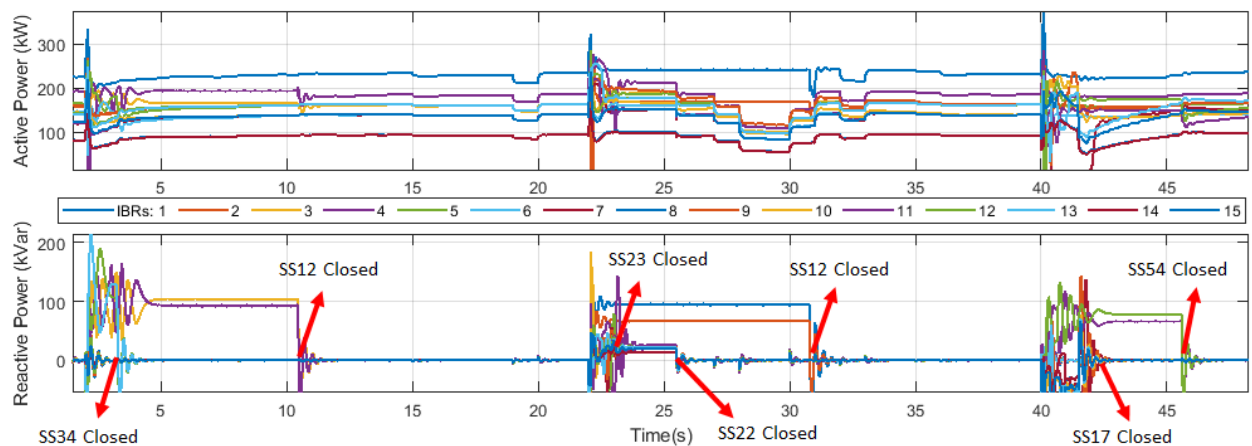


Figure 6.10: IBR active and reactive power graphs during case 1 through case 3. IN grid-connected mode IBRs operate in unity power factor mode delivering active power as per the MPP set-points. In islanded mode, IBRs share the loads in the respective MGs.

closure of SS12 (see Fig. 6.6 and Fig. 6.9b) at around 31 s.

In *Case 3*, where the fault is simulated in MG4, post-fault detection boundary SSs open as shown in Fig. 6.8h. Once the RL agent receives the data from the environment due to the change in the state, the optimal path to connect back the healthy MGs is computed as the closing of SS17 (see Fig. 6.8i). Once the fault flag in MG4 is cleared, MG4 is connected back to the network by closing SS34 (see Fig. 6.8j). From Fig. 6.6 it can be seen that fault in MG4 leads to the opening of SS34, and SS54 at 40.06 s resulting in islanding of the MG4, MG5, MG6, and MG7 (see Fig. 6.9c). Detecting the event ( $e_5$ ), RL agent issues SS17 *close* signal received in the environment at 40.15 s. SS17 closes at 41.4 s when grid synchronization

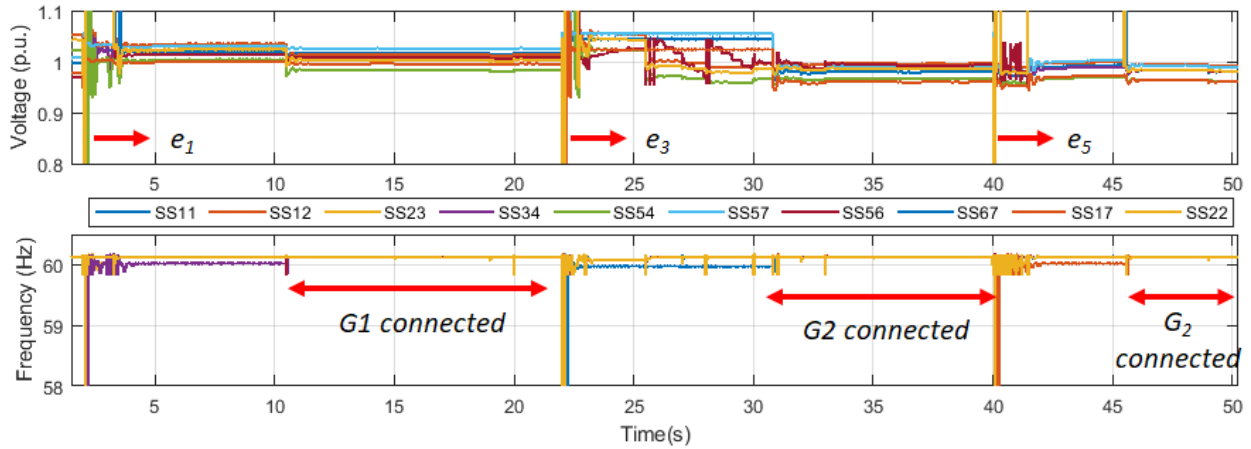


Figure 6.11: Voltage and frequency measured at each of the SS during *Case 1* through *Case 3*. Due to the ride-through capability implemented at PC, IBRs do not disconnect during short-term faults.

conditions are met (see Fig. 6.6). Thus all the healthy MGs connect back to grid post ( $e_1$ ) at 41.4 s (see Fig. 6.9c). Once the fault flag is cleared ( $e_6$ ), MG4 connects back to the grid through the closure of SS34 (see Fig. 6.6 and Fig. 6.9c) at around 45.5 s.

### 6.5.5 Timing Analysis during an Event

An example timing analysis is provided for ( $e_1$ ) of *Case 1* in Fig. 6.7. The LLLG fault is simulated at 2 s in the environment, and the fault detection algorithm detects the fault in approximately 61 ms. The rate at which voltage sag occurs in the environment, RMS voltage computation delays, and the protection algorithm execution time delays contribute towards the fault detection time. When the fault is detected and located, the decision to *trip* the faulty MG is taken and communicated to the RL agent. Actual tripping of the SS occurs in the environment after the modeled delay of  $T_r^{ss}$ . Therefore, in this case, SS12 and SS23 trip after 91 ms and 103 ms respectively, post the simulated time of the fault. RL agent issues SS34 *close* signal to achieve the optimal reconfiguration of the network and the environment receives this signal at 2.112 s. This leads to the closed loop cycle time of 61 ms post  $e_1$ , accounting mainly for the RL agent execution time of the proposed method in the closed loop. Actual closure of the SS34 occurs at 3.264 s, when the synchronization conditions are met in the environment. The network reconfiguration time of 1.2 s - 1.5 s is observed after the occurrence of events using the event-driven framework.

### 6.5.6 IBR Powers during Reconfiguration

The recorded IBR active and reactive powers starting from *Case 1* through *Case 3* are illustrated in Fig. 6.10. In grid-connected mode, IBRs operate in unity power factor mode and deliver active power as per the MPP power set-points. In islanded mode, IBRs share the active and reactive load power. From the figure, post-islanding reactive power sharing is evident and once the SSs are closed, IBR reactive power delivery goes to zero. In reference to the MG states as shown in Fig 6.9, corresponding stable power tracking/sharing is observed from Fig 6.10, across all the cases with reasonable transients.

### 6.5.7 MG Voltage and Frequency during Reconfiguration

In grid-connected mode, grid nodes are responsible for maintaining the voltage and frequency in the network, while in islanded mode, the secondary controller of the MGs regulates voltage and frequency to the nominal values. From Fig. 6.11 it is evident that the voltage and frequency are close to the nominal values and their dynamics reflect the change in the states of the environment. Only during fault duration  $e_1, e_3, \text{ and } e_5$  and fault recovery time (around 200-300 ms), both voltage and frequency deviate from the nominal values and are outside the thresholds mentioned in IEEE 1547-2018 requirement. At 41.5 s, and 45.5s when islanded MGs are connected back to the grid, short-term voltage magnitude transients (above 1.1 p.u.) are observed. Since the primary controller incorporates ride-through logic, IBRs continue to operate and post-fault recovery, voltages, and frequency are regulated to the nominal values. When the entire network is connected to G1 or G2, frequencies at all of the SSs are very close to each other as frequency is a global state and is maintained by the grid node.

## 6.6 Summary

In this chapter, the dynamic reconfiguration of networked MGs is showcased using the Q-routing method. RT event-driven closed-loop framework is established between the environment (IEEE 123 node networked MG model) and the RL reconfiguration agent (running in Python server) with a closed loop cycle time of around 60 ms. Through test cases, it is showcased that the MGs do not encounter long-term outages during short-term faults as the RL agent ensures closure of SS on the optimum path to the substation (including alternate substations). IBR powers in critical zones are observed to be stable and MG voltage and frequency are maintained close to the nominal values. Though the execution time of the proposed method is higher than the BFS method, the key advantage in comparison to conventional shortest path algorithms is that the proposed methodology is model-free and offers the adaptive discovery of multiple optimal paths in dynamic and large-scale networks.

## CHAPTER 7: Participation of Networked Microgrids in Energy-as-a-Service Model for Enhancing Grid Resiliency

*That which does not kill us makes us  
stronger.*

---

Friedrich Nietzsche

High penetration of DERs in the power distribution network has led to the emergence of networked MGs. A networked MG can be termed as an SoS, and in an SoS *only resilient systems can evolve*. The network of multiple MGs can bring value to end-users through the combination of technology aggregation and promising business models such as energy-as-a-service (EaaS). The technology deployment of networked MGs is feasible as more end users are willing to install in-house generation and storage either by owning or leasing the assets to reduce electricity costs and secure critical loads. In this chapter, the author presents the networked MGs with dynamic boundaries, technology aggregation, and resiliency service offering through a layered architecture of the EaaS delivery model. Such models can successfully match the distributed generation with highly dynamic local or neighboring loads with or without the availability of the grid. The author further develops a framework to offer resiliency-as-a-service to the end-users through resiliency metrics and emphasizes the need for sustainable business model innovation by big players, new players, and utilities to position themselves in the market.

### 7.1 Introduction

The impact of climate change has increased the frequency and severity of weather-related events globally. The year 2019 is the sixth consecutive year in which 10 or more billion-dollar weather and climate disaster events have affected the United States [1]. The prevailing electric power infrastructure is prone to disastrous events leading to larger power outages in a distribution system. The present power market and delivery model is highly centralized and vertically integrated. To enable grid resiliency under the circumstances, traditional reliability requirements such as contingency criterion (N-1, or N-2) are not sufficient to ensure the availability of power. Such measures are rather feasible for low-impact/highly-probable events than high-impact events [4].

Hence there is a need for peer-to-peer (P2P) power delivery and market mechanism to cater to the energy needs of the end user. Decarbonization targets due to the concerns of climate change and loss of traditional economies of scale have led to the rapid integration

of distributed energy resources (DER) in the power distribution systems [2]. The objectives of deploying an MG, such as economic benefits, sustainable generation and consumption, reliability, energy security, and resiliency during extreme weather events are implicit in the business case for the respective stakeholders [3].

A distribution system operator (DSO) over a secure communication network can manage the MGs within the same distribution system. MGs will be operating in parallel with the power grid until the grid fails due to a large disturbance or a severe weather event. Perceiving such events, either through a signal from DSO or self-detection, with acceptable transients MGs transition to islanded mode. In the islanded mode of operation, each MG has a grid-forming DER that regulates the MG voltage and frequency. To summarize, during extreme events, MGs can actively disconnect themselves from the main grid, and function as an autonomous entity to provide local power. In a distribution system, MGs with sufficient generation capacity can deliver power to the critical loads outside its boundary [190, 191]. The islanded MGs that are on the same distribution feeder and spatially close to each other can be connected to form a cluster that can function as a single islanded MG [170]. Thus, a networked MG is a cluster of interconnected MGs with a coordinated energy management system that can reduce the duration of power outages. Since the networked MG spans across a small geographical region, the restoration process during extreme events would be faster. Furthermore, it is feasible to automate some parts of the restoration process utilizing controllable breakers such as smart switches (SS) and transient management techniques [171].

The power distribution system is evolving towards a highly sustainable and resilient cyber-physical decentralized energy platform, where multiple MGs can be seamlessly interconnected. An aggregatory layer can be built to coordinate and distribute the energy and information in RT, enabling market opportunity for emerging business models such as the energy-as-service (EaaS) model. At the retail level, EaaS providers can offer solutions to commercial and industrial establishments to meet their energy supply, energy efficiency, power backup needs, and carbon reduction goals. At a neighborhood level, it could be the aggregator acting as a service provider, who can cluster several smart buildings or campuses into virtual MGs, link them to the DSO, and provide layers of load balancing and control [192].

In this chapter, the author reviews the opportunity for the networked MG to participate in the EaaS model to offer resiliency-as-a-service to the end user. By assessing the state-of-the-art technology as well as a business opportunity, the author has attempted to come up with a meta-delivery model that can pave the way for a disruptive business model in the context of grid resiliency enhancement. The technology potential and market opportunity for networked MGs are discussed in Section 7.2. In Section 7.3 layered delivery meta-model is proposed and

the services that can be offered including further investigation of the resiliency-as-a-service (RaaS) framework that can be integrated into the EaaS model. In Section 7.4 sustainable business model innovation that is enabled by EaaS architecture is discussed followed by the Conclusion in Section 7.5.

## 7.2 Technology Potential of Networked MGs

The usual objective of deploying MGs is to aggregate and manage existing on-site generation to cater to multiple loads within identified geographical boundaries. Typical categories of MGs include community-based, commercial or industrial, institutional, rural or remote off-grid systems, and military base MGs. In this section, the author discusses the recent advancement in technology that can enable dynamic connectivity among such MGs providing business value to the stakeholders.

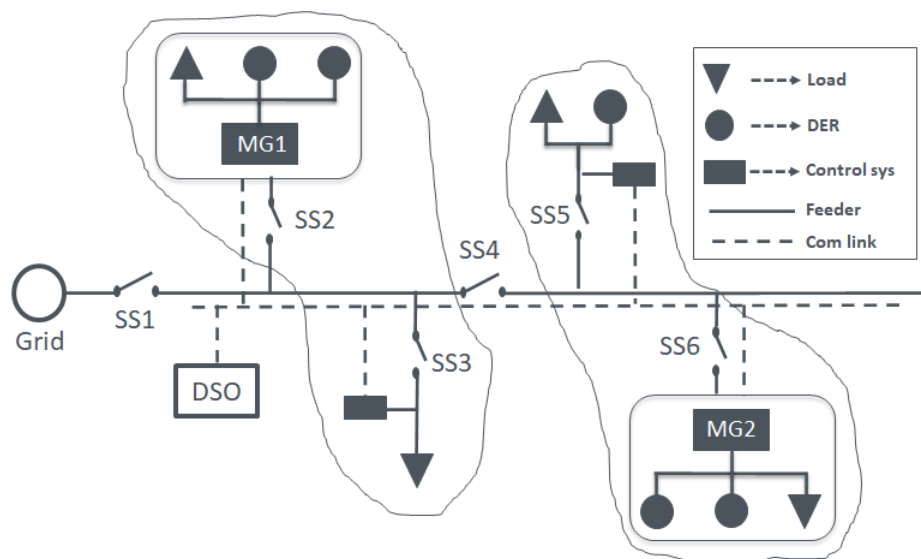


Figure 7.1: Simplistic representation of networked MG: as per the requirement networked MGs can dynamically expand or reconfigure their boundaries shown by cursive boundaries

### 7.2.1 Networked MGs in Distribution System

Fig. 7.1 depicts the simplistic representation of a distribution system feeder with a networked MG where multiple MGs, controllable loads, and controllable DERs can be interconnected and communicate with central DSO simultaneously. All the DERs in the distribution system can operate in a grid-connected during normal operating conditions and islanded mode during grid disturbances. MGs in the network have sufficient storage capacity so that they can be dispatched. DER connected at SS5 is variable renewable energy-based, having no storage facility such as rooftop photovoltaic (PV) and hence can not be dispatched. Each of the six smart switches can aid in dynamically sectionalizing the network based on the DSO commands.

During the normal operating condition, the exchange of power in the network is achieved based on the economic dispatch strategy. The objective of economic dispatch is to achieve the cost minimization of the supplied power [193]. The generation from a variety of DERs

can reach the load in any part of the network at a reduced cost. Smart meter driven advanced metering infrastructure (AMI) can facilitate dynamic pricing policies such as time of use, RT pricing in a P2P framework [194]. Thus, networked MGs can reduce the cost of electricity and enhance the reliability of the distribution system [195]. With the real-time demand requirement and DER supply capacity along with the historical data, it is possible to build efficient market mechanisms to achieve dynamic pricing. Moreover, the reliability of the network can be improved where the deficit power from any DER can be supplied directly through the other DERs with the surplus generation, or through the grid. When collective generation from DERs is more than load demand, power can be exported to the grid. Thus, networked MGs can reduce the cost of electricity and enhance the reliability of the distribution system [195].

It is also feasible to perform optimal power dispatch for an end-user-driven MG in grid-connected as well as islanded mode of operation [190]. When the grid is disconnected, one of the IBRs in the MG can operate in grid-forming mode and the rest of the IBRs operate in the grid-following mode within a designated electrical boundary. However, in the networked MG mentioned in Fig. 7.1 with curvilinear boundary, IBR modes, as well as the electrical boundaries, can dynamically change based on the availability and capacity of the DERs. Furthermore, SS4 can be operated to control the exchange of power between the two dynamic sections of the network. Control of such networked MGs is carried out with hierarchical architecture to improve the grid operation flexibility. Thus sectionalizing the grid with a networked MG can be achieved based on the optimal scheduling of grid resources and appropriate transient management [196]. This facilitates the efficient restoration of grid services at critical infrastructures during extreme events. Grid resiliency is defined as the reciprocal of the system's loss of performance [4] and networked MG reduces this loss and improves the grid resiliency significantly.

### 7.2.2 Market Needs and Underlying Opportunities

Alongside the advancement of communication and control technology, considerable cost reduction in DER technology paves a way for mass deployment for MGs. Solar Energy Technologies Office reports: in the U.S. DOE [48], the cost targets of solar electricity by 2030 are \$0.05/kWh, \$0.04/kWh, and \$0.03/kWh for residential, commercial, and utility-scale PV applications, respectively. These costs support greater affordability of DERs by lowering the solar energy costs by around 50% and battery energy storage costs in the range of 40-70% [49] around between 2020 and 2030. Such a dramatic cost reduction for DERs will trigger the increasing integration of MGs in the distribution system. The cost reduction in DER deployment has also led to the rise of prosumers such as house owners with rooftop PV, uninterrupted power supply (UPS), and electric vehicle (EV) owners. Large-scale small-

energy prosumers can be clustered into virtual MGs and can participate in networked MG operations. With the support of alternate energy sources, prosumers can reduce the cost of electricity and/or support their critical loads during the unavailability of grid power. Some of the prosumers own these energy assets, and operation and maintenance are provided by technology solution providers while some others may lease these assets. There is a gap in the market with respect to the overall cost and ownership of DERs, that can be addressed with a disruptive business model, provided an appropriate business case is identified. New business models should justify the cost, ownership, and revenue of DER-based MG deployment, and regulatory bodies should design incentives and subsidies to increase the prosumer base.

### 7.3 EaaS Delivery Model for the Networked MG

EaaS is an emerging delivery model for the end-users who are residential, commercial, and industrial building owners. EaaS service provider usually owns as well as manages the assets and associated system. In this structure, end users are relieved from the high expenditure for purchasing the assets upfront and also from subsequent repair and maintenance costs. Usually, EaaS offers energy efficiency services and demand management through cutting-edge digital technology and analytics. In this section, the author discusses the architecture and properties of the delivery model for the manifestation of networked MGs to enhance grid resiliency.

#### 7.3.1 EaaS Delivery Model Architecture

The EaaS delivery model bundles a heterogeneous system to a single service offering personalized as per the requirements of the end-user. Depending on the EaaS service types, the market is primarily segmented into energy supply services, operation, and maintenance services, and optimization and efficiency services [197]. The author focuses on resiliency-related services vastly categorized under the operation and maintenance service segment. The EaaS delivery meta-model is described in Fig. 7.2, as a layered architecture to offer the identified services. The relevance of this dissertation is provided at each of the layers.

The edge layer represents the distributed energy system analogous to Fig. 7.1. This layer is an interconnected system consisting of various devices and assets such as DERs, controllers, phasor measurement units (PMU), gateway, smart meter, smart switches, controllable load, and others. Every device belonging to different end-users would have its application, such as EV charging, storage management, demand management, and various others. Alongside this, devices would differ in hardware resources, operating systems, and capabilities posing challenges of integration. This challenge is addressed by cyber-physical systems of interoperable connected devices [198], that adopt edge computing technology backed with reliable and efficient software-defined networks (SDN). The data distribution service (DDS) based

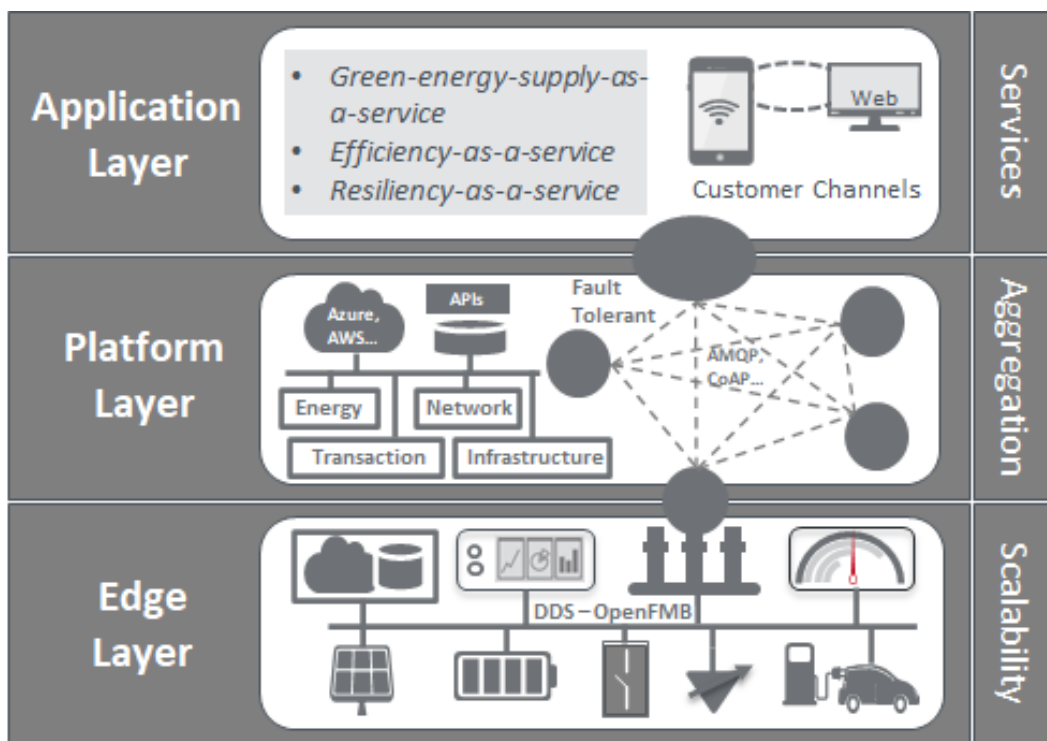


Figure 7.2: Three layer EaaS delivery model along with primary properties of each of the layer

databus supporting the OpenFMB smart grid data model is one of the verified approaches to develop scalable and inter-operable edge layers [199]. The deployment of such an edge layer would decrease the cost of high availability power, improve operation continuity, and fasten disaster recovery during high-impact events through appropriate service agreements. In EaaS service provisioning, multi-device support will be the key differentiator in scaling the system cost-effectively. In the context of this dissertation, device-level, and MG-level technology solutions (Chapters 3 through 5) can be executed as a part of the edge layer.

The platform layer aims at aggregating the edge devices and technology through the internet of things (IoT) as a backbone network using protocols like advanced message queuing protocol (AMQP), the constrained application protocol (CoAP). By utilizing cloud computing ecosystems (Microsoft Azure, Amazon AWS, and others), an integrated development environment (IDE) developers can build APIs featuring scalability, high availability, and multi-tenant capability. Such ecosystems also provide tools to analyze and mine power grid data, gain insights and identify patterns through learning from historical and online data, and make appropriate decisions on the operation and condition of edge devices. The composition of the edge layer encompasses the heterogeneous system presenting a challenge for the seamless interworking of the EaaS model. While the platform layer through technology aggregation, efficiently manages multi-user, multi-application, multi-technology-based decentralized systems. The main components of the platform framework would be network and security management, energy distribution management, transaction management, and critical infrastructure management. Such a platform framework can perform system-wide analyses and predictions based on history as well as online data by coordinating with edge devices. The platform layer is also responsible for handling device and communication fail-

ures seamlessly, updating the current applications, and maintaining network redundancy and data lineage. In the context of this dissertation, a network-level technology solution (Chapter 6) can be executed as a part of the platform layer.

The application layer is designed to offer the services as per the end-user requirement interfaced through channels such as mobile and web applications. Through service offering, the EaaS model should aim at owning the end-user relationship as well as being able to scale that relationship. Green energy-supply-as-a-service is provided by selling renewable energy credits (RECs) to the interested end-users who can not produce in-house renewable generation. Every REC is uniquely numbered and contains information on where it is generated and the type of renewable resource. The EaaS model can facilitate the buying and selling of such RECs along with the exchange of RECs being tracked and recorded. Efficiency-as-a-service is more of demand-side management with a focus on effective ways of lighting and air condition management, building automation, and asset monitoring and upgrades. Using the EaaS delivery model that incorporates system-wide energy storage and energy management, novel efficiency measures can be offered to the end-users as a part of this service. RaaS offerings are typically designed to support guaranteed higher standards of the asset and operational reliability. In this dissertation, a basic operational resiliency framework is attempted, however, a thorough investigation of this research topic is identified as the future scope of work in Chapter 8.1.

### 7.3.2 Resiliency-as-a-Service Framework

Power system resiliency can be classified as operational resiliency and infrastructure resiliency. Both classifications are based on different indicators proposed in [200] can be quantified into multi-phase resiliency trapezoid metrics. Infrastructure resiliency refers to the physical strength of networked MGs for mitigating the portion of the system that becomes nonfunctional. This can be enhanced at the planning phase through infrastructure hardening [201] and the optimal size and location of flexible resources such as battery storage [202]. RaaS framework is intended to enhance the operational strength of networked MGs which requires temporal resiliency metrics identification pre and post-extreme events.

The author proposes a RaaS framework as shown in Fig. 7.3 considering the resiliency service requirements of the end-user [3] that are interfaced through web services. The performance of these services can be enhanced through learning, optimization, coordination, and prioritization techniques developed at the platform and edge layer of the EaaS delivery model. Operational resiliency is enhanced by enforcing predictive and preventive conditions during the normal operation of the distribution system that enables the system to prepare and adapt to the impacts of extreme events. The robustness of the system signifies the ability of the system to sustain a disturbance event, while the time and effort needed to return to

a pre-disturbance level are attributed to a restorative condition. When the extreme event is ongoing, and the grid has poor power quality or is disconnected, participating MGs in RaaS can coordinate as well as ride-through disturbances to offer uninterrupted services.

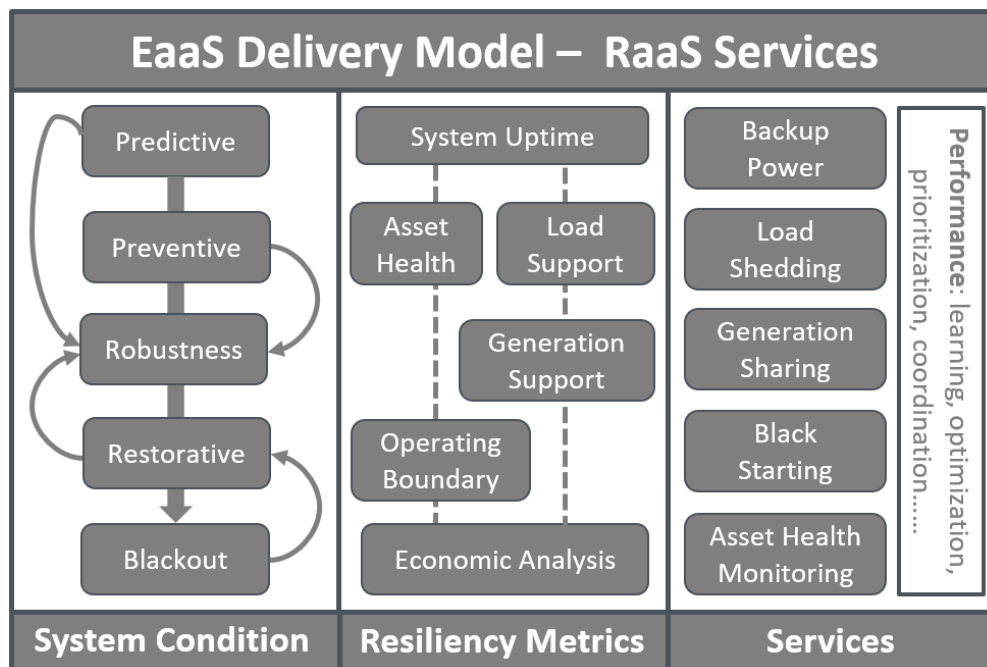


Figure 7.3: RaaS framework considers the system conditions, metrics, and the services offered to the end user to mainly enhance the operational resiliency of the entire system.

After the extreme events system must undergo restorative conditions, which is identified as the function of resourcefulness. In this condition, the utilization of materials such as monetary, technological, informational, and human resources are optimized to establish, prioritize, and achieve the operational goals to the level of pre-disturbance condition [203]. In the final stage, due to long-duration power outages, the distribution system gets de-energized leading to blackout conditions. MGs with black-start capability can first support their electrical boundaries before providing additional cranking power to DERs in other MGs, as well as energize the power network. Resiliency metrics are used to effectively and systematically quantify the resiliency of a networked MG integrated distribution system subject to an extreme event [200, 201, 204]. Fig. 7.3 reflects different resiliency indicators (such as system uptime, and load support) that can be used for expressing and quantifying the operational resiliency levels pre and post-extreme events. The development of resilient metrics may include but is not limited to (i) identifying an area within the distribution system boundary (miles); (ii) an aggregated health index of underlying assets (%); (iii) the amount of generation and load support (kW) from the networked MG; (iv) pre and post extreme event system up-time (hours) contribution; (v) overall economic analysis for the designated end-user (\$). Including the indicators of different dimensions aid in capturing distinct properties of the system that would enable building more precise resiliency metrics.

### 7.3.3 Demonstration of Load Support Use Case

Two MG systems, MG1 and MG2 are installed at node 1 and node 13 respectively, in a section of the IEEE 123 bus system as depicted in Fig. (7.4) (a). MG1 capacity is of 500 kVA generation with priority support to the local load of 100 kW, 10 kVAr while MG2 has a capacity of 200 kVA with priority support to the local load of 50 kW, 10 kVAr. The objective of the test case is to test the resiliency level (RL) of the identified system for at-least 50%, and the load restoration algorithm is implemented accordingly. In the grid-connected mode of operation, RaaS framework does not play its role, and RL is assumed to be 100%. The dynamic model as well as part of the RaaS framework is implemented using MATLAB/Simulink tool and Fig. (7.4) (b) depicts the workflow.

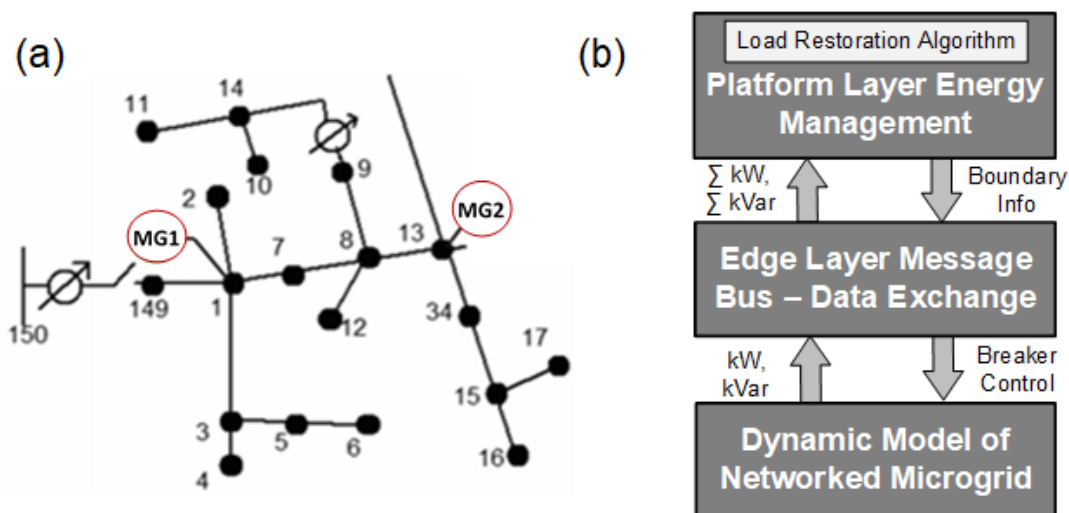


Figure 7.4: (a) Section of IEEE 123 bus system with two of MGs at node 1 and 13 (b) Workflow for achieving desired RLs in a desired system.

Section of IEEE 123 bus model has a total load of 550 kW, 220 kVAr, including the local load of MGs at node 1 and node 13. Clustered load in the system is prioritized (P1 to P4) based on the nature of the load and customer subscription. From high to low priority clustered load is described in Table 7.1 along with the associated nodes and up-time. The test system undergoes two extreme events: the first event causes breaker at node 149 to open at 4s, leading to an islanded system; the second event causes MG2 to shut down at 6s and is restored at 8s as seen from Fig. 7.5. Upon islanding MG1 and MG2 share, the load in the system until 5 s hence the RL of the system is 100% even in absence of a grid. Furthermore, after the loss of MG2 generation at 6s, MG1 supports the P1 load cluster, including the local load of MG2. Up-time of load clusters are recorded in Table 7.1, and from Fig. 7.5 it is observed that RL (reciprocal of the system's loss of performance) is at least 50% at any given point of time post islanding.

TABLE 7.1: Critical load clustering in the section of IEEE 123 bus system.

Cluster Up-time	Nodes of Test System	Load Power (P, Q)
P1: 4s - 10s	1, 2, 7, 8, 12, 13	(250 kW, 70 kVar)
P2: 4s - 7s, 9s - 10s	9, 10, 11, 14	(100 kW, 50 kVar)
P3: 4s - 6.2s	15, 16, 17, 34	(100 kW, 50 kVar)
P4: 4s - 5s	3, 4, 5, 6	(100 kW, 50 kVar)

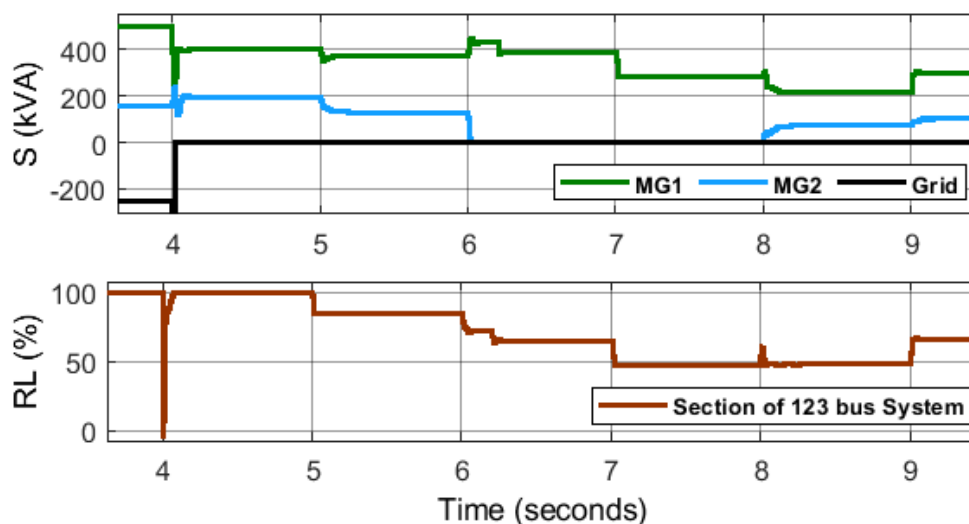


Figure 7.5: Critical load support use-case in a section of IEEE 123 bus system.

#### 7.4 Need for Sustainable Business Model Innovation

The capability to quickly and successfully move into new business models is key leverage to improve the sustained performance of any business organization. Conceptualization and implementation of sustainable business models can comprise the development of entirely new business models, diversification into additional business models, the transformation from one business model to another, or the acquisition of new business models [205].

Big players in the market such as technology providers and original equipment manufacturers (OEM) may consider re-structuring their product portfolio to fulfill the market requirements of MGs. There is a strong need for OEMs to shift from being product-centric to platform-driven service provisioning. Enhancing the levels of digitization across products and building novel services utilizing cloud platforms will help in systematic aggregation to achieve P2P transactive power delivery. Such measures would lead to novel, diversified, or transformed business models for OEMs. In alignment with the product roadmap, OEMs may acquire start-ups leading to the acquisition of new business models. Technology solutions necessarily should support a secure, interoperable, self-healing, robust hardware/software platform that can scale cost-efficiently, with increasing numbers of MG nodes [206]. In the context of the RaaS framework, the need of the hour is to systematically outline the

requirements at national and regional levels and address the interoperability challenges.

Start-ups are focused on developing solutions in cutting-edge technology areas such as blockchain-based decentralized energy trading platforms, achieving system-wide efficiency, and resiliency using big data and machine learning. Start-ups in collaboration with utilities and OEMs, may attempt to use disruptive web-based digital service platforms, to facilitate the sharing of DERs for the support of critical infrastructure, in a highly scalable way, thus may dynamically create resilient EaaS areas, thereby creating an entirely new market segment. Nevertheless, technology solutions from OEM and start-ups necessarily should support a secure, interoperable, self-healing, robust hardware/software platform that can scale cost-efficiently, with increasing numbers of MG nodes [206].

Utility franchise agreements, and local and state regulations provide the privilege to the incumbent utility over electricity sales and distribution infrastructure. This limits private MG owners from supplying energy to the third-party infrastructure [207]. EaaS providers can bring in the technology aggregation platform and resiliency service offerings to systematically identify revenue streams that would benefit utilities and themselves. Since the networked MG-based EaaS provider utilizes distribution system infrastructure, the entire ecosystem involves multiple entities with heterogeneous ownerships. There is a strong requirement for mutual agreements and interoperability standards to support critical infrastructure. Moreover, it is foreseeable that electricity assets at the end-user site will be owned, operated, and maintained by EaaS providers. The end users would end up paying a significantly lesser amount - mainly for the services, while the assets act as the resources in the EaaS model utilized for providing service to multiple end users.

For the operation of the networked MG, one of the MGs in the network has to support the loads owned by other MG entities, over a utility-owned conductor, for which the utility might grant franchise benefits to respective MG owners. The prevailing utility infrastructure would need costly upgrades, additional energy storage facilities, and modifications to protection schemes which must be addressed by identifying the right business case for utilities in collaboration with EaaS provider. Incumbent utility policies and planning practices must evolve to meet the increasing challenges and opportunities of large-scale MGs.

The electricity market comprises diversified stakeholders, wherein networked MG technology can offer a cost-efficient multi-sided platform model that will allow all parties to both create and extract value. EaaS providers can bring in the technology aggregation platform and resiliency service offerings to systematically identify revenue streams that would benefit utilities and themselves. Since the networked MG-based EaaS provider utilizes distribution system infrastructure, the entire ecosystem involves multiple entities with heterogeneous ownerships. There is a strong requirement for mutual agreements and interoperability stan-

dards to support critical infrastructure. Moreover, it is foreseeable that electricity assets at the end-user site will be owned, operated, and maintained by EaaS providers. The end users would end up paying a significantly lesser amount - mainly for the services, while the assets act as the resources in the EaaS model utilized for providing service to multiple end users.

### 7.5 Summary

In this chapter, the author reviewed the technology potential of networked MGs to enhance the grid resiliency and manifestation of the EaaS model to offer resiliency services to the end-users. The author emphasizes the design of the delivery model for achieving resiliency enhancement and through our proposed meta-model and demonstrated the use case of critical load support. Future research activities on resiliency services may include end-user consent-based backup power support, black start support, load shedding, and generation sharing, and full-scale deployment of the proposed framework. The EaaS model can foster the market for resiliency services. To participate in resiliency services, the model can improve the market readiness level of MGs, which are often operated independently. The regulatory framework and ownership agreements need to evolve to support the delivery model acceptable to all the involved stakeholders. To maximize the revenue for technology and service providers, sophisticated technology aggregation must be achieved and cost structure, as well as cost estimation of resiliency services, must be framed through systematic economic analysis.

## CHAPTER 8: Conclusions

*Imagination is more important than knowledge. For knowledge is limited to all we now know and understand, while imagination embraces the entire world, and all there ever will be to know and understand.*

---

Albert Einstein

Contemporary electric power technology providers are facing unique challenges at multiple spatiotemporal scales due to the large-scale distributed energy resources (DER) integration into the power distribution network. Every stakeholder in the ecosystem has to be determined to advance the existing and new critical infrastructure for the greater benefit of society as a whole. Continuous stakeholder engagement is needed to generate the values such as stability, safety, power quality, and economic benefit to the end users. In this dissertation work, control technology challenges are identified, classified, and addressed in decentralized hierarchical procedures. The technology solutions provided herein are applicable to both immediate (DER and microgrid level) and futuristic (network level) problems.

A prime aspect of the immediate research problem is the design of the primary controller facilitating the coexistence of multiple DERs in an unbalanced grid with multiple operating mode capabilities. This problem is addressed in Chapter 3, through a unified control architecture which is verified in an unbalanced system using the detailed converter switching-based real-time model. Through the simulation results, four main capabilities of the architecture are showcased. Firstly, utilizing positive sequence power control laws, DERs can share load power accurately and the network voltage and frequency are maintained at nominal values. Secondly, a negative sequence power control strategy, mitigation of second harmonic power ripples is demonstrated during unbalanced fault scenarios. Thirdly, inverter-based resource (IBR) capabilities to meet the ride-through requirement for both types of IBRs are showcased. Lastly, stable operation of the network is achieved during seamless mode transitioning and during dynamic IBR-type change. The solution offered for DER primary control problems provides a great deal of autonomy to the DER management system to conduct network-level operations. The performance of the proposed solution is in good agreement with the IEEE 1547-2018 standards and the grid codes.

In Chapters 4 and 5, another aspect of the current research problem of secondary control in microgrids (MG) is addressed. A decentralized secondary frequency and voltage control of MGs is proposed utilizing a model predictive control framework. The frequency restoration solution is demonstrated without the need for communication, and the design is robust against measurement errors and system disturbances. Though voltage restoration requires a communication network, scalability and tolerance towards traffic congestion are showcased considering higher communication latency. A generic, straightforward design, robustness against system faults using the constraint integral model predictive control (IMPC) framework, and plug-and-play capability enable stable operation of 100% IBR-based autonomous MGs in the distribution grid. The framework is further extended to cases where IBR model parameters are unavailable. This extension is based on the proposed decentralized online system identification and state estimation technique mapped to the identification-based IMPC (IIMPC) framework. This framework is as well validated in a real-time environment for the identified use cases and a superior restoration performance is showcased.

The distribution network is evolving with sectionalization and reconfiguration of the network with the help of reclosures and other protection devices. The future is near where such technology has to be improved when 100% IBR-based network operation is a possibility. To address the long-term research problem of optimal network reconfiguration in presence of multiple networked MGs, a reinforcement learning (RL) agent is explored to facilitate appropriate optimal action post-event in the network. The entire agent-environment interaction is showcased through an event-driven communication-based real-time test environment in Chapter 6. Through multiple sequential event-based use cases, a closed-loop reconfiguration time of a few hundred ms is demonstrated. Furthermore, stable power sharing among IBRs and healthy voltage and frequency in the network are showcased before and after the event in the network. Lastly, the commercialization of proposed technology solutions requires a delivery model that ensures all the relevant services are offered to the end user. A bird's eye view of a three-layer delivery model is presented in Chapter 7, with a simple demonstration of the load restoration use case. The achievement of a target resiliency level of 50% is showcased through the load prioritization verification process. Though a simplified test case is performed to demonstrate the underlying concept, a more sophisticated formulation of resiliency enhancement is needed considering network-level constraints. The majority of the contributions of the dissertation work are technical in nature and related to the interdisciplinary domain of power, control, and communication technology. However, as a concluding remark in Chapter 7, the author makes an honest attempt to emphasize the need for sustainable business model innovation for the sustainable power grid for the betterment of the future of human society.

## 8.1 Future Research Directions

The main contribution of the dissertation work is to assure stability and enhance resiliency in the modern power distribution network through a hierarchical decentralized control approach. The relevant theoretical treatment alongside the controller design methodology is provided to achieve the defined control goals. Since the power network is ever-changing, new problems and concerns definitely draw attention from interdisciplinary research groups focused on control theory, power system theory, machine learning, communication technology, and electricity markets. The focus of the dissertation is on the selected research problems at different levels, hence provisioning for the future scope of work. The unified architecture proposed in Chapter 3 is very specific to the DERs in the distribution network, hence may not be generalized to other domain problems. However, optimal control and reconfiguration methods proposed in Chapter 4 through Chapter 7 are generic enough to find application in other domains. Future research directions (not necessarily comprehensive) identified during the concluding time of this dissertation are described below.

- **Grid support functions and anti-islanding schemes:** the proposed approach in Chapter 3 requires measurements at PCC and SS nodes that are usually readily available in the power grid. The remote parameters such as load sharing set-point, SS status, and synchronization error signals are communicated to the IBR controller through the appropriate communication network. Controller robustness to the communication latency is showcased through appropriate delay modeling of the underlying communication network. In case of communication failure and if the system voltage and/or frequency are not within the acceptable range as per IEC 1547 guidelines, islanded system needs to be shut down. Current limiter specific to functionality and applications can be designed on top of the proposed architecture such as P-priority, and Q-priority. However, this is beyond the scope of this dissertation work. Future research work may align with the investigation of the supply of reactive power by the IBRs during low-voltage ride-through. Furthermore, the disconnection and reconnection with islanding detection when there are harmonics/nonlinear loading conditions and other abnormalities qualify for future research work.
- **Communication-free decentralized voltage regulation:** in Chapter 4 and Chapter 5, communication-free decentralized voltage regulation is demonstrated, through a model-based and data-driven approach. However, in both approaches voltage regulation requires a global measurement at the POI and the measurement data needs to be communicated to all the decentralized control subsystems. However, robust decentralized control solutions should avoid dependency on any type of communication

network. The network model-based decentralized approach is one direction available in the literature [146,157]. As the network size increases, the solution is computationally expensive to deploy on grid edge devices. Therefore, a physics-inspired learning approach [208,209] can be a good candidate to investigate the estimation of POI voltage utilizing the point of common coupling (PCC) measurements without any dependency on the communication network.

- **Robustness of IMPC and IIMPC framework towards the time-varying non-Gaussian noise:** The IMPC and IIMPC framework proposed in Chapter 4 and Chapter 5 respectively utilizes a decentralized estimation designed by applying an extended Kalman filter to achieve the dynamic synchronization of system states. The proposed controller performance is verified for the Gaussian noise with fixed variance. Investigation of the proposed estimator performance for the time-varying noises (such as the heavy-tailed Laplace or Cauchy noise) and improving the estimator to tackle such noises have practical significance. It is also worth noting that oscillatory modes identification is one of the applications where accurate estimation of time-varying and non-Gaussian noises is necessary.
- **Extending IMPC/IIMPC framework when voltage and frequency states are partially observable:** the proposed IMPC/IIMPC framework requires observability of frequency at PCC and POI nodes. In this dissertation work, the author assumes these states are observable, and usually, in real-world networks, voltage and frequency are observable at nodes such as PCCs and POI. In the context of the emergence of a large-scale prosumer base (with rooftop PV, electric vehicles, etc.), behind the meter produced electricity is directly supplied to the homes and buildings. Further research investigation is necessary to advance the IMPC/IIMPC framework to be suitable for the behind-the-meter with a possible improvement to state estimation methodology.
- **Large-scale network optimal reconfiguration for resiliency enhancement:** in Chapter 6, the proposed RL-agent-based reconfiguration is verified in an event-driven real-time environment. When a large-scale network such as 2500 node distribution system is considered, resiliency enhancement can be formulated as a two-level optimization problem. At the first level, the proposed Q-routing can be further extended to include different weights for the edges of the network. At the second level, an optimization problem can be formulated to assign appropriate weights to the edges by considering power network level constraints, load priorities, and economic evaluation. Though the Q-routing approach is suitable for cyclic and acyclic networks, the benefits of adopting the proposed method for meshed power networks need further investigation.

- **Design of a value-sensitive RaaS framework:** in Chapter 7, an overview of the resiliency-as-a-service (RaaS) framework is provided considering the deployability of networked-MG as a technology solution. A sophisticated value-oriented framework can be further designed through risk and price modeling. The risk model can be a function of the criticality levels of the assets derived based on the resiliency metrics. Moreover, real-time risk modeling can consider environmental conditions as another parameter to dynamically assess the risk associated with assets. On the other side, price modeling can be a function of solution cost. The solution cost can be obtained from various criteria such as energy requirements for the asset class, the average duration of power outages, customer tolerance towards the risk, and various others. The derived solution cost needs to be quantified and further utilized to define a trade-off between risk and cost the end user willing to opt for. Building and connecting the risk and price models can be the first step towards a value-sensitive RaaS framework that can benefit involved stakeholders immediately as well as in the long term. The framework can be continuously improved through continual tracking of framework performance by discovering the prevailing inefficiencies and eliminating them.

## CHAPTER 9: List of Publications

1. A. Ingalalli, S. Kamalasan, Z. Dong, G. Bharati and S. Chakraborty, "An Extended Q-routing-based Event-driven Dynamic Reconfiguration of Networked Microgrids," 2022 IEEE Industry Applications Society Annual Meeting (IAS), 2022, pp. 1-6, doi: 10.1109/IAS54023.2022.9939942.
2. A. Ingalalli and S. Kamalasan, "Decentralized State Estimation-based Optimal Integral Model Predictive Control of Voltage and Frequency in the Distribution System Microgrids," in IEEE Transactions on Smart Grid, 2022, doi: 10.1109/TSG.2022.3220714.
3. A. Ingalalli and S. Kamalasan, "A Novel Sequence-based Unified Control Architecture for Multiple Inverter Modes of Operation In Unbalanced Distribution System," in IEEE Transactions on Power Delivery, 2022, doi: 10.1109/TPWRD.2022.3210151.
4. A. Ingalalli and S. Kamalasan, "A Universal Multiple Inverter Control Architecture with Droop For Unbalanced Distribution Grid," 2021 IEEE Power Energy Society Innovative Smart Grid Technologies Conference (ISGT), 2021, pp. 1-5, doi: 10.1109/ISGT49243.2021.9372208.
5. A. Ingalalli and S. Kamalasan, "Participation of Networked MGs in Energy-as-a-Service Model for Enhancing Grid Resiliency," IEEE Power Energy Society Innovative Smart Grid Technologies Conference, 2021, pp. 1-5, doi:10.1109/ISGT49243.2021.9372223.
6. A. Ingalalli and S. Kamalasan, "An Integrated State-Space Model For Grid Feeding and Grid Forming Inverters," IEEE International Conference on Power Electronics, Drives and Energy Systems, 2020, pp. 1-6, doi: 10.1109/PEDES49360.2020.9379872.

## REFERENCES

- [1] “NOAA National Centers for Environmental Information (NCEI), *U.S. Billion-Dollar Weather and Climate Disasters* (2020), <https://www.ncdc.noaa.gov/billions/>, (accessed: 09.02.2020).”
- [2] R. H. Lasseter, “Smart distribution: Coupled microgrids,” *Proceedings of the IEEE*, vol. 99, no. 6, pp. 1074–1082, 2011.
- [3] “IEEE Standard for the Specification of Microgrid Controllers 2030.7-2017, [https://standards.ieee.org/standard/2030\\_7-2017.html](https://standards.ieee.org/standard/2030_7-2017.html), (accessed: 09.02.2020).”
- [4] Z. Li, M. Shahidehpour, F. Aminifar, A. Alabdulwahab, and Y. Al-Turki, “Networked microgrids for enhancing the power system resilience,” *Proceedings of the IEEE*, vol. 105, no. 7, pp. 1289–1310, 2017.
- [5] B. Chen, J. Wang, X. Lu, C. Chen, and S. Zhao, “Networked microgrids for grid resilience, robustness, and efficiency: A review,” *IEEE Transactions on Smart Grid*, vol. 12, no. 1, pp. 18–32, 2021.
- [6] A. Ingalalli and S. Kamalasadani, “Participation of networked microgrids in energy-as-a-service model for enhancing grid resiliency,” in *2021 IEEE Power Energy Society Innovative Smart Grid Technologies Conference (ISGT)*, pp. 1–5, 2021.
- [7] T. Dragicevic, D. Wu, Q. Shafiee, and L. Meng, “Distributed and decentralized control architectures for converter-interfaced microgrids,” *Chinese Journal of Electrical Engineering*, vol. 3, no. 2, pp. 41–52, 2017.
- [8] Y. Han, H. Li, P. Shen, E. A. A. Coelho, and J. M. Guerrero, “Review of active and reactive power sharing strategies in hierarchical controlled microgrids,” *IEEE Transactions on Power Electronics*, vol. 32, no. 3, pp. 2427–2451, 2017.
- [9] T. Wang, D. O’Neill, and H. Kamath, “Dynamic control and optimization of distributed energy resources in a microgrid,” *IEEE Transactions on Smart Grid*, vol. 6, pp. 2884–2894, Nov 2015.
- [10] J. D. Watson and I. Lestas, “Frequency and voltage regulation in hybrid ac/dc networks,” *IEEE Transactions on Control Systems Technology*, vol. 29, pp. 1839–1849, Sept. 2021.
- [11] Y. Xu, H. Sun, W. Gu, Y. Xu, and Z. Li, “Optimal distributed control for secondary frequency and voltage regulation in an islanded microgrid,” *IEEE Transactions on Industrial Informatics*, vol. 15, pp. 225–235, Jan. 2019.
- [12] Y. Khayat, M. Naderi, Q. Shafiee, Y. Batmani, M. Fathi, J. M. Guerrero, and H. Bevrani, “Decentralized optimal frequency control in autonomous microgrids,” *IEEE Transactions on Power Systems*, vol. 34, no. 3, pp. 2345–2353, 2019.
- [13] H. Xin, R. Zhao, L. Zhang, Z. Wang, K. P. Wong, and W. Wei, “A decentralized hierarchical control structure and self-optimizing control strategy for f-p type dgs in islanded microgrids,” *IEEE Transactions on Smart Grid*, vol. 7, no. 1, pp. 3–5, 2016.
- [14] E. A. Coelho, D. Wu, J. M. Guerrero, J. C. Vasquez, T. Dragičević, C. Stefanović, and P. Popovski, “Small-signal analysis of the microgrid secondary control considering a communication time delay,” *IEEE Transactions on Industrial Electronics*, vol. 63, no. 10, pp. 6257–6269, 2016.
- [15] X. Lu, X. Yu, J. Lai, J. M. Guerrero, and H. Zhou, “Distributed secondary voltage and frequency control for islanded microgrids with uncertain communication links,” *IEEE Transactions on Industrial Informatics*, vol. 13, no. 2, pp. 448–460, 2017.
- [16] P. Gadde, S. Brahma, and T. Patel, “Real-time hardware-in-the-loop implementation of protection and self-healing of microgrids,” *IEEE Transactions on Industry Applications*, pp. 1–9, 2022.

- [17] S. Pradhan, S. Patra, and D. Chowdhury, “Decentralized decision making by an ant colony: drift-diffusion model of individual choice, quorum and collective decision,” 05 2021.
- [18] H.-K. Hsin, E.-J. Chang, K.-Y. Su, and A.-Y. Wu, “Ant colony optimization-based adaptive network-on-chip routing framework using network information region,” *IEEE Transactions on Computers*, vol. 64, no. 8, pp. 2119–2131, 2015.
- [19] V. Dwivedi, A. Norta, A. Wulf, B. Leiding, S. Saxena, and C. Udokwu, “A formal specification smart-contract language for legally binding decentralized autonomous organizations,” *IEEE Access*, vol. 9, pp. 76069–76082, 2021.
- [20] E. Bischof, A. Botezatu, S. Jakimov, I. Suharenko, A. Ostrovski, A. Verbitsky, Y. Yanovich, A. Zhavoronkov, and G. Zmudze, “Longevity foundation: Perspective on decentralized autonomous organization for special-purpose financing,” *IEEE Access*, vol. 10, pp. 33048–33058, 2022.
- [21] S. Wang, W. Ding, J. Li, Y. Yuan, L. Ouyang, and F.-Y. Wang, “Decentralized autonomous organizations: Concept, model, and applications,” *IEEE Transactions on Computational Social Systems*, vol. 6, no. 5, pp. 870–878, 2019.
- [22] J. L. Crespo-Vazquez, T. AlSkaif, Ã. M. González-Rueda, and M. Gibescu, “A community-based energy market design using decentralized decision-making under uncertainty,” *IEEE Transactions on Smart Grid*, vol. 12, no. 2, pp. 1782–1793, 2021.
- [23] D. H. Nguyen, “Optimal solution analysis and decentralized mechanisms for peer-to-peer energy markets,” *IEEE Transactions on Power Systems*, vol. 36, no. 2, pp. 1470–1481, 2021.
- [24] J. Jiang, S. Peyghami, C. Coates, and F. Blaabjerg, “A decentralized reliability-enhanced power sharing strategy for pv-based microgrids,” *IEEE Transactions on Power Electronics*, vol. 36, no. 6, pp. 7281–7293, 2021.
- [25] X. Fan, E. Crisostomi, D. Thomopoulos, B. Zhang, R. Shorten, and S. Yang, “An optimized decentralized power sharing strategy for wind farm de-loading,” *IEEE Transactions on Power Systems*, vol. 36, no. 1, pp. 136–146, 2021.
- [26] Y. A.-R. I. Mohamed and E. F. El-Saadany, “Adaptive decentralized droop controller to preserve power sharing stability of paralleled inverters in distributed generation microgrids,” *IEEE Transactions on Power Electronics*, vol. 23, no. 6, pp. 2806–2816, 2008.
- [27] A. K. Sahoo, K. Mahmud, M. Crittenden, J. Ravishankar, S. Padmanaban, and F. Blaabjerg, “Communication-less primary and secondary control in inverter-interfaced ac microgrid: An overview,” *IEEE Journal of Emerging and Selected Topics in Power Electronics*, vol. 9, no. 5, pp. 5164–5182, 2021.
- [28] Q. Zhong and Y. Zeng, “Universal droop control of inverters with different types of output impedance,” *IEEE Access*, vol. 4, pp. 702–712, 2016.
- [29] Q. Zhong, “Robust droop controller for accurate proportional load sharing among inverters operated in parallel,” *IEEE Transactions on Industrial Electronics*, vol. 60, no. 4, pp. 1281–1290, 2013.
- [30] J. C. Vasquez, J. M. Guerrero, A. Luna, P. Rodriguez, and R. Teodorescu, “Adaptive droop control applied to voltage-source inverters operating in grid-connected and islanded modes,” *IEEE Transactions on Industrial Electronics*, vol. 56, no. 10, pp. 4088–4096, 2009.
- [31] M. Lu, S. Dutta, V. Purba, S. Dhople, and B. Johnson, “A grid-compatible virtual oscillator controller: Analysis and design,” in *2019 IEEE Energy Conversion Congress and Exposition (ECCE)*, pp. 2643–2649, 2019.

- [32] V. Purba, X. Wu, M. Sinha, S. V. Dhople, and M. R. Jovanović, “Design of optimal coupling gains for synchronization of nonlinear oscillators,” in *2015 54th IEEE Conference on Decision and Control (CDC)*, pp. 1310–1315, 2015.
- [33] A. Haddadi, A. Yazdani, G. Joos, and B. Boulet, “A gain-scheduled decoupling control strategy for enhanced transient performance and stability of an islanded active distribution network,” *IEEE Transactions on Power Delivery*, vol. 29, pp. 560–569, April 2014.
- [34] C. Li, X. Liu, K. Sun, Y. Cao, F. Ma, and B. Zhou, “Industrial Active Distribution Networks,” *IEEE Transactions on Power Delivery*, vol. 33, no. 6, pp. 2590–2602, 2018.
- [35] P. H. Gadde and S. Brahma, “Realistic microgrid test bed for protection and resiliency studies,” in *2019 North American Power Symposium (NAPS)*, pp. 1–6, 2019.
- [36] I. Erlich, T. Neumann, F. Shewarega, P. Schegner, and J. Meyer, “Wind turbine negative sequence current control and its effect on power system protection,” in *2013 IEEE Power Energy Society General Meeting*, pp. 1–5, 2013.
- [37] *IEEE Draft Standard for Interconnection and Interoperability of Inverter-Based Resources (IBR) Interconnecting with Associated Transmission Electric Power Systems*, P2800/D6.3, Dec. 2021.
- [38] M. N. Kabir, Y. Mishra, G. Ledwich, Z. Y. Dong, and K. P. Wong, “Coordinated control of grid-connected photovoltaic reactive power and battery energy storage systems to improve the voltage profile of a residential distribution feeder,” *IEEE Transactions on Industrial Informatics*, vol. 10, no. 2, pp. 967–977, 2014.
- [39] W. Liu, W. Gu, W. Sheng, X. Meng, Z. Wu, and W. Chen, “Decentralized multi-agent system-based cooperative frequency control for autonomous microgrids with communication constraints,” *IEEE Transactions on Sustainable Energy*, vol. 5, no. 2, pp. 446–456, 2014.
- [40] H. Xu, A. D. Domínguez-García, and P. W. Sauer, “Data-driven coordination of distributed energy resources for active power provision,” *IEEE Transactions on Power Systems*, vol. 34, no. 4, pp. 3047–3058, 2019.
- [41] H. Zhang, J. Zhou, Q. Sun, J. M. Guerrero, and D. Ma, “Data-driven control for interlinked ac/dc microgrids via model-free adaptive control and dual-droop control,” *IEEE Transactions on Smart Grid*, vol. 8, no. 2, pp. 557–571, 2017.
- [42] H. Xu, A. D. Domínguez-García, V. V. Veeravalli, and P. W. Sauer, “Data-driven voltage regulation in radial power distribution systems,” *IEEE Transactions on Power Systems*, vol. 35, no. 3, pp. 2133–2143, 2020.
- [43] P. Bagheri and W. Xu, “Model-Free Volt-Var Control Based on Measurement Data Analytics,” *IEEE Transactions on Power Systems*, vol. 34, no. 2, pp. 1471–1482, 2019.
- [44] Y. Liu, Y. Li, H. Xin, H. B. Gooi, and J. Pan, “Distributed Optimal Tie-Line Power Flow Control for Multiple Interconnected AC Microgrids,” *IEEE Transactions on Power Systems*, vol. 34, no. 3, pp. 1869–1880, 2019.
- [45] H. Xu, A. D. Dominguez-Garcia, and P. W. Sauer, “Data-Driven Coordination of Distributed Energy Resources for Active Power Provision,” *IEEE Transactions on Power Systems*, vol. 34, no. 4, pp. 3047–3058, 2019.
- [46] R. Anilkumar, G. Devriese, and A. K. Srivastava, “Voltage and Reactive Power Control to Maximize the Energy Savings in Power Distribution System With Wind Energy,” *IEEE Transactions on Industry Applications*, vol. 54, no. 1, pp. 656–664, 2018.
- [47] “North Carolina Clean Energy Plan, [https://files.nc.gov/governor/documents/files/nc\\_clean\\_energy\\_plan\\_oct\\_2019\\_.pdf](https://files.nc.gov/governor/documents/files/nc_clean_energy_plan_oct_2019_.pdf). (accessed: 06.12.2022).”
- [48] “Goals of the Solar Energy Technologies Office, <https://www.energy.gov/eere/solar/goals-solarenergy-technologies-office>, (accessed: 09.02.2020).”

- [49] W. J. Cole and A. Frazier, “Cost projections for utility-scale battery storage: 2020 update NREL/TP-6A20-75385,” *National Renewable Energy Laboratory*, Jun 2020.
- [50] W. H. Kersting, *Distribution system modeling and analysis*. 2017.
- [51] I. Ray and L. M. Tolbert, “The case against phase-locked loops in weak ac grids,” in *2019 IEEE Electrical Power and Energy Conference (EPEC)*, pp. 1–5, 2019.
- [52] D. E. Olivares, A. Mehrizi-Sani, A. H. Etemadi, C. A. Canizares, R. Iravani, M. Kazerani, A. H. Hajimiragha, O. Gomis-Bellmunt, M. Saeedifard, R. Palma-Behnke, G. A. Jimenez-Estevez, and N. D. Hatziargyriou, “Trends in microgrid control,” *IEEE Transactions on Smart Grid*, vol. 5, no. 4, pp. 1905–1919, 2014.
- [53] A. Ingalalli and S. Kamalasadán, “A universal multiple inverter control architecture with droop for unbalanced distribution grid,” in *2021 IEEE Power Energy Society Innovative Smart Grid Technologies Conference (ISGT)*, pp. 1–5, 2021.
- [54] B. B. Johnson, S. V. Dhople, J. L. Cale, A. O. Hamadeh, and P. T. Krein, “Oscillator-based inverter control for islanded three-phase microgrids,” *IEEE Journal of Photovoltaics*, vol. 4, no. 1, pp. 387–395, 2014.
- [55] M. Li, B. Wei, P. xie, S. Tan, J. M. Guerrero, and J. C. Vasquez, “Synchronization and current sharing for nonlinear-oscillator-based inverters in islanded three-phase microgrid,” in *2019 IEEE Energy Conversion Congress and Exposition (ECCE)*, pp. 2566–2571, 2019.
- [56] M. A. Awal and I. Husain, “Unified virtual oscillator control for grid-forming and grid-following converters,” *IEEE Journal of Emerging and Selected Topics in Power Electronics*, pp. 1–1, 2020.
- [57] B. B. Johnson, S. V. Dhople, A. O. Hamadeh, and P. T. Krein, “Synchronization of parallel single-phase inverters with virtual oscillator control,” *IEEE Transactions on Power Electronics*, vol. 29, no. 11, pp. 6124–6138, 2014.
- [58] P. H. Gadde and S. Brahma, “Comparison of pr and pi controllers for inverter control in an unbalanced microgrid,” in *2020 52nd North American Power Symposium (NAPS)*, pp. 1–6, 2021.
- [59] A. Parisio, E. Rikos, L. Glielmo, and S. Member, “A Model Predictive Control Approach to Microgrid Operation Optimization,” *IEEE Transactions on Control Systems Technology*, vol. 22, no. 5, pp. 1813–1827, 2014.
- [60] N. Karthikeyan, J. R. Pillai, B. Bak-Jensen, and J. W. Simpson-Porco, “Predictive Control of Flexible Resources for Demand Response in Active Distribution Networks,” *IEEE Transactions on Power Systems*, vol. 34, no. 4, pp. 2957–2969, 2019.
- [61] X. Su, M. A. Masoum, and P. J. Wolfs, “Optimal PV inverter reactive power control and real power curtailment to improve performance of unbalanced four-wire LV distribution networks,” *IEEE Transactions on Sustainable Energy*, vol. 5, no. 3, pp. 967–977, 2014.
- [62] S. Moghadasi and S. Kamalasadán, “Optimal Fast Control and Scheduling of Power Distribution System Using Integrated Receding Horizon Control and Convex Conic Programming,” *IEEE Transactions on Industry Applications*, vol. 52, no. 3, pp. 2596–2606, 2016.
- [63] S. J. Hossain, T. G. Paul, R. Bisht, A. Suresh, and S. Kamalasadán, “An Integrated Battery Optimal Power Dispatch Architecture for End-User-Driven Microgrid in Islanded and Grid-Connected Mode of Operation,” *IEEE Transactions on Industry Applications*, vol. 54, no. 4, pp. 3806–3819, 2018.
- [64] S. Gholami, M. Aldeen, and S. Saha, “Control strategy for dispatchable distributed energy resources in islanded microgrids,” *IEEE Transactions on Power Systems*, vol. 33, pp. 141–152, Jan. 2018.

- [65] S. Kewat and B. Singh, "Grid synchronization of wec-pv-bes based distributed generation system using robust control strategy," *IEEE Transactions on Industry Applications*, vol. 56, no. 6, pp. 7088–7098, 2020.
- [66] Q. Huang and K. Rajashekara, "An improved delayed signal cancellation pll for fast grid synchronization under distorted and unbalanced grid condition," *IEEE Transactions on Industry Applications*, vol. 53, no. 5, pp. 4985–4997, 2017.
- [67] Q. Shafiee, J. M. Guerrero, and J. C. Vasquez, "Distributed secondary control for islanded microgrids—a novel approach," *IEEE Transactions on Power Electronics*, vol. 29, no. 2, pp. 1018–1031, 2014.
- [68] F. Guo, C. Wen, J. Mao, and Y. D. Song, "Distributed Secondary Voltage and Frequency Restoration Control of Droop-Controlled Inverter-Based Microgrids," *IEEE Transactions on Industrial Electronics*, vol. 62, no. 7, pp. 4355–4364, 2015.
- [69] Z. Li, C. Zang, P. Zeng, H. Yu, and S. Li, "Fully distributed hierarchical control of parallel grid-supporting inverters in islanded AC microgrids," *IEEE Transactions on Industrial Informatics*, vol. 14, no. 2, pp. 679–690, 2018.
- [70] A. Bidram, A. Davoudi, F. L. Lewis, and J. M. Guerrero, "Distributed cooperative secondary control of microgrids using feedback linearization," *IEEE Transactions on Power Systems*, vol. 28, no. 3, pp. 3462–3470, 2013.
- [71] N. M. Dehkordi, N. Sadati, and M. Hamzeh, "Fully distributed cooperative secondary frequency and voltage control of islanded microgrids," *IEEE Transactions on Energy Conversion*, vol. 32, no. 2, pp. 675–685, 2017.
- [72] N. M. Dehkordi, N. Sadati, and M. Hamzeh, "Distributed robust finite-time secondary voltage and frequency control of islanded microgrids," *IEEE Transactions on Power Systems*, vol. 32, no. 5, pp. 3648–3659, 2017.
- [73] F. Guo, C. Wen, J. Mao, and Y.-D. Song, "Distributed secondary voltage and frequency restoration control of droop-controlled inverter-based microgrids," *IEEE Transactions on Industrial Electronics*, vol. 62, no. 7, pp. 4355–4364, 2015.
- [74] Q. Shafiee, J. M. Guerrero, and J. C. Vasquez, "Distributed secondary control for islanded microgrids—a novel approach," *IEEE Transactions on Power Electronics*, vol. 29, no. 2, pp. 1018–1031, 2014.
- [75] J. W. Simpson-Porco, Q. Shafiee, F. Dorfler, J. C. Vasquez, J. M. Guerrero, and F. Bullo, "Secondary frequency and voltage control of islanded microgrids via distributed averaging," *IEEE Transactions on Industrial Electronics*, vol. 62, no. 11, pp. 7025–7038, 2015.
- [76] S. Sivaranjani, E. Agarwal, V. Gupta, P. Antsaklis, and L. Xie, "Distributed mixed voltage angle and frequency droop control of microgrid interconnections with loss of distribution-pmu measurements," *IEEE Open Access Journal of Power and Energy*, vol. 8, pp. 45–56, 2021.
- [77] M. Chen, X. Xiao, and J. M. Guerrero, "Secondary restoration control of islanded microgrids with a decentralized event-triggered strategy," *IEEE Transactions on Industrial Informatics*, vol. 14, no. 9, pp. 3870–3880, 2018.
- [78] W. Liu, J. Zhan, and C. Y. Chung, "A novel transactive energy control mechanism for collaborative networked microgrids," *IEEE Transactions on Power Systems*, vol. 34, no. 3, pp. 2048–2060, 2019.
- [79] Z. Tang, D. J. Hill, and T. Liu, "Fast distributed reactive power control for voltage regulation in distribution networks," *IEEE Transactions on Power Systems*, vol. 34, no. 1, pp. 802–805, 2019.
- [80] A. Ingalalli and S. Kamalasan, "An integrated state-space model for grid feeding and grid forming inverters," in *2020 IEEE International Conference on Power Electronics, Drives and Energy Systems (PEDES)*, pp. 1–6, 2020.

- [81] A. Ingalalli and S. Kamalasadán, “A novel sequence-based unified control architecture for multiple inverter modes of operation in unbalanced distribution system,” *IEEE Transactions on Power Delivery*, pp. 1–14, 2022.
- [82] A. Bani-Ahmed, M. Rashidi, A. Nasiri, and H. Hosseini, “Reliability analysis of a decentralized microgrid control architecture,” *IEEE Transactions on Smart Grid*, vol. 10, pp. 3910–3918, July 2019.
- [83] M. Farrokhbabadi, C. A. Canizares, and K. Bhattacharya, “Frequency control in isolated/islanded microgrids through voltage regulation,” *IEEE Transactions on Smart Grid*, vol. 8, pp. 1185–1194, May 2017.
- [84] H. Shi, F. Zhuo, H. Yi, F. Wang, D. Zhang, and Z. Geng, “A novel real-time voltage and frequency compensation strategy for photovoltaic-based microgrid,” *IEEE Transactions on Industrial Electronics*, vol. 62, pp. 3545–3556, June 2015.
- [85] N. Bottrell and T. C. Green, “Comparison of current-limiting strategies during fault ride-through of inverters to prevent latch-up and wind-up,” *IEEE Transactions on Power Electronics*, vol. 29, no. 7, pp. 3786–3797, 2014.
- [86] D. G. Holmes, T. A. Lipo, B. P. McGrath, and W. Y. Kong, “Optimized design of stationary frame three phase ac current regulators,” *IEEE Transactions on Power Electronics*, vol. 24, no. 11, pp. 2417–2426, 2009.
- [87] A. Ingalalli, U. Tamrakar, T. M. Hansen, and R. Tonkoski, “Modeling hydro power system frequency dynamics for virtual inertia emulation,” in *2019 IEEE 28th International Symposium on Industrial Electronics (ISIE)*, pp. 2565–2570, 2019.
- [88] D. Di Ruscio, “Model Predictive Control with Integral Action: A simple MPC algorithm,” *Modeling, Identification and Control*, vol. 34, no. 3, pp. 119–129, 2013.
- [89] X. Xing, J. Lin, C. Wan, and Y. Song, “Model Predictive Control of LPC-Looped Active Distribution Network With High Penetration of Distributed Generation,” *IEEE Transactions on Sustainable Energy*, vol. 8, no. 3, pp. 1051–1063, 2017.
- [90] C. Savaglio, P. Pace, G. Aloï, A. Liotta, and G. Fortino, “Lightweight reinforcement learning for energy efficient communications in wireless sensor networks,” *IEEE Access*, vol. 7, pp. 29355–29364, 2019.
- [91] R. S. Sutton and A. G. Barto, *Reinforcement learning: An introduction (2nd ed.)*. The MIT Press, 2018.
- [92] M. S. Rana, H. R. Pota, and I. R. Petersen, “Nonlinearity effects reduction of an afm piezoelectric tube scanner using mimo mpc,” *IEEE/ASME Transactions on Mechatronics*, vol. 20, no. 3, pp. 1458–1469, 2015.
- [93] M. S. Ashraf, M. U. Sajjad, F. Haider, S. Hannan, S. Aslam, and M. Hamza, “Model predictive control implementation for mimo system in presence of soft constraints and non-linear disturbance,” in *2020 International Conference on Electrical, Communication, and Computer Engineering (ICECCE)*, pp. 1–6, 2020.
- [94] V. Skiparev, J. Belikov, and E. Petlenkov, “Mimo reinforcement learning based approach for frequency support in microgrids with high renewable energy penetration,” in *2021 IEEE Power Energy Society General Meeting (PESGM)*, pp. 01–05, 2021.
- [95] L. Luo, J. Zhang, S. Chen, X. Zhang, B. Ai, and D. W. K. Ng, “Downlink power control for cell-free massive mimo with deep reinforcement learning,” *IEEE Transactions on Vehicular Technology*, vol. 71, no. 6, pp. 6772–6777, 2022.
- [96] X. Guo, W. Yan, and R. Cui, “Integral reinforcement learning-based adaptive nn control for continuous-time nonlinear mimo systems with unknown control directions,” *IEEE Transactions on Systems, Man, and Cybernetics: Systems*, vol. 50, no. 11, pp. 4068–4077, 2020.

- [97] H. Spieker, “Constraint-guided reinforcement learning: Augmenting the agent-environment-interaction,” in *2021 International Joint Conference on Neural Networks (IJCNN)*, pp. 1–8, 2021.
- [98] D. Liu, X. Yang, D. Wang, and Q. Wei, “Reinforcement-learning-based robust controller design for continuous-time uncertain nonlinear systems subject to input constraints,” *IEEE Transactions on Cybernetics*, vol. 45, no. 7, pp. 1372–1385, 2015.
- [99] A. Ingalalli and S. Kamalasadana, “Decentralized state estimation-based optimal integral model predictive control of voltage and frequency in the distribution system microgrids,” *IEEE Transactions on Smart Grid*, pp. 1–13, 2022.
- [100] M. S. Rana, H. R. Pota, and I. R. Petersen, “Performance of sinusoidal scanning with mpc in afm imaging,” *IEEE/ASME Transactions on Mechatronics*, vol. 20, no. 1, pp. 73–83, 2015.
- [101] E. O. Arwa and K. A. Folly, “Reinforcement learning techniques for optimal power control in grid-connected microgrids: A comprehensive review,” *IEEE Access*, vol. 8, pp. 208992–209007, 2020.
- [102] M. Adibi and J. van der Woude, “A reinforcement learning approach for frequency control of inverted-based microgrids,” *IFAC-PapersOnLine*, vol. 52, no. 4, pp. 111–116, 2019. IFAC Workshop on Control of Smart Grid and Renewable Energy Systems CSGRES 2019.
- [103] Z. Yan and Y. Xu, “Data-driven load frequency control for stochastic power systems: A deep reinforcement learning method with continuous action search,” *IEEE Transactions on Power Systems*, vol. 34, no. 2, pp. 1653–1656, 2019.
- [104] Z. Yang, K. Merrick, L. Jin, and H. A. Abbass, “Hierarchical deep reinforcement learning for continuous action control,” *IEEE Transactions on Neural Networks and Learning Systems*, vol. 29, no. 11, pp. 5174–5184, 2018.
- [105] H. Modares and F. L. Lewis, “Linear quadratic tracking control of partially-unknown continuous-time systems using reinforcement learning,” *IEEE Transactions on Automatic Control*, vol. 59, no. 11, pp. 3051–3056, 2014.
- [106] R. Yan and T. K. Saha, “Investigation of voltage imbalance due to distribution network unbalanced line configurations and load levels,” *IEEE Transactions on Power Systems*, vol. 28, no. 2, pp. 1829–1838, 2013.
- [107] T. Tran, T. Chun, H. Lee, H. Kim, and E. Nho, “PLL-based seamless transfer control between grid-connected and islanding modes in grid-connected inverters,” *IEEE Transactions on Power Electronics*, vol. 29, no. 10, pp. 5218–5228, 2014.
- [108] B. Mahamedi, M. Eskandari, J. E. Fletcher, and J. Zhu, “Sequence-based control strategy with current limiting for the fault ride-through of inverter-interfaced distributed generators,” *IEEE Transactions on Sustainable Energy*, vol. 11, no. 1, pp. 165–174, 2020.
- [109] N. S. Gurule, J. Hernandez-Alvidrez, M. J. Reno, A. Summers, S. Gonzalez, and J. Flicker, “Grid-forming inverter experimental testing of fault current contributions,” in *2019 IEEE 46th Photovoltaic Specialists Conference (PVSC)*, pp. 3150–3155, 2019.
- [110] A. Mojallal and S. Lotfifard, “Improving during and postfault response of fuel cells in symmetrical and asymmetrical grid fault cases,” *IEEE Transactions on Sustainable Energy*, vol. 9, no. 3, pp. 1407–1418, 2018.
- [111] D. Siemaszko, “Positive and negative sequence control for power converters under weak unbalanced networks,” in *2012 Electrical Systems for Aircraft, Railway and Ship Propulsion*, pp. 1–6, 2012.
- [112] *Power Generating Plants in the Low Voltage Grid*, VDE-AR-N 4105, 2019.

- [113] Y. Lin, J. H. Eto, B. B. Johnson, J. D. Flicker, R. H. Lasseter, H. N. Villegas Pico, G.-S. Seo, B. J. Pierre, and A. Ellis, "Research roadmap on grid-forming inverters,"
- [114] *IEEE Standard for Interconnection and Interoperability of Distributed Energy Resources with Associated Electric Power Systems Interfaces*, IEEE 1547-2018, 2018.
- [115] A. Camacho, M. Castilla, J. Miret, A. Borrell, and L. G. de Vicuna, "Active and reactive power strategies with peak current limitation for distributed generation inverters during unbalanced grid faults," *IEEE Transactions on Industrial Electronics*, vol. 62, no. 3, pp. 1515–1525, 2015.
- [116] I. Sadeghkhan, M. E. Hamedani Golshan, J. M. Guerrero, and A. Mehrizi-Sani, "A current limiting strategy to improve fault ride-through of inverter interfaced autonomous microgrids," *IEEE Transactions on Smart Grid*, vol. 8, no. 5, pp. 2138–2148, 2017.
- [117] N. R. Merritt, C. Chakraborty, and P. Bajpai, "New voltage control strategies for vsc-based dg units in an unbalanced microgrid," *IEEE Transactions on Sustainable Energy*, vol. 8, no. 3, pp. 1127–1139, 2017.
- [118] C. Guzman, A. Cardenas, and K. Agbossou, "Load sharing strategy for autonomous ac microgrids based on fpga implementation of adaline fl," *IEEE Transactions on Energy Conversion*, vol. 29, no. 3, pp. 663–672, 2014.
- [119] R. Majumder, A. Ghosh, G. Ledwich, and F. Zare, "Angle droop versus frequency droop in a voltage source converter based autonomous microgrid," in *2009 IEEE Power Energy Society General Meeting*, 2009.
- [120] M. Dai, M. N. Marwali, J.-W. Jung, and A. Keyhani, "Power flow control of a single distributed generation unit," *IEEE Transactions on Power Electronics*, vol. 23, no. 1, pp. 343–352, 2008.
- [121] J. M. Guerrero, J. C. Vasquez, J. Matas, L. G. de Vicuna, and M. Castilla, "Hierarchical control of droop-controlled ac and dc microgrids—a general approach toward standardization," *IEEE Transactions on Industrial Electronics*, vol. 58, no. 1, pp. 158–172, 2011.
- [122] S. M. Manson, A. Upreti, and M. J. Thompson, "Case study: Smart automatic synchronization in islanded power systems," *IEEE Transactions on Industry Applications*, vol. 52, no. 2, pp. 1241–1249, 2016.
- [123] W. T. Elsayed, H. Farag, H. H. Zeineldin, and E. F. El-Saadany, "Dynamic transitional droops for seamless line-switching in islanded microgrids," *IEEE Transactions on Power Systems*, vol. 36, no. 6, pp. 5590–5601, 2021.
- [124] M. Ganjian-Aboukheili, M. Shahabi, Q. Shafiee, and J. M. Guerrero, "Seamless transition of microgrids operation from grid-connected to islanded mode," *IEEE Transactions on Smart Grid*, vol. 11, no. 3, pp. 2106–2114, 2020.
- [125] X. Hou, Y. Sun, J. Lu, X. Zhang, L. H. Koh, M. Su, and J. M. Guerrero, "Distributed hierarchical control of ac microgrid operating in grid-connected, islanded and their transition modes," *IEEE Access*, vol. 6, pp. 77388–77401, 2018.
- [126] Y. A.-R. I. Mohamed and A. A. Radwan, "Hierarchical control system for robust microgrid operation and seamless mode transfer in active distribution systems," *IEEE Transactions on Smart Grid*, vol. 2, no. 2, pp. 352–362, 2011.
- [127] G. Lou, W. Gu, J. Wang, J. Wang, and B. Gu, "A unified control scheme based on a disturbance observer for seamless transition operation of inverter-interfaced distributed generation," *IEEE Transactions on Smart Grid*, vol. 9, no. 5, pp. 5444–5454, 2018.
- [128] R. Pena-Alzola, M. Liserre, F. Blaabjerg, R. Sebastian, J. Dannehl, and F. W. Fuchs, "Analysis of the passive damping losses in lcl-filter-based grid converters," *IEEE Transactions on Power Electronics*, vol. 28, no. 6, pp. 2642–2646, 2013.

- [129] J. Svensson, M. Bongiorno, and A. Sannino, "Practical implementation of delayed signal cancellation method for phase-sequence separation," *IEEE Transactions on Power Delivery*, vol. 22, no. 1, pp. 18–26, 2007.
- [130] J. L. Agorreta, M. Borrega, J. Lopez, and L. Marroyo, "Modeling and control of  $n$ -paralleled grid-connected inverters with lcl filter coupled due to grid impedance in pv plants," *IEEE Transactions on Power Electronics*, vol. 26, no. 3, pp. 770–785, 2011.
- [131] C. Z. Ally and E. C. W. de Jong, "Robust pi control of a grid-connected voltage source inverter for virtual inertia response in weak grid conditions," in *2019 International Conference on Smart Energy Systems and Technologies (SEST)*, pp. 1–6, 2019.
- [132] A. Ingalalli, K. S. Silpa, and R. Gore, "Scd based iec 61850 traffic estimation for substation automation networks," in *2017 22nd IEEE International Conference on Emerging Technologies and Factory Automation (ETFA)*, pp. 1–8, 2017.
- [133] K. Ma, W. Chen, M. Liserre, and F. Blaabjerg, "Power controllability of a three-phase converter with an unbalanced ac source," *IEEE Transactions on Power Electronics*, vol. 30, no. 3, pp. 1591–1604, 2015.
- [134] A. Ingalalli and J. V. V. N. Bapiraju, "Analytical model for real time simulation of low voltage induction motor drive," in *2017 IEEE International Electric Machines and Drives Conference (IEMDC)*, pp. 1–8, 2017.
- [135] A. Ingalalli, S. K. Bhadra, and A. Shyamaprasad, "Digitalization of electromechanical auxiliary relays in substation automation system," in *Proceedings of the 1st International Workshop on Future Industrial Communication Networks, FICN '18*, (New York, NY, USA), p. 9â14, Association for Computing Machinery, 2018.
- [136] P. H. Gadde and S. M. Brahma, "Topology-agnostic, scalable, self-healing and cost-aware protection of microgrids," *IEEE Transactions on Power Delivery*, pp. 1–1, 2021.
- [137] S. Huang, Q. Wu, W. Liao, G. Wu, X. Li, and J. Wei, "Adaptive droop-based hierarchical optimal voltage control scheme for vsc-hvdc connected offshore wind farm," *IEEE Transactions on Industrial Informatics*, vol. 17, pp. 8165–8176, Dec. 2021.
- [138] B.-S. Ko, G.-Y. Lee, K.-Y. Choi, R.-Y. Kim, S. Kim, J. Cho, and S.-I. Kim, "Flexible control structure for enhancement of scalability in dc microgrids," *IEEE Systems Journal*, vol. 14, pp. 4591–4601, Sept. 2020.
- [139] Q. Zhou, M. Shahidehpour, Z. Li, and X. Xu, "Two-layer control scheme for maintaining the frequency and the optimal economic operation of hybrid ac/dc microgrids," *IEEE Transactions on Power Systems*, vol. 34, pp. 64–75, Jan. 2019.
- [140] J. C. Vasquez, J. M. Guerrero, M. Savaghebi, J. Eloy-Garcia, and R. Teodorescu, "Modeling, analysis, and design of stationary-reference-frame droop-controlled parallel three-phase voltage source inverters," *IEEE Transactions on Industrial Electronics*, vol. 60, no. 4, pp. 1271–1280, 2013.
- [141] P. H. Divshali, A. Alimardani, S. H. Hosseinian, and M. Abedi, "Decentralized cooperative control strategy of microsources for stabilizing autonomous vsc-based microgrids," *IEEE Transactions on Power Systems*, vol. 27, no. 4, pp. 1949–1959, 2012.
- [142] A. Bidram and A. Davoudi, "Hierarchical structure of microgrids control system," *IEEE Transactions on Smart Grid*, vol. 3, no. 4, pp. 1963–1976, 2012.
- [143] Y. Han, H. Li, L. Xu, X. Zhao, and J. M. Guerrero, "Analysis of washout filter-based power sharing strategyâan equivalent secondary controller for islanded microgrid without lbc lines," *IEEE Transactions on Smart Grid*, vol. 9, pp. 4061–4076, Sept. 2018.
- [144] J. M. Rey, P. MartÃ, M. Velasco, J. Miret, and M. Castilla, "Secondary switched control with no communications for islanded microgrids," *IEEE Transactions on Industrial Electronics*, vol. 64, no. 11, pp. 8534–8545, 2017.

- [145] P. Ge, Y. Zhu, T. C. Green, and F. Teng, “Resilient secondary voltage control of islanded microgrids: An eskbf-based distributed fast terminal sliding mode control approach,” *IEEE Transactions on Power Systems*, vol. 36, pp. 1059–1070, March 2021.
- [146] W. Gu, G. Lou, W. Tan, and X. Yuan, “A nonlinear state estimator-based decentralized secondary voltage control scheme for autonomous microgrids,” *IEEE Transactions on Power Systems*, vol. 32, no. 6, pp. 4794–4804, 2017.
- [147] H. Haes Alhelou, M. E. Hamedani Golshan, and N. D. Hatziargyriou, “Deterministic dynamic state estimation-based optimal lfc for interconnected power systems using unknown input observer,” *IEEE Transactions on Smart Grid*, vol. 11, pp. 1582–1592, March 2020.
- [148] Y. Khayat, R. Heydari, M. Naderi, T. Dragicevic, Q. Shafiee, M. Fathi, H. Bevrani, and F. Blaabjerg, “Decentralized frequency control of ac microgrids: An estimation-based consensus approach,” *IEEE Journal of Emerging and Selected Topics in Power Electronics*, vol. 9, pp. 5183–5191, Oct. 2021.
- [149] G. Lou, W. Gu, Y. Xu, M. Cheng, and W. Liu, “Distributed mpc-based secondary voltage control scheme for autonomous droop-controlled microgrids,” *IEEE Transactions on Sustainable Energy*, vol. 8, no. 2, pp. 792–804, 2017.
- [150] Q. Yang, J. Zhou, X. Chen, and J. Wen, “Distributed mpc-based secondary control for energy storage systems in a dc microgrid,” *IEEE Transactions on Power Systems*, vol. 36, pp. 5633–5644, Nov. 2021.
- [151] K. Liu, T. Liu, Z. Tang, and D. J. Hill, “Distributed mpc-based frequency control in networked microgrids with voltage constraints,” *IEEE Transactions on Smart Grid*, vol. 10, pp. 6343–6354, Nov. 2019.
- [152] J. W. Simpson-Porco, F. Dorfler, and F. Bullo, “Synchronization and power sharing for droop-controlled inverters in islanded microgrids,” *Automatica*, vol. 49, no. 9, pp. 2603–2611, 2013.
- [153] C.-Y. Chang and W. Zhang, “Distributed control of inverter-based lossy microgrids for power sharing and frequency regulation under voltage constraints,” *Automatica*, vol. 66, pp. 85–95, 2016.
- [154] S. Puthusserypady and A. P. Kurian, “Variants of kalman filter for the synchronization of chaotic systems,” in *Kalman Filter* (V. Kordic, ed.), ch. 11, Rijeka: IntechOpen, 2010.
- [155] G. Ravikumar, D. Ameme, S. Misra, S. Brahma, and R. Tourani, “icasm: An information-centric network architecture for wide area measurement systems,” *IEEE Transactions on Smart Grid*, vol. 11, no. 4, pp. 3418–3427, 2020.
- [156] A. Ingalalli, H. Satheesh, and M. Kande, “Platform for hardware in loop simulation,” in *2016 International Symposium on Power Electronics, Electrical Drives, Automation and Motion (SPEEDAM)*, pp. 41–46, 2016.
- [157] Y. Xu, “Robust finite-time control for autonomous operation of an inverter-based microgrid,” *IEEE Transactions on Industrial Informatics*, vol. 13, no. 5, pp. 2717–2725, 2017.
- [158] Q. Yang, G. Wang, A. Sadeghi, G. B. Giannakis, and J. Sun, “Two-timescale voltage control in distribution grids using deep reinforcement learning,” *IEEE Transactions on Smart Grid*, vol. 11, no. 3, pp. 2313–2323, 2020.
- [159] J. Duan, Z. Yi, D. Shi, C. Lin, X. Lu, and Z. Wang, “Reinforcement-learning-based optimal control of hybrid energy storage systems in hybrid ac&dc microgrids,” *IEEE Transactions on Industrial Informatics*, vol. 15, no. 9, pp. 5355–5364, 2019.
- [160] D.-D. Zheng, S. S. Madani, and A. Karimi, “Data-driven distributed online learning control for islanded microgrids,” *IEEE Journal on Emerging and Selected Topics in Circuits and Systems*, vol. 12, no. 1, pp. 194–204, 2022.

- [161] S. S. Madani, C. Kammer, and A. Karimi, “Data-driven distributed combined primary and secondary control in microgrids,” *IEEE Transactions on Control Systems Technology*, vol. 29, no. 3, pp. 1340–1347, 2021.
- [162] R. Chai, A. Tsourdos, H. Gao, S. Chai, and Y. Xia, “Attitude tracking control for reentry vehicles using centralised robust model predictive control,” *Automatica*, vol. 145, p. 110561, 2022.
- [163] R. Chai, A. Tsourdos, H. Gao, Y. Xia, and S. Chai, “Dual-loop tube-based robust model predictive attitude tracking control for spacecraft with system constraints and additive disturbances,” *IEEE Transactions on Industrial Electronics*, vol. 69, no. 4, pp. 4022–4033, 2022.
- [164] S. Boyd and L. Vandenberghe, *Convex Optimization*. Cambridge University Press, 2004.
- [165] “Powering Real-Time Simulation, (2022), <https://www.opal-rt.com/software-rt-lab-2-2/>. (accessed: 06.04.2022).”
- [166] *IEEE Standard for Harmonic Control in Electric Power Systems*, 2022.
- [167] Z. Wang and J. Wang, “Self-healing resilient distribution systems based on sectionalization into microgrids,” *IEEE Transactions on Power Systems*, vol. 30, no. 6, pp. 3139–3149, 2015.
- [168] C. Chen, J. Wang, F. Qiu, and D. Zhao, “Resilient distribution system by microgrids formation after natural disasters,” *IEEE Transactions on Smart Grid*, vol. 7, no. 2, pp. 958–966, 2016.
- [169] S. Chanda and A. K. Srivastava, “Defining and enabling resiliency of electric distribution systems with multiple microgrids,” *IEEE Transactions on Smart Grid*, vol. 7, no. 6, pp. 2859–2868, 2016.
- [170] S. A. Taher, M. Zolfaghari, C. Cho, M. Abedi, and M. Shahidehpour, “A new approach for soft synchronization of microgrid using robust control theory,” *IEEE Transactions on Power Delivery*, vol. 32, no. 3, pp. 1370–1381, 2017.
- [171] Y. Kim, J. Wang, and X. Lu, “A framework for load service restoration using dynamic change in boundaries of advanced microgrids with synchronous-machine dgs,” *IEEE Transactions on Smart Grid*, vol. 9, no. 4, pp. 3676–3690, 2018.
- [172] S. Thakar, A. S. Vijay, and S. Doolla, “Effect of p-q limits on microgrid reconfiguration: A capability curve perspective,” *IEEE Transactions on Sustainable Energy*, vol. 11, no. 3, pp. 2040–2048, 2020.
- [173] Y. Gupta, R. Nellikkath, K. Chatterjee, and S. Doolla, “Voltâvar optimization and reconfiguration: Reducing power demand and losses in a droop-based microgrid,” *IEEE Transactions on Industry Applications*, vol. 57, no. 3, pp. 2769–2781, 2021.
- [174] D. K. Dheer, O. V. Kulkarni, S. Doolla, and A. K. Rathore, “Effect of reconfiguration and meshed networks on the small-signal stability margin of droop-based islanded microgrids,” *IEEE Transactions on Industry Applications*, vol. 54, no. 3, pp. 2821–2833, 2018.
- [175] Y. Men, Y. Du, and X. Lu, “Distributed control framework and scalable small-signal stability analysis for dynamic microgrids,” *Chinese Journal of Electrical Engineering*, vol. 7, no. 4, pp. 49–59, 2021.
- [176] X. Cao, J. Wang, J. Wang, and B. Zeng, “A risk-averse conic model for networked microgrids planning with reconfiguration and reorganizations,” *IEEE Transactions on Smart Grid*, vol. 11, no. 1, pp. 696–709, 2020.
- [177] K. Duwadi, A. Ingalalli, and T. M. Hansen, “Monte carlo analysis of high penetration residential solar voltage impacts using high performance computing,” in *2019 IEEE International Conference on Electro Information Technology (EIT)*, pp. 1–6, 2019.

- [178] M. M. A. Abdelaziz, H. E. Farag, and E. F. El-Saadany, "Optimum reconfiguration of droop-controlled islanded microgrids," *IEEE Transactions on Power Systems*, vol. 31, no. 3, pp. 2144–2153, 2016.
- [179] S. Lei, C. Chen, Y. Song, and Y. Hou, "Radiality constraints for resilient reconfiguration of distribution systems: Formulation and application to microgrid formation," *IEEE Transactions on Smart Grid*, vol. 11, no. 5, pp. 3944–3956, 2020.
- [180] F. Shariatzadeh, C. B. Vellaithurai, S. S. Biswas, R. Zamora, and A. K. Srivastava, "Real-time implementation of intelligent reconfiguration algorithm for microgrid," *IEEE Transactions on Sustainable Energy*, vol. 5, no. 2, pp. 598–607, 2014.
- [181] M. Choobineh, D. Silva-Ortiz, and S. Mohagheghi, "An automation scheme for emergency operation of a multi-microgrid industrial park," *IEEE Transactions on Industry Applications*, vol. 54, no. 6, pp. 6450–6459, 2018.
- [182] S. Kamalasadán and A. Ghandakly, "A neural network based intelligent model reference adaptive controller," in *2004 IEEE International Conference on Computational Intelligence for Measurement Systems and Applications, 2004. CIMSA.*, pp. 174–179, 2004.
- [183] R. Yousefian and S. Kamalasadán, "A lyapunov function based optimal hybrid power system controller for improved transient stability," *Electric Power Systems Research*, vol. 137, pp. 6–15, 2016.
- [184] X. He, H. Jiang, Y. Song, C. He, and H. Xiao, "Routing selection with reinforcement learning for energy harvesting multi-hop crn," *IEEE Access*, vol. 7, pp. 54435–54448, 2019.
- [185] A. Rovira-Sugranes, F. Afghah, J. Qu, and A. Razi, "Fully-echoed q-routing with simulated annealing inference for flying adhoc networks," *IEEE Transactions on Network Science and Engineering*, vol. 8, no. 3, pp. 2223–2234, 2021.
- [186] R. Errouissi, H. Shareef, and A. Wahyudie, "A novel design of pr controller with antiwindup scheme for single-phase interconnected pv systems," *IEEE Transactions on Industry Applications*, vol. 57, no. 5, pp. 5461–5475, 2021.
- [187] T. Patel, P. Gadde, S. Brahma, J. Hernandez-Alvidrez, and M. J. Reno, "Real-time microgrid test bed for protection and resiliency studies," in *2020 52nd North American Power Symposium (NAPS)*, pp. 1–6, 2021.
- [188] J. L. Blackburn and T. J. Domin, *Protective Relaying, Principles and Applications*, (3rd ed.). New York: CRC Press, 2006.
- [189] A. Ingalalli, S. Kamalasadán, Z. Dong, G. Bharati, and S. Chakraborty, "An extended q-routing-based event-driven dynamic reconfiguration of networked microgrids," in *2022 IEEE Industry Applications Society Annual Meeting (IAS)*, pp. 1–6, 2022.
- [190] S. J. Hossain, T. G. Paul, R. Bisht, A. Suresh, and S. Kamalasadán, "An integrated battery optimal power dispatch architecture for end-user-driven microgrid in islanded and grid-connected mode of operation," *IEEE Transactions on Industry Applications*, vol. 54, no. 4, pp. 3806–3819, 2018.
- [191] T. G. Paul, S. J. Hossain, S. Ghosh, P. Mandal, and S. Kamalasadán, "A quadratic programming based optimal power and battery dispatch for grid-connected microgrid," *IEEE Transactions on Industry Applications*, vol. 54, no. 2, pp. 1793–1805, 2018.
- [192] "Deloitte, *Energy-as-a-Service: The lights are on. Is anyone home?* (2020), <https://www2.deloitte.com/uk/en/pages/energy-and-resources/articles/energy-as-a-service.html>, (accessed: 09.02.2020)."
- [193] Zhaoyu Wang, Bokan Chen, Jianhui Wang, M. Begovic, and Chen Chen, "Coordinated energy management of networked microgrids in distribution systems," in *2015 IEEE Power Energy Society General Meeting*, pp. 1–1, 2015.

- [194] M. Erol-Kantarci and H. T. Mouftah, “Energy-efficient information and communication infrastructures in the smart grid: A survey on interactions and open issues,” *IEEE Communications Surveys Tutorials*, vol. 17, no. 1, pp. 179–197, 2015.
- [195] S. N. Backhaus, L. Dobriansky, S. Glover, C.-C. Liu, P. Looney, S. Mashayekh, A. Pratt, K. Schneider, M. Stadler, M. Starke, J. Wang, and M. Yue, “Networked microgrids scoping study,” Dec 2016.
- [196] Y. Du, X. Lu, H. Tu, J. Wang, and S. Lukic, “Dynamic microgrids with self-organized grid-forming inverters in unbalanced distribution feeders,” *IEEE Journal of Emerging and Selected Topics in Power Electronics*, vol. 8, no. 2, pp. 1097–1107, 2020.
- [197] “Fortune Business Insights, *Energy-as-a-Service Market Size, Share, and Industry Analysis* (2020), <https://www.fortunebusinessinsights.com/industry-reports/energy-as-a-service-market-101204>, (accessed: 09.02.2020).”
- [198] A. Ingalalli, R. Kumar, and S. K. Bhadra, “Ontological formulation of microgrid control system for interoperability,” in *2018 IEEE 23rd International Conference on Emerging Technologies and Factory Automation (ETFA)*, vol. 1, pp. 1391–1398, 2018.
- [199] “An Industrial Internet Consortium, *Applying the Industrial Internet Reference Architecture to a Smart Grid Testbed* (2016), <https://www.iiconsortium.org/pdf/applying-iira-to-smart-grid-testbed-wp-pub.pdf>, (accessed: 09.02.2020).”
- [200] M. Panteli, P. Mancarella, D. N. Trakas, E. Kyriakides, and N. D. Hatziargyriou, “Metrics and quantification of operational and infrastructure resilience in power systems,” *IEEE Transactions on Power Systems*, vol. 32, no. 6, pp. 4732–4742, 2017.
- [201] M. Panteli, D. N. Trakas, P. Mancarella, and N. D. Hatziargyriou, “Power systems resilience assessment: Hardening and smart operational enhancement strategies,” *Proceedings of the IEEE*, vol. 105, no. 7, pp. 1202–1213, 2017.
- [202] A. Ingalalli, A. Luna, V. Durvasulu, T. M. Hansen, R. Tonkoski, D. A. Copp, and T. A. Nguyen, “Energy storage systems in emerging electricity markets: Frequency regulation and resiliency,” in *2019 IEEE Power Energy Society General Meeting (PESGM)*, pp. 1–5, 2019.
- [203] S. P. Simonovic and R. Arunkumar, “Comparison of static and dynamic resilience for a multipurpose reservoir operation,” *Water Resources Research*, vol. 52, no. 11, pp. 8630–8649.
- [204] K. P. Schneider, S. Member, S. Laval, S. Member, J. Hansen, R. B. Melton, S. Member, L. Ponder, L. Fox, J. Hart, J. Hambrick, A. Smallwood, A. Jayantilal, and S. Member, “A Distributed Power System Control Architecture for Improved Distribution System Resiliency,” *IEEE Access*, vol. 7, pp. 9957–9970, 2019.
- [205] M. Geissdoerfer, D. Vladimirova, and S. Evans, “Sustainable business model innovation: A review,” *Journal of Cleaner Production*, vol. 198, pp. 401 – 416, 2018.
- [206] S. Rusitschka, M. Sturm, and M. Lehofer, “Disruptive potential and business model innovation through elastic microgrid-as-a-service (maas) platforms,” in *CIREN Workshop*, pp. 93 (5 .)–93 (5 .), 01 2016.
- [207] J. G. Francisco Flores-Espino and A. Pratt, “*Networked Microgrid Optimal Design and Operations Tool: Regulatory and Business Environment Study* (2020), <https://www.nrel.gov/docs/fy20osti/70944.pdf>, (accessed: 09.02.2020).”
- [208] S. Lakshminarayana, S. Sthapit, and C. Maple, “Application of physics-informed machine learning techniques for power grid parameter estimation,” *Sustainability*, vol. 14, no. 4, 2022.
- [209] L. Zhang, G. Wang, and G. B. Giannakis, “Real-time power system state estimation and forecasting via deep unrolled neural networks,” *IEEE Transactions on Signal Processing*, vol. 67, no. 15, pp. 4069–4077, 2019.